On Conductance and Interface Effects in Molecular Devices

ON CONDUCTANCE AND INTERFACE EFFECTS IN MOLECULAR DEVICES

Proefschrift

ter verkrijging van de graad van doctor
aan de Technische Universiteit Delft,
op gezag van de Rector Magnificus prof. ir. K. C. A. M. Luyben,
voorzitter van het College voor Promoties,
in het openbaar te verdedigen op dinsdag 27 november 2012 om 10:00 uur

door

Christopher Jon Oliver VERZIJL

wiskundig ingenieur &
ingenieur luchtvaart en ruimtevaart
geboren te Willemstad, Curaçao, Nederlandse Antillen.

Dit proefschrift is goedgekeurd door de promotor:

Prof. dr. ir. H. S. J. van der Zant

Copromotor: Dr. J. M. Thijssen

Samenstelling promotiecommissie:

Rector Magnificus,	voorzitter
Prof. dr. ir. H. S. J. van der Zant,	Technische Universiteit Delft (promotor)
Dr. J. M. Thijssen,	Technische Universiteit Delft (co-promotor)
Prof. dr. L. D. A. Siebbeles	Technische Universiteit Delft
Prof. dr. J. M. van Ruitenbeek,	Universiteit Leiden
Prof. dr. F. Evers,	Karlsruher Institut für Technologie
Prof. dr. K. Park,	Virginia Tech
Dr. S. J. A. van Gisbergen,	Scientific Computing & Modelling
Prof. dr. ir. T. M. Klapwijk,	Technische Universiteit Delft (reservelid)

Keywords: single-molecule devices · DFT · NEGF · image charges · interface effects · level alignment

Printed by: Gildeprint Drukkerijen

Casimir PhD Series, Delft-Leiden 2012-22

ISBN 978-90-8593-143-0

An electronic version of this dissertation is available at
`http://repository.tudelft.nl/`.

I'm driving through the desert I,
met a man
Who told me of his crazy plan
He'd been walking there
for 20 days
He was going to walk on
for 20 more.

Dave Matthews Band

CONTENTS

SYMBOLS & ABBREVIATIONS

T, β	Temperature, $\beta = (k_\mathrm{B}T)^{-1}$
μ	Chemical Potential
$f(\epsilon)$	Fermi-Dirac distribution: $f(\epsilon) = \left(e^{\epsilon/k_BT} + 1\right)^{-1}$
$f(\epsilon;\mu)$	idem, energy relative to μ: $f(\epsilon;\mu) = \left(e^{(\epsilon-\mu)/k_BT} + 1\right)^{-1}$

DFT	Density Functional Theory
NEGF	Non-Equilibrium Green's Functions
SCF	Self-Consistent Field
WBL	Wide-Band Limit
HOMO	Highest Occupied Molecular Orbital
LUMO	Lowest Unoccupied Molecular Orbital
EA	Electron Affinity
IP	Ionization Potential
KS	Kohn-Sham
TB	Tight-Binding
EM	Extended Molecule
DIIS	Direct Inversion of Iterative Subspaces
CDIIS	Constrained DIIS
CDFT	Constrained Density Functional Theory
MCBJ	Mechanically Controlled Break Junction
EBJ	Electromigrated Break Junction
ICE	Image-charge Effect

SZ	Single-ζ (basis set)
DZ	Double-ζ
TZP	Triple-ζ-plus-polarization
TZ2P	Triple-ζ-double-polarization

1

INTRODUCTION

In this chapter we introduce the field of molecular electronics, and link it to the broader discipline of quantum transport. We note the major open questions in the context of the advances in the field over the past decade, and outline the organization of the work presented in this thesis.

1.1 MOLECULAR ELECTRONICS

The scientific motivation for work in the field of molecular electronics is typically based on one of three viewpoints.

The first is the field's promise as a way of bypassing problems in traditional silicon (computing) technology, which arise when scaling down to structures of only a few nanometers. There, thermal dissipation problems and a lack of reliability in fabrication set a "atomic-scale limit" to the remaining achievable gains in performance.[1] The hope is that molecules as active components in devices can be mass-produced cheaply through synthetic chemistry, and can be designed to have low enough activation energies that thermal dissipation becomes a less critical issue.

The second motivation comes from the scope for exploiting molecular functionality in devices, originating in the versatility of design by synthetic chemistry.[2,3] Whereas in semiconductors the main functionality comes from intrinsic electronic structure and tuning the concentration of dopants, in molecules one can experiment with resonant *vs.* off-resonant transport,[4–7] mechanical and electrical switching,[8–10] spin as an information carrier,[11–15] molecular magnetism,[16,17] the absorption and emission of light,[18,19] and interplay between all of the above, besides the introduction of traditional functionality such as transistor/rectifier characteristics, as originally suggested by Aviram & Ratner.[20]

The third viewpoint however, is that using molecules and designing devices on this scale creates a fascinating playground for exploring fundamental physics. Devices demonstrated in recent years combine functionality and structural design as building blocks, and exploit electrical, vibrational, magnetic and optical effects, often intertwined with one another, and intrinsically quantum mechanical in nature.

These three motivations clearly aren't mutually exclusive, and while different parts of the molecular electronics community approach their work from one viewpoint more dominantly than another, they clearly reinforce each other.

We will focus particularly on single-molecule– rather than bulk devices (where the functionality of a particular molecule is less important than the behavior of the molecules collectively). In this case, the path to the current state of the art began with developing experimental techniques to contact the molecule. These include scanning-tunneling microscopy (STM),[21–23] mechanically controlled break-junctions (MCBJs)[24–26] and electromigrated break-junctions (EBJs).[27–30]

With these developments it became possible to observe conductance plateaus down to a single conductance quantum ($1G_0 = \frac{2e^2}{h} \approx 7.75 \cdot 10^{-5}\Omega^{-1}$) as a function of "breaking" the junction by progressively narrowing a constriction down to a single atomic channel. With a molecule in the junction acting as a conducting pathway, this same $1G_0$ plateau can be observed in resonant transport, while in general, statistical analysis of measurements can be used to resolve sub-G_0 conductance peaks, corresponding to off-resonant molecular transport.[31–33]

With the addition of a gate electrode coupled only electrostatically to the device, three-terminal transistor configurations became possible, first in EBJs[28,34] and later in MCBJs as well.[33,35] These allowed the taking of stability diagrams, differential conductance plotted *vs.* both gate and bias-voltage: $\frac{\partial I}{\partial V}(V, V_g)$, which were a first step in distinguishing true molecular junctions from setups contaminated by the presence of gold grains.[28,29] Gold grains were a large problem, as they give rise to features remarkably similar to those occurring in molecular transport junctions in current-voltage or $I(V)$ measurements, but luckily they can be distinguished more clearly with the extra information contained in stability diagrams.

These advances led to further development of techniques for "molecular fingerprinting," such as the identification of molecules by their vibrational modes,[36,37] as well as spin-dependent effects in magnetic molecules,[13,38] which in turn suggested the possibility of "molecular spintronics."[15]

Facing the future, there are a number of challenges that are currently being addressed. The first is identification; answering the dual questions of whether a molecular junction has indeed been formed, and whether this is truly a single-molecule junction, when that is the stated goal. The most promising approaches in that direction appear to lie along the lines of molecular fingerprinting, backed by solid theoretical modeling, which is a first motivation for the work in this thesis.

A second challenge is to overcome the lack of reproducibility in the experiments, which are often characterized by low experimental yields and an approach best characterized by "loving the one you have, rather than having the one you love." If identification can be handled satisfactorily, this does not get in the way of doing beautiful physics with the devices obtained (witness the rapid growth of the field over the past decade), but it does hinder the path forward to the first motivation: integration with computing technology.

The problem of how to integrate such (single-) molecular devices in a scalable mass-production approach to device fabrication is in many ways still an open question. While we cannot hope to address this in theoretical work, it is our hope that a better understanding of the origins of molecular-device functionality and the role of the metal-molecule interface, which we can address, will contribute to the solution of this problem in the (near) future.

Returning to the domain of theory, we observe that at the nanometer scale, the classical description of charge transport (Ohm's law) is supplanted by the consequences of quantum mechanics for charge transport. When the functionality of the device at the (quantum-)chemical level is paramount, we need a microscopic understanding from first principles.

Problems in this field are often treated using either "toy models" focusing on only the essential physics, or more computationally intensive "atomistic" or "*ab initio* models" which attempt to take the full chemical complexity of the metal-molecule systems into account.[a] These are considered large systems, because a full description

---

[a] Note that throughout this thesis we intend *ab initio* in the sense used by physicists, indicating parameter-free methods based on only a description of the chemical constituents of the system, their positions

requires treating the combination of electrodes *and* the molecule(s): systems on the order of a few thousand electrons in total. Precisely this challenging problem is also a most interesting one: treating quantum charge transport in molecular systems where the chemistry matters. A viable approach to this is the subject of the present work, and we briefly introduce the main ideas of quantum transport in the next section, to set the stage.

1.2 QUANTUM TRANSPORT

Let us introduce a few of the main ideas of quantum transport qualitatively. We want to describe the transport of electrons through some nanoscale junction, which we may refer to as an "active," "scattering," or "device" region equivalently, with the electrons being injected from and absorbed back into very large (macroscopic) reservoirs, both in thermodynamic equilibrium very far away from the junction, but usually at different chemical potentials.

Our aim is to study molecular electronics in this framework, and we will generally discuss transport in the Landauer picture,[39,40] with the active region in the device being one or more molecules connected to two conducting electrodes or contacts. These are each open to reservoirs of electrons. The formalism is based on three key assumptions:

1. There are no dynamical correlations between the electrons in the system, though they may still interact at a mean-field level.
2. Transport is assumed to take place in an ideal steady-state, corresponding to the long-time limit of the dynamics of the device.
3. The reservoirs to which the device region is coupled are in equilibrium, though usually at different chemical potentials and/or temperatures (which is relevant for thermoelectric effects), with distributions given by the Fermi-Dirac function $f_i(\epsilon) = \left(e^{(\epsilon-\mu_i)/k_B T_i} + 1\right)^{-1}$ for the i^{th} reservoir.

It is essential that the first assumption still allows for Coulomb interactions between the electrons to be accounted for in a mean-field picture, lending itself to electronic structure methods such as density-functional theory, which we discuss in Chapter 2.

Under these assumptions it can be shown that, as discussed in detail in the textbooks by Datta,[41] Di Ventra[42] and Nazarov and Blanter,[43] the resulting transport through the device is captured in two quantities of interest: a generally bias-dependent transmission $\mathcal{T}(\epsilon, V_b)$, where the bias $V_b = (\mu_1 - \mu_2)/e$, and the steady-

---

and possibly the chemical potentials of the electrodes, and not the sense used by chemists, indicating typically post Hartree-Fock methods of increasing sophistication.

state current I, given by the Landauer formula:

$$I(V_b) = \frac{2e}{h} \int_{-\infty}^{\infty} \mathrm{d}\epsilon \, [f_1(\epsilon) - f_2(\epsilon)] \, \mathcal{T}(\epsilon, V_b). \tag{1.1}$$

In the zero-bias limit this yields the zero-bias current (to first order in $(\mu_1 - \mu_2)$):

$$I = \frac{2e^2}{h} \mathcal{T}(\epsilon = \epsilon_f) V_b \, ,$$

with ϵ_f the Fermi energy of the electrodes, and $\frac{2e^2}{h}$ again the conductance quantum.[b] Note also that this describes ballistic transport, rather than the diffusive transport regime (resulting from scattering on impurities) which leads to Ohm's law. As such the conductance quantum (or equivalently the implication of a minimum resistance) reflects that the conductance is determined by the number of channels available for transport, and not by material properties.

The Landauer picture of transport also lends itself well to application in the Green's function formulation of transport, which is fully equivalent to the scattering approach usually used to derive Eq. (1.1) for effective single-particle problems. It can also be extended in powerful ways beyond an effective single-particle theory, and we discuss it in Chapter 2 as the basis of our computational approach to molecular transport.

1.3 OUTLINE

The molecular transport calculations discussed in this thesis are based on the combination of density functional theory (DFT) with the non-equilibrium Green's function (NEGF) formalism for transport, developed within the Landauer formalism. As noted above, treating the quantum-chemistry at an *ab initio* or first-principles level implies large-scale calculations. In order to make these feasible, we have implemented this formalism as a custom, scalable extension to the ADF/BAND quantum-chemistry package.[44–47] In this thesis we will report on the framework, the implementation, and its validation, before considering studies of novel systems performed with our code. The thesis is organized as follows.

Chapter 2 discusses the theoretical framework behind our implementation schematically, focusing on the combination of density functional theory calculations with the non-equilibrium Green's function formalism for transport.

In **Chapter 3** we outline the actual implementation of the method in detail, commenting on some subtle points in relation to the BAND code, which are critical to the efficiency of the calculations.

Chapters 4–5 discuss calculations performed for validation of the method and our implementation. In the one-dimensional case we present benchmark results

---

[b] Assuming $\mathcal{T}(\epsilon = \mu_1) \approx \mathcal{T}(\epsilon = \mu_2) \approx \mathcal{T}(\epsilon_f)$ in the limit where the difference between the chemical potentials goes to zero in such a way that both go to the Fermi energy of the electron gas at equilibrium.

on lithium (Li) and aluminum (Al) monatomic chain systems. In the general three-dimensional case we discuss the benchmark calculations of benzene-dithiol (BDT) and oligo-phenylene-ethynylene-dithiols (OPE's) on gold (Au) electrodes in two-terminal geometries.

In **Chapter 6**, we study a device based on tetraphenyl-porphyrin molecules sandwiched between gold contacts in a mechanically-controlled break junction (MCBJ) geometry. For this system we discuss the importance of interface effects, in particular image-charge effects, which dramatically influence the level alignment at the interface, and thereby transport. In this study we also make use of a rudimentary implementation of a gate field, as a first approximation to a true three-terminal device geometry.

Finally, in **Chapter 7**, we turn our attention to the performance of simplifying approximations to full transport calculations, where we will show that the balance between the importance of the molecule and the metal-molecule interface, respectively, determines the quality of approximate transport calculations for molecular systems.

A number of important details, which are not essential to the main thesis, are discussed in the appendices. **Appendix A** discusses the determination of surface Green's functions and self-energies of the electrodes in molecular devices. Next, in **Appendix B** we discuss the technique for peak decompositions we will use to study transmissions through the devices. **Appendix C** discusses transport through one dimensional tight-binding chains, with which we will compare the computational results for monatomic wires. In **Appendix D** we describe our constrained DIIS algorithm, which can drastically accelerate the alignment stage of the transport calculations. For reference, **Appendix E** outlines the structure and dependencies of the code in the multi-stage calculation, and **Appendix F** provides sample input files for each stage. Finally, in **Appendix G** the context and valorization of the implementation work underlying this thesis is discussed.

REFERENCES

[1] M. Schulz, *The End of the Road for Silicon?*, Nature **399**, 729 (1999).

[2] K. Moth-Poulsen and T. Bjørnholm, *Molecular electronics with single molecules in solid-state devices*, Nat. Nano **4**, 551 (2009).

[3] H. Song, M. A. Reed, and T. Lee, *Single Molecule Electronic Devices*, Adv. Mat. pp. n/a–n/a (2011).

[4] S. Y. Quek, H. J. Choi, S. G. Louie, and J. B. Neaton, *Length Dependence of Conductance in Aromatic Single-Molecule Junctions*, Nano Lett. **9**, 3949 (2009).

[5] I. V. Krive, A. Palevski, R. I. Shekhter, and M. Jonson, *Resonant tunneling of electrons in quantum wires (Review)*, Low Temperature Physics **36**, 119 (2010).

[6] Z.-L. Cheng, R. Skouta, H. Vazquez, J. R., Widawsky, S. Schneebeli, W. Chen, M. S., Hybertsen, R. Breslow, and L. Venkataraman, *In situ formation of highly conducting covalent Au-C contacts for single-molecule junctions*, Nat. Nano pp. – (2011).

[7] D. Secker, S. Wagner, S. Ballmann, R. Härtle, M. Thoss, and H. B. Weber, *Resonant Vibrations, Peak Broadening, and Noise in Single Molecule Contacts: The Nature of the First Conductance Peak*, Phys. Rev. Lett. **106**, 136807 (2011).

[8] A. C. Whalley, M. L. Steigerwald, X. Guo, and C. Nuckolls, *Reversible Switching in Molecular Electronic Devices*, J. Am. Chem. Soc. **129**, 12590 (2007).

[9] F. Pistolesi, Y. M. Blanter, and I. Martin, *Self-consistent theory of molecular switching*, Phys. Rev. B **78**, 085127 (2008).

[10] S. J. van der Molen and P. Liljeroth, *Charge transport through molecular switches*, J. Phys.: Condens. Matter **22**, 133001 (2010).

[11] S. A. Wolf, D. D. Awschalom, R. A. Buhrman, J. M. Daughton, S. von Molnár, M. L. Roukes, A. Y. Chtchelkanova, and D. M. Treger, *Spintronics: A Spin-Based Electronics Vision for the Future*, Science **294**, 1488 (2001).

[12] J. R. Petta, S. K. Slater, and D. C. Ralph, *Spin-Dependent Transport in Molecular Tunnel Junctions*, Phys. Rev. Lett. **93**, 136601 (2004).

[13] A. R. Rocha, V. M. Garcia-suarez, S. W. Bailey, C. J. Lambert, J. Ferrer, and S. Sanvito, *Towards molecular spintronics*, Nat. Mater. **4**, 335 (2005).

[14] J. J. Parks, A. R. Champagne, T. A. Costi, W. W. Shum, A. N. Pasupathy, E. Neuscamman, S. Flores-Torres, P. S. Cornaglia, A. A. Aligia, C. A. Balseiro, et al., *Mechanical Control of Spin States in Spin-1 Molecules and the Underscreened Kondo Effect*, Science **328**, 1370 (2010).

[15] S. Sanvito, *Molecular spintronics*, Chem. Soc. Rev. **40**, 3336 (2011).

[16] H. B. Heersche, Z. de Groot, J. A. Folk, H. S. J. van der Zant, C. Romeike, M. R. Wegewijs, L. Zobbi, D. Barreca, E. Tondello, and A. Cornia, *Electron Transport through Single* Mn_{12} *Molecular Magnets*, Phys. Rev. Lett. **96**, 206801 (2006).

[17] C. J. Milios, A. Vinslava, W. Wernsdorfer, S. Moggach, S. Parsons, S. P. Perlepes, G. Christou, and E. K. Brechin, *A Record Anisotropy Barrier for a Single-Molecule Magnet*, J. Am. Chem. Soc. **129**, 2754 (2007).

[18] O. Sato, T. Kawakami, M. Kimura, S. Hishiya, S. Kubo, and Y. Einaga, *Electric-Field-Induced Conductance Switching in FeCo Prussian Blue Analogues*, J. Am. Chem. Soc. **126**, 13176 (2004).

[19] D. Li, R. Clérac, O. Roubeau, E. Harté, C. Mathonière, R. Le Bris, and S. M. Holmes, *Magnetic and Optical Bistability Driven by Thermally and Photoinduced Intramolecular Electron Transfer in a Molecular Cobalt-Iron Prussian Blue Analogue*, J. Am. Chem. Soc. **130**, 252 (2008).

[20] A. Aviram and M. A. Ratner, *Molecular rectifiers*, Chem. Phys. Lett. **29**, 277 (1974).

[21] L. A. Bumm, J. J. Arnold, M. T. Cygan, T. D. Dunbar, T. P. Burgin, L. Jones, D. L. Allara, J. M. Tour, and P. S. Weiss, *Are Single Molecular Wires Conducting?*, Science **271**, 1705 (1996).

[22] B. C. Stipe, M. A. Rezaei, and W. Ho, *Single-Molecule Vibrational Spectroscopy and Microscopy*, Science **280**, 1732 (1998).

[23] B. Xu and N. J. Tao, *Measurement of Single-Molecule Resistance by Repeated Formation of Molecular Junctions*, Science **301**, 1221 (2003).

[24] J. M. van Ruitenbeek, A. Alvarez, I. Pineyro, C. Grahmann, P. Joyez, M. H. Devoret, D. Esteve, and C. Urbina, *Adjustable nanofabricated atomic size contacts*, Rev. Sci. Instrum. **67**, 108 (1996).

[25] M. A. Reed, C. Zhou, C. J. Muller, T. P. Burgin, and J. M. Tour, *Conductance of a Molecular Junction*, Science **278**, 252 (1997).

[26] R. H. M. Smit, Y. Noat, C. Untiedt, N. D. Lang, M. C. van Hemert, and J. M. van Ruitenbeek, *Measurement of the conductance of a hydrogen molecule*, Nature **419**, 906 (2002).

[27] H. Park, A. K. L. Lim, A. P. Alivisatos, J. Park, and P. L. McEuen, *Fabrication of metallic electrodes with nanometer separation by electromigration*, Appl. Phys. Lett. **75**, 301 (1999).

[28] S. Kubatkin, A. Danilov, M. Hjort, J. Cornil, J.-L. Bredas, N. Stuhr-Hansen, P. Hedegård, and T. Bjornholm, *Single-electron transistor of a single organic molecule with access to several redox states*, Nature **425**, 698 (2003).

[29] E. A. Osorio, K. O'Neill, M. Wegewijs, N. Stuhr-Hansen, J. Paaske, T. Bjørnholm, and H. S. J. van der Zant, *Electronic excitations of a single molecule contacted in a three-terminal configuration*, Nano Lett. **7**, 3336 (2007).

[30] F. Prins, T. Hayashi, B. J. A. de Vos van Steenwijk, B. Gao, E. A. Osorio, K. Muraki, and H. S. J. van der Zant, *Room-temperature stability of Pt nanogaps formed by self-breaking*, Appl. Phys. Lett. **94**, 123108 (pages 3) (2009).

[31] S. Quek, L. Venkataraman, H. Choi, S. Louie, M. Hybertsen, and J. Neaton, *Amine–Gold Linked Single-Molecule Circuits: Experiment and Theory*, Nano Lett. **11**, 3477 (2007).

[32] M. Hybertsen, L. Venkataraman, J. Klare, A. Whalley, M. Steigerwald, and C. Nuckolls, *Amine-Linked Single Molecule Circuits: Systematic Trends Across Molecular Families*, J. Phys.: Condens. Matter **20**, 374115 (2008).

[33] C. A. Martin, D. Ding, H. S. J. van der Zant, and J. M. van Ruitenbeek, *Lithographic mechanical break junctions for single-molecule measurements in vacuum: possibilities and limitations*, New J. Phys. **10**, 065008 (2008).

[34] H. van der Zant, Y. Kervennic, M. Poot, K. O'Neill, Z. de Groot, J. Thijssen, H. Heersche, N. Stuhr-Hansen, T. Bjornholm, D. Vanmaekelbergh, et al., *Molecular three-terminal devices: fabrication and measurements*, Faraday Discuss. **131**, 347 (2006).

[35] C. A. Martin, J. M. van Ruitenbeek, and H. S. J. van der Zant, *Sandwich-type gated mechanical break junctions*, Nanotechnology **21**, 265201 (2010).

[36] E. Osorio, K. O'Neill, N. Stuhr-Hansen, O. Nielsen, T. Bjørnholm, and H. S. J. van der Zant, *Addition Energies and Vibrational Fine Structure Measured in Electromigrated Single-Molecule Junctions Based on an Oligophenylenevinylene Derivative*, Adv. Mat. **19**, 281 (2007).

[37] Y. Kim, H. Song, F. Strigl, H.-F. Pernau, T. Lee, and E. Scheer, *Conductance and Vibrational States of Single-Molecule Junctions Controlled by Mechanical Stretching and Material Variation*, Phys. Rev. Lett. **106**, 196804 (2011).

[38] E. A. Osorio, K. Moth-Poulsen, H. S. J. van der Zant, J. Paaske, P. Hedegård, K. Flensberg, J. Bendix, and T. Bjørnholm, *Electrical Manipulation of Spin States in a Single Electrostatically Gated Transition-Metal Complex*, Nano Lett. pp. – (2009).

[39] R. Landauer, *Conductance determined by transmission: probes and quantised constriction resistance*, J. Phys.: Condens. Matter **1**, 8099 (1989).

[40] Y. Meir and N. S. Wingreen, *Landauer formula for the current through an interacting electron region*, Phys. Rev. Lett. **68**, 2512 (1992).

[41] S. Datta, *Electronic Transport in Mesoscopic Systems* (Cambridge University Press, 1997), 1st ed.

[42] M. Di Ventra, *Electrical Transport in Nanoscale Systems* (Cambridge University Press, 2008), 1st ed.

[43] Y. V. Nazarov and Y. M. Blanter, *Quantum Transport: Introduction to Nanoscience* (Cambridge University Press, 2009), 1st ed.

[44] C. Fonseca Guerra, J. G. Snijders, G. te Velde, and E. J. Baerends, *Towards an order-N DFT method*, Theor. Chem. Acc. **99**, 391 (1998).

[45] G. te Velde, F. Bickelhaupt, S. van Gisbergen, C. Fonseca Guerra, E. Baerends, J. Snijders, and T. Ziegler, *Chemistry with ADF*, J. Comput. Chem. **22**, 931 (2001).

[46] G. te Velde and E. J. Baerends, *Precise density-functional method for periodic structures*, Phys. Rev. B **44**, 7888 (1991).

[47] G. Wiesenekker and E. J. Baerends, *Quadratic integration over the three-dimensional Brillouin zone*, J. Phys.: Condens. Matter **3**, 6721 (1991).

2

THEORETICAL FRAMEWORK

The ab initio molecular transport calculations discussed in this thesis are based on the DFT+NEGF approach to molecular transport. This chapter outlines the density functional theory (DFT) and non-equilibrium Green's functions (NEGF) formalisms, and then discusses the assumptions behind their combined use, as well as the consequent limitations to the computational results presented in the following chapters.

In this chapter we lay out the theoretical framework on which our computational methods are built. We summarize the essential features of our two main theoretical tools, density-functional theory (DFT) and the non-equilibrium Green's function (NEGF) formalism, and then discuss the way we combine them into an effective single-particle theory of molecular transport. This has been implemented as an integral part of the BAND DFT code for extended systems (sister-code to the ADF molecular DFT code), as described in detail in the next chapter.

2.1 DFT+NEGF

In recent years, approaches to molecular transport based on density-functional theory (DFT) in combination with the non-equilibrium Green's function formalism (NEGF) have received considerable attention in the literature, driven by the rapid progress in experimental work on realizing single-molecule nano-devices.[1–4] A number of research codes,[5–7] as well as the SIESTA,[8–10] TurboMole[11–14] and SMEAGOL[15] production codes have been developed.

The attractiveness of the combined approach is based on the strengths of DFT for treating realistic atomistic and molecular transport configurations self-consistently, starting from an *ab initio* quantum chemical description. DFT is the workhorse of state-of-the-art quantum chemistry calculations,[16] with advanced uses achieving quantitative accuracy in predicting the chemical structure and properties of novel molecular systems. This strength is then combined with an intuitive mapping to the Landauer expression for the conductance and current of Eq. (1.1), through the very powerful Green's function formalism for transport.[17,18]

Concretely, the DFT+NEGF approach we take effectively removes the heart of the DFT code, and replaces the closed-system density (obtained from a diagonalizing the DFT Hamiltonian) with one derived from the NEGF formalism, for the molecular device in the presence of semi-infinite contacts. Already at the simplest local-density approximation (LDA) level of density-functional theory, this is known to work well for transport in the strongly-coupled regime[19,20] and through off-resonant transport levels.[21] It has, for example, been used successfully to describe transport through metallic wires and non-conjugated hydrocarbons (alkanes).[19,21–23]

The strengths of DFT in this approach are, however, balanced by known weaknesses of the often-used LDA, which introduces self-interaction errors[24–26] and incorrect charging behavior due to the lack of a correct derivative discontinuity.[27–29] The failure of common exchange correlation functionals to predict excited many-body states, as well as their mean-field character, hampers a proper handling of dynamic Coulomb correlations. This renders the method less suitable for weakly-coupled systems, particularly when one or more resonances are present inside the bias-window.

Nonetheless, despite the attractiveness of conceptually better-founded methods such as the GW approximation for dynamical response,[30,31] computational tractability has favored the popularity of the DFT+NEGF approach, especially when combined with LDA, or better: GGA functionals (which scale an order of magnitude more efficiently than methods based on the Hartree-Fock or GW approximations, *cf.* section

3.11). The approach has, for example, led to a better understanding of charge transport in thiolated phenyl systems[14,20,32,33] and single-molecule magnets,[34,35] among other systems of interest. Recent work on *e.g.* self-interaction corrections,[25,26] accounting for lead-renormalization and dielectric effects[4,36–38] and better functionals for the description of molecule-substrate interfaces,[39] also strongly suggest that some of the problematic issues related to the neglect of dynamical correlations can be handled satisfactorily for many systems.

It is in this spirit that we will outline the DFT and NEGF approaches in the present chapter. In Chapter 3, we will discuss the combination of them into a DFT+NEGF method, as implemented in the BAND periodic-system DFT code,[40–42] which enables us to study novel single-molecule systems in subsequent chapters. A number of unique features of BAND, in particular the freedom to choose the number of dimensions in which periodicity is imposed, enables us to perform accurate modeling of the contacts, as well as (in principle) the electric potential in the presence of a gate. This should help to resolve a number of the issues critical to the full understanding of experimental results, although a full treatment of the Coulomb potential in the presence of a gate electrode has not yet been implemented in our method.

2.2 DENSITY FUNCTIONAL THEORY

The total Hamiltonian of a system of interacting electrons labeled i with masses m_e, moving in the presence of fixed nuclei I with masses M_I and charge Z_I, is given by:

$$\hat{H}_{\text{tot}} = -\frac{\hbar^2}{2m_e}\sum_i \nabla_i^2 + \frac{1}{2}\sum_{i\neq j}\frac{e^2}{|\boldsymbol{r}_i - \boldsymbol{r}_j|} - \sum_{i,J}\frac{Z_J e^2}{|\boldsymbol{r}_i - \boldsymbol{R}_J|} - \sum_I \frac{\hbar^2}{2M_I}\nabla_I^2 + \frac{1}{2}\sum_{I\neq J}\frac{Z_I Z_J e^2}{|\boldsymbol{R}_I - \boldsymbol{R}_J|}. \tag{2.1}$$

First, the Born-Oppenheimer approximation is made, which assumes that because of the difference in time-scales between the dynamics of the electrons (fast) and the nuclei (slow), the eigenstates are separable:[43]

$$\Psi(\vec{\boldsymbol{r}}, \vec{\boldsymbol{R}}) \approx \Psi_e(\vec{\boldsymbol{r}})\Psi_n(\vec{\boldsymbol{R}}),$$

where $\vec{\boldsymbol{r}}$ the vector of the set $\{\boldsymbol{r}_i\}$ of (vector) electron coordinates, and $\vec{\boldsymbol{R}}$ likewise for the nuclei. This leads us to consider the dynamics of the electrons in a quasi-static background potential determined by the nuclei. Consequently we solve the usual Schrödinger equation for only the electrons:

$$i\hbar\frac{\partial\Psi_e}{\partial t} = \hat{H}\,\Psi_e, \tag{2.2}$$

with $\hat{H}$ now given by:

$$\hat{H} = -\frac{\hbar^2}{2m_e}\sum_i \nabla_i^2 + \frac{1}{2}\sum_{i\neq j}\frac{e^2}{|\boldsymbol{r}_i - \boldsymbol{r}_j|} - \sum_{i,J}\frac{Z_J e^2}{|\boldsymbol{r}_i - \boldsymbol{R}_J|},$$

or using atomic units, for which $\hbar^2/m_e = e = 4\pi\epsilon_0 = 1$:

$$\hat{H} = -\frac{1}{2}\sum_i \nabla_i^2 + \frac{1}{2}\sum_{i\neq j}\frac{1}{|\boldsymbol{r}_i - \boldsymbol{r}_j|} - \sum_{i,J}\frac{Z_J}{|\boldsymbol{r}_i - \boldsymbol{R}_J|}. \tag{2.3}$$

The unit of energy is 1 Hartree ≈ 27.211 eV. In this Hamiltonian we recognize:

- a kinetic term $\hat{T} = -\frac{1}{2}\sum_i \nabla_i^2$,
- an interaction potential $\hat{V}_{\text{int}} = \frac{1}{2}\sum_{i\neq j}\frac{1}{|\boldsymbol{r}_i - \boldsymbol{r}_j|}$, and
- an external potential due to the nuclei $\hat{V}_{\text{ext}} = -\sum_{i,J}\frac{Z_J}{|\boldsymbol{r}_i - \boldsymbol{R}_J|}$.

This is a prototypical many-body problem, and the difficulty in solving it lies in the electrostatic interaction potential, which is an inherently long-ranged two-particle interaction. Usually we write this Hamiltonian as $\hat{H} = \hat{H}_{\text{se}} + \hat{H}_{\text{int}}$, where $\hat{H}_{\text{se}} = \hat{T} + \hat{V}_{\text{ext}}$ can be thought of as a *single electron* Hamiltonian, and $\hat{H}_{\text{int}} = \hat{V}_{\text{int}}$ as the many-body *interaction* Hamiltonian.

The solutions to the single-electron Hamiltonian for n fermionic particles can be written as an antisymmetrized product of n single-particle wavefunctions:[a]

$$\Phi_{\boldsymbol{m}}(\vec{\boldsymbol{r}}) = \frac{1}{\sqrt{n!}}\begin{vmatrix} \phi_{m_1}(\boldsymbol{r}_1) & \phi_{m_1}(\boldsymbol{r}_2) & \cdots & \phi_{m_1}(\boldsymbol{r}_n) \\ \phi_{m_2}(\boldsymbol{r}_1) & \phi_{m_2}(\boldsymbol{r}_2) & \cdots & \phi_{m_2}(\boldsymbol{r}_n) \\ \vdots & \vdots & \ddots & \vdots \\ \phi_{m_n}(\boldsymbol{r}_1) & \phi_{m_n}(\boldsymbol{r}_2) & \cdots & \phi_{m_n}(\boldsymbol{r}_n) \end{vmatrix} \tag{2.4}$$

which is a Slater determinant, with $\boldsymbol{m}$ the vector of the set $\{m_i\}$ of quantum numbers describing the electrons (spin, *etc.*). The set of all such Slater determinants that can be constructed from a complete single-particle basis form a complete basis of the many-fermion Hilbert space,[44] and thus the interacting many-electron wavefunction can be written as a linear combination of these basis-functions:

$$\Psi_e(\vec{\boldsymbol{r}}) = \sum_{\boldsymbol{m}} c_{\boldsymbol{m}}\Phi_{\boldsymbol{m}}(\vec{\boldsymbol{r}})\ . \tag{2.5}$$

The key idea behind Density Functional Theory (DFT) is to replace this many-body Hamiltonian by a single-particle Hamiltonian, which is a functional of only

---

[a] As such, it accounts for exchange, but not many-body correlation effects, and is thus itself still a single-particle wavefunction.

the ground-state density (from which all other properties may be obtained). This means that instead of a wavefunction depending on $3N$ coordinates, we can now characterize the ground state by its density $n(\boldsymbol{r})$, a function of only 3 coordinates. That this is possible, for the general many-body problem, is the content of the Hohenberg-Kohn theorems.

2.2.1 THE HOHENBERG-KOHN THEOREMS

Our approach will be to construct an energy-functional of a single variable (the density), which leads to an appropriate single-body problem for the ground-state of the interacting system. This is possible because of the Hohenberg-Kohn the theorems, proved by the eponymous in 1964,[45] which we state here in the formulation of Martin:[43]

1. For any system of interacting particles in an external potential $V_{\text{ext}}(\boldsymbol{r})$, this potential (and so the Hamiltonian) is determined uniquely (up to a constant) by the ground state density $n_0(\boldsymbol{r})$. Consequently, as all properties of the system are governed by the Hamiltonian, they are completely determined given *only* this ground-state density.

2. A functional $E[n(\boldsymbol{r})]$ can be defined for the energy, which is valid for any such potential $V_{\text{ext}}(\boldsymbol{r})$, such that the global minimum of the functional is the ground-state energy of the system. Consequently, the density $n(\boldsymbol{r})$ which minimizes this functional *is* the ground-state density $n_0(\boldsymbol{r})$, and minimization of $E[n(\boldsymbol{r})]$ alone is enough to fully determine the exact ground-state energy and density.

It is important to point out that the Hamiltonian (2.3) contains a universal interaction term, plus an external potential which is specific to a particular system. In the next section we see that the effect of the interactions in the system can be captured by a universal potential which does not depend on this external potential.

A further comment is in order on the meaning of *exact* density functional theory. The above theorems restate the many-body problem in terms of the ground-state density, but we cannot yet exploit this because the form of the energy functional which yields the exact ground-state is unknown (and in practice will be approximated). If it were known, however, this functional would fully determine the Hamiltonian, and so also determine all other properties of the system, including the excitations, though these would not correspond to the *minimum* of the energy functional.[43]

2.2.2 THE KOHN-SHAM EQUATIONS

In order to make DFT practicable we must make a further step, in replacing the original many-body problem by an equivalent *independent* single-particle problem. This combination of independent single particles with an interacting density is the crux of the Kohn-Sham *Ansatz*.[46] The Ansatz, specifically, is that for any V_{ext}, the ground state density of the original interacting system is equal to that of an auxiliary non-interacting system. This is referred to as "non-interacting V-representability," though no rigorous proofs for this exist to date.

Formally, we write the energy E_{KS} as a density-functional:

$$
\begin{aligned}
n(\boldsymbol{r}) &= \sum_{\sigma} n(\boldsymbol{r},\sigma) = \sum_{\sigma}\sum_{i=1}^{N_\sigma} |\psi_i^\sigma(\boldsymbol{r})|^2, && \text{(2.6a)}\\
T_s &= -\frac{1}{2}\sum_{\sigma}\sum_{i=1}^{N_\sigma}\langle\psi_i^\sigma|\nabla^2|\psi_i^\sigma\rangle = \frac{1}{2}\sum_{\sigma}\sum_{i=1}^{N_\sigma}\int \mathrm{d}^3r\, |\nabla\psi_i^\sigma(\boldsymbol{r})|^2, && \text{(2.6b)}\\
E_H[n] &= \frac{1}{2}\int \mathrm{d}^3r \int \mathrm{d}^3r'\, \frac{n(\boldsymbol{r})n(\boldsymbol{r}')}{|\boldsymbol{r}-\boldsymbol{r}'|}, && \text{(2.6c)}\\
E_{\text{KS}} &= T_s[n] + \int \mathrm{d}^3r\, V_{\text{ext}}(\boldsymbol{r})n(\boldsymbol{r}) + E_H[n] + E_{\text{II}} + E_{\text{xc}}[n] && \text{(2.6d)}
\end{aligned}
$$

with the density $n(\boldsymbol{r})$ obtained from summing over all occupied spin-orbitals ψ_i^σ, T_s the single-particle kinetic energy,[b] $E_H[n(\boldsymbol{r})]$ the Hartree energy, E_{II} the ion-ion interactions between nuclei, and $E_{\text{xc}}[n(\boldsymbol{r})]$ the exchange-correlation energy. The latter in principle carries the property of exchange antisymmetry for fermions, in addition to the many-body correlations as they are expressed through the density, and in practice is where the approximation to the unknown exchange-correlation energy enters our considerations.

The auxiliary single-particle Hamiltonian and Kohn-Sham equations are derived from this by taking the variation of this energy with respect to the orbitals:

$$
\frac{\delta E_{\text{KS}}}{\delta\psi_i^{\sigma *}(\boldsymbol{r})} = \frac{\delta T_s}{\delta\psi_i^{\sigma *}(\boldsymbol{r})} + \left[\frac{\delta E_{\text{ext}}}{\delta n(\boldsymbol{r},\sigma)} + \frac{\delta E_H}{\delta n(\boldsymbol{r},\sigma)} + \frac{\delta E_{\text{xc}}}{\delta n(\boldsymbol{r},\sigma)}\right]\frac{\delta n(\boldsymbol{r},\sigma)}{\delta\psi_i^{\sigma *}(\boldsymbol{r})},
$$

using the chain rule, and subjection to the orthonormalization $\langle\psi_i^\sigma|\psi_j^{\sigma'}\rangle = \delta_{ij}\delta_{\sigma\sigma'}$. This variation yields the Kohn-Sham equation (a time-independent Schrödinger-like equation) whose solution (see *e.g.* Martin[43] or Jones & Gunnarsson[47]) gives the Kohn-Sham eigenvalues[c] ϵ_i^σ and orbitals $\psi_j^\sigma(\boldsymbol{r})$:

$$
H^{\text{KS}}\,\psi_i^\sigma(\boldsymbol{r}) = \epsilon_i^\sigma\,\psi_i^\sigma(\boldsymbol{r}),
$$

with the Kohn-Sham Hamiltonian given by:

$$
\begin{aligned}
H^{\text{KS}} &= -\frac{1}{2}\nabla^2 - \sum_n \frac{Z_n}{|\boldsymbol{r}-\boldsymbol{r}_n|} + \int \mathrm{d}^3r'\,\frac{n(\boldsymbol{r}')}{|\boldsymbol{r}-\boldsymbol{r}'|} + V_{\text{xc}}[n](\boldsymbol{r}) && \text{(2.7)}\\
&= -\frac{1}{2}\nabla^2 + V_{\text{ext}}(\boldsymbol{r}) + V_{\text{H}}[n](\boldsymbol{r}) + V_{\text{xc}}[n](\boldsymbol{r}).
\end{aligned}
$$

---

[b] Formally, the definition of $E_{\text{xc}}[n]$ also contains $\langle\hat{T}\rangle[n(\boldsymbol{r})] - T_s$, since T_s as defined in Eq. (2.6) is a function of the *orbitals* rather than the density, while the full many-body kinetic energy is a function of $n(\boldsymbol{r})$ by the HK theorems.

[c] These are in fact the Lagrange multipliers for the orthonormalization constraint.

Considering the density to be fixed on the right-hand side, this Hamiltonian describes independent particles moving in an effective potential $V_{\text{eff}} = V_{\text{ext}}(\boldsymbol{r}) + V_{\text{H}}[n](\boldsymbol{r}) + V_{\text{xc}}[n](\boldsymbol{r})$. The expression recalls the single-electron terms $\hat{T} + \hat{V}_{\text{ext}}$ of Eq. (2.3), but with the interaction term included, split into a Hartree potential $V_H[n] = \frac{\delta E_H[n]}{\delta n(\boldsymbol{r},\sigma)}$ and an exchange-correlation potential $V_{\text{xc}}[n] = \frac{\delta E_{\text{xc}}[n]}{\delta n(\boldsymbol{r},\sigma)}$, which corrects the mean-field Hartree interaction for many-body exchange- and correlation effects.

The density, in turn, is constructed from the orbitals, the single-particle eigenfunctions of this Hamiltonian: $n(\boldsymbol{r}) = \sum_{\text{occ}} \sum_{\sigma} |\psi_i^{\sigma}(\boldsymbol{r})|^2$. However, these themselves depend on the solution of the eigenvalue problem, and this cyclical dependency is resolved using a self-consistent field (SCF) approach, where the density is frozen to find the orbitals, from which a new density is calculated, which is iterated back and forth until convergence.

Such a formulation becomes a set of matrix-vector equations once we choose a basis $\{\phi_i(\boldsymbol{r})\}$, in which case the KS Hamiltonian Eq. (2.7) is referred to as the “Fock” matrix. The eigenvalues ϵ_i^{σ} obtained by solving the eigenvalue problem have an interpretation suggestive of the differential analogue of chemical potentials: derivatives of the total energy with respect to the occupation n_i^{σ} of a state, which is the content of the Slater-Janak theorem:[48]

$$\epsilon_i^{\sigma} = \frac{\mathrm{d}E_{\text{total}}}{\mathrm{d}n_i^{\sigma}} = \int \mathrm{d}^3 r \, \frac{\delta E_{\text{total}}}{\delta n(\boldsymbol{r},\sigma)} \frac{\mathrm{d}n(\boldsymbol{r},\sigma)}{\mathrm{d}n_i^{\sigma}}. \tag{2.8}$$

For the *exact* exchange-correlation, it is also true that the eigenvalue ϵ_{HOMO} of the highest occupied molecular orbital (HOMO) corresponds to the negative of molecule’s ionization potential, the true chemical potential of the level, though this is generally not true.

Ahead of the discussion on the limits of the DFT+NEGF approach in section 2.5, we note the issue of derivative discontinuity[27,28] here. $V_{\text{xc}}[n]$, introduced above as the exchange-correlation potential, should have discontinuous jumps with the occupations of states, at integer values of these occupations. This is especially relevant in the limit where transport is through a weakly-coupled device-region, for which the dominant mechanism will likely be single-electron tunneling. However, when the exchange correlation energy is a continuous function of the density, this may not be the case, yielding problems with the interpretation of the ϵ_i^{σ} as addition and removal energies (chemical potentials) associated with discrete states with integer occupation.

2.2.3 Exchange-Correlation Functionals

In the Kohn-Sham energy functional Eq. (2.6d), a vital part of the energy is the exchange-correlation term, which captures all many-body interactions beyond the mean-field Coulomb interaction of the Hartree term. In some cases it can be found exactly (in particular for the homogeneous electron gas), but in all practical quantum-chemistry calculations it is approximated. The results of calculations are tied to the quality of the approximation, which remains true when we discuss combined DFT+NEGF approaches later.

The simplest approximation is the local density approximation (LDA),[46] or more generally the local spin-density approximation (LSDA) when the Kohn-Sham equations are generalized to include spin. This assumes that the exchange-correlation energy density $\varepsilon_{\mathrm{xc}}^{\mathrm{LDA}}$ at each point in space is the same as that of a homogeneous electron gas at the same density:

$$E_{\mathrm{xc}}[n(\boldsymbol{r})] = \int \mathrm{d}^3 r \, \varepsilon_{\mathrm{xc}}^{\mathrm{LDA}} [n(\boldsymbol{r})] \cdot n(\boldsymbol{r}),$$

for which exchange and correlation expressions are available.[43] The major flaw in LDA is spurious self-interaction via the Hartree term, which in the Hartree-Fock method would be *exactly* canceled by the (non-local) exchange interaction.[d] In a local approximation to exchange, the cancellation is only approximate. The error made may be negligible for extended, homogeneous systems, but tends to be important in more confined systems such as atoms and molecules.

It turns out that LDA still works relatively well in solids (particularly when the electron density is in fact relatively homogeneous), but fares less well in describing molecules (overestimating binding energies), which motivated the development of generalized gradient approximations to the XC functional. These are expansions in gradients of the local density, $f_{xc}\left(n(\boldsymbol{r}), \nabla n(\boldsymbol{r}), \nabla^2 n(\boldsymbol{r}), \ldots\right)$, modified such that certain fundamental requirements are satisfied. Well-known ones are the PW91[49] and PBE[50] functionals, which usually produce sufficient accuracy for chemical calculations.

Later, hybrid functionals were introduced, which replace a fraction of the GGA exchange term by Hartree-Fock exchange, leading to the development of *e.g.* the B3LYP functional.[51,52] This is now considered the standard for predictive accuracy in DFT calculations, although less popular in the condensed matter physics community due to its *ad hoc* nature and the fact that it restores the dependency of the Hamiltonian on the orbitals rather than only the density. The preference there (in particular for extended systems) remains PBE GGA, which together with LDA and B3LYP, may be considered the "standard approximations."

Attempts have also been made to directly correct for spurious self-interaction, rather than the inclusion of exact exchange. This typically leads to approximate, orbital-dependent corrections to existing functionals,[25,26,53] which we will not make use of in the present work.

2.3 GREEN'S FUNCTIONS

We now proceed to discuss the main ideas behind the non-equilibrium Green's function (NEGF) formalism, and its application to transport. The discussion that follows may be found in considerably expanded detail in many pedagogical and research texts.[54–59]

---

[d] In the Hartree-Fock approach, an exchange or "Fock" term is added to the Hartree potential which we have introduced, which exactly cancels the self-interaction error made in the latter.

The Schrödinger equation in Eq. (2.2) can be written in the form:

$$\hat{\mathcal{L}}\Psi(\boldsymbol{r},t) = f(t) \quad \text{with:}$$

$$\hat{\mathcal{L}} = i\hbar\,\partial_t - \hat{H} \tag{2.9}$$

a linear differential operator and $f(t) = 0$. A *Green's function* can be defined which is the impulse response of the system to this linear operator, satisfying:

$$\hat{\mathcal{L}}\hat{G}(t) = \hat{1}\delta(t), \tag{2.10}$$

which has a formal solution, split into a forward time and backward time part by introducing the Heaviside (or step-) function $\theta(x)$:

$$\hat{G}^{+}(t) = -\theta(t)\frac{i}{\hbar}e^{-i\hat{H}t/\hbar}, \tag{2.11a}$$

$$\hat{G}^{-}(t) = \theta(-t)\frac{i}{\hbar}e^{-i\hat{H}t/\hbar}. \tag{2.11b}$$

These are the retarded and advanced Green's functions, such that $\hat{G}^{+}$ propagates a state vector $|\Psi(t)\rangle$ forward in time, and $\hat{G}^{-}$ the reverse:

$$|\Psi(t)\rangle = i\hbar\hat{G}^{+}(t-t_0)|\Psi(t_0)\rangle \quad \forall t > t_0\ , \tag{2.12}$$

$$|\Psi(t)\rangle = -i\hbar\hat{G}^{-}(t-t_0)|\Psi(t_0)\rangle \quad \forall t < t_0\ . \tag{2.13}$$

Since the Hamiltonian is Hermitian, we also have that:

$$\left(\hat{G}^{+}(t)\right)^{\dagger} = \hat{G}^{-}(-t)\ .$$

In transport our particles propagate from reservoirs into an active region, which is coupled to the unperturbed dynamics contained (for both, in the absence of the coupling) in $\hat{H}_0$ by an interaction potential $\hat{V}$, such that $\hat{H} = \hat{H}_0 + \hat{V}$. For the unperturbed part of the Hamiltonian we define the advanced/retarded pair $\hat{G}_0^{\pm}$, the inverse of which satisfies:

$$i\hbar\,\partial_t - \hat{H}_0 = \hat{1}\delta(t)\left(\hat{G}_0^{\pm}\right)^{-1},$$

such that for the full retarded/advanced pair:

$$\hat{1}\delta(t)\hat{G}^{\pm}(t) = \hat{1}\delta(t)\hat{G}_0^{\pm}(t) + \hat{G}_0^{\pm}(t)\ \hat{V}(t)\ \hat{G}^{\pm}(t)\ .$$

Focusing only on the retarded Green's function for the moment, we find that on integrating over time:[e]

$$\hat{G}^{+}(t-t_0) = \hat{G}_0^{+}(t-t_0) + \int_{t_0}^{t} \mathrm{d}t'\ \hat{G}_0^{+}(t'-t_0)\hat{V}\hat{G}^{+}(t'-t_0). \tag{2.14}$$

---

[e] Time dependence of $\hat{V}$ suppressed for compactness.

This is the Lippmann-Schwinger equation. Iterating this equation we obtain the series expansion:

$$\begin{aligned}\hat{G}^{+}(t-t_0) = \hat{G}_0^{+}(t-t_0) &+ \int_{t_0}^{t} \mathrm{d}t'\ \hat{G}_0^{+}(t-t')\hat{V}\hat{G}_0^{+}(t'-t_0)\\ &+ \int_{t_0}^{t} \mathrm{d}t' \int_{t_0}^{t'} \mathrm{d}t''\ \hat{G}_0^{+}(t-t')\ \hat{V}\ \hat{G}_0^{+}(t'-t'')\ \hat{V}\ \hat{G}_0^{+}(t''-t_0) + \cdots\end{aligned}$$

Each term includes an increasing number of interactions with $\hat{V}$, integrated over all intermediate times at which they may have occurred. If the series converges, we write the resulting effective interaction as a *self-energy* $\hat{\Sigma}^{+}(t'-t'')$, such that:

$$\hat{G}^{+}(t-t_0) = \hat{G}_0^{+}(t-t_0) + \int_{t_0}^{t} \mathrm{d}t' \int_{t_0}^{t'} \mathrm{d}t''\ \hat{G}_0^{+}(t-t')\hat{\Sigma}^{+}(t'-t'')\hat{G}^{+}(t''-t_0). \tag{2.15}$$

This is the Dyson equation.

If we Fourier-transform the retarded/advanced Green's function, we find the complementary expressions in the energy/frequency domain:

$$\hat{G}^{\pm}(\epsilon) = \lim_{\eta\to 0} \int_{-\infty}^{\infty} \mathrm{d}(t-t_0)\ e^{\mathrm{i}\frac{\epsilon(t-t_0)}{\hbar}}\ \hat{G}^{\pm}(t-t_0)\ e^{\mp\frac{\eta(t-t_0)}{\hbar}},$$

where an infinitesimal real $\eta > 0$ has been added to ensure convergence of the integral. On substituting Eq. (2.11) we obtain the propagator in energy space:

$$\hat{G}^{\pm}(\epsilon) = \lim_{\eta\to 0} \frac{\hat{1}}{(\epsilon \pm i\eta)\,\hat{1} - \hat{H}}\ . \tag{2.16}$$

Note that the singularities of $\hat{G}(\epsilon)$ correspond precisely to the spectrum of $\hat{H}$, and due to η these poles are shifted off the real line slightly, into the negative complex half-plane for $\hat{G}^{+}$ and into the positive complex half-plane for $\hat{G}^{-}$. The two Green's functions in Fourier space are related by:

$$\left(\hat{G}^{+}(\epsilon)\right)^{\dagger} = \hat{G}^{-}(\epsilon).$$

Next, turning to the Lippmann-Schwinger equation, we find that:

$$\hat{G}^{\pm}(\epsilon) = \hat{G}_0^{\pm}(\epsilon) + \hat{G}_0^{\pm}(\epsilon)\ \hat{V}\ \hat{G}^{\pm}(\epsilon), \tag{2.17}$$

while the Dyson equation is Fourier transformed to:

$$\hat{G}^{\pm}(\epsilon) = \hat{G}_0^{\pm}(\epsilon) + \hat{G}_0^{\pm}(\epsilon)\ \hat{\Sigma}^{\pm}\ \hat{G}^{\pm}(\epsilon). \tag{2.18}$$

This can be turned into an explicit equation for the full propagator: $\hat{G}^{\pm}(\epsilon) = \left(\left(\hat{G}_0^{\pm}(\epsilon)\right)^{-1} - \hat{\Sigma}^{\pm}(\epsilon)\right)^{-1}$, which we use repeatedly.

We now turn to the particular case where the perturbation $\hat{V}$ represents the coupling to a reservoir contact c to a molecular device m. The general structure of the self-energies can then be derived by considering the Schrödinger equation for the system and the reservoir:

$$\begin{pmatrix} \hat{1} & 0 \\ 0 & \hat{1} \end{pmatrix} = \begin{pmatrix} \epsilon\hat{1} - \hat{H}_m & \hat{V}^\dagger \\ \hat{V} & \epsilon\hat{1} - \hat{H}_c \end{pmatrix} \begin{pmatrix} \hat{G}^\pm_m & \hat{G}^\pm_{mc} \\ \hat{G}^\pm_{cm} & \hat{G}^\pm_c \end{pmatrix} . \tag{2.19}$$

From this it is easily found that:

$$\hat{G}^\pm_m(\epsilon) = \frac{\hat{1}}{\epsilon\hat{1} - \hat{H}_m - \hat{V}^\dagger \frac{\hat{1}}{\epsilon\hat{1} - \hat{H}_c} \hat{V}}, \tag{2.20}$$

where the final term in the denominator is the self-energy $\hat{\Sigma}^\pm$. This may be explicitly written as a Dyson equation by introducing the unperturbed propagators $\hat{G}^\pm_{c,0}$ and $\hat{G}^\pm_{m,0}$ of the reservoir and molecular device regions respectively:

$$\hat{\Sigma}^\pm(\epsilon) = V^\dagger\, \hat{G}^\pm_{c,0}(\epsilon)\, \hat{V}, \tag{2.21}$$

$$\hat{G}^\pm_m(\epsilon) = \left(\left(\hat{G}^\pm_{m,0}(\epsilon)\right)^{-1} - \hat{\Sigma}^\pm(\epsilon)\right)^{-1} . \tag{2.22}$$

The coupling operators are defined as

$$\hat{\Gamma}_i(\epsilon) = \mathrm{i}\left(\hat{\Sigma}^+_i(\epsilon) - \hat{\Sigma}^-_i(\epsilon)\right) = -2\mathrm{Im}\left\{\hat{\Sigma}^+_i(\epsilon)\right\} \tag{2.23}$$

for the i^{th} reservoir. Note that the $\hat{\Gamma}_i$ are the non-Hermitian part of the self-energies $\hat{\Sigma}^+_i$, the existence of which corresponds to the open nature of the system, allowing particles to move in and out of the molecular region.

For application of the formalism within a DFT+NEGF context, we are primarily interested in density operators and matrices, and we now directly define the spectral function:

$$\hat{A}(\epsilon) = \mathrm{i}\left(\hat{G}^+(\epsilon) - \hat{G}^-(\epsilon)\right), \tag{2.24}$$

which acts like a density of states operator in the sense that it counts the available states. Evaluated in a positional basis, we obtain the density correlation:

$$\begin{aligned} \rho(\boldsymbol{r}, \boldsymbol{r}', \epsilon) &\equiv \frac{1}{2\pi}\langle \boldsymbol{r}|\hat{A}(\epsilon)|\boldsymbol{r}'\rangle = \mathrm{i}\frac{G^+(\boldsymbol{r}, \boldsymbol{r}', \epsilon) - G^-(\boldsymbol{r}, \boldsymbol{r}', \epsilon)}{2\pi} \\ &= -\frac{1}{\pi}\mathrm{Im}\left\{G^+(\boldsymbol{r}, \boldsymbol{r}', \epsilon)\right\} \end{aligned} \tag{2.25}$$

which, traced over energy (and expressed in a discrete basis) yields the density matrix $\boldsymbol{\rho}$. Setting $\boldsymbol{r}' = \boldsymbol{r}$ yields the local density of states (LDOS), which can be integrated to yield the density of states (DOS):

$$D(\boldsymbol{r},\epsilon) = -\frac{1}{\pi}\mathrm{Im}\left\{G^{+}(\boldsymbol{r},\boldsymbol{r},\epsilon)\right\}, \tag{2.26}$$

$$D(\epsilon) = -\frac{1}{\pi}\int_{\boldsymbol{r}} \mathrm{d}^3 r\ \mathrm{Im}\left\{G^{+}(\boldsymbol{r},\boldsymbol{r},\epsilon)\right\}\ . \tag{2.27}$$

In a discrete basis (*e.g.* in a DFT code), the latter becomes a trace over all basis-functions. If we integrate Eq. (2.26) over energy instead we obtain the spatial density:

$$n(\boldsymbol{r}) = \int \mathrm{d}\epsilon\ D(\boldsymbol{r},\epsilon)\ . \tag{2.28}$$

The derivation of the current as $I = \mathrm{Tr}\left[\hat{\rho}\,\hat{J}\right]$ with $\hat{J}$ the quantum mechanical current operator is involved,[17] and we will only give enough details to make it plausible in what follows. For full details we refer to the textbooks noted at the start of the present section, but for our purposes it is enough to note that it can be shown[60] that the spectral function is given by:

$$\hat{A}(\epsilon) = \hat{G}^{+}(\epsilon)\,\hat{\Gamma}(\epsilon)\,\hat{G}^{-}(\epsilon)$$

with $\hat{\Gamma}$ as in Eq. (2.23). By specifying $\hat{\Gamma}$ further for each reservoir i, the total spectral function may be split into parts $\hat{A}_i(\epsilon) = \hat{G}^{+}(\epsilon)\,\hat{\Gamma}_i(\epsilon)\,\hat{G}^{-}(\epsilon)$ such that:

$$\hat{A}(\epsilon) = \mathrm{i}\left(\hat{G}^{+}(\epsilon) - \hat{G}^{-}(\epsilon)\right) = \hat{A}_1(\epsilon) + \hat{A}_2(\epsilon)$$

in the two reservoir case. These “left-” and “right-”contact spectral functions describe the in- and outflow from each reservoir when there is no direct coupling between them, each populated according to their respective Fermi distributions. It can then be shown that:[18,60]

$$\begin{aligned} I &= \frac{2e}{h}\int \mathrm{d}\epsilon\ \mathrm{Tr}\left[\hat{\Gamma}_1(\epsilon)\hat{A}_2(\epsilon)\right]\left[f(\epsilon;\mu_1) - f(\epsilon;\mu_2)\right] \quad \text{at contact 1 or} \\ &= \frac{2e}{h}\int \mathrm{d}\epsilon\ \mathrm{Tr}\left[\hat{\Gamma}_2(\epsilon)\hat{A}_1(\epsilon)\right]\left[f(\epsilon;\mu_1) - f(\epsilon;\mu_2)\right] \quad \text{at contact 2.} \end{aligned} \tag{2.29}$$

We expand these and identify with the Landauer transmission $T(\epsilon)$ of Eq. (1.1) to find[f] $T(\epsilon) = \mathrm{Tr}\left[\hat{\Gamma}_1\,\hat{G}^{+}(\epsilon)\,\hat{\Gamma}_2(\epsilon)\,\hat{G}^{-}(\epsilon)\right]$, such that in this formalism the Landauer current becomes:

$$I = \frac{2e}{h}\int_{-\infty}^{\infty} \mathrm{d}\epsilon\left[f(\epsilon;\mu_1) - f(\epsilon;\mu_2)\right]\mathrm{Tr}\left[\hat{\Gamma}_1(\epsilon)\ \hat{G}^{+}(\epsilon)\ \hat{\Gamma}_2(\epsilon)\hat{G}^{-}(\epsilon)\right]. \tag{2.30}$$

The bias dependence is implicit in the $\hat{\Sigma}_i^{+}(\epsilon;\mu_i)$ (and therefore the $\hat{\Gamma}_i(\epsilon)$), and explicit in the distributions $f(\epsilon;\mu_i)$ for each reservoir.

---

[f] The equivalence of the results of Eq. (2.29) are contained in the cyclic invariance of the trace.

The departure from equilibrium in the above expressions enters by the fact that the reservoirs, while locally in equilibrium and thus described by a chemical potential μ_i and a Fermi distribution, are *not* in equilibrium with each other, and so the charge flow from reservoir 1 to 2 will not equal the reverse flow from reservoir 2 to 1 (which is already taken into account in Eq. (2.29) where $I = I_{\text{in}} - I_{\text{out}}$). Hence $\mu_1 \neq \mu_2$ leads to a net current in expression (2.30).

We have already noted that the density (matrix) obtained from the spectral function is the essential tool in the NEGF formalism, particularly as used to obtain the (non-equilibrium) density necessary to couple NEGF with DFT. Out of equilibrium, the density is obtained not from the simple form of Eq. (2.26), but from the spectral function rewritten using the contact spectral functions introduced above:

$$\hat{A}(\epsilon) = \hat{G}^{+}(\epsilon)\,\hat{\Gamma}_1(\epsilon)\,\hat{G}^{-}(\epsilon) + \hat{G}^{+}(\epsilon)\,\hat{\Gamma}_2(\epsilon)\,\hat{G}^{-}(\epsilon) \; ,$$

which in matrix-vector notation ultimately yields an expression for the density matrix $\boldsymbol{\rho}$ of the form:

$$\boldsymbol{\rho} = \frac{1}{2\pi} \int \mathrm{d}\epsilon \; [\boldsymbol{G}\boldsymbol{\Gamma}_1\boldsymbol{G}^{\dagger} f(\epsilon;\mu_1) + \boldsymbol{G}\boldsymbol{\Gamma}_2\boldsymbol{G}^{\dagger} f(\epsilon;\mu_2)]$$

as we will discuss in Chapter 3.

2.4 Two Limits

Before continuing our discussion, we pause to acknowledge a significant point remarked by Evers *et al.*[13,61] In incorporating NEGF into a DFT calculation we have made a choice about what it means to combine the methodologies, when in fact there are two options:

1. Calculate the DFT Hamiltonian operator from the converged density of an extended molecule, and then use this $\hat{H}^{\text{KS}}$ in an *external* Green's function method for transport. In this approach to obtaining $n(\boldsymbol{r})$, when the limit of increasing (well-conducting) contact size is taken (in the extended molecule), the details of the interface become less and less important due to screening, and the necessary boundary conditions effectively reduce to "sufficiently absorbing."

2. Calculate the density from the Green's function formalism *during* the self-consistency cycle of a DFT calculation, allowing the (non-equilibrium) "ground-state" to adjust to transport. Then again take the limit of increasing size of the contacts contained in the extended molecule, where the same limiting result is true, though the convergence may be quicker.

That we choose the second option in our main implementation is based on the hope that with increasing system size, it converges to the "true" (Landauer) steady-state transport more quickly. As the calculations are exposed to the effects of the open contacts at an earlier conceptual stage, this is not unreasonable, but we remark that the other side of the coin is that we may pay some price in terms of stability in the convergence of the method due to our choice to add significant complexity to the SCF cycle itself.

2.5 LIMITATIONS AND STRENGTHS OF DFT+NEGF

We now consider how well this combined approach should perform, and the limitations imposed by basing it on DFT.

As we have previously remarked, DFT is the workhorse of quantum-chemistry calculations.[16] In transport calculations, the goal of combining it with the non-equilibrium Green's function (NEGF) method is to describe a molecule (and part of the metal electrodes) embedded between semi-infinite metal leads as an open system.[9,10,13,15,62]

Kohn-Sham DFT involves the calculation of the Hartree potential, which takes static polarization into account. However, it does not describe polarization effects induced by changes in the charge distribution such as those which occur during transport. Together with the presence of spurious self-interactions,[24] this is responsible for the incorrect predictions for one- and two-particle excitations (band gaps and exciton energies, respectively). This can at least partly be formulated in terms of a lack of a correct derivative discontinuity in the DFT functional.[27,28]

In weakly-coupled systems, where the (integer) charge fluctuations are substantial, these shortcomings become apparent. In this limit, transport is dominated by a set of transporting levels which correspond to transitions between the discrete many-body states of the isolated molecule. These transitions show up as peaks in the spectral density, with a width determined by the coupling to the leads. If the molecule is (approximately) neutral at zero bias, the HOMO and LUMO orbitals are the main candidate channels for low-bias transport.

In the gas phase, the difference between the HOMO and the ionization potential (IP), and between the LUMO and the electron affinity (EA), can easily be obtained as the difference between the DFT orbital levels and the corresponding chemical potentials from ΔSCF calculations.[47] Neaton *et al.*[36] have suggested that these differences are similar for the molecule in the junction, which leads to the so-called 'scissors-operator' procedure, where the transmission peaks corresponding to HOMO and LUMO are corrected statically by a shift obtained from gas phase.

The polarization effects due to the contacts give an additional difference between gas phase and junction, and it is these last effects that we focus on in Chapter 6. Kaasbjerg & Flensberg[38] and Mowbray & Thygesen[37] have shown that such an approach significantly corrects the calculated transport gap, which (together with the scissors operator) brings it into much better agreement with experimental observations, particularly when a gate is present near the molecule (which provides additional screening).[38]

However, since we can obtain good ground-state charge distributions using DFT for a given charge state, we will now show how we incorporate these into an appropriate generalization of the simple case discussed previously, Eqs. (6.1)-(6.2).

Notwithstanding justified criticism against using DFT for transport (which we acknowledge in the following chapters), it should not be forgotten that DFT is arguably the single most effective computational tool ever developed for understanding the properties of molecules, solids and liquids. While in practice we must use imperfect functionals, there is a lot that can be learned from DFT+NEGF approaches, although the interpretation and the use of the results is often nontrivial. Methods more reliable than DFT exist (*e.g.* GW calculations, configuration interaction calculations, exact-exchange methods), but these are typically *at least* an order of magnitude worse in scaling with the size of the problem.

For a recent overview, we refer to the excellent, accessible review by Kieron Burke,[16] and the older one by Jones & Gunnarsson.[47] Standard textbooks in the field are those by Parr & Yang,[63] Dreizler & Gross[64] and Martin[43] respectively.

2.6 CHEMISTRY WITH ADF, TRANSPORT WITH BAND

For our concrete implementation of this molecular transport method, we have chosen to build on the ADF/BAND quantum chemistry package. The underlying DFT code in which it is implemented, BAND,[40] is a periodic structure code which uses a *local* basis, rather than the more common plane-wave basis used for studying extended systems. This comes from its kinship with the ADF molecular code.[42] Additionally, it uses a combination of Slater-type (STO) and numerical atomic orbitals (NAO) as basis-functions,[g] which behave much better at the wavefunction cusp near the nucleus, as well as in the long tail (in contrast to the use of Gaussian or plane-wave basis sets). Such basis sets are available from the single-ζ (SZ) through triple-ζ-plus-double-polarization (TZ2P) quality for most atoms in the periodic table.

A second feature that played a role in the decision to build on BAND in the present work is the concept of variable periodicity. BAND can handle not only fully 3D extended systems (bulk crystals), but also 2D (planar materials, *e.g.* graphene[65]), 1D (atomic chains) and 0D systems (effectively gas-phase "molecular" calculations, as in ADF). This flexibility allows us to first model 3D bulk electrodes, and later incorporate them into transport calculations either with (1D-3D) or *without* periodic boundary conditions (0D), at our discretion.

Both codes allow for the incorporation of relativistic effects at the level of the zero-order regular approximation (ZORA),[66,67] either in scalar relativistic form or via full spin-orbit coupling. The former, in particular, should not be neglected in modeling metals such as gold (Au) commonly used for the electrodes in molecular transport experiments, as the size of the nucleus increases.

A number of techniques for computational speedup are also inherited by our implementation:

---

[g] STO's are optimal fits of functions of type $\phi(\boldsymbol{r}) = x^a y^b z^c e^{-\zeta r}$ to the Slater orbitals introduced in Eq. 2.4.

- The code is parallelized and has been tuned on high-performance computing systems based on Intel and IBM architectures. For details of the parallelization in general, we refer to te Velde *et al.*[42] Note however, that since publication, the original SPMD[h] approach has been supplanted by a robust shared-memory approach, allowing calculations to scale to considerably larger systems without exceeding the memory capacity of a typical modern workstation.[i]

- Linear-scaling techniques[68] have been implemented in order to significantly speed up large calculations, and have been demonstrated on the architectures noted in the previous point.[69,70]

- The code allows for the use of frozen-cores in calculations to efficiently treat the inner atomic shells, but does not require it, which conversely allows for all-electron calculations, if desired.

Two techniques in particular have, however, not yet been exploited in the work presented in this thesis:

- Space-group symmetry is used by BAND to reduce the computational effort in performing integrations over the Brillouin zone. This should allow significant computational speedup for the systems we consider as well, but its extension to our method has not yet been implemented.

- Calculations beyond the Γ-point approximation ($\boldsymbol{k} = \mathbf{0}$) are parallelized in BAND's implementation. We do not make use of this, and the natural path for the implementation of beyond-Γ-point calculations in treating the electrodes may not make use of it either.

It bears remarking that this localized-basis approach using STO/NAO basis sets is, in principle, a competing approach to both plane-wave and Gaussian-basis codes. The choices made in using the ADF/BAND package:

- Make the code perhaps slightly less computationally efficient in handling large extended systems than plane-wave codes, but make it significantly more suitable for handling the molecular device region in a transport junction, where the charge density is significantly more localized in nature. The BAND code uses essentially the same basis sets as its gas-phase molecular counterpart, ADF, making DFT results extremely comparable between the two.

- On the other hand, compared with Gaussian basis sets, the code trades more expensive 3D integrations (*e.g.* in evaluating the Coulomb and XC-potentials) against the fact that STO/NAO's are both physically better motivated, and cause the electronic wavefunctions and density to have more correct behavior near

---

[h] Single Process Multiple Data

[i] Typically 8-16 cores running at roughly 3 GHz, as of 2012.

the nuclei and in the tails. Moreover, they allow efficient evaluation, with roughly a factor 3 fewer basis-functions than the number of Gaussians.[68]

Finally, we also note our extensive use of electronic structure and geometry-optimization calculations using the ADF code, performed in order to gain insight into the molecules of interest in this thesis.

REFERENCES

[1] N. Agraït, A. L. Yeyati, and J. M. van Ruitenbeek, *Quantum properties of atomic-sized conductors*, Phys. Rep. **377**, 81 (2003).

[2] L. Venkataraman, J. E. Klare, C. Nuckolls, M. S. Hybertsen, and M. L. Steigerwald, *Dependence of single-molecule junction conductance on molecular conformation*, Nature **442**, 904 (2006).

[3] E. A. Osorio, K. O'Neill, M. Wegewijs, N. Stuhr-Hansen, J. Paaske, T. Bjørnholm, and H. S. J. van der Zant, *Electronic excitations of a single molecule contacted in a three-terminal configuration*, Nano Lett. **7**, 3336 (2007).

[4] S. Quek, L. Venkataraman, H. Choi, S. Louie, M. Hybertsen, and J. Neaton, *Amine–Gold Linked Single-Molecule Circuits: Experiment and Theory*, Nano Lett. **11**, 3477 (2007).

[5] J. Taylor, H. Guo, and J. Wang, *Ab initio modeling of quantum transport properties of molecular electronic devices*, Phys. Rev. B **63**, 245407 (2001).

[6] Y. Xue, S. Datta, and M. A. Ratner, *First-principles based matrix Green's function approach to molecular electronic devices: general formalism*, Chem. Phys. **281**, 151 (2002).

[7] Z. Qian, R. Li, S. Hou, Z. Xue, and S. Sanvito, *An efficient nonequilibrium Green's function formalism combined with density functional theory approach for calculating electron transport properties of molecular devices with quasi-one-dimensional electrodes*, J. Chem. Phys. **127**, 194710 (2007).

[8] J. M. Soler, E. Artacho, J. D. Gale, A. Garcia, J. Junquera, P. Ordejon, and D. Sanchez-Portal, *The SIESTA method for ab initio order-N materials simulation*, J. Phys.: Condens. Matter **14**, 2745 (2002).

[9] M. Brandbyge, J.-L. Mozos, P. Ordejón, J. Taylor, and K. Stokbro, *Density-functional method for nonequilibrium electron transport*, Phys. Rev. B **65**, 165401 (2002).

[10] K. Stokbro, J. Taylor, M. Brandbyge, and P. Ordejón, *TranSIESTA – A Spice for Molecular Electronics*, Ann. N.Y. Acad. Sci. **1006**, 212 (2003).

[11] R. Ahlrichs, M. Bär, M. Häser, H. Horn, and C. Kölmel, *Electronic structure calculations on workstation computers: The program system TurboMole*, Chem. Phys. Lett. **162**, 165 (1989).

[12] F. Evers, F. Weigend, and M. Koentopp, *Coherent transport through a molecular wire: DFT calculation*, Physica E: Low-dimensional Systems and Nanostructures **18**, 255 (2003), 23rd International Conference on Low Temperature Physics (LT23).

[13] F. Evers and A. Arnold, *CFN Lectures on Functional Nanostructures*, vol. 2 of *Springer Lecture Notes in Physics* (Springer, 2006), 1st ed.

[14] A. Arnold, F. Weigend, and F. Evers, *Quantum chemistry calculations for molecules coupled to reservoirs: Formalism, implementation, and application to benzenedithiol*, J. Chem. Phys. **126**, 174101 (2007).

[15] A. R. Rocha, V. M. García-Suárez, S. Bailey, C. Lambert, J. Ferrer, and S. Sanvito, *Spin and molecular electronics in atomically generated orbital landscapes*, Phys. Rev. B **73**, 085414 (2006).

[16] K. Burke, *Perspective on density functional theory*, J. Chem. Phys. **136**, 150901 (pages 9) (2012).

[17] Y. Meir and N. S. Wingreen, *Landauer formula for the current through an interacting electron region*, Phys. Rev. Lett. **68**, 2512 (1992).

[18] S. Datta, *Nanoscale device modeling: the Green's function method*, Superlatt. Microstruct. **28**, 253 (2000).

[19] J. L. Mozos, P. Ordejón, M. Brandbyge, J. Taylor, and K. Stokbro, *Simulations of quantum transport in nanoscale systems: application to atomic gold and silver wires*, Nanotechnology **13**, 346 (2002).

[20] K. Stokbro, J. Taylor, M. Brandbyge, J. L. Mozos, and P. Ordejón, *Theoretical study of the nonlinear conductance of di-thiol benzene coupled to Au(111) surfaces via thiol and thiolate bonds*, Comp. Mat. Sci. **27**, 151 (2003).

[21] C. Li, I. Pobelov, T. Wandlowski, A. Bagrets, A. Arnold, and F. Evers, *Charge Transport in Single Au-Alkanedithiol-Au Junctions: Coordination Geometries and Conformational Degrees of Freedom*, J. Am. Chem. Soc. **130**, 318 (2008).

[22] J. Prasongkit, A. Grigoriev, G. Wendin, and R. Ahuja, *Cumulene molecular wire conductance from first principles*, Phys. Rev. B **81**, 115404 (2010).

[23] Z. Zanolli, G. Onida, and J.-C. Charlier, *Quantum Spin Transport in Carbon Chains*, ACS Nano **4**, 5174 (2010).

[24] J. P. Perdew and A. Zunger, *Self-interaction correction to density-functional approximations for many-electron systems*, Phys. Rev. B **23**, 5048 (1981).

[25] C. Toher, A. Filippetti, S. Sanvito, and K. Burke, *Self-Interaction Errors in Density-Functional Calculations of Electronic Transport*, Phys. Rev. Lett. **95**, 146402 (2005).

[26] C. Toher and S. Sanvito, *Efficient Atomic Self-Interaction Correction Scheme for Nonequilibrium Quantum Transport*, Phys. Rev. Lett. **99**, 056801 (2007).

[27] J. P. Perdew, R. G. Parr, M. Levy, and J. L. Balduz, *Density-Functional Theory for Fractional Particle Number: Derivative Discontinuities of the Energy*, Phys. Rev. Lett. **49**, 1691 (1982).

[28] J. P. Perdew and M. Levy, *Physical Content of the Exact Kohn-Sham Orbital Energies: Band Gaps and Derivative Discontinuities*, Phys. Rev. Lett. **51**, 1884 (1983).

[29] M. Koentopp, K. Burke, and F. Evers, *Zero-bias molecular electronics: Exchange-correlation corrections to Landauer's formula*, Phys. Rev. B **73**, 121403 (2006).

[30] F. Aryasetiawan and O. Gunnarsson, *The GW method*, Rep. Prog. Phys. **61**, 237 (1998).

[31] K. S. Thygesen and A. Rubio, *Renormalization of Molecular Quasiparticle Levels at Metal-Molecule Interfaces: Trends across Binding Regimes*, Phys. Rev. Lett. **102**, 046802 (2009).

[32] Y. Xue and M. A. Ratner, *Microscopic study of electrical transport through individual molecules with metallic contacts. I. Band lineup, voltage drop, and high-field transport*, Phys. Rev. B **68**, 115406 (2003).

[33] Y. Xue and M. A. Ratner, *Microscopic study of electrical transport through individual molecules with metallic contacts. II. Effect of the interface structure*, Phys. Rev. B **68**, 115407 (2003).

[34] S. Barraza-Lopez, M. C. Avery, and K. Park, *First-principles study of a single-molecule magnet $Mn12$ monolayer on the Au(111) surface*, Phys. Rev. B **76**, 224413 (2007).

[35] K. Park, S. Barraza-Lopez, V. M. García-Suárez, and J. Ferrer, *Effects of bonding type and interface geometry on coherent transport through the single-molecule magnet $Mn12$*, Phys. Rev. B **81**, 125447 (2010).

[36] J. B. Neaton, M. S. Hybertsen, and S. G. Louie, *Renormalization of Molecular Electronic Levels at Metal-Molecule Interfaces*, Phys. Rev. Lett. **97**, 216405 (2006).

[37] D. J. Mowbray, G. Jones, and K. S. Thygesen, *Influence of functional groups on charge transport in molecular junctions*, J. Chem. Phys. **128**, 111103 (pages 5) (2008).

[38] K. Kaasbjerg and K. Flensberg, *Strong Polarization-Induced Reduction of Addition Energies in Single-Molecule Nanojunctions*, Nano Lett. **8**, 3809 (2008).

[39] R. Baer, E. Livshits, and U. Salzner, *Tuned Range-Separated Hybrids in Density Functional Theory*, Annu. Rev. Phys. Chem. **61**, 85 (2010).

[40] G. te Velde and E. J. Baerends, *Precise density-functional method for periodic structures*, Phys. Rev. B **44**, 7888 (1991).

[41] G. Wiesenekker and E. J. Baerends, *Quadratic integration over the three-dimensional Brillouin zone*, J. Phys.: Condens. Matter **3**, 6721 (1991).

[42] G. te Velde, F. Bickelhaupt, S. van Gisbergen, C. Fonseca Guerra, E. Baerends, J. Snijders, and T. Ziegler, *Chemistry with ADF*, J. Comput. Chem. **22**, 931 (2001).

[43] R. Martin, *Electronic Structure* (Cambridge University Press, 2004), 1st ed.

[44] J. C. Slater, *The Theory of Complex Spectra*, Phys. Rev. **34**, 1293 (1929).

[45] P. Hohenberg and W. Kohn, *Inhomogeneous Electron Gas*, Phys. Rev. **136**, B864 (1964).

[46] W. Kohn and L. J. Sham, *Self-Consistent Equations Including Exchange and Correlation Effects*, Phys. Rev. **140**, A1133 (1965).

[47] R. O. Jones and O. Gunnarsson, *The density functional formalism, its applications and prospects*, Rev. Mod. Phys. **61**, 689 (1989).

[48] J. F. Janak, *Proof that $\partial E/\partial ni = \epsilon$ in density-functional theory*, Phys. Rev. B **18**, 7165 (1978).

[49] J. P. Perdew and Y. Wang, *Accurate and simple analytic representation of the electron-gas correlation energy*, Phys. Rev. B **45**, 13244 (1992), pW86.

[50] J. P. Perdew, K. Burke, and M. Ernzerhof, *Generalized Gradient Approximation Made Simple*, Phys. Rev. Lett. **77**, 3865 (1996), pBE.

[51] C. Lee, W. Yang, and R. G. Parr, *Development of the Colle-Salvetti correlation-energy formula into a functional of the electron density*, Phys. Rev. B **37**, 785 (1988).

[52] A. D. Becke, *A new mixing of Hartree–Fock and local density-functional theories*, J. Chem. Phys. **98**, 1372 (1993).

[53] C. D. Pemmaraju, T. Archer, D. Sanchez-Portal, and S. Sanvito, *Atomic-orbital-based approximate self-interaction correction scheme for molecules and solids*, Phys. Rev. B **75**, 045101 (pages 16) (2007).

[54] R. Mattuck, *A Guide to Feynman Diagrams in the Many-Body Problem* (Dover, 1976).

[55] A.-P. Jauho, N. S. Wingreen, and Y. Meir, *Time-dependent transport in interacting and noninteracting resonant-tunneling systems*, Phys. Rev. B **50**, 5528 (1994).

[56] H. Haug and A.-P. Jauho, *Quantum Kinetics in Transport and Optics of Semi-conductors* (Springer-Verlag, 1997), 1st ed.

[57] J. Rammer, *Quantum Transport Theory* (Perseus Books, 1998), 1st ed.

[58] J. Rammer, *Quantum Field Theory of Non-equilibrium States* (Cambridge University Press, 2007), 1st ed.

[59] M. Di Ventra, *Electrical Transport in Nanoscale Systems* (Cambridge University Press, 2008), 1st ed.

[60] S. Datta, *Electronic Transport in Mesoscopic Systems* (Cambridge University Press, 1997), 1st ed.

[61] F. Evers, F. Weigend, and M. Koentopp, *Conductance of molecular wires and transport calculations based on density-functional theory*, Phys. Rev. B **69**, 235411 (2004).

[62] C. J. O. Verzijl and J. M. Thijssen, *A DFT-based Molecular Transport Implementation in ADF/BAND*, J. Phys. Chem. C (2012), accepted.

[63] R. G. Parr and Y. Weitao, *Density-Functional Theory of Atoms and Molecules*, no. 16 in International Series of Monographs on Chemistry (Oxford University Press, 1989), 1st ed.

[64] R. Dreizler and E. K. U. Gross, *Density Functional Theory: An Approach to the Quantum Many-Body Problem* (Springer, 1990), 1st ed.

[65] K. S. Novoselov, A. K. Geim, S. V. Morozov, D. Jiang, Y. Zhang, S. V. Dubonos, I. V. Grigorieva, and A. A. Firsov, *Electric Field Effect in Atomically Thin Carbon Films*, Science **306**, 666 (2004).

[66] E. van Lenthe, E. J. Baerends, and J. G. Snijders, *Relativistic total energy using regular approximations*, J. Chem. Phys. **101**, 9783 (1994).

[67] E. van Lenthe, A. Ehlers, and E.-J. Baerends, *Geometry optimizations in the zero order regular approximation for relativistic effects*, J. Chem. Phys. **110**, 8943 (1999).

[68] C. Fonseca Guerra, J. G. Snijders, G. te Velde, and E. J. Baerends, *Towards an order-N DFT method*, Theor. Chem. Acc. **99**, 391 (1998).

[69] Hewlett-Packard Development Company, L.P., *HP Clusters in Computational Chemistry - Case Study with Amsterdam Density Functional (ADF) Software* (2006), White Paper.

[70] Hewlett-Packard Development Company, L.P., *HP Systems in Computational Chemistry - Case Study with Amsterdam Density Functional (ADF) Software II* (2009), White Paper.

3

A DFT+NEGF TRANSPORT IMPLEMENTATION

We present a novel implementation of the first-principles approach to molecular charge transport, combining density function theory (DFT) with the non-equilibrium Green's function (NEGF) formalism. We have implemented this in the ADF/BAND quantum chemistry package. This chapter focuses solely on the implementation, adding previously unpublished details of complementary techniques, such as the implementation of density-constrained convergence acceleration, constant gating of the molecular region, wide-band limit (WBL) approximations and post self-consistent transport calculations.

Parts of this chapter have been published in J. Phys. Chem. C (2012)
at `http://dx.doi.org/10.1021/jp3044225`.

This chapter will expand on the key implementation issues faced in developing our molecular transport method. As the reader will recall from section 2.6, the underlying DFT code in which the DFT+NEGF method is implemented, BAND,[1–3] is a periodic structure code which uses a *local* basis and a combination of Slater-type (STO) and numerical atomic orbital (NAO) basis sets. These are usually complemented by frozen-core approximations of the inner electron shells of the atoms in the system. Smooth radial confinement of the basis-functions can be applied using a Fermi-Dirac function of the distance from the nucleus. The code also supports variable periodicity, ranging from 0D (none), 1D (chain), 2D (slab) and finally to 3D (bulk) geometries.

The normal "path" of the multi-stage transport calculation is roughly:

1. Calculation of infinite bulk contacts' Hamiltonian $\boldsymbol{H}^{\text{KS}}$,
2. Determination of a tight-binding representation of the converged $\boldsymbol{H}^{\text{KS}}$,
3. Calculation of the self-energies $\boldsymbol{\Sigma}_{1,2}(\epsilon)$ of semi-infinite bulk contacts,
4. Alignment of the leads with the central extended-molecule region composed of bulk material,
5. Transport calculation proper, with extended-molecule region now comprising the molecule coupled to part of the electrodes.

We begin by outlining the way we implement the NEGF formalism of Chapter 2 in matrix-vector notation in **§3.1**. Then, we discuss the partitioning of the model system in **§3.2**, the treatment of the Hamiltonian obtained from the periodic band-structure calculation in **§3.3**, and how we obtain surface Green's functions and self-energies coupling the infinite leads to an "extended molecule" in **§3.4**. The evaluation of the equilibrium density matrix is outlined in **§3.5**, which is necessary for any full alignment or zero-bias transport calculation. In **§3.6** we then discuss the alignment of the potential between computational stages, and its deeper physical relation with the accurate determination of the Fermi-levels of the contacts. The details of the non-equilibrium two-terminal calculations are treated in **§3.7**, and in **§3.8** we discuss our implementation of gating, as a rudimentary model for three-terminal calculations.

The code can also be used to perform two types of approximate transport calculations: post-SCF transport calculations are discussed in **§3.9**, and the implementation of wide-band limit (WBL) calculations are discussed in **§3.10**. The chapter then closes with a brief discussion of scaling and performance in **§3.11**.

Finally, as we discuss only implementation in this chapter and not the code itself, we note that the code structure and flow is discussed briefly as Appendix E, and that we include sample input files in Appendix F. Besides these, our constrained DIIS algorithm extension may also be of interest, and is included as Appendix D.

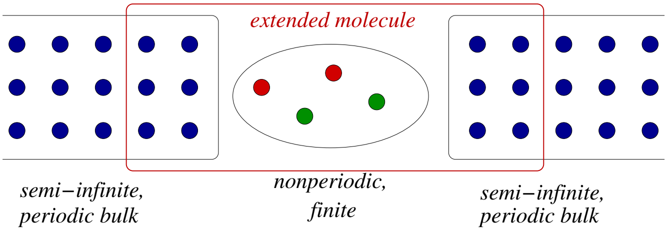

Figure 3.1: Schematic geometry of the extended molecule (physical molecule and portion of the contacts to which it is attached) and semi-infinite bulk portion of the contacts.

3.1 Modeling Overview

In order to model the molecular system and the contacts to which it is connected using *ab initio* techniques, we need to reduce the size of the system being modeled from a molecule between infinitely large contacts to something more manageable. To this end we use the "extended molecule" (EM) scheme,[4,5] illustrated in Fig. 3.1. The system is partitioned into a central extended molecule comprised of the actual molecule and some connecting parts of the leads on each side. This extended molecule, in turn, is then connected to true semi-infinite bulk leads via a well-defined metal-metal interface. Thus, in our model the leads are described by a finite-dimensional Hamiltonian $\hat{H}$ corresponding to a portion of true bulk metal, corrected by a self-energy $\hat{\Sigma}$ containing the response of the leads.

The key benefits of modeling the system in this way are first that we are able to place the interface between the leads and the active portion of the single-molecule system between metal layers, an interface which is much better understood than the complex molecule-metal binding geometries which may occur. The details of these binding geometries may then be varied, without the need to recalculate the contributions from the bulk contacts. A subtler point is that, as argued by Evers *et al.*[6,7], this approach allows us to increase the size of the extended molecule in order to test convergence to transport properties which correspond to truly bulk-reservoir electrodes, which they have shown for tight-binding chains and cluster Au electrodes of varying sizes. Furthermore, the metallic parts of the extended molecule allow us to take simple polarization effects in the leads into account. Finally, the approach allows us to obtain the propagator for the entire extended molecule in a simple way, which we derived in the operator formalism of section 2.3 and implement here.

To treat the metallic contacts, a calculation is first performed in the band-structure DFT code BAND to obtain the Fock matrix for a bulk unit cell from the self-consistent density via the Kohn-Sham Hamiltonian of Eq. (2.7). The density is constructed from the occupied Kohn-Sham orbitals as $n(\boldsymbol{r}) = \sum_{i_{\mathrm{occ}}} |\psi_i(\boldsymbol{r})|^2$, but in the following, it should be kept in mind that the Kohn-Sham Hamiltonian implicitly depends on the bias voltage V_b, the spin and the electron density $n(\boldsymbol{r})$, which we will usually omit for compactness of notation.

In BAND we represent the Hamiltonian (2.7) in a non-orthogonal basis, and so obtain the Fock matrix as $\boldsymbol{H}^{\text{KS}} = [\langle\phi_i|\hat{H}^{\text{KS}}|\phi_j\rangle]$ and the overlap matrix as $\boldsymbol{S}^{\text{KS}} = [\langle\phi_i|\phi_j\rangle]$. From the Fock and overlap matrices for the bulk leads we calculate the (matrix) surface Green's functions $\boldsymbol{G}_c(\epsilon)$ by an efficient recursion algorithm.[8,9] We then find the corresponding (matrix) self-energies $\boldsymbol{\Sigma}_{c=1,2}(\epsilon) \sim \boldsymbol{\tau}\,\boldsymbol{G}_c(\epsilon)\,\boldsymbol{\tau}^\dagger$ of the two contacts and $\boldsymbol{\tau}$ the coupling between layers in the leads. These are then combined with the Hamiltonian of the extended molecule to find the full Green's function:

$$\boldsymbol{G}_{\text{EM}}(\epsilon) = \Big(\epsilon\,\boldsymbol{S}_{\text{EM}} - \boldsymbol{H}_{\text{EM}} - (\boldsymbol{\Sigma}_1(\epsilon) + \boldsymbol{\Sigma}_2(\epsilon))\Big)^{-1} . \tag{3.1}$$

where $\boldsymbol{G}(\epsilon)$, $\boldsymbol{\Sigma}_{1,2}(\epsilon)$ refer to the retarded (causal) Green's function and self-energies, respectively. The Green's functions are then used in a modified self-consistent field (SCF) approach based on the density derived from the Green's function:

$$\begin{aligned}\phi_j^{(0)}(\boldsymbol{r}) \to n^{(0)}(\boldsymbol{r}) \to \boldsymbol{H}^{\text{KS}} + \boldsymbol{\Sigma}_1 + \boldsymbol{\Sigma}_2 \to \boldsymbol{G}(\epsilon) \to \boldsymbol{\rho} \to n^{(1)}(\boldsymbol{r}) \to \\ \boldsymbol{H}^{\text{KS}} + \boldsymbol{\Sigma}_1 + \boldsymbol{\Sigma}_2 \to \boldsymbol{G}(\epsilon) \to \boldsymbol{\rho} \to n^{(2)}(\boldsymbol{r}) \to \dots\end{aligned} \tag{3.2}$$

which may be compared to the usual SCF cycle in DFT:

$$\phi_j^{(0)}(\boldsymbol{r}) \to n^{(0)}(\boldsymbol{r}) \to \boldsymbol{H}^{\text{KS}} \to \phi_j^{(1)}(\boldsymbol{r}) \to n^{(1)}(\boldsymbol{r}) \to \boldsymbol{H}^{\text{KS}} \dots$$

If we assume that the contacts each couple only with the central extended molecule, then we can simplify the general Green's function formalism and obtain the density matrix from the Green's function at each iteration as an integral over the real-valued energies:

$$\boldsymbol{\rho} = \frac{1}{2\pi}\int \mathrm{d}\epsilon\,[\,\boldsymbol{G}(\epsilon)\boldsymbol{\Gamma}_1(\epsilon)\boldsymbol{G}^\dagger(\epsilon)f(\epsilon,\mu_1) + \boldsymbol{G}(\epsilon)\boldsymbol{\Gamma}_2(\epsilon)\boldsymbol{G}^\dagger(\epsilon)f(\epsilon,\mu_2)\,] . \tag{3.3}$$

$\boldsymbol{\Gamma}(\epsilon)$ is defined as $\mathrm{i}\big(\boldsymbol{\Sigma}(\epsilon) - \boldsymbol{\Sigma}^\dagger(\epsilon)\big)$ for each contact. μ_1 and μ_2 are the chemical potential of source and drain electrodes. The bias voltage follows as $V_b = \frac{\mu_1-\mu_2}{e}$.

This is general to the case of differing chemical potentials (*e.g.* biased devices or different contact materials), but doesn't take *e.g.* direct coupling between leads into account. In the equilibrium case with a single chemical potential in both leads, the expression further simplifies to:

$$\boldsymbol{\rho} = -\frac{1}{\pi}\int \mathrm{d}\epsilon\,\mathrm{Im}\,\{\boldsymbol{G}(\epsilon)\}\,f(\epsilon,\mu) . \tag{3.4}$$

When the SCF cycle (3.2) converges, some interesting properties of the molecular system may be evaluated, using the converged $G(\epsilon)$ to obtain *e.g.* the density of states (DOS) by:

$$D(\epsilon) = -\frac{1}{\pi}\mathrm{Tr}\,[\,\mathrm{Im}\,\{\,\boldsymbol{G}(\epsilon)\,\}\,\boldsymbol{S}\,] , \tag{3.5}$$

and the current by a Landauer-like expression, with $T(\epsilon) \sim \mathrm{Tr}\left[\mathbf{\Gamma}_1 \boldsymbol{G} \mathbf{\Gamma}_2 \boldsymbol{G}^\dagger\right]$ such that:

$$I = \frac{2e}{h} \int \mathrm{d}\epsilon \, \mathrm{Tr}\left[\mathbf{\Gamma}_1(\epsilon)\boldsymbol{G}(\epsilon)\mathbf{\Gamma}_2(\epsilon)\boldsymbol{G}^\dagger(\epsilon)\right](f(\epsilon,\mu_1) - f(\epsilon,\mu_2)) \; . \tag{3.6}$$

The integral above is over the real line, but can be performed much more efficiently by using analytic continuation and complex contour integration,[10] which we discuss in the next chapter.

An important technical issue is that the offset of the potential cannot be expected to be the same in the junction geometry as that used for the bulk metal calculation for the contacts, due both to the controlled approximation in the tight-binding fit, and the much larger intrinsic issue of a floating-potential effect in the periodic band-structure code. The latter arises because in any band-structure DFT code the potential, and thus the Hamiltonian, are only determined up to some additive constant, *i.e.* $\boldsymbol{H}$ and $\boldsymbol{H} + \Delta\phi \boldsymbol{S}$ give the same spectrum for an (energy-independent) constant offset $\Delta\phi$. However, as our approach to transport involves several stages (bulk calculation of contacts, self-energy calculation, self-consistent alignment and transport calculation), we must take care to ensure that the (arbitrary) offset in the potential is consistent across all stages.

To find the offset $\Delta\phi$, an alignment calculation is carried out next, such that for the contacts in the transport calculation, it holds that:

$$\boldsymbol{H}^{\text{KS}} \approx \boldsymbol{H}^{\text{TB}} + \Delta\phi \cdot \boldsymbol{S}^{\text{TB}} \; ,$$

to within some acceptable tolerance. Once converged, we proceed to the calculation of an arbitrary molecular system, which may be under bias.

3.2 SYSTEM PARTITIONING

The partitioning illustrated in Fig. 3.1 is made precise in terms of the operators in the formalism in Fig. 3.2. The partitioning of the Hamiltonian into extended molecule ($\boldsymbol{H}_m$) plus contacts ($\boldsymbol{H}_c = \boldsymbol{H}_1 \oplus \boldsymbol{H}_2$) is as follows:

$$\boldsymbol{H} = \begin{pmatrix} \boldsymbol{H}_m & \boldsymbol{\tau}_1^\dagger & \boldsymbol{\tau}_2^\dagger \\ \boldsymbol{\tau}_1 & \boldsymbol{H}_1 & 0 \\ \boldsymbol{\tau}_2 & 0 & \boldsymbol{H}_2 \end{pmatrix} \equiv \begin{pmatrix} \boldsymbol{H}_m & \boldsymbol{\tau}^\dagger \\ \boldsymbol{\tau} & \boldsymbol{H}_c \end{pmatrix} \tag{3.7}$$

such that the Green's function for the entire system is determined by inverting:

$$(\epsilon \boldsymbol{S} - \boldsymbol{H})\boldsymbol{G}(\epsilon) = \boldsymbol{I} \; . \tag{3.8}$$

The specific approximation behind this partitioning is that we require the full Hamiltonian for contacts and extended molecule to be correct in the Kohn-Sham sense at each iteration, while the density matrix need only be correct for the extended molecule. This is justified by its spatial separation from the (expected) field- and charge-errors at the outer edges of the finite system. The errors there, in turn, are minimized by replacing $\boldsymbol{H}_{1,2}$ by the stored bulk operators, as we discuss in section 3.6.

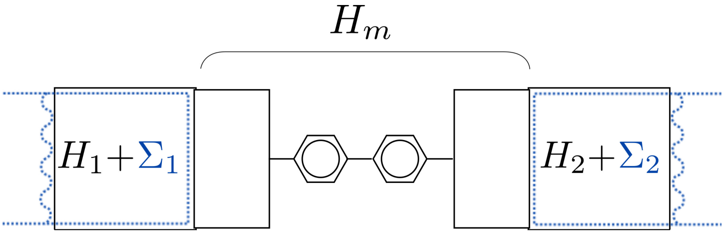

Figure 3.2: Schematic geometry of the extended molecule and semi-infinite bulk portion of the contacts indicating the regions on which each operator in the formalism is active

3.3 The Tight-binding Representation

From the bulk calculation, the Fock matrix is known with respect to BAND's basis-functions for many Bloch boundary conditions, represented by a dense set of Bloch wavevectors $\boldsymbol{k}$ inside the Brillouin zone. We search for a tight-binding Fock matrix, given in terms of BAND's localized basis-functions, which reproduces BAND's Fock matrices as closely as possible.

The basis-functions are denoted $\left|\phi_i^\alpha\right\rangle$, where i denotes a unit cell and α denotes a particular orbital type:

$$\langle \boldsymbol{r}|\phi_i^\alpha\rangle = \phi^\alpha(\boldsymbol{r}-\boldsymbol{r}_i^\alpha).$$

Here, $\boldsymbol{r}_i^\alpha$ is the position of the atom in unit cell i about which the α-orbital is centered. Taking the cell index $i = 0$ without loss of generality, we denote the real-space tight-binding matrix elements in relation to k-space as:

$$H^{\text{TB}}_{\alpha\beta}(\boldsymbol{k}) = \sum_{\boldsymbol{R}_j} H^{\text{TB}}_{i\alpha,j\beta}\, e^{i\boldsymbol{k}\cdot\boldsymbol{R}_j} \ , \tag{3.9}$$

The requirement that the matrix on the left-hand side is equivalent to Band's Fock operator suggests that:

$$F = \sum_{\alpha\beta}\sum_{l}\left|H^{\text{TB}}_{\alpha\beta}(\boldsymbol{k}_l) - H^{\text{KS}}_{\alpha\beta}(\boldsymbol{k}_l)\right|^2 \ ,$$

be minimized with respect to the real-space matrix elements $H^{\text{TB}}_{i\alpha,j\beta}$.

This minimization is done using the L-BFGS algorithm,[11] with a cut-off radius which is increased as needed to meet a user-specified tolerance for the fit. As each element of the tight-binding fit is calculated using only the lattice positions and the reference value of the Fock matrix, it can be calculated independently, so that this calculation is trivially parallelized, with linear scaling in the number of cores.

We emphasize, however, that we make a tight-binding *fit* H^{TB} of H^{KS} in terms of the (known) lattice of the contact, as opposed to switching to a traditional tight-binding *model* for the electronic structure. These TB Fock and overlap matrices, together with the lattice, then form the input for our calculation of the surface

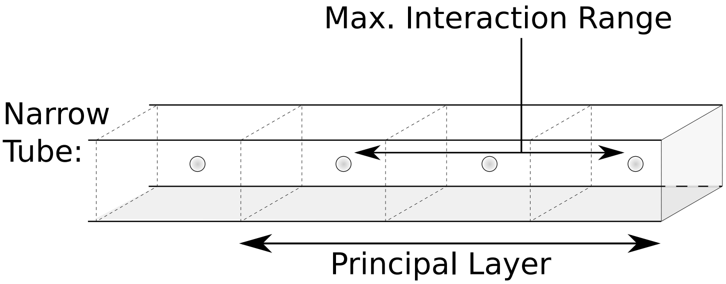

Figure 3.3: Narrow tube (NT) in the infinite contact based on a single unit cell. Partitioning based on principal layers, which due to electronic screening interact only with neighboring principal layers (discussed in section 3.4).

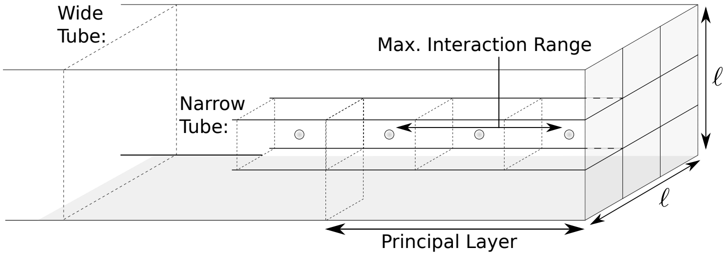

Figure 3.4: Wide tube (WT) in the infinite contact based on an $\ell \times \ell$ grid of unit cells in the surface plane. Compare Fig. 3.3 for the relation with the narrow tube.

Green's functions.

We now have a set of Fock and overlap matrices corresponding to $\boldsymbol{k}$-vectors in the Brillouin zone, from which we can calculate self-energies, for a 'tube' extending into the contact as in Fig. 3.3. From these, we can calculate self-energies on the same grid of $\boldsymbol{k}$-vectors. We assume the number of $\boldsymbol{k}$ vectors in the Brillouin zone to be N^2. From these matrices, it is then possible to calculate their counterparts for a wider tube with periodic boundary conditions, *cf.* Fig. 3.4. We now denote the original (narrow) tube by NT, and the wide tube as WT.

We assume that the 2D unit cell of the wide tube is an integer multiple ($\ell \times \ell$) of that of the narrow tube. Within the narrow tube, we can write the Fourier transform of the matrix M (which may be the Hamiltonian or the overlap matrix) for any wave vector $\boldsymbol{k}$ as

$$M^{\mathrm{NT}}_{\alpha\beta}(\boldsymbol{k}) = \sum_{\boldsymbol{r}_{\|}} M_{\alpha\beta}(\boldsymbol{r}_{\|}) e^{i\boldsymbol{k}\cdot\boldsymbol{r}_{\|}},$$

where the sum $\sum_{\boldsymbol{r}_{\|}}$ is over *all* relative positions $\boldsymbol{r}^{\alpha}_{i} - \boldsymbol{r}^{\beta}_{j}$ within the large volume corresponding to the N^2 $\boldsymbol{k}$-vectors in the two-dimensional BZ in the surface plane.

Taking the wide tube with periodic boundary conditions (i.e. at the Γ-point), we have

$$M^{\mathrm{WT}}_{\alpha\beta}(\boldsymbol{r}_{\|}) = \sum_{\boldsymbol{R}^{\mathrm{WT}}} M_{\alpha\beta}(\boldsymbol{r}_{\|} + \boldsymbol{R}^{\mathrm{WT}}) \ ,$$

where $\boldsymbol{R}^{\mathrm{WT}}$ is any $m \cdot \boldsymbol{a}^{w}_{1} + n \cdot \boldsymbol{a}^{w}_{2}$, linear combination of wide-tube basis vectors ($\boldsymbol{a}^{w}_{i} = \ell \boldsymbol{a}^{n}_{i}$ in terms of the NT basis vectors). This equation expresses the periodicity of M^{WT}. On the other hand we can write:

$$M_{\alpha\beta}(\boldsymbol{r}_{\|} + \boldsymbol{R}^{\mathrm{WT}}) = \frac{(2\pi)^2}{\Omega} \int d^2k \ M_{\alpha\beta}(\boldsymbol{k}) e^{i\boldsymbol{k}\cdot(\boldsymbol{r}_{\|}+\boldsymbol{R}^{\mathrm{WT}})}.$$

Combining these two ingredients, we can write

$$M^{\mathrm{WT}}_{\alpha\beta}(\boldsymbol{r}) = \sum_{\boldsymbol{R}^{\mathrm{WT}}} \frac{1}{N^2} \sum_{\boldsymbol{k}_{\mathrm{BZ}}} M_{\alpha\beta}(\boldsymbol{k}_{\mathrm{BZ}}) e^{i\boldsymbol{k}\cdot(\boldsymbol{r}_{\|}+\boldsymbol{R}^{\mathrm{WT}})}.$$

The sum over the wide tube vectors $\boldsymbol{R}^{\mathrm{WT}}$ singles out the reciprocal lattice vectors (lying inside the NT Brillouin zone) of the wide tube:

$$\sum_{\boldsymbol{R}^{\mathrm{WT}}} e^{i\boldsymbol{k}\cdot\boldsymbol{R}^{\mathrm{WT}}} = \frac{N^2}{\ell^2} \sum_{\boldsymbol{K}^{\mathrm{WT}} \in BZ^{\mathrm{NT}}} \delta(\boldsymbol{k} - \boldsymbol{K}^{\mathrm{WT}}),$$

from which we immediately have:

$$M^{\mathrm{WT}}_{\alpha\beta}(\boldsymbol{r}_{\|}) = \frac{1}{\ell^2} \sum_{\boldsymbol{K}^{\mathrm{WT}} \in \mathrm{BZ}^{\mathrm{NT}}} M^{\mathrm{NT}}_{\alpha\beta}(\boldsymbol{K}^{\mathrm{WT}}) e^{i\boldsymbol{K}^{\mathrm{WT}}\cdot\boldsymbol{r}_{\|}} \ .$$

This expression tells us how to obtain the matrix elements between any two points inside the wide tube from the matrix elements on the reciprocal lattice points of the WT, lying inside the Brillouin zone of the NT.

3.4 Surface Green's Function & Self-Energies

Expanding Eq. (3.8) for the matrix Green's function in the case of a non-orthogonal basis yields the matrix relation:

$$\begin{pmatrix} \boldsymbol{I} & 0 \\ 0 & \boldsymbol{I} \end{pmatrix} = \begin{pmatrix} \epsilon \boldsymbol{S}_m - \boldsymbol{H}_m & \epsilon \boldsymbol{S}_\tau^\dagger - \boldsymbol{\tau}^\dagger \\ \epsilon \boldsymbol{S}_\tau - \boldsymbol{\tau} & \epsilon \boldsymbol{S}_c - \boldsymbol{H}_c \end{pmatrix} \begin{pmatrix} \boldsymbol{G}_m & \boldsymbol{G}_{mc} \\ \boldsymbol{G}_{cm} & \boldsymbol{G}_c \end{pmatrix} \tag{3.10}$$

(omitting the ϵ-dependence from the Green's functions on the right-hand side). From this follow closed expressions for the propagator $\boldsymbol{G}_m$ of the extended molecule using self-energies, in the presence of a contact:

$$\boldsymbol{G}_m = \left(\epsilon \boldsymbol{S}_m - \boldsymbol{H}_m - (\epsilon \boldsymbol{S}_\tau^\dagger - \boldsymbol{\tau}^\dagger)\, \boldsymbol{G}_c\, (\epsilon \boldsymbol{S}_\tau - \boldsymbol{\tau}) \right)^{-1} , \tag{3.11}$$

and we identify:

$$\boldsymbol{\Sigma}_c \equiv (\epsilon \boldsymbol{S}_\tau^\dagger - \boldsymbol{\tau}^\dagger)\, \boldsymbol{G}_c\, (\epsilon \boldsymbol{S}_\tau - \boldsymbol{\tau})$$

as the self-energy of the contacts, which may be split as $\Sigma_1 + \Sigma_2$.[a] For two contacts we specify the propagator further as $G(\epsilon) = (\epsilon S_m - H_m - \Sigma_1 - \Sigma_2)^{-1}$, and it is this subsystem which we subsequently focus on.

Two further remarks are important before continuing. First, we note that the determination of Σ_c only requires knowing the surface couplings in $(G_\mathrm{c})_{ij \in \mathrm{surf}}$, which makes this practical to implement in a DFT code with localized basis functions (such as BAND). Second, we note that while the above is an exact description within the limits of the one-electron picture (*i.e.* neglecting electron-electron interaction beyond the mean-field level), in practice when calculating by an approximate method such as an actual DFT implementation, we need to be aware of the consequences of the limited spatial extent of the extended molecule, which may be felt by the central region due to the Hartree term in the potential if it is insufficiently screened. Generally, for metals, the screening is strong enough to justify the approach for contacts of a few atomic layers deep.

Now, our approach to obtaining the Green's function $\boldsymbol{G}(\epsilon)$ relies on the fact that the metallic system has a finite interaction-range in real-space due to electronic screening. This implies a local– and neighbor-coupling structure of the Fock matrices which is tridiagonally structured as $(\tau,\ h,\ \tau^\dagger)$ in a basis organized into adjacent layers of atoms, and a similarly tridiagonally structured $(s_\tau,\ s,\ s_\tau^\dagger)$ overlap matrix.

We introduce the concept of "principal layers," because it is well known that electronic screening limits the interaction range of the Coulomb potential to just a few atomic layers in a metal.[12] This implies that we can give a description in terms of blocks of 3-4 atomic layers called a "principal layer," which interact only with the

---

[a] In the literature $\Sigma = \tau g \tau^\dagger$ is often used as the definition of the self-energy; then τ corresponds precisely to our $(\epsilon S_\tau - \tau)$ expression for the coupling of device and contact.

neighboring principal layers, as in Figs. 3.3–3.4. Together with the use of localized basis-functions, this allows us to use the structure of a Hamiltonian matrix as in Eq. (3.12) corresponding to principal and adjacent (interacting) layers, as illustrated in Fig. 3.3.

$$\boldsymbol{H} = \begin{pmatrix} h & \tau^{\dagger} & 0 & \cdots & \\ \tau & h & \tau^{\dagger} & 0 & \cdots \\ 0 & \tau & h & \tau^{\dagger} & 0 \\ \vdots & 0 & \ddots & \ddots & \ddots \end{pmatrix} . \tag{3.12}$$

We consider the metal as being composed of an infinite number of layers in space, and then find the relation between elements of the Green's function for 2^k and 2^{k+1} principal layers by recursively eliminating the layers in between.[8,9]

From this we obtain the Green's function for the surface and the bulk of an infinite contact, and can study the latter's convergence with respect to the bulk calculation in BAND. This method is easily extended to evaluation over a Monkhorst-Pack grid[13] in k-space, and parallelized in energy. This approach converges quickly, and a sample calculation of the surface and bulk DOS is illustrated in Fig. 3.5 for different grid densities in k-space in the plane of the contacts. In principle this k-space dependence also carries over to the alignment and transport calculations, and in the previous section we discussed a method for the construction of an expanded self-energy for the contacts. However, we will present only calculations in the Γ-point approximation in the remainder of this thesis, excluding the present chapter.

The key computational steps in this stage of the calculation are the complex contour integrals over the Green's functions (expressions (3.3)–(3.4)), which are a more efficient way[10] to evaluate the density matrix from the Green's function than direct integration over the real line. The reason for the latter is that in general $\boldsymbol{G}(\epsilon)$ may have poles quite near the real axis, necessitating a very dense integration grid, while the contour may be taken safely away from these in the upper half of the complex plane, drastically reducing the computational effort. The algorithmic details of the implementation of this calculation are discussed further in Appendix A.

We pre-calculate the contours themselves and the corresponding self-energies $\boldsymbol{\Sigma}_{1,2}(\epsilon_i)$ over all points on the contour $\{\epsilon_i\}$, given that the self-energies can be calculated independently for each energy point on the contour.

3.5 EVALUATING THE DENSITY MATRIX

In the next section we will consider the alignment calculation, which like any transport calculation requires the density matrix $\boldsymbol{\rho}$. As we remarked in section 2.1, this integral over the real line can be more efficiently obtained by complex contour integration, as detailed by Zeller *et al.*[10]

As in Eq. (3.4):

$$\boldsymbol{\rho} = -\frac{1}{\pi}\int_{-\infty}^{\infty} \mathrm{d}\epsilon \; \mathrm{Im}\left\{\boldsymbol{G}(\epsilon)\right\} f(\epsilon,\mu) \ ,$$

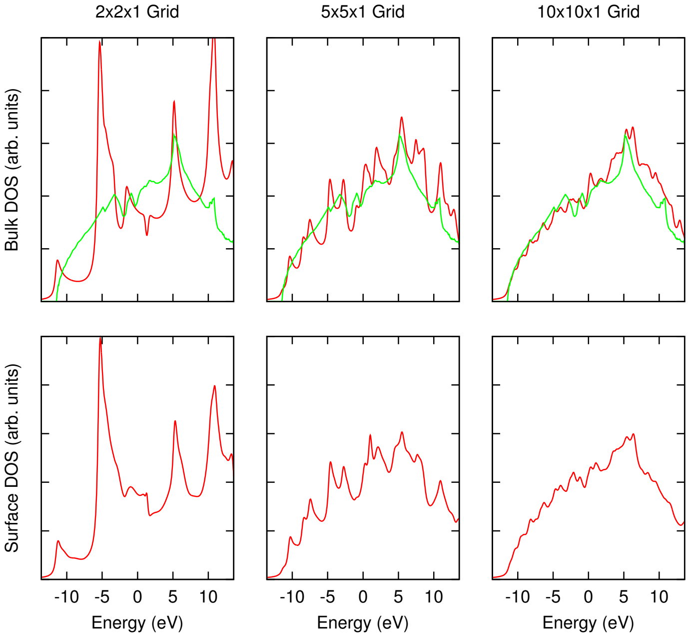

FIGURE 3.5: Convergence of the bulk aluminum DOS with increasingly dense grid in k-space. Top: bulk DOS from the Green's function (**red**) compared with normal DFT calculations (**green**): convergence for finer k-grids. Bottom: surface DOS for a [111]–cut surface (from the surface Green's function), which cannot be obtained directly from DFT. DFT calculations performed with the LDA functional, using a DZP-quality basis set.

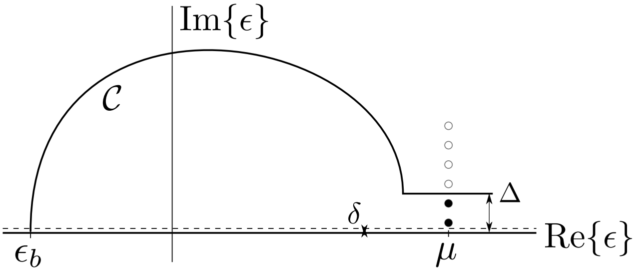

FIGURE 3.6: Contour in the complex plane which yields equivalent integral over the real line. Key parameters are the bottom of the valence band ϵ_b, the chemical potential μ and the offset Δ of the line segment which passes between the complex Fermi poles. δ is the offset of the line for the non-equilibrium calculations, which is much closer to the real axis.

where the integral is over the real line. In typical calculations the infinitesimal η shifts the poles of $\boldsymbol{G}(\epsilon)$ off the real line, but they may still be close enough to cause singularities. To handle these one might take a very dense grid of integration points, but they can instead be avoided by integrating over a contour as illustrated in Fig. 3.6, which avoids the poles entirely:

$$\int_{-\infty}^{\infty} \underbrace{\mathrm{d}\epsilon \,\mathrm{Im}\{\boldsymbol{G}(\epsilon)\}\, f(\epsilon,\mu)}_{g(z)\mathrm{d}z} = -\int_C \mathrm{d}z \,\mathrm{Im}\{\boldsymbol{G}(z)\}\, f(z,\mu) - 2\pi i \sum_i \mathrm{Res}_g(a_i)$$

with z correpsonding to ϵ in the analytic continuation of $g(z) = \mathrm{Im}\{\boldsymbol{G}(z)\}\, f(z,\mu)$ into the complex plane. The poles enclosed by the contour are solely those of the Fermi function, located at $\mu + i\pi k_B T(2n+1)$ for all integer $n > 0$, since the poles of the integrand lie strictly below the real axis. The residues are simply $-k_B T$.

In the non-equilibrium case this approach doesn't work, however, since the expressions for the density matrix (Eqs. (3.15)–(3.16)) will be shown to depend on the coupling matrices $\boldsymbol{\Gamma}_{1,2}(\epsilon)$ which has a pole structure which cannot be similarly predicted to be localized to *e.g.* below/above the real axis. In that case a very dense grid of integration points will have to be used. This is illustrated in Fig. 3.6 as well, with an offset δ corresponding to the smoothing.

3.6 ALIGNMENT: DETERMINATION OF THE FERMI LEVEL

As noted above, the zero of the potential is not uniquely determined in this type of DFT calculation. As our approach to transport involves a sequence of relatively independent computations (bulk calculation of contacts, self-energy calculation, self-consistent alignment and transport calculation), we must ensure that the (arbitrary) offset in the potential is consistent across all stages, keeping in mind that the self-energies also implicitly reference the chemical potential of their respective contact: $\boldsymbol{\Sigma}_{1,2}(\epsilon_i;\mu_{1,2})$. A number of codes take different approaches to this,[14,15] but we are not aware of any approach that has handled the problem self-consistently to date.

In order to ensure the alignment of the potentials in the leads (and their self-energies) with those of the extended molecule, we first note that there is a natural criterion for determining the offset: the charge neutrality of bulk material. Clearly, the chemical potential is directly related to the number of electrons in the metal. Consequently, when the unbiased extended molecule is itself composed of the same material as the contacts, we can self-consistently determine the offset by requiring the (valence) charge on the extended molecule to equal the bulk (valence) charge for the same number of atoms. We tune this charge by iteratively shifting the potential during the SCF until the criterion is met. We have also implemented a novel constrained-DIIS (CDIIS) scheme in our code to accelerate the convergence of this alignment procedure for difficult systems; it is briefly outlined in Appendix D.

Our approach is to split the shift into the two components illustrated in Fig. 3.7. The first is the offset between the bulk run (periodic cell, used to construct the

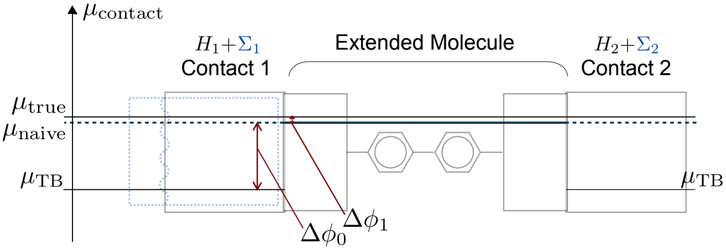

FIGURE 3.7: Differing computational stages' zeros of the potential induce differing chemical potentials, which are reconciled in alignment. Shown is the analog of Fig. 3.2, where we now include the contact offset $\Delta\phi_0$ and fine-tuning of charge-neutrality $\Delta\phi_1$ as discussed, yielding a consistent μ_{true} after alignment.

self-energies for the semi-infinite contacts) and the alignment run (longitudinally aperiodic transport geometry composed of contacts + extended molecule). This offset is estimated at each iteration as follows:

$$\Delta\phi_0 = \frac{1}{n_{\text{bas}}} \sum_{i\in \mathrm{C1}\oplus\mathrm{C2}} \frac{\left(H^{\text{TB}}_{ii} - H^{\text{KS}}_{ii}\right)}{S_{ii}} , \tag{3.13}$$

where $n_{\text{bas}} = n^{\text{C1}}_{\text{bas}} + n^{\text{C2}}_{\text{bas}}$ is the dimension of the basis of the Hamiltonian for the two contacts and $\boldsymbol{H}^{\text{TB}}$ and $\boldsymbol{H}^{\text{KS}}$ refer to the tight-binding representation of these bulk contact Hamiltonians and the transport geometry's contact Hamiltonians respectively (*cf.* Fig. 3.1). We now shift the system by the offset: $\boldsymbol{H}^{\text{KS}} \to \boldsymbol{H}^{\text{KS}} + \Delta\phi_0\, \boldsymbol{S}^{\text{KS}}$. Next, we overwrite the Hamiltonian and overlap matrix $\boldsymbol{S}^{\text{KS}}$ of the contact regions by those obtained from the bulk calculations, which do not suffer from edge effects and are now aligned with the rest of the system. This is updated at each iteration, allowing for fluctuations in the density-dependent potential $V[n(\mathbf{r})](\mathbf{r})$, such that the extended system is always as close as possible to precisely aligned with the bulk contacts' potential.[b]

The second shift is the correction to the extended system which brings the Fermi level into alignment with the implicit chemical potential encoded in the open-boundary self-energies. We obtain it by determining the density matrix from the Green's function for the extended system via equation (3.4), which yields the valence charge in the extended molecule region by tracing over the relevant basis functions as $Q_{\text{EM}} \equiv \mathrm{Tr}\left[\, \rho S\, \right]_{\text{EM}}$. This is in practice typically not charge-neutral. To achieve $Q_{\text{EM}} \to Q^0_{\text{EM}}$, the latter the correct (valence) charge, we use an offset which is calculated iteratively to ensure charge neutrality:

$$\Delta\phi_1^{(k+1)} = \Delta\phi_1^{(k)} + \alpha\left(\mathrm{Tr}\left[\, \rho S\, \right]_{\text{EM}} - Q^0_{\text{EM}}\right) \tag{3.14}$$

until convergence is achieved. The shifts $\Delta\phi_1$ are applied to the entire system. Note that the parameter α has the dimensions of a capacitance, and indeed can be chosen

---

[b] Convergence of these shifts is thus a natural heuristic for the proper alignment of the system with this algorithm.

proportional to the inverse of the density of states, evaluated at the Fermi-energy. In practice, such an implementation easily becomes numerically unstable, and we have opted for a fixed, small mixing parameter α instead.

Both shifts, $\Delta\phi_0$, $\Delta\phi_1$, must converge for the alignment stage to be considered successful. This procedure may be accelerated by extending the DIIS scheme[16] as outlined in Appendix D, and we illustrate a representative performance of the accelerated method in Fig. D.1 for a one-dimensional Al chain, as well as in figures Figs. 4.14-4.15 for Au contacts. Moreover, for each set of contacts we discuss, we check that re-running the alignment "bulk" geometry as a zero-bias transport calculation using the shifts calculated as static inputs indeed results in charge-neutrality in the extended molecule.

To summarize, when the SCF calculation converges, we have obtained two potential shifts: the contact shift $\Delta\phi_0$ and the charge-neutrality shift $\Delta\phi_1$. The former is a runtime iterative adjustment to ensure that the active region of the transporting system is aligned to the bulk Hamiltonians with which the contacts are overwritten, while the latter is a runtime constant which ensures that the potential of the entire system is such that a bulk extended molecule is precisely charge neutral. This in turn determines the Fermi level completely. The alignment calculation is separate from our transport calculations, and performed just once for every new set of (deep) contacts.

The subtlety of our approach lies in realizing that by aligning the transport system to the bulk calculation, we tie it to the picture of contacts as reservoirs with well-defined chemical potentials. Consequently, from this point onward the Fermi level is no longer an estimated quantity, but an exactly fixed quantity, stemming directly from the bulk periodic contact calculation.

The procedure outlined here performs well in practice, correcting the offsets illustrated in Fig. 3.7, and produces a PDOS on the extended molecule which matches the PDOS of the bulk contacts very well, *cf.* sections 4.1–4.2. The resulting electronic structure, moreover, compares well with a bulk calculation of the true periodic system, as shown in appendix 4.4.

3.7 NON-EQUILIBRIUM CALCULATIONS

The procedure described in the previous section yields the "total shift" $\Delta\phi = \Delta\phi_0 + \Delta\phi_1$, and from this point on $\Delta\phi_1$ is a constant shift applied at every iteration during a transport run. However, in order to treat the non-equilibrium transport case, we also need to consider both the effects of the applied bias and fields, and the calculation of the non-equilibrium density from the NEGF formalism.

The system in the transport run is, as we have outlined, shifted from the unmodified $\boldsymbol{H}^{\text{KS}}$ for the extended molecule with contacts to the correct potential zero as $\boldsymbol{H} + (\Delta\phi_0 + \Delta\phi_1)\boldsymbol{S}$. To this we add the bias $\phi_b(\mathbf{r})$ and (possibly) gate $\phi_g(\mathbf{r})$ fields being applied to extended molecule region.[c] The potential profile implementing these fields is usually a ramp whose end points lie sufficiently far from the electrodes' surface for the layers of contact material in between to sufficiently screen the local distortions and produce the correct self-consistent potential drop within the extended-molecule region. We discuss this further for the case of biased gold-phenyl-gold junctions in section 5.1.3.

In order to calculate the current in the presence of a bias voltage, we need to calculate the non-equilibrium density matrix. Our approach is splitting expression (3.3) into the equilibrium term we have used thus far, and a new non-equilibrium correction, given by the following expressions (3.15)-(3.16), analogous to the approach of Stokbro *et al.*:[14]

$$\boldsymbol{\rho} = \frac{1}{2\pi}\int \mathrm{d}\epsilon\ [\boldsymbol{G}(\epsilon)\boldsymbol{\Gamma}_1\boldsymbol{G}^\dagger(\epsilon)f(\epsilon,\mu_1) + \boldsymbol{G}(\epsilon)\boldsymbol{\Gamma}_2\boldsymbol{G}^\dagger(\epsilon)f(\epsilon,\mu_2)],$$

which may be worked out to yield:

$$\begin{aligned}\boldsymbol{\rho} = &\underbrace{-\frac{1}{\pi}\int \mathrm{d}\epsilon\ f(\epsilon,\mu_1)\mathrm{Im}\{\boldsymbol{G}(\epsilon)\}}_{\boldsymbol{\rho}^{\mathrm{A}}_{\mathrm{eq}}} \\ &+\underbrace{\frac{1}{2\pi}\int \mathrm{d}\epsilon\ [f(\epsilon,\mu_1)-f(\epsilon,\mu_2)]\boldsymbol{G}(\epsilon)\,\boldsymbol{\Gamma}_2(\epsilon)\,\boldsymbol{G}^\dagger(\epsilon)}_{\boldsymbol{\rho}^{\mathrm{A}}_{\mathrm{neq}}}\end{aligned} \tag{3.15}$$

or equivalently:

$$\begin{aligned}\boldsymbol{\rho} = &\underbrace{-\frac{1}{\pi}\int \mathrm{d}\epsilon\ f(\epsilon,\mu_2)\mathrm{Im}\{\boldsymbol{G}(\epsilon)\}}_{\boldsymbol{\rho}^{\mathrm{B}}_{\mathrm{eq}}} \\ &+\underbrace{\frac{1}{2\pi}\int \mathrm{d}\epsilon\ [f(\epsilon,\mu_2)-f(\epsilon,\mu_1)]\boldsymbol{G}(\epsilon)\,\boldsymbol{\Gamma}_1(\epsilon)\,\boldsymbol{G}^\dagger(\epsilon)}_{\boldsymbol{\rho}^{\mathrm{B}}_{\mathrm{neq}}}\ .\end{aligned} \tag{3.16}$$

$\boldsymbol{\rho}^{\mathrm{A}}_{\mathrm{eq,neq}}$ and $\boldsymbol{\rho}^{\mathrm{B}}_{\mathrm{eq,neq}}$ are two equivalent ways of obtaining the equilibrium and non-equilibrium density matrix, from which we obtain the terms by a weighted average.

The equilibrium terms' integrals may be evaluated as before by complex contour integration, but it is important to observe that the argument underpinning the analytic continuation into the complex plane was the localization of the poles of $\boldsymbol{G}(\epsilon)$ in the lower half-plane. This is no longer true for the more complicated pole structure of terms like $\boldsymbol{G}(\epsilon)\,\boldsymbol{\Gamma}_1(\epsilon)\,\boldsymbol{G}(\epsilon)^\dagger$, and so the non-equilibrium integral must be evaluated along a dense grid as near to the real axis as is reasonable, while avoiding numerical inaccuracies due to nearby poles.

---

[c] Not to the deep contacts and self-energies, which are already at the right chemical potentials.

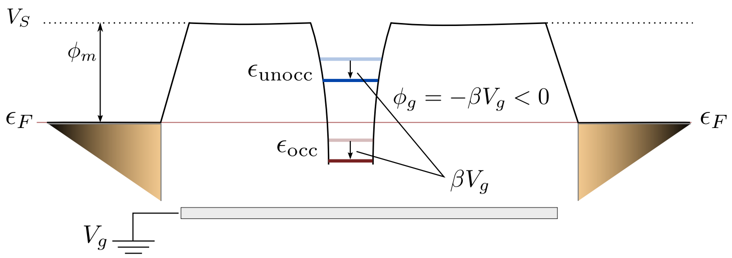

FIGURE 3.8: Effect of gating the molecular levels in the junction by a gate voltage V_g that couples as $-\beta V_g$ in the potential.

3.8 GATE FIELDS

In order to realize the gating of the system, we have implemented a simple approach which serves as a (relatively crude) first approximation to a realistic three-terminal transistor geometry (where the active region is not only coupled to a source and drain electrode, but also capacitatively coupled to a gate electrode).

The most basic gate implementation is the same as an alignment- or contact shift:

$$\boldsymbol{H}_m \mapsto \boldsymbol{H}_m + \phi_g \boldsymbol{S}_m \tag{3.17}$$

where $\boldsymbol{H}_m$, $\boldsymbol{S}_m$ are the submatrices corresponding to the molecule only, *not* the full extended molecule. $\phi_g = -\beta V_g$ with β the gate coupling and V_g the bias applied to the gate electrode, such that for $V_g > 0$ there is an additional attractive potential felt by electrons in molecular levels, which lowers the levels relative to when $V_g = 0$. After shifting, we check the effect on the charge distribution first by calculating $Q_m(\phi_g) = \text{Tr}\left[\boldsymbol{\rho}(\phi_g)\boldsymbol{S}_m\right]$, the number of charges on the molecule proper. This should be the largest contribution to the changing charge on the extended molecule Q_{EM}, as the influx of electrons in the leads will compensate any stray effect felt on the metal side of the metal-molecule interface.

As we illustrate in Fig. 3.8, for HOMO-dominated transport, (sufficient) $\phi_g < 0$ should push the unoccupied levels below ϵ_f, causing the number of electrons on the molecule to increase, if there are unoccupied levels nearby. If not, there will be little to no effect. By contrast, again for HOMO-dominated transport, $\phi_g > 0$ will push the levels over ϵ_f, progressively depopulating the molecule. Conversely, in the case of LUMO-dominated transport, the directions of the shifts are the same, but we may now shift a LUMO-like peak (electron transport) to a HOMO-like peak (hole transport), assuming that the gap between occupied and unoccupied levels is sufficiently large as to not involve the occupied levels for modest gate fields.

This effect manifests itself in transport through a particular level in the following ways. The distance of the level with respect to the Fermi level of the metal is a measure for how far off-resonant the reference state (level at zero gate- and bias voltage) is, and so:

1. The next (occupied or unoccupied) level can be brought into resonance by applying a bias, in which case the bias applied is proportional to that distance. Gating the level changes the distance, and thus the bias necessary to address the level in resonant transport.

2. Consequently, even if we leave the junction unbiased, we can still achieve resonant transport purely by gating, by shifting the nearest unoccupied level down, or the nearest occupied level up into resonance at with the Fermi energy of the leads.

The shortcoming of this implementation of the gate field is that it is formulated as a direct shift of part of the Fock matrix, *i.e.* applied to the basis-functions directly. This means that we miss some geometry-related effects, and in particular:

1. Do not model the screening of the potential profile near the metal contacts, except implicitly via the adjustment of the density to V_g during the SCF calculation. To model this explicitly, one would need to actually physically model the gate field in the potential, either with an empirical profile, or by modeling a third atomistic contact geometry, backed by an appropriate gate dielectric.

2. Miss the effect that the field isn't necessarily uniform over a molecule with a "vertical" profile, as it assumes that the field couples equally strongly to the top and bottom of the molecule, despite the gate being located significantly below the junction (in experiments).

With respect to the first point, our implementation is ready to be extended with a pre-calculated empirical potential profile (parametric in V_g), but dielectric screening is more complicated, if we want to *obtain*, rather than *impose* the real potential profile. While this might be addressed in future work, and is extremely relevant to a fully *ab initio* treatment of a three-terminal junction, it is not essential to simply studying qualitative gating effects on molecular level alignment. This can in principle be addressed as we have currently implemented gating, and has previously been shown to yield useful alignment and charging information by Stadler and collaborators.[17,18]

We will discuss calculations performed using this extension of our method in detail in Chapter 6.

3.9 Post-SCF Transport Calculations

Our implementation also allows Post-SCF transport calculations, which correspond to the first approach in section 2.4, where a closed-system DFT calculation is performed, and the resulting Fock matrix passed to an implementation of the NEGF formalism after the full SCF procedure has converged.

This may better converge difficult systems due to a simpler physical system in the SCF cycles (only the extended molecule in isolation). The converged result may then be used as a better starting point for a further Full-SCF calculation if desired. This convergence improvement is in fact the main motivation for this class of methods, as they use the same number of atoms as a Full-SCF calculations, and so do not noticeably reduce the computational cost of the calculation.

Rather than using the DFT+NEGF cycle of Eq. (3.2), the system is first converged in isolation using the normal DFT self-consistent procedure (without transport extensions). After this, the converged density and Fock matrix are corrected with a one-off estimate of $\Delta\phi_0$ from the contacts as in section 3.6, and the full system is again corrected by the stored fine-tuning $\Delta\phi_1$, after which transport properties are derived from the resulting Green's function:

$$\psi_j^{(0)}(\boldsymbol{r}) \to n^{(0)}(\boldsymbol{r}) \to \boldsymbol{H}^{\text{KS}} \to \psi_j^{(1)}(\boldsymbol{r}) \to n^{(1)}(\boldsymbol{r}) \to \boldsymbol{H}^{\text{KS}} \to \cdots$$
$$\cdots \to \boldsymbol{H}^{\text{KS}} + (\Delta\phi_0 + \Delta\phi_1)\boldsymbol{S} \to \boldsymbol{G}_{\text{PSCF}}(\epsilon) \to T_{\text{PSCF}}(\epsilon)$$

Implicit in this implementation, however, is the comparison with the contacts $\boldsymbol{H}^{\text{TB}}$ corresponding to the self-energies $\boldsymbol{\Sigma}_{1,2}(\epsilon)$ (to obtain $\Delta\phi_0$), which are then *together* used to construct the Green's functions from which the transmission and current are obtained by Eq. (2.30). We use the full self-energies[d] to calculate $\boldsymbol{\Gamma}_{1,2}(\epsilon)$ in:

$$T_{\text{PSCF}}(\epsilon) \sim \operatorname{Tr}\left[\boldsymbol{\Gamma}_1(\epsilon)\,\boldsymbol{G}_{\text{PSCF}}(\epsilon)\boldsymbol{\Gamma}_2(\epsilon)\,\boldsymbol{G}^{\dagger}_{\text{PSCF}}(\epsilon)\right].$$

This is not a strictly Post-SCF calculation as commonly understood, as we substitute bulk contacts for the results from what is effectively a cluster calculation. However, in our experience it performs better than a "pure" Post-SCF approach, producing results very similar to the Full-SCF results we will present, as the description of the contacts then matches the self-energies which are added in transport. However, this default behavior can be turned off to make the method a pure Post-SCF approach.

The latter has been used for calculations such as those presented in Chapter 7. However, the implementation benchmarked there is the essentially identical code by J. S. Seldenthuis in ADF, as opposed to our implementation in BAND, which is faster due to other implementation differences between the codes themselves, which are beyond the scope of our work.

3.10 WIDE-BAND LIMIT APPROXIMATIONS

The theory behind the wide-band limit (WBL) approximation for the self-energies of the contacts is actually an (extreme) simplification of the full treatment of the self-energies outlined previously in Chapter 2 and section 3.4, which we discuss in

---

[d] In principle these Σ may also be substituted by Σ_{WBL} by combining the input keys, *cf.* §3.10.

more detail in Chapter 7. For the moment we note our implementation of the usual parameter-based WBL:

$$\mathbf{\Sigma} = \mathrm{i}\Gamma \boldsymbol{S} \tag{3.18}$$

in a non-orthogonal basis, with Γ a user-defined parameter. We have also implemented a more subtle non-parametric option:

$$\mathbf{\Sigma} = \mathbf{\Sigma}(\epsilon_f) \tag{3.19}$$

where the self-energy of the contacts is frozen at the Fermi level. To the best of our knowledge this has not been previously used in the literature. While not strictly a wide-band limit approximation in that it doesn't derive from assuming a flat DOS (in a non-orthogonal basis), it does freeze the structure of $\mathbf{\Sigma}(\epsilon)$ across the entire energy-band to the structure at the Fermi level ϵ_f. This is motivated by the spirit of the WBL approximation: that the structure of the contacts DOS *near the Fermi level* is sufficiently flat as to replace it by the WBL DOS and self-energies.

Two further remarks are in order:

1. These approximations to the self-energies, in particular the usual $\mathbf{\Sigma} = \mathrm{i}\Gamma\boldsymbol{S}$, do not apply in the non-equilibrium case, as they do not account properly for the difference in Fermi energies of the leads, which are encoded precisely in $\mathbf{\Sigma}(\epsilon)$ in our method.

2. Our implementation allows a further flexibility: it can be run *after* convergence of the SCF procedure, *i.e.* after either a Post- or Full-SCF calculation, such that the density and Fock matrix of the extended molecule region *are* correctly converged in the presence of open leads, and the WBL approximation is made only for the contacts which couple to the EM. This is implemented purely for testing purposes, as it does not correspond to a consistent physical description.

We discuss the performance of such approximations extensively in Chapter 7, but remark that as with the Post-SCF approach the implementation benchmarked there is the essentially identical implementation of Eq. (3.18) by J. S. Seldenthuis in ADF, as opposed to our implementation in BAND, as the former performs better due to implementation differences between ADF and BAND which we do not control. We also discuss a number of interesting details of the WBL further for one-dimensional systems, where analytical results can be obtained, in Appendix C.3.

3.11 COMPUTATIONAL COST & SCALING

In the development of the approach described in this chapter, significant effort has been put into ensuring good performance on high-performance computing architectures, which we address here and in Appendix D. There are two basic aspects to the computational cost of atomistic quantum-chemistry methods such as DFT, and their extension to quantum transport by combination with the NEGF formalism.

First, rather than studying the cost of a single computation, we are interested in the scaling with number of atoms, or rather with the number of basis-functions used to describe them. In a local-basis approach, the basis-functions are associated with a given atom's electrons, and there are $N \equiv n_{\text{bas}} = \sum_{i=1}^{n_{\text{atoms}}} n_i^{\text{bas}}$ total basis-functions, where n_i^{bas} is the number of basis-functions per atom. This n_{bas}, which we refer to as N in discussing the scaling, determines the size of the vectors and matrices in the problem, and so we immediately turn to the question of which computational step dominates the effort in a DFT calculation.

In normal DFT calculations, from the perspective of linear algebra, the most expensive single step is expected to be the diagonalization of the Fock matrix in order to obtain the Kohn-Sham eigenvalues and orbitals, which has an $\mathcal{O}\left(N^3\right)$ scaling in terms of basis-functions. In the DFT+NEGF formalism, the most expensive step becomes the inversion of matrices (to obtain Green's functions), which would still have $\mathcal{O}\left(N^3\right)$ scaling in basis-functions, but with a different (significantly larger) prefactor.

However, in practice this is not the computationally dominant step: there are in fact a number of steps which depend critically on the number of discrete integration grid points $P \gg N$. The most important entail:[19]

- Determination of the fit functions for the density: $\mathcal{O}\left(N^2\right)$
- Evaluating potentials and similar spatial functions in the grid points: $\mathcal{O}\left(PN\right)$
- Setting up the Fock matrix (integration): $\mathcal{O}\left(PN^2\right)$

Taken together, these completely dominate the effort of the single eigenvalue problem to be solved for realistic systems. Performance tuning these necessary parts of the computational method is highly non-trivial, and the goal has recently been to achieve near-$\mathcal{O}(N)$ scaling by implementing precisely these steps more efficiently. This has been addressed, *e.g.*, in the work of Soler *et al.*[20] on the SIESTA package and Fonseca Guerra *et al.*[19] on the ADF package.

Next, there is a second metric for the scaling of such a code which deserves separate attention from an implementation perspective. Large scientific codes are usually run on large multi-core workstations,[e] and should ideally scale to high-performance architectures,[f] ideally with $\mathcal{O}(M)$ scaling in the number of cores M.

Achieving this is mostly a function of the combination of exploiting the (implicit) parallelism of a problem, together with optimizing load-balancing across distributed processors, memory and disk. The prefactor of this scaling is also an issue, and it turns out that there may be different regimes of (piecewise) linear scaling as the number of cores increases, as is the case for the ADF package.[21,22] The key point remains that the problem must contain sufficient implicit parallelism in order to make

---

[e] 8-16 cores typical as of 2012.

[f] 32-1024 cores per job typical as of 2012.

such scaling feasible, and some parts of the problem in DFT and the DFT+NEGF approach to molecular transport do enable this.

We now summarize the highlights in our implementation in the ADF package:

- In the DFT calculations, particularly for solids, a trivial parallelization in k-space is possible when there is no k-dependent scattering physics present. However, in our current implementation we do not exploit this in the DFT+NEGF calculations since they are performed exclusively at the Γ-point: $k = 0$.
- In the tight-binding representations of the contact Fock and overlap matrices, trivial parallelization is likewise possible since the matrix elements clearly do not depend on each other, and so can be fit independently. [*cf.* section 3.3]
- In the NEGF calculations of transport properties, key quantities are determined by complex contour integrals over independent energy points. When discretized to a grid of energy points ϵ_i, this again lends itself to trivial parallelization, which we exploit. [*cf.* section 3.5]
- However, other keys steps are not so trivially parallelized, such as the diagonalization of large matrices,[11] and likewise for the inversion of such matrices. In the NEGF calculations, such inversions of a Green's function is run in parallel for different ϵ_i, exploiting the independence of discrete energy grid-points just mentioned. [*cf.* section 2.1]
- Complex matrix traces such as those occurring in the calculations of partial DOS plots and in the Landauer expression for the transmission and current, Eq. (1.1), have been optimized to significantly reduce the amount of linear algebra flops required. [*cf.* section 2.1]
- Memory management for load-balancing has also been taken into account in the recently introduced shared-memory implementation of large arrays in ADF/BAND, and also by us in our treatment of the large Σ-matrices. We use a scheme where the data is redistributed to temporary files held by each node in a calculation, containing only the data-points needed on the node. This avoids the bottleneck of a single node doing all the I/O to load these matrices at each iteration of a run. [*cf.* section 3.4]
- We have also addressed the load-imbalance inherent in the calculation of the Green's functions, by interleaving the energy-points on the calculation grid across the cores, rather than distributing them in blocks. This helps to balance the surface Green's function calculations, where convergence effort may vary significantly depending on the proximity of poles in the calculation, which is an energy-local effect leading to significant imbalance if repeated “difficult” points are handled by the same processor. [*cf.* section 3.4]

- We have also implemented a “defer” option to load the self-energies only at calculation time, which should help accelerate the code on machines with limited memory and relatively fast disks, by avoiding the paging of large arrays in- and out of memory at runtime.

REFERENCES

[1] G. te Velde and E. J. Baerends, *Precise density-functional method for periodic structures*, Phys. Rev. B **44**, 7888 (1991).

[2] G. Wiesenekker and E. J. Baerends, *Quadratic integration over the three-dimensional Brillouin zone*, J. Phys.: Condens. Matter **3**, 6721 (1991).

[3] G. te Velde, F. Bickelhaupt, S. van Gisbergen, C. Fonseca Guerra, E. Baerends, J. Snijders, and T. Ziegler, *Chemistry with ADF*, J. Comput. Chem. **22**, 931 (2001).

[4] Y. Xue, S. Datta, and M. A. Ratner, *First-principles based matrix Green's function approach to molecular electronic devices: general formalism*, Chem. Phys. **281**, 151 (2002).

[5] M. Brandbyge, J.-L. Mozos, P. Ordejón, J. Taylor, and K. Stokbro, *Density-functional method for nonequilibrium electron transport*, Phys. Rev. B **65**, 165401 (2002).

[6] F. Evers and A. Arnold, *CFN Lectures on Functional Nanostructures*, vol. 2 of *Springer Lecture Notes in Physics* (Springer, 2006), 1st ed.

[7] A. Arnold, F. Weigend, and F. Evers, *Quantum chemistry calculations for molecules coupled to reservoirs: Formalism, implementation, and application to benzenedithiol*, J. Chem. Phys. **126**, 174101 (2007).

[8] M. P. López-Sancho, J. M. López-Sancho, and J. Rubio, *Highly convergent schemes for the calculation of bulk and surface Green functions*, J. Phys. F: Met. Phys. **15**, 851 (1985).

[9] J. Henk and W. Schattke, *A subroutine package for computing Green's functions of relaxed surfaces by the renormalization method*, Comput. Phys. Commun. **77**, 69 (1993).

[10] R. Zeller, J. Deutz, and P. H. Dederichs, *Application of complex energy integration to self-consistent electronic structure calculations*, Solid State Commun. **44**, 993 (1982).

[11] W. Press, S. Teukolsky, W. Vetterling, and B. Flannery, *Numerical Recipes* (Cambridge University Press, 2007), 3rd ed., the Art of Scientific Computing.

[12] N. Ashcroft and N. Mermin, *Solid State Physics* (Brooks/Cole, 1976).

[13] H. J. Monkhorst and J. D. Pack, *Special points for Brillouin-zone integrations*, Phys. Rev. B **13**, 5188 (1976).

[14] K. Stokbro, J. Taylor, M. Brandbyge, and P. Ordejón, *TranSIESTA – A Spice for Molecular Electronics*, Ann. N.Y. Acad. Sci. **1006**, 212 (2003).

[15] A. R. Rocha, V. M. García-Suárez, S. Bailey, C. Lambert, J. Ferrer, and S. Sanvito, *Spin and molecular electronics in atomically generated orbital landscapes*, Phys. Rev. B **73**, 085414 (2006).

[16] P. Pulay, *Convergence acceleration of iterative sequences. The case of SCF iteration*, Chem. Phys. Lett. **73**, 393 (1980).

[17] R. Stadler, V. Geskin, and J. Cornil, *Towards a theoretical description of molecular junctions in the Coulomb blockade regime based on density functional theory*, Phys. Rev. B **78**, 113402 (2008).

[18] R. Stadler, V. Geskin, and J. Cornil, *Screening effects in a density functional theory based description of molecular junctions in the Coulomb blockade regime*, Phys. Rev. B **79**, 113408 (2009).

[19] C. Fonseca Guerra, J. G. Snijders, G. te Velde, and E. J. Baerends, *Towards an order-N DFT method*, Theor. Chem. Acc. **99**, 391 (1998).

[20] J. M. Soler, E. Artacho, J. D. Gale, A. Garcia, J. Junquera, P. Ordejon, and D. Sanchez-Portal, *The SIESTA method for ab initio order-N materials simulation*, J. Phys.: Condens. Matter **14**, 2745 (2002).

[21] Hewlett-Packard Development Company, L.P., *HP Clusters in Computational Chemistry - Case Study with Amsterdam Density Functional (ADF) Software* (2006), White Paper.

[22] Hewlett-Packard Development Company, L.P., *HP Systems in Computational Chemistry - Case Study with Amsterdam Density Functional (ADF) Software II* (2009), White Paper.

4

VALIDATION: MODELING METAL CONTACTS

We now discuss the first major test of our methods, on simple one- and three-dimensional metal contacts. We consider lithium, aluminum and gold as contact materials. Since we use gold contacts extensively in the work presented in this thesis, we give only a preliminary discussion here, and revisit them in the context of results for prototype molecular devices in Chapter 5.

Parts of this chapter have been published in J. Phys. Chem. C (2012) at `http://dx.doi.org/10.1021/jp3044225`.

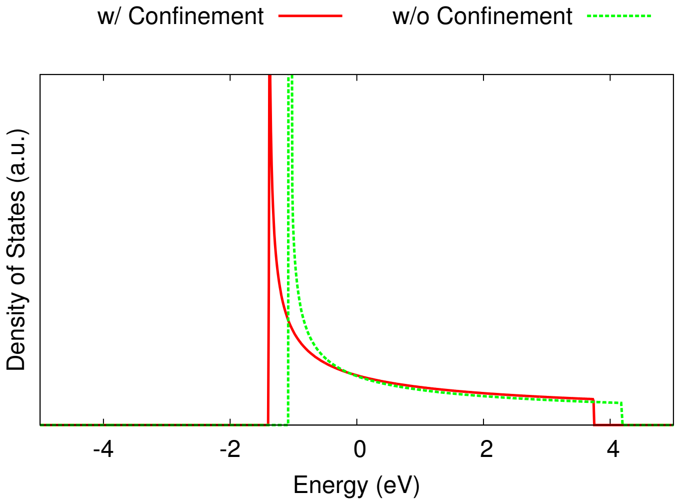

FIGURE 4.1: DOS of a lithium chain, with a lattice spacing of 2.88Å, SZ basis and GGA exchange-correlation functional. Figure also illustrates the results with and without radial confinement of the basis functions (to 4.6Å before a smooth Fermi-Dirac cutoff).

In this chapter, we discuss validation calculations on lithium and aluminum systems in one dimension, and three-dimensional gold systems with and without transverse periodic boundary conditions. These are not intended to achieve quantitative chemical accuracy, and in fact we will typically limit ourselves to the LDA approximation in the calculations. Rather, we intend to validate the results generated by our code against chemical intuition for such relatively simple systems, which (gold in particular) will later become building blocks of our model single-molecule devices.

4.1 LITHIUM CHAINS

We begin with a discussion of one of the most trivially simple metals in the periodic table, lithium (Li), which has the simplest chemical structure of the metals we consider. Its DOS is discussed in the literature for one- and three-dimensional structures,[1–4] and we illustrate a calculation (using BAND) of the monatomic chain we will focus on in Fig. 4.1. For reference, we use a GGA functional (there is no difference with the results using LDA). Using a single-ζ (SZ) basis captures the physics of the outermost valence electron which gives rise to a single band with van Hove singularities at the edges.

In section 3.6 we outlined the use of a self-consistent procedure to fix the potential zero and the Fermi level consistently for the full system of extended molecule with contacts, by requiring charge neutrality of a bulk "extended molecule." If we apply this to the one-dimensional Li chain, we obtain a charge-density profile and

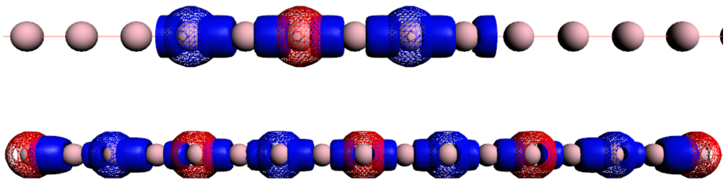

Figure 4.2: Bulk charge density profile (solid) and HOMO wavefunction (hatched) calculated in a bulk 1D chain (top) and the converged alignment configuration for our finite extended system (bottom). Both were calculated using LDA and a SZ basis set. Edge effects on the outer atoms on the finite chain are clearly visible, but in the inner extended-molecule region there is excellent agreement, including the 4-atom periodicity of the wavefunction.

HOMO wavefunction as illustrated in Fig. 4.2, where these are compared with the bulk result obtained from a conventional periodic DFT calculation, using the LDA exchange-correlation functional and a single-ζ (SZ) basis for Li. The lattice spacing (2.876 Å) for the cell was obtained by energy minimization, using the same LDA functional and basis for consistency.

The exact 4-atom periodicity observed in Fig. 4.2 is a signature result: we can derive the "HOMO" level (the highest occupied state in the infinite system) from a model of fermion sites in a finite chain by filling the outer s-orbital of Li at each site. Take a $M+1$-site chain of length L, with lattice constant a, which will hold $2(M+1)$ electrons. Each electron will sit in a band formed by a standing wave pattern because of the periodic boundary conditions, and so:

$$\psi_n(x) = e^{i\pi n x/L} \; .$$

The states may be labeled by the $2(M+1)$ set of $k_n = \pm\frac{\pi n}{L}$ instead, where the maximum value of N is $M/2$ such that:

$$\lambda_{\max} = \frac{2\pi}{k_{\max}} \sim 4a \tag{4.1}$$

Consequently, the wavelength of the highest occupied mode in the infinite chain is 4 lattice spacings, which is exactly what we see in Fig. 4.2.

The PDOS and transmission are illustrated in Fig. 4.3, where we note that the transmission has a clear plateau at G_0 corresponding to the transmission through a single channel over the range of energy corresponding to nonzero density of states in the chain. The prediction of the wavefunction shape of the highest occupied mode is general for a single electron in an outermost atomic shell without degeneracy, such as the Li $2s$ orbital, as opposed to the Al chain (see below). We also note oscillations in the DOS and transmission, which likely reflect the finite extent of the contacts (the edges acting as scattering potentials), and the bad screening of a 1D chain in particular.

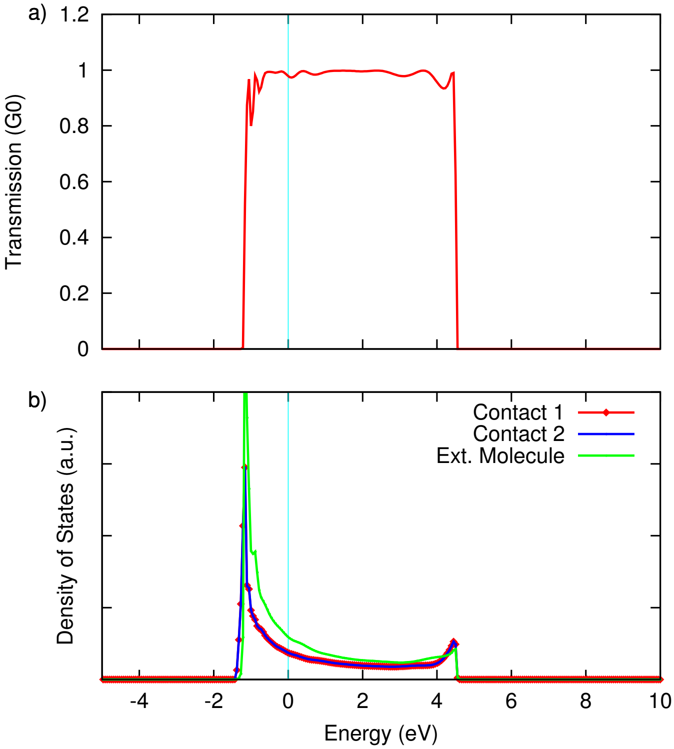

Figure 4.3: (a) Zero-bias transmission through and (b) density of states of the 1D Li chain (using a SZ basis set), showing a single s−band enabling transport, over an energy range corresponding to the (projected) DOS on each part of the model structure.

We next performed a zero-bias transport calculation with a H_2 molecule placed in between the chain contacts. We calculate the transmission and PDOS for the structure under zero bias, see Fig. 4.4. We observe that the transmission is reduced in the presence of the H_2, an effect of H_2 partially interrupting the transport path through the s-orbitals in $1s^2 2s^1$ Li chain (transmission ~ 1, effectively an ideal Landauer conductance channel). The H_2 LUMO does have an s-orbital character, and so there is transport as it does in fact couple more broadly to a number of Li states, but its coupling to the Li is different, so that the transmission becomes somewhat attenuated at different energies along the band. On the high-energy side of the DOS plots, we also note a lone peak in the extended-molecule DOS: this corresponds to the LUMO orbital of H_2, and since its resonance is beyond the limited extent of the Li chain's DOS, it should not couple in transport. That is indeed what we observe in the transmission: the lack of a feature at the corresponding energy in the top panel of Fig. 4.4. The HOMO and LUMO+1 levels, by contrast, are considerably further away, and do not couple at all.

4.2 ALUMINUM CHAINS

A similar analysis can be performed for experimentally more realistic Al chains. The key difference is the addition of electrons, which in this case contribute both $s-$ and $p-$bands for transport, as we now discuss.

For reference, we again first give a "bulk" one-dimensional calculation with lateral periodic boundary conditions in Fig. 4.5. We see that there are still van Hove singularities, and that the calculation without confinement is again lower in energy, but also that there are richer features. This calculation will be our reference, but since we are not primarily interested in its full complexity we will focus on slightly different technical settings for validation.

We thus treat transport through a homogeneous chain, and then one-dimensional Al contacts to a H_2 molecule, with calculations performed using LDA and a DZP-quality basis set on all atoms. The alignment procedure discussed in the main text converges well, and is significantly accelerated by the constrained DIIS extension we discuss in section 4.4 and Appendix D, and which we illustrate in Fig. D.1.

The resulting charge density and HOMO wavefunction again compare very well to the bulk 1D calculation, likewise performed with BAND and illustrated in Fig. 4.7. This also mirrors what we observed earlier in Fig. 4.2 for Li chains. Considering the projected DOS on the different spatial segments of the calculation in Fig. 4.6, we note that the features line up well over the contact regions and the (bulk) extended molecule, with the usual van Hove singularities at the edges of the bands, which are easily identified as the $s-$ and $p-$bands of Al, corresponding to $1G_0$ and $3G_0$ conduction channels respectively.

Turning to the orbitals, in Fig. 4.7 we observe a signature 12-atom periodicity, analogous to the 4-atom periodicity observed previously in Li. Reconsidering the occupation of the highest level of a chain of fermion sites, we now fill the outer

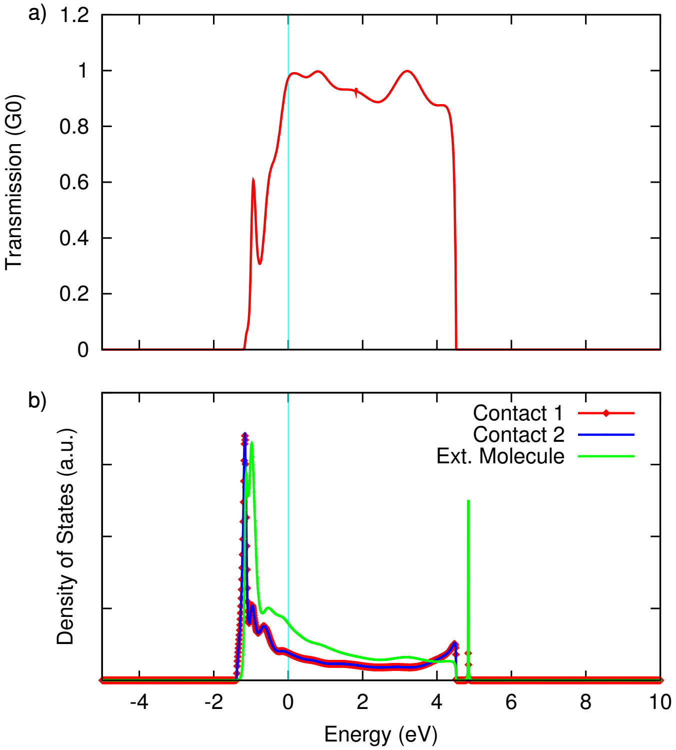

Figure 4.4: (a) Zero-bias transmission through and (b) density of states of the 1D Li chain with an H_2 molecule (using a SZ basis set on Li, DZ basis on H_2). We see a decline of the transmission when a H_2 molecule is placed in the junction. Given the small size of the molecule, its primary effect is to slightly weaken the coupling in the chain.

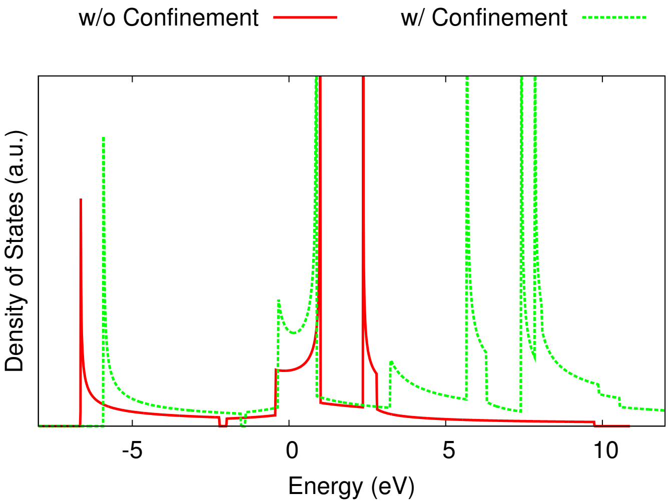

Figure 4.5: DOS of a aluminum chain, with an optimized lattice spacing of 2.83Å, DZ basis and GGA exchange-correlation functional. Figure also illustrates the results with and without radial confinement of the basis functions (to 4.6Å before a smooth Fermi-Dirac cutoff).

3-fold degenerate $3p$-orbitals of Al. The argument outlined earlier then leads us to conclude that $\lambda_{\text{max}} \sim 12a$ (compare Eq. (4.1)): the wavelength of the highest occupied mode should be precisely 12 lattice spacings, which we indeed find.

The converged Al alignment calculation fixes the correct Fermi level for a transport calculation, with the extended-molecule geometry shown in Fig. 4.9. The effects of inserting a H_2 molecule in the chain of Fig. 4.6 are reflected in the PDOS for each part of the system in Fig. 4.8, where we see that they are slightly deformed from their characteristic bulk shapes. In particular, there is a satellite peak corresponding to the $1s^1$ HOMO state on the molecule, and a hump in the extended molecule DOS near 5 eV corresponding to a transmission resonance through the $1s^2$ LUMO state of H_2, orbitals illustrated in Fig. 4.9. There, we recognize the origin of the sharpness of the decoupled HOMO peak, in contrast to the broadened LUMO peak which has more strongly hybridized with the leads.

As a three dimensional bulk crystal, aluminum is structurally quite similar to gold, with both having face-centered cubic (FCC) lattice structures and lattice constants of 4.05Å resp. 4.08Å. We now turn to Au, for present purposes perhaps the most important metal system.

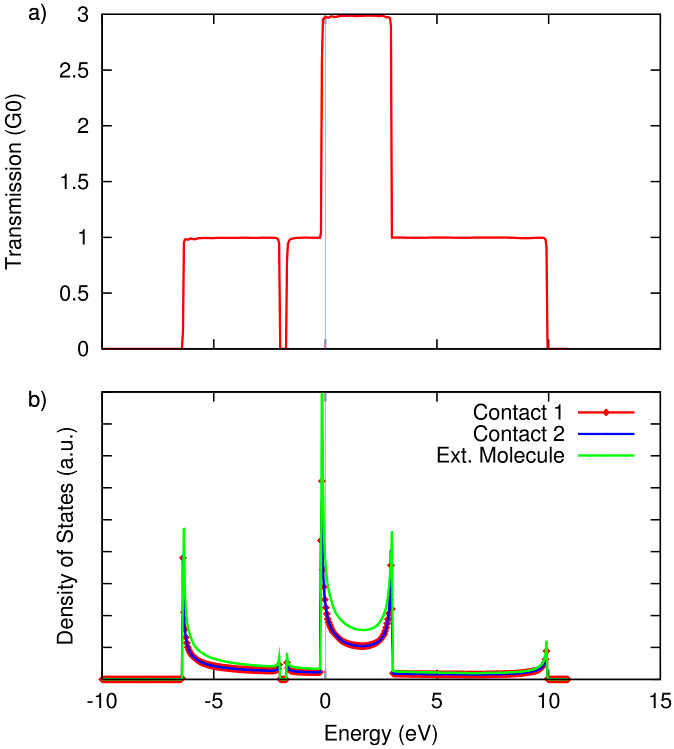

FIGURE 4.6: (a) Zero-bias transmission through and (b) density of states of the Al chain. Note the position of the Fermi level (thin vertical line near 0 eV), determined as offset by 85 meV from the original bulk calculation by our self-consistent alignment procedure.

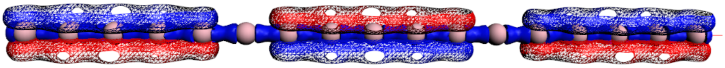

FIGURE 4.7: Bulk charge density profile (solid) and HOMO wavefunction (hatched) calculated in the converged alignment configuration for our finite extended Al system, illustrating the 12-atom periodicity of the wavefunction discussed in the text.

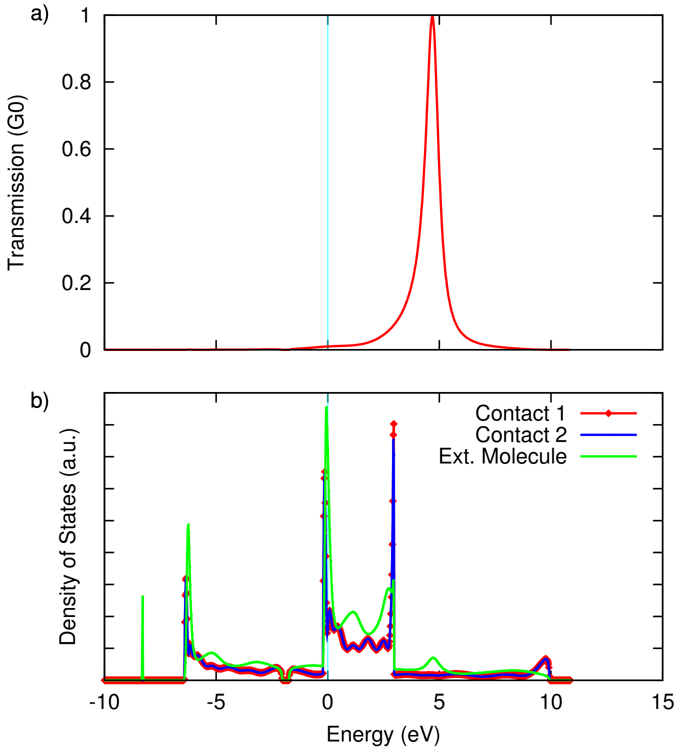

Figure 4.8: (a) Zero-bias transmission through and (b) density of states of the Al–H_2–Al junction, together with the $T(\epsilon)$ characteristic of the junction, which is now entirely determined by the H_2 molecule in the gap, as compared with Fig. 4.6.

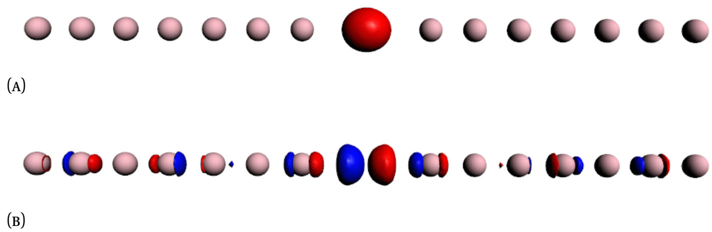

(a)

(b)

Figure 4.9: Wavefunctions of the (a) HOMO and (b) LUMO orbitals of H_2 in zero-bias transport between Al leads. The LUMO level would be most relevant to transport, corresponding to the resonance in Fig. 4.8. The HOMO, by contrast, does not hybridize, but shows up as the leftmost peak in that figure, near −8 eV.

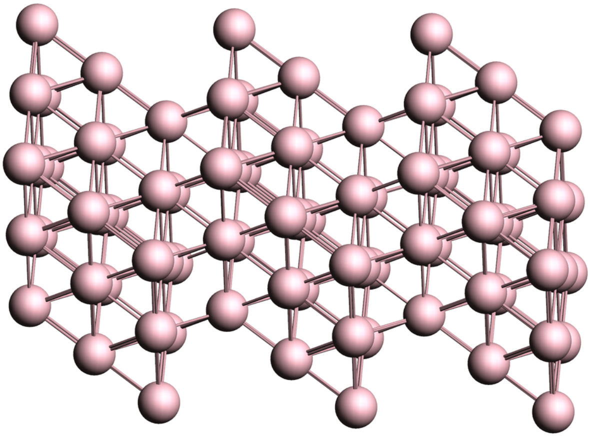

(A) Regular Stacking

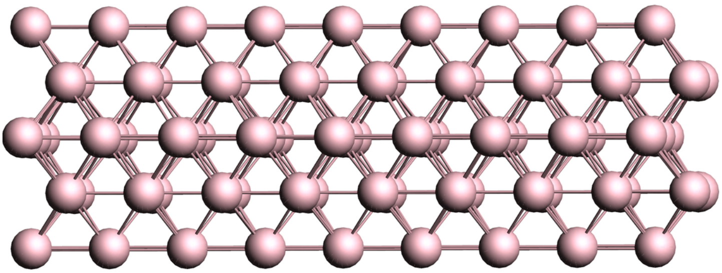

(B) Smooth Stacking

FIGURE 4.10: Stacking geometries of the gold contacts used. (a) The regular stacking, which is also used when transverse periodic boundary conditions are applied. (b) The smooth stacking used to simulate the needle-like contacts used in break-junction experiments.

4.3 GOLD CONTACTS

Before proceeding to transport calculations using “bulky” Au contacts, which will be a building block in all following sections, we first discuss their construction. We will emphasize, in particular, the difference between applying transverse periodic boundary conditions and their omission. We begin the discussion with Fig. 4.11 (and refer ahead to Fig. 5.1), where we illustrate 3 representative geometries one might use for the contacts, and the transmission through their bulk structure (*without* molecules) in Fig. 4.11. These are all FCC stacked with a (111) face perpendicular to the axis, and we compare a transverse 2×2–atom surface with the 3×3–surface case, the latter both with and without periodic boundary conditions. Calculations were performed with the LDA functional and a SZ basis with 11 valence electrons.

In section 4.4 we show the convergence of the alignment shifts (Figs. 4.14–4.13), with the conclusion that in contrast to the case without periodic boundary conditions, the shifts obtained in order to converge the extended-molecule structure with periodic boundary conditions can be quite large.[a]

It appears that for the case of periodic boundary conditions, the bulk run in BAND is significantly offset in potential with respect to the alignment and transport runs. The strong difference with the alignment run argues for fixing the Fermi level via the correction $\Delta\phi_0 + \Delta\phi_1$ (as opposed to simply neglecting a numerical error incorrectly assumed small). The continuing difference in the transport run further argues for a dynamic (runtime) correction $\Delta\phi_0$, as implemented, rather than assuming a static correction $\Delta\phi_0$ in transport.

In Fig. 4.11, the typical transmission characteristics of these “bulk” junctions exhibit clear conductance plateaus, as we expect from what is essentially a “bulky” monatomic chain. We note that the number of channels found is similar near the Fermi level, while further away, in particular in the region from -8 to -2 eV, the structure *without* periodic boundary conditions is considerably noisier, and has fewer channels. This may be due in part to the electrons moving to the surface boundaries in the structure without periodic boundary conditions, effectively reducing the number of transport channels.

4.4 ALIGNMENT & VALIDATION

We now discuss the validation of the alignment procedure and the constrained DIIS algorithm we have implemented, outlined in Appendix D.

For Al chains, we previously illustrated the result of alignment in Figs. 4.6–4.7, and the density of states projected onto the different segments of the calculation is shown in Fig. 4.12. We conclude from these that the calculations reproduce the bulk results well. The major features line up over the contact regions and the extended molecule, and the calculations reproduce easily identified $s-$ and $p-$bands

---

[a] We emphasize that this is an algorithmically-determined rather than an arbitrarily imposed shift, and that as we illustrate in Fig. 4.13, the PDOS indicate that the structure is correctly converged.

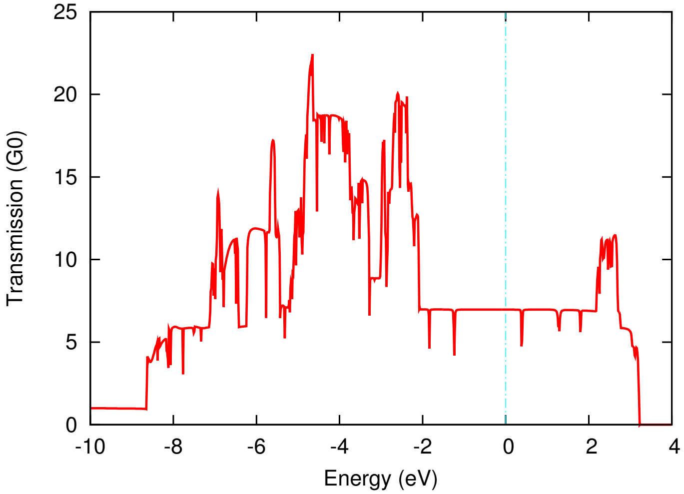

(a)

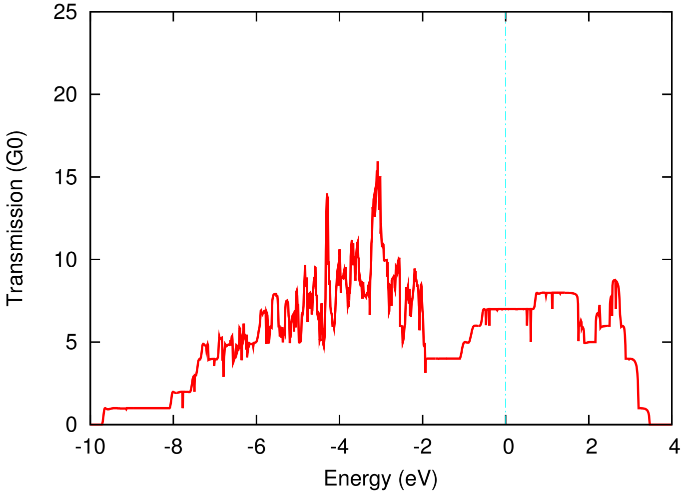

(b)

Figure 4.11: Transmission through the "bulk" Au contacts (LDA calculations using a SZ, 11*e* basis per atom). (a) with– and (b) without periodic boundary conditions. Note the transmission plateaus at integer units of the conductance quantization G_0, as we expect from a system that is essentially a larger-diameter version of a single Au-atom chain.

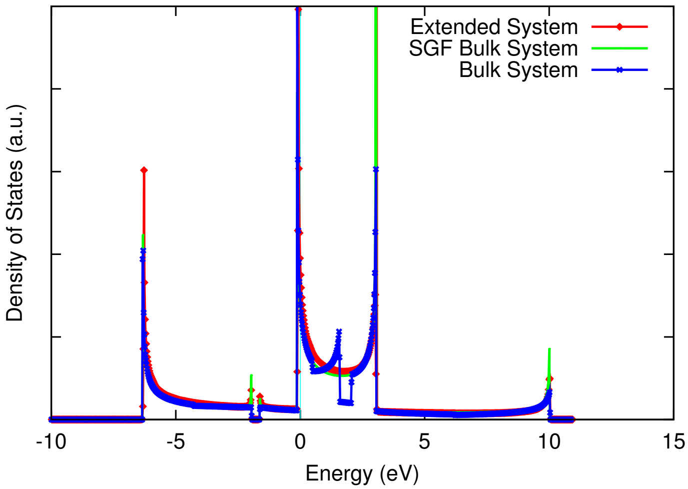

FIGURE 4.12: Alignment PDOS for infinite Al chain contacts (periodic along transport direction), compared with the bulk calculation of the same chain contacts. LDA-level DFT calculations, with a double-ζ basis used; k-dependent calculations beyond the Γ-point approximation are necessary to reproduce the feature near 2 eV in the bulk system.

corresponding to $1G_0$ and $3G_0$ conduction channels respectively. We will return to the physics of such one dimensional systems later in Chapter 7, where we discuss Al chains in the context of different approximations to the fully self-consistent calculations we use here.

We next turn our consideration to the case of “bulky” Au contacts. In Fig. 4.10, we showed representative geometries, which were all FCC stacked with a (111) face perpendicular to the transport direction. Here we compare alignment of different sized transverse surfaces, and for a 3×3–surface the results both with and without periodic boundary conditions.

In the systems without periodic boundary conditions, we find comparable offsets in Fig. 4.14. By contrast, in Fig. 4.15 we immediately see that for periodic boundary conditions–contacts, the shifts necessary to align the “bulk” extended-molecule structure with the bulk contacts are quite large, while the fine-tuning for charge neutrality is comparable to the cases without periodic boundary conditions. We emphasize that this is an algorithmically-determined shift, and that as we illustrate in Fig. 4.13, the agreement of the PDOS for the different spatial segments indicates that the structure is correctly converged.

Having examined the alignment, convergence and bulk structure of the extended-molecules in different cases, we now proceed to single-molecule calculations. We will mainly use 3×3 surfaces of Au, both with and without periodic boundary conditions.

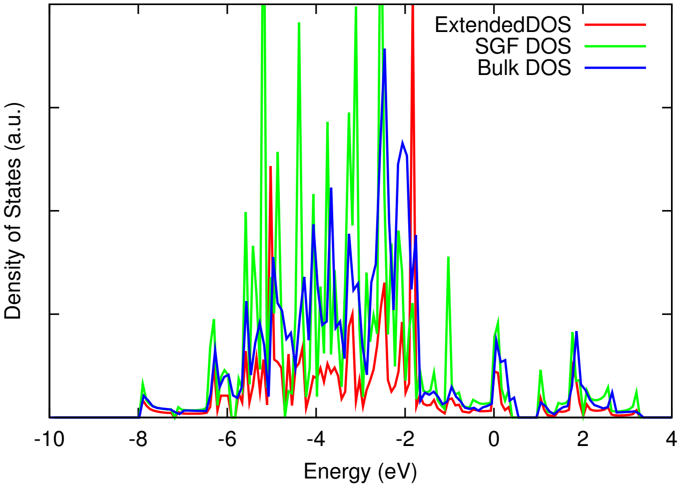

Figure 4.13: Converged PDOS for 2 × 2 Au contacts and "bulk" extended molecule, as compared with the bulk DOS for Au with the same basis set; agreement is also typical for larger contacts.

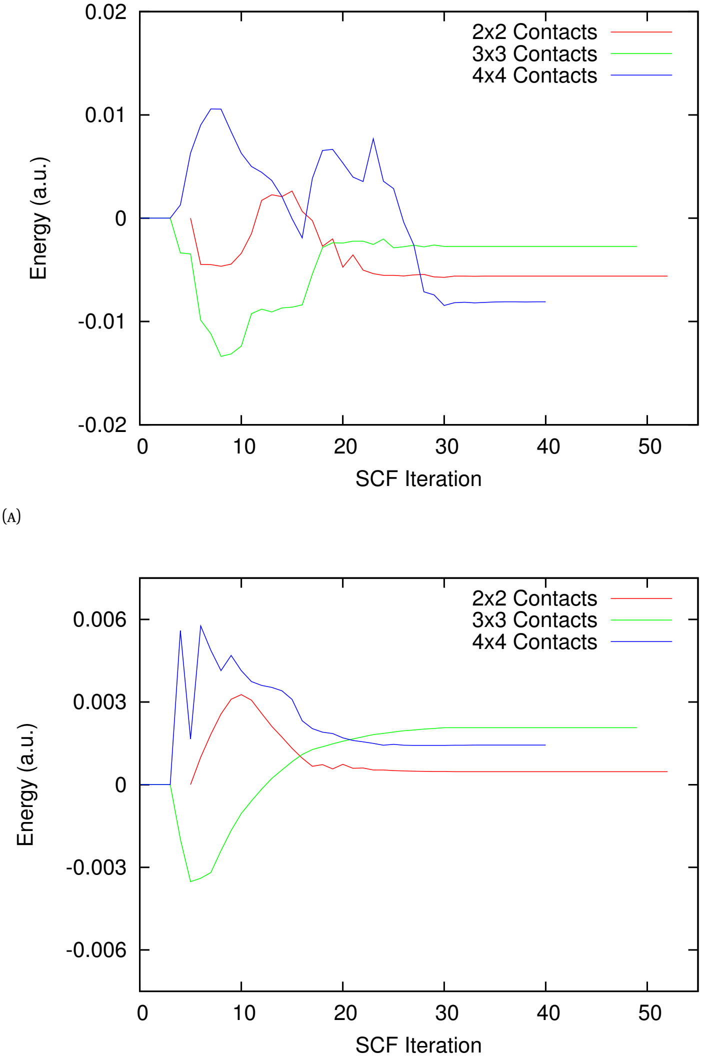

(A)

(B)

FIGURE 4.14: Alignment shift convergence for Au contacts without periodic boundary conditions, for 2×2, 3×3 and 4×4 contacts. (a) the contact shift (zero of the potential) $\Delta\phi_0$, and (b) the alignment shift $\Delta\phi_1$.

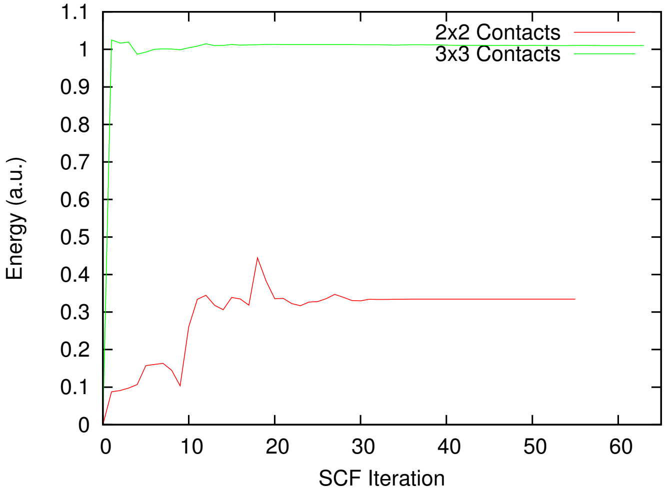

(A)

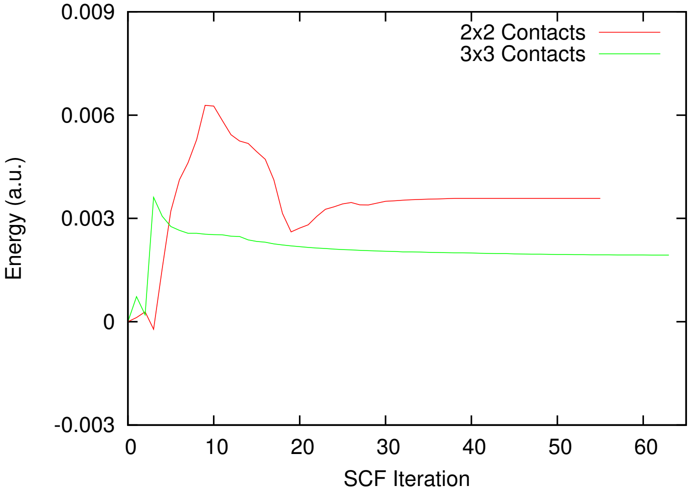

(B)

FIGURE 4.15: Alignment shift convergence for Au contacts with periodic boundary conditions, for 2×2 and 3×3 contacts. (a) The contact shift (zero of the potential) $\Delta\phi_0$, which is much larger in magnitude for the case where periodic boundary conditions are applied, contrasts with (b) the alignment shift $\Delta\phi_1$, of similar magnitude as those in Fig. 4.14.

REFERENCES

[1] J. Callaway, X. Zou, and D. Bagayoko, *Total energy of metallic lithium*, Phys. Rev. B **27**, 631 (1983).

[2] M. M. Dacorogna and M. L. Cohen, *First-principles study of the structural properties of alkali metals*, Phys. Rev. B **34**, 4996 (1986).

[3] J. A. Nobel, S. B. Trickey, P. Blaha, and K. Schwarz, *Low-pressure crystalline phases of lithium*, Phys. Rev. B **45**, 5012 (1992).

[4] H. Sabzyan and F. Mohammadi, *DFT study of one-dimensional lithium lattices as nanowires*, Chem. Phys. **301**, 141 (2004).

5

VALIDATION: TRANSPORT THROUGH PHENYL SYSTEMS

We next discuss a second major test of our methods, on phenyl-ring systems. We consider discuss the prototype which has been perhaps most thoroughly studied in the literature: a benzenedithiol (BDT) single-molecule device. We show the agreement of our results with the literature, and illustrate where they diverge due to subtle modeling choices. Increasing chemical complexity from these single-ring systems, we next study conjugated multi-ring systems. We focus on the next few systems from the oligophenylene-ethynylene family, with 2 (OPE-2) and 3 rings (OPE-3) in particular.

Parts of this chapter have been published in J. Phys. Chem. C (2012)
at `http://dx.doi.org/10.1021/jp3044225`.

5.1 BENZENEDITHIOL SINGLE-MOLECULE JUNCTIONS

We begin with the well-studied "test case" of a gold-benzenedithiol-gold (Au-BDT-Au) junction,[1–6] and will pay particular attention to the effects of contact geometry and boundary conditions on the results obtained.

5.1.1 TRANSPORT WITH SMOOTH NON-PERIODIC CONTACTS

We consider Au-BDT-Au junctions with contacts designed in the same way as in the previous chapter, with Au (111) faces consisting of 2×2 and 3×3 atoms, illustrated in Fig. 5.1. Except where stated otherwise, we perform transport calculations in our code and gas-phase calculations in ADF using the LDA functional with a SZ basis on the Au contacts and a TZP basis on the molecule. In Fig. 5.2 we present the results of our calculations without periodic boundary conditions.

We first note that on increasing the size of the surface perpendicular to transport, there is a relatively quick convergence to a recognizable result with a broad HOMO-like peak below ϵ_f, followed by a 2–3 eV low-conductance gap separating it from a LUMO peak beyond the gap, around 2 eV. This confirms that the size of contacts does matter to the calculation, though the major features already become established for modest contact sizes.

Fig. 5.3 shows the main orbitals derived from the BDT molecule, labeled by their correspondence to the gas-phase orbitals. We use these in order to construct Fig. 5.4, showing the compositions of the peaks in the transmission through the Au–BDT–Au junction near ϵ_f.

We have determined these by using a fragment-decomposition technique, outlined in Appendix B, in which we project the eigenstates of the transport calculation onto the orbitals of a molecular fragment. As a fragment we use the gas-phase BDT molecule geometry with thiolate bonds to a single Au atom on each side (outermost H's of the gas-phase BDT are removed, leaving an Au–S bond), as expected for the preferred bonding of a molecule ending on a thiol group, *e.g.* BDT, to an Au surface.[7–9]

We can identify the orbitals of the fragment with those of either the BDT molecule or radical, and this flexibility also provides extra information on the complicated orbital compositions which we find in the junction. We find that adding the Au adatoms induces the formation of hybrid Au–BDT–Au states which may couple well in transport, labeled $\mathrm{H_A}$ and $\mathrm{H_B}$ in Fig. 5.3, to reflect their energy ordering as the "apparent" HOMO and HOMO-1 states on the fragment. We discuss their role in more detail later. The rest of the states in Fig. 5.3 are labeled by their correspondence to the orbitals of gas-phase BDT. We now focus on the geometry of Fig. 5.2b in particular, as we later use it to model OPE-2 and OPE-3 as well.

We find that the broad HOMO-resonance appears to be mainly composed of 2 separate peaks, which we identify by our decomposition analysis as the HOMO and HOMO-1 peaks of the gas-phase BDT molecule, with a bit of HOMO-3 playing a role as well. $\mathrm{H_A}$ and $\mathrm{H_B}$ also appear here. In the fragment they are split by about 120 meV, and appear as a result of hybridization with Au, or more generally, for collinear

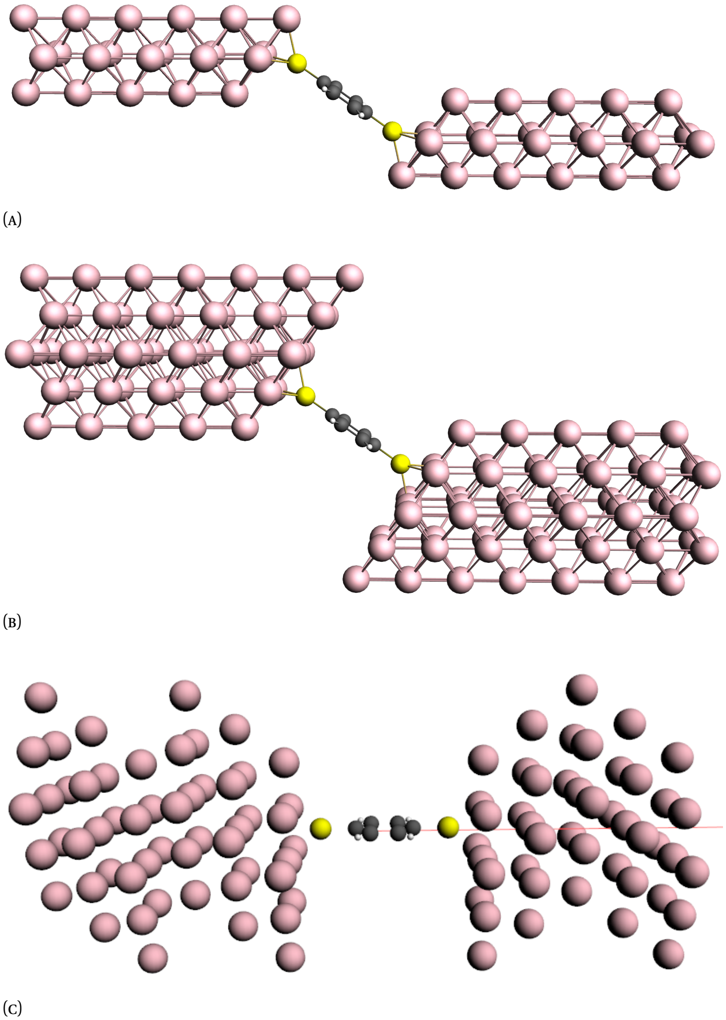

(A)

(B)

(C)

FIGURE 5.1: Au contacts' geometry for (a) the 2 × 2 surface case, (b) the 3 × 3 surface case, both with hollow-site binding with 2.40 Å Au-S distance. (c) An alternate 3 × 3 surface used in calculations with bias, resp. with periodic boundary conditions, *cf.* Fig. 5.5b. Calculations typically performed using the LDA functional and a SZ basis with 11 valence electrons.

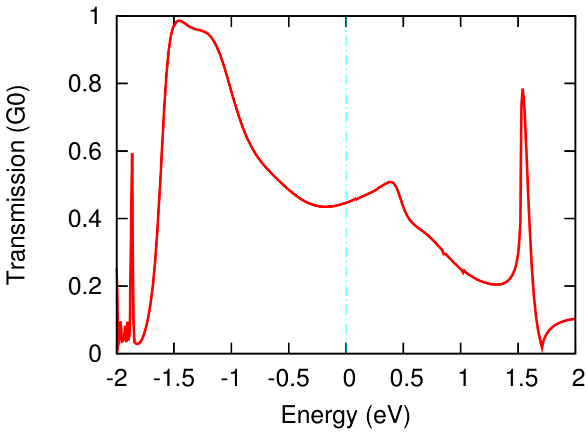

(a) 2 × 2 contacts

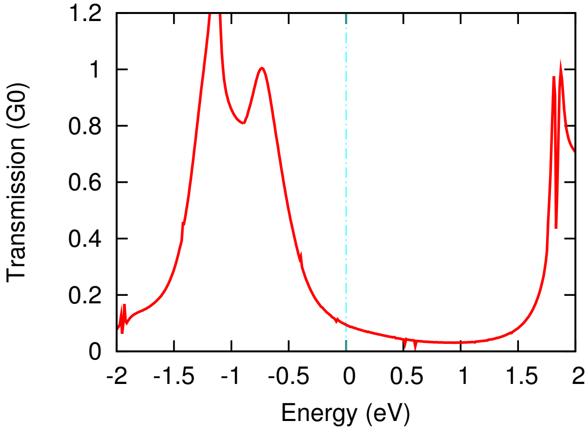

(b) 3 × 3 contacts

Figure 5.2: Transmission through the Au-BDT-Au junction, using (a) 2×2 and (b) 3×3 Au contacts without periodic boundary conditions. We see that the transport gap opens, becoming recognizably linked to the smooth structure visible below in Fig. 5.5b for the case of periodic boundary conditions. The main peaks map between the two sets of calculations, and we illustrate the orbitals that play the dominant role for the 3 × 3 case in Fig. 5.3 below.

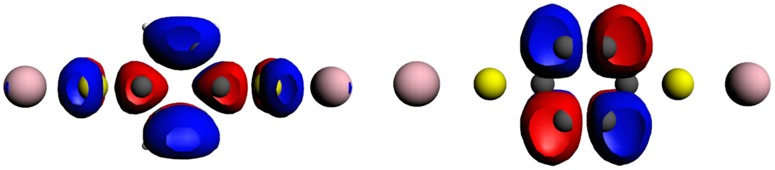

(a) LUMO+1, acts as LUMO

(b) LUMO, does not couple

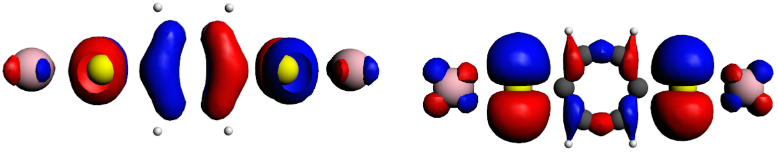

(c) HOMO

(d) H_A: apparent HOMO state on fragment

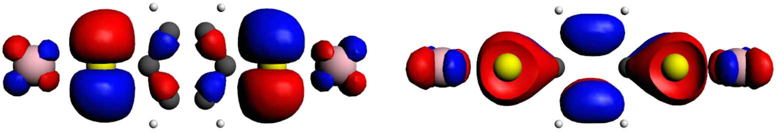

(e) H_B: apparent HOMO-1 state on fragment

(f) HOMO-1

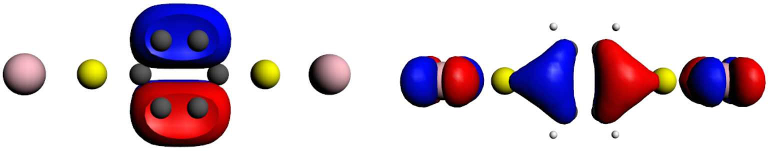

(g) HOMO-2, does not couple

(h) HOMO-3, couples below -2eV

Figure 5.3: Transport-coupled orbitals of the BDT junction as compared with the gas-phase molecular levels when decoupled from contacts, ordered by decreasing energy. (a)–(c) and (f)–(h) label the fragment's transport-coupled orbitals nearest the Fermi level which directly map onto the orbitals of the gas-phase molecule, while (d)–(e) are two examples of intermediate states that are the present in the radical but not the neutral BDT molecule, and survive the thiolate coupling to Au adatoms instead of the terminal -SH bond.

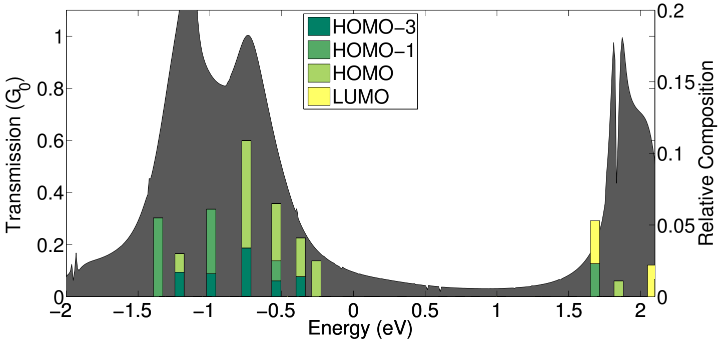

(A) Transmission and decomposition with gas-phase orbitals only

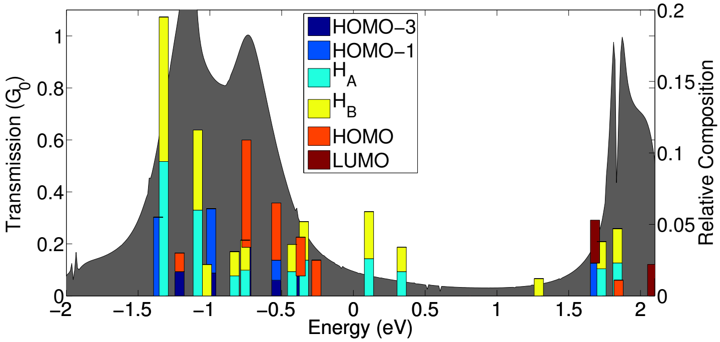

(B) Transmission and decomposition with H_A, H_B ("apparent" HOMO and HOMO-1 orbitals) also included

FIGURE 5.4: Transmission and peak decompositions for the 3×3 Au–BDT–Au junction. Distance between clearest frontier peaks at -0.26 eV and 1.68 eV suggests an effective gap of roughly 1.93 eV. (a) Illustrates the decomposition onto the main gas-phase orbitals, while (b) also includes the H_A and H_B orbitals of Fig. 5.3d and Fig. 5.3e.

termination on the thiol (*i.e.* they also occur when the -SH bond in gas-phase BDT is collinear). This suggests that they may represent a bonding/anti-bonding pair which interferes nearly perfectly destructively, and as a result does not contribute much to transport.[10,11] In this context we further note that despite the $\sim$ 120 meV splitting, they indeed consistently appear in roughly equal measure in each contribution in Fig. 5.4b, once coupled to Au. The LUMO and HOMO-2 states, by contrast, are sufficiently localized to the center of the molecule that they do not couple in transport; rather, for the unoccupied states it is the LUMO+1 which appears as the lowest unoccupied transport peak above the transport gap. We return to this point in discussing the OPE-series in the next section. We do find the HOMO-2 peak present in our decomposition around -2.45 eV, as a considerably purer state, consistent with the lack of coupling to the Au contacts. By contrast, the HOMO-3 has an orbital structure which suggests coupling in transport, and it is present, mixed with the HOMO and HOMO-1 states, in Fig. 5.4. This may suggest an analogy to the HOMO-2 states of the OPE-series.

Finally, we also remark on the presence of some small discontinuities in the transmissions in Fig. 5.2, in the 3×3 case near *e.g.* -0.4 eV, -0.1 eV and 0.5 eV. We have investigated these using the projected DOS on the molecule proper, extended molecule and deep contacts. We find that these are not numerical artifacts, but rather are related to effects in the potential in the contacts. While these may be relevant for very sharp, needle-like contacts, they would probably not play a role for relatively large, bulk-like electrodes.

While we remarked that the results of Fig. 5.2 indicate a gradual convergence towards a “bulk” face result (the single benzenedithiol atom coupled to an infinite plane of Au on each side), they should be distinguished from the “classic” Au–BDT–Au junction results calculated using DFT+NEGF in the literature.[1–3] The difference is the absence of periodic boundary conditions here, a relatively important modeling decision not typically discussed in the early literature, in large part because few codes allow for explicitly breaking transverse periodicity. We illustrate this difference explicitly in Fig. 5.5a below, which should be compared with Fig. 5.2b. The implications of the use of periodic boundary conditions for a junction with such a small face evident in Fig. 5.5b, where we see that the model in this case is qualitatively more similar to a self-assembled monolayer than to a true single-molecule configuration. Conversely, the geometry without periodic boundary conditions are particularly useful for modeling the small, needle-shaped contacts used in break-junction experiments. This difference has consequences for the conductance of the system,[12] but for larger inter-molecular separation this need not be an issue per se, as long as the system being modeled is not actually needle-like in geometry.

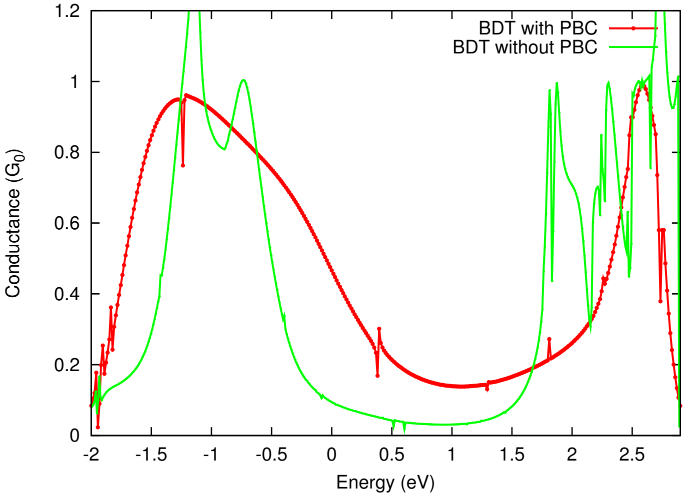

(a)

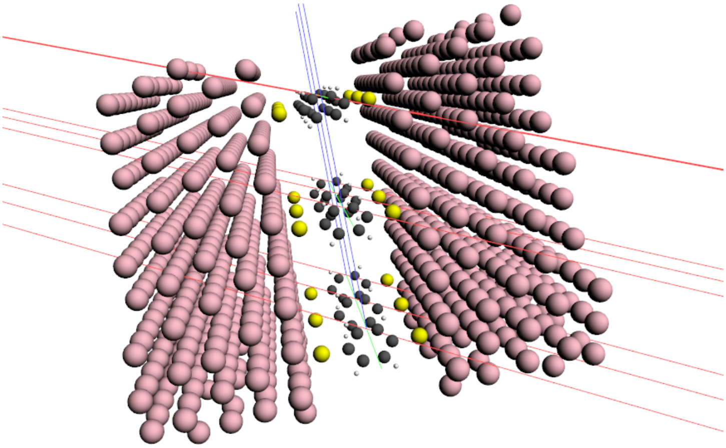

(b)

Figure 5.5: (a) Transmission through the Au–BDT–Au junction with periodic boundary conditions, compared with the previous result without periodic boundary conditions, Fig. 5.2. (b) Implied geometry of the model 3 × 3 Au–BDT–Au junction, using periodic boundary conditions. Overall, we observe a further opening of the gap and a broadening of the HOMO-like peaks, which themselves are reduced in magnitude back to G_0 transmission.

5.1.2 TRANSPORT WITH PERIODIC CONTACTS

Finally, for Fig. 5.5a we find the same general picture in terms of peaks (compositions not illustrated). The predominance of the HOMO, HOMO-1 and their "apparent" counterpart states in transport is, moreover, in excellent agreement with the findings of Stokbro and others.[3,13]

Our work indicates that the convergence towards this bulk result is primarily dependent on having a sufficient number of transport channels available in the contacts to couple to, as in Fig. 4.11. This has implications for contacts which do not couple to as many channels, where a broad peak from the strongly-coupled regime may break apart into a number of narrower (less strongly-coupled) resonances, though still enabling transport. A noteworthy feature is that the transmission *at* the Fermi level $T(\epsilon_f)$ may be significantly reduced, bringing the value closer to the experimental one,[14,15] where one typically would expect to be in the weakly– rather than strongly-coupled regime.

We would argue, however, that since the experiments typically take place in the weakly-coupled regime, detailed understanding of the nearby peak structure and peak compositions (in terms of the original molecular levels) is *far* more useful than the single (often quoted, and disputed) number $T(\epsilon_f)$.

5.1.3 TRANSPORT UNDER BIAS

Let us also briefly consider calculations of transport through BDT under bias, using the perpendicular-face contacts of Fig. 5.1c, and the same basis set as before. In Fig. 5.6a we show the potential drop averaged transverse to the transport direction, and observe that the potential is already relatively stable within a few layers of the extended molecule's inner surface. The potential drop is mostly over the thiol end-groups, which may be contrasted with a slightly lower slope of the potential averaged over the core benzene fragment within the extended molecule region, in agreement with the results of Datta *et al.*[16] and Xue and Ratner.[17]

We also illustrate the influence of adjusting the location at which the ramp begins further back into the junction. We see that the largest charge accumulation at the interface occurs when the ramp is initiated between the first layers at $-0.5d$ from the innermost Au layer (where d is the interlayer spacing of 2.88Å), suggesting that it should begin further back to avoid this. However, we see that as we move the ramp further back, the junction has more difficulty screening the applied potential, reflected in the longer extent of its deviation from ±250mV deeper into the contacts. This implies practical limitations on minimum junction depth, which are likely more relevant in our models without periodic boundary conditions, given their lower capacity to screen high fields inside the conducting leads.

In Fig. 5.10 we plot the transmission on logarithmic scale, compared with the zero-bias calculation of Fig. 5.2b. We see that the main effect is the shift in Fermi level and the attenuation of the peaks, as is commonly observed in the presence of an electric field. There do not appear to be further large changes for this relatively small bias, and all prominent features are still clearly recognizable.

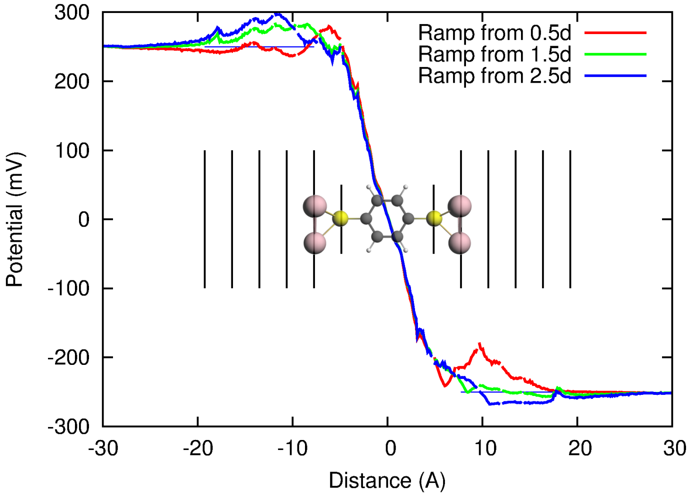

(A)

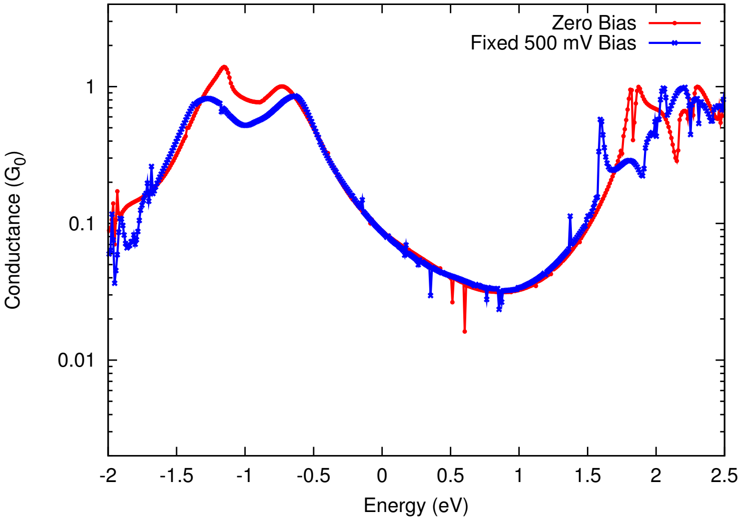

(B)

FIGURE 5.6: (a) Potential drop with fixed ramps starting at 0.5*d*, 1.5*d*, and 2.5*d* from the innermost Au layer of the device region, where *d*=2.88Å the interlayer spacing. 500mV bias is applied, results are relative to a zero-bias self-consistent calculation. Molecule with nearest Au neighbors indicated, together with vertical black lines showing position of subsequent layers of Au. Note the decreased slope of the potential drop over the benzene ring, as compared with the Au-S bond region. (b) Transmission through the biased 3 × 3 Au–BDT–Au junction, as compared with the unbiased result, both without periodic boundary conditions.

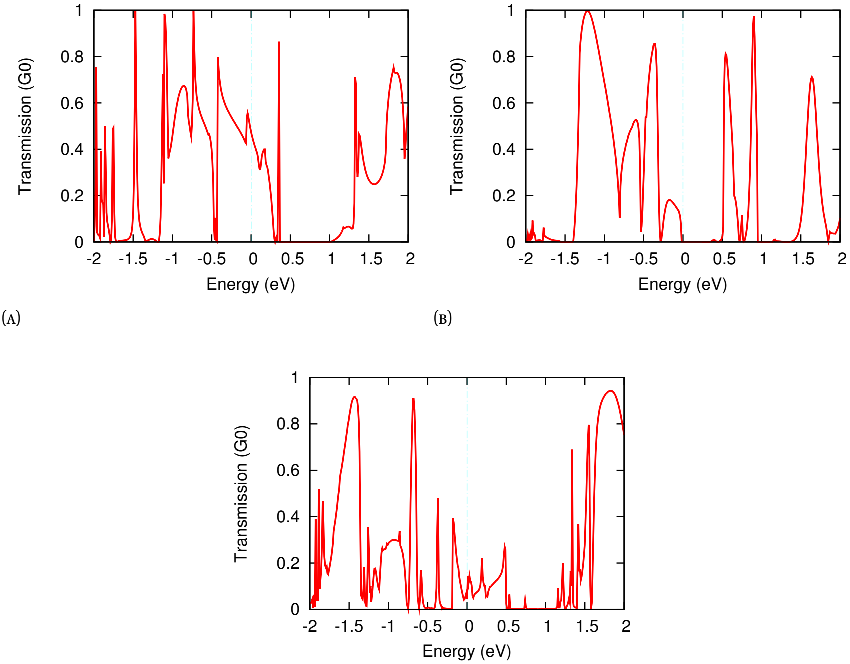

(a)

(b)

(c)

Figure 5.7: Transmission through the Au-BDT-Au junction, using (a) 2 × 2, (b) 3 × 3 and (c) 4 × 4 "badly-coupled" Au contacts without periodic boundary conditions; *cf.* Fig. 5.1.

5.1.4 Transport with Badly-Coupled Contacts

The results we have presented so far show the effectiveness of the method when we apply it to a system with good coupling of the contacts to the molecule, as reflected in the transmission of the alignment geometry, which resembles that of the system with transverse periodic boundary conditions, subject to the caveats pointed out in the previous section. However, there is a subtle point thus far omitted in the discussion which we should consider here, given that it does not appear to be discussed in the literature, to the best of the author's knowledge.

Consider the Au-BDT-Au junction as stacked in Fig. 4.10a. In Fig. 5.7 we present the results without periodic boundary conditions. The contacts used are designed in the same way as in the previous section, with Au (111) faces with 2 × 2, 3 × 3 and 4 × 4 atoms respectively.

These results do indicate a gradual convergence towards a "bulk" face result (as we see a gap opening between clusters of peaks in Fig. 5.7), for large faces of Au on each side of a single benzenedithiol molecule. However, we emphasize that these results are (clearly) not directly the comparable with the “classic” Au-BDT-Au junction results calculated by DFT+NEGF in the literature,[1–3] or even for the results shown previously in section 5.1.1. This is due to the fact that there are far fewer transmission channels through Au with these contacts, as compared with the smooth contacts we have discussed previously in section 4.3.

In the bottom figure 5.10 we plot the transmission on logarithmic scale, for biased calculations with these “non-smooth” contacts. We again compare with the zero-bias calculation of figure 5.2b, and see that while the bias induces significant changes in the structure of peaks, particularly in the gap, the main peaks for the occupied, HOMO-like levels on the left and unoccupied, LUMO-like levels on the right is still clearly present, and not significantly shifted in energy. The lowest of the four peaks is split , indicating a difference in the coupling of the HOMO and HOMO-1 orbitals, while the third and fourth are strongly suppressed, suggesting distortion of the orbitals’ coupling to Au. The “hidden” plateau right above the Fermi level is suppressed as well, but a feature near 0.4 eV in the gap is amplified, as is a feature near 1.2 eV, which appears to shift with bias as well.

The fact that most peaks do not shift in energy implies that the states on the molecule dominanting transport *do not* shift strongly at low bias, which is consistent with the very symmetric nature of the orbitals identified as responsible previously. In fact, for symmetric coupling to the leads, we would expect the structure to remain unchanged, and so suggest that the features (*e.g.* near 1.2 eV) which do shift somewhat are most likely associated with the metal contacts rather than the molecular eigenstates.

5.2 OPE-n Single-Molecule Junctions

We now proceed by considering the first two of the thiol-anchored oligophenylene-ethynylene family of molecules. Except where stated otherwise, we again perform transport calculations in our code and gas-phase calculations in ADF using the LDA functional with a SZ basis on the Au contacts and a TZP basis on the molecule. We show the results of modeling OPE-2 and OPE-3 single-molecule junctions, with 2 and 3 phenyl rings respectively; the junction geometries are illustrated in Fig. 5.11a–b respectively. These calculations use the same contacts as with BDT, and therefore have a common and well-determined Fermi level ϵ_f, as discussed previously. These molecules have also been studied experimentally as promising benchmark systems in molecular electronics.[18–21]

5.2.1 Transport through OPE-2

The transmission through a junction composed of OPE-2 coupled to 3 × 3 atom Au (111) face contacts is illustrated in Fig. 5.12, where the peak decompositions are constructed as outlined above for BDT. The fragment states to which the figure refers are illustrated in Fig. 5.13, again labeled according to the gas-phase OPE-2 molecule’s orbitals. In combination with these orbitals, we analyze the nature of transport, and

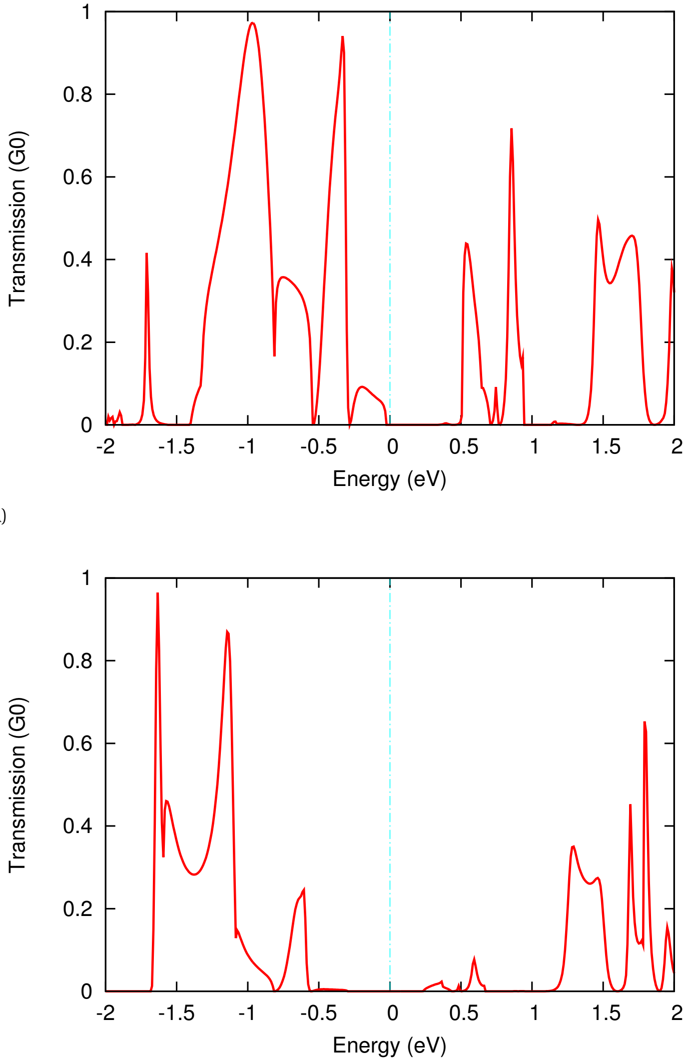

(a)

(b)

Figure 5.8: Transmission through the (a) 3×3 Au–OPE-2–Au junction, and (b) 3×3 Au–OPE-3–Au junction, without periodic boundary conditions, for "badly-coupled" contacts.

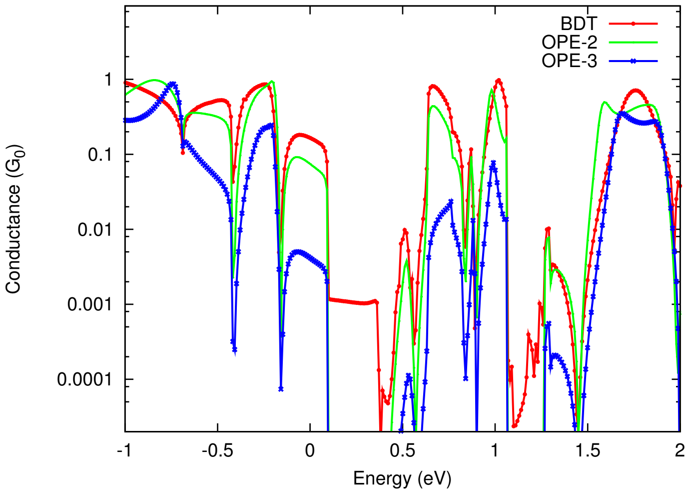

FIGURE 5.9: Comparison of transmissions on a logarithmic scale showing evolution of main features near the Fermi level as the molecule in the junction is substituted by 1 to 3 phenyl-ring variants.

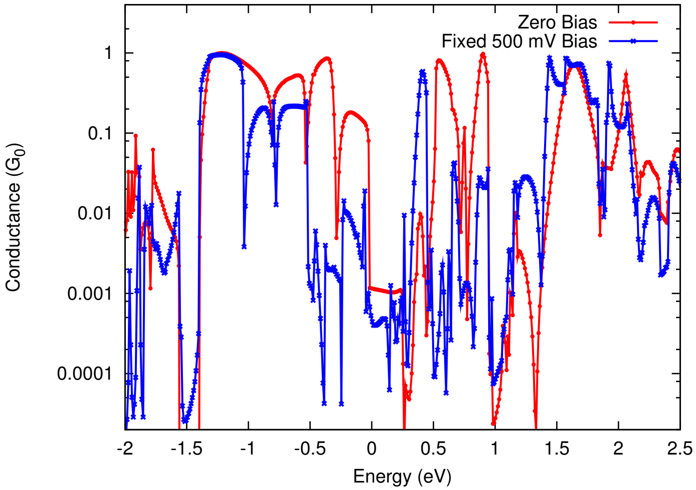

FIGURE 5.10: Transmission through a biased 3 × 3 Au-BDT-Au junction, without periodic boundary conditions, for “badly-coupled” contacts.

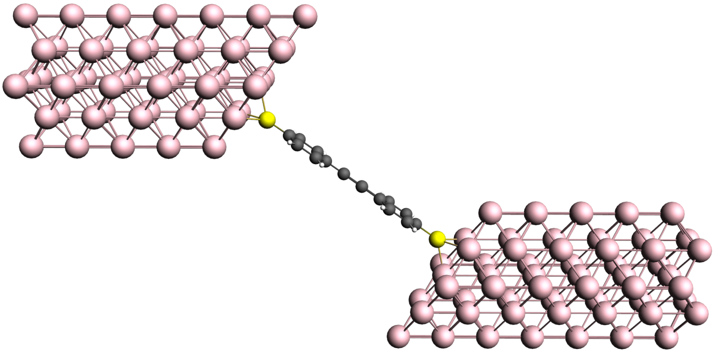

(a) Au–OPE-2–Au Junction Geometry

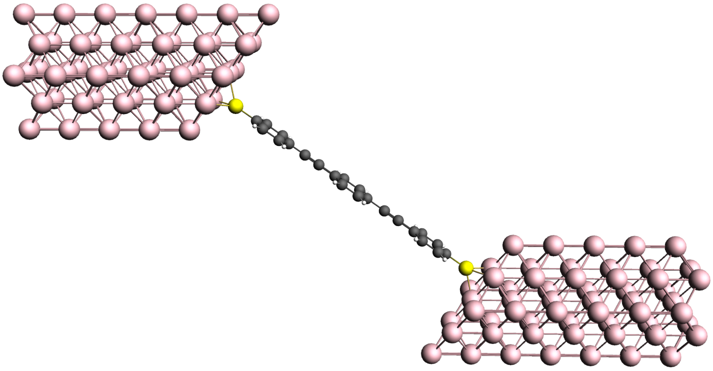

(b) Au–OPE-3–Au Junction Geometry

Figure 5.11: Geometry of 3 × 3 atom (111) surface-bound (a) Au–OPE-2–Au and (b) Au–OPE-3–Au junctions, both without periodic boundary conditions. Hollow-site binding with 2.40 Å Au-S distance, compare Fig. 5.1.

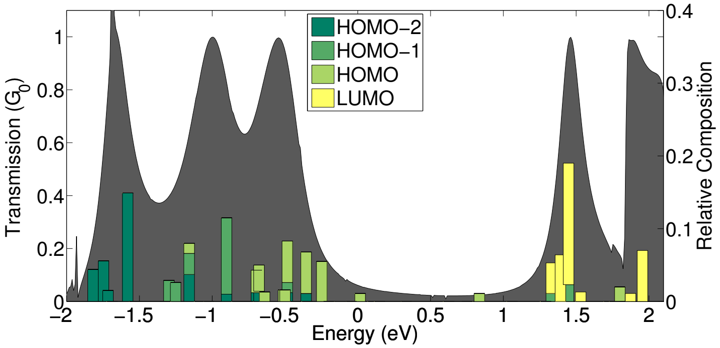

Figure 5.12: Peak compositions near $\epsilon_f = 0$ eV for the Au–OPE-2–Au junction. Distance between clearest frontier peaks at -0.25 eV and 1.33 eV suggests an effective gap of roughly 1.6 eV.

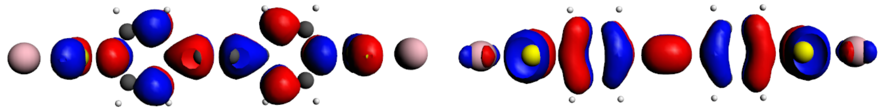

(a) LUMO, *cf.* Fig. 5.3 (b) HOMO

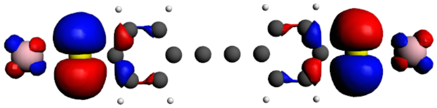

(c) H_A: apparent HOMO state on fragment (d) H_B: apparent HOMO-1 state on fragment

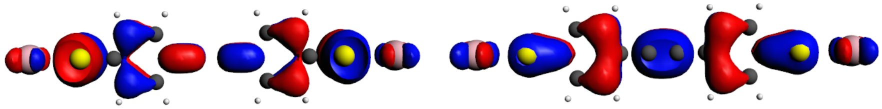

(e) HOMO-1 (f) HOMO-2

Figure 5.13: (a)–(f) Fragment transport-coupled orbitals nearest the Fermi level (compare Fig. 5.3). We note again H_A and H_B, the “apparent” HOMO and HOMO-1 states, which are now better localized at the interface and whose wavefunctions do not extend all the way across the molecule.

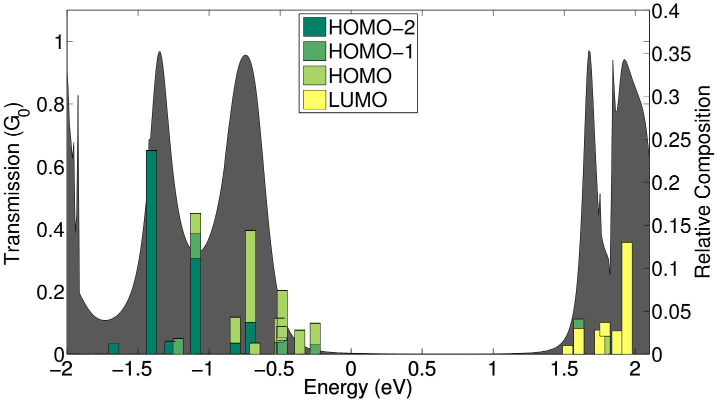

Figure 5.14: Peak compositions near $\epsilon_f = 0$ eV for the Au–OPE-3–Au junction. Distance between clearest frontier peaks at -0.25 eV and 1.52 eV suggests an effective gap of roughly 1.8 eV.

the relation to the single-phenyl BDT system discussed previously.

The electronic structure near ϵ_f immediately recalls the results for the BDT junction. We again find a broad resonance, now split over three peaks below the Fermi level which are identified with the HOMO-2, –1 and HOMO states. The broad peaks are further composed of mixtures with the H_A and H_B states of the Au-OPE fragments and Au-derived states that are mainly localized at the Au-S bond. Beyond the transport gap, at 1.5 eV, we again find a peak which is identified predominantly with the gas-phase LUMO. This is a state which on the OPE-2 (and OPE-3) junction has an orbital symmetry that immediately recalls the LUMO+1 of BDT. The LUMO+1 states on these two molecules, conversely, recall the LUMO of BDT, and do not play a strong role in transport due to the localization of electrons away from the contacts.

5.2.2 Transport through OPE-3 and Beyond

For OPE-3, the transmission is illustrated in Fig. 5.14 together with the peak decompositions. The orbitals referred to are illustrated in Fig. 5.15, which further confirms the picture nature of transport in this family. When comparing with the Au–BDT–Au and Au–OPE-2–Au junctions' results, it appears that the gap slightly reopens. This, however, still appears to be part of a progression towards a smaller transport gap for the longer molecules, following the trend towards smaller HOMO-LUMO gap. This is illustrated in the log-scale plot of Fig. 5.16, where we show the transmission for OPE-4 and OPE-5 junctions as well.

Again, it is the gas-phase HOMO which dominates the conductance near the Fermi level, with the HOMO-1 and HOMO-2 below it composing the lower-lying peaks. The LUMO dominates beyond the transport gap around 1.5–2 eV. The LUMO of OPE-3 again recalls the LUMO+1 orbital of BDT found to compose the "effective

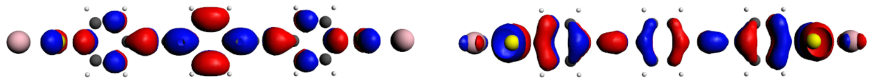

(a) LUMO (b) HOMO

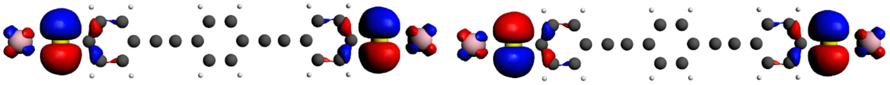

(c) H_A: apparent HOMO state on fragment (d) H_B: apparent HOMO-1 state on fragment

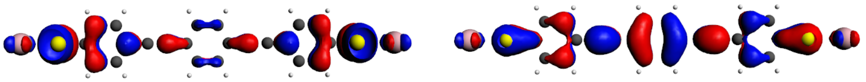

(e) HOMO-1 (f) HOMO-2

Figure 5.15: (a)–(f) Fragment transport-coupled orbitals nearest the Fermi level (compare figures Fig. 5.3 and Fig. 5.13). We again note H_A and H_B, again the "apparent" HOMO and HOMO-1 states, and analogues of Fig. 5.13 (c)–(d) which are again localized mostly near the S atom, and as with OPE-2 have wavefunctions which do not extend all the way across the molecule.

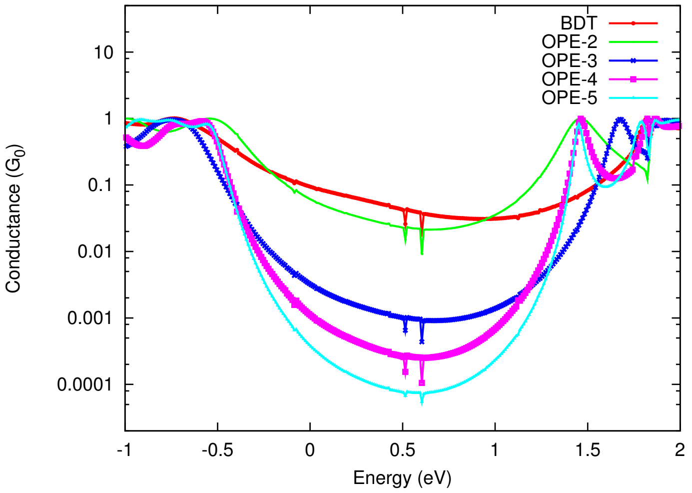

Figure 5.16: Comparison of transmissions on log-scale showing evolution of main features near the Fermi level as molecule in junction is varied from 1 to 3 phenyl rings. Opening of the transport gap is visible, as well as narrowing of the peaks near ϵ_f and a general spectral shift backwards of the HOMO-like peaks.

LUMO" peak there, and so we confirm the role of the orbital symmetries between the respective "LUMO," HOMO, HOMO-1 and HOMO-2 states for each of the three molecules.

The H_A and H_B states, *cf.* Fig. 5.15, are likewise present in all 3 junctions, but as the molecule becomes larger, they become more localized in nature than conjugated, and so should play progressively less of a role in transport through the longer molecules of the family. However, in practice, we find them present in roughly similar proportion to the HOMO and HOMO-1 states in the broad peaks right below ϵ_f in our decompositions for all 3 systems, as well as in the low-conductance transport gap, which suggests that, as argued above, these two states may not really be contributing to transport.

The big picture then, appears to be a slightly erratic change of the gap, which seems to converge from the third or fourth member of the OPE$-n$ family on, narrowing the gap as the number of phenyl-rings in the junction molecule increases. As pointed out by Ke *et al.*,[22] this should converge to a gap similar to the infinite-OPE-chain band gap of ~ 1.7 eV,[a] dominated by the molecular orbitals as the influence of the contacts begins to decrease with wire length. We remark that using carbon nanotube contacts, they observe similarly erratic behavior where the gap-size is concerned. Finally, we remark on the clear trend towards steadily lower values of $T(\epsilon_f)$ as the molecular wire length increases, also visible in Fig. 5.16.

5.3 Conclusions

In concluding this chapter, we conclude both our work on phenyl systems, and the implementation and validation of our DFT+NEGF method in the ADF quantum chemistry package. A few remarks are in order.

A combination of the NEGF approach with a DFT description of the bulk contacts is a flexible, efficient and scalable computational method for transport calculations on realistic geometries of single-molecule devices. A key advantage of our implementation is the ability to break periodicity in 1-3 dimensions within a band-structure code, which allows accurate simulation of the metal contacts for different systems, while allowing us to simulate geometries akin to *e.g.* mechanically controlled break junctions without the need to impose periodic boundary conditions.

We have studied one-dimensional chains and found transport behavior that is in line with what is expected based on simple theoretical considerations, and then extended our scope to three-dimensional junctions involving a series of phenyl-ring molecules from the OPE-family with related gas-phase electronic structures. For benzenedithiol we recover the signature transmission characteristic with periodic boundary conditions, but if we go beyond this by breaking periodicity we gain a deeper understanding of the more complex transmission-peak structure, as the simple broad HOMO-like peak is separated into smaller peaks that we identify with

---

[a] The value of $\Delta \sim 1.72$ eV calculated by us using the BAND code, with 1D periodicity using LDA with a TZP basis set to match the transport calculations; compare ~ 1.5 eV as calculated using GGA with unspecified basis set, by Ke *et al.*

particular molecular orbitals hybridizing with Au in transport. This may better reflect what happens in experiments with sharp nanocontacts.

Such characteristic features are seen to evolve in a clear way for the OPE-based molecular wires as well, with the orbitals determining transport near the Fermi level clearly related to the orbital symmetries we identify across the family of molecules. In particular, we see a related cluster of occupied orbitals near ϵ_f which dominate transport. As we consider progressively longer molecular wires, we find an at first erratic trend, leading finally to convergence in reducing the transport gap between these and the lowest unoccupied-level resonances. Finally, in the low-bias regime, we find that for the simplest phenyl junction the symmetry of coupling ensures that we find no significant spectral shifts, but we do find amplification and attenuation of specific transmission features.

In looking towards the future, we note first the utility of the implementation of a gate,[23,24] an end to which we have previously outlined some preliminary work which will feature prominently in the analysis in the following chapter. Beyond this, we envision an extension to a model for the weak-coupling regime using discrete-charge-state Green's functions, along the lines of recent work by Mirjani and Thijssen,[25] for which we anticipate the utility of our underlying charge-constrained (DIIS) algorithm, here used (only) for convergence acceleration.

REFERENCES

[1] Y. Xue and M. A. Ratner, *Microscopic study of electrical transport through individual molecules with metallic contacts. I. Band lineup, voltage drop, and high-field transport*, Phys. Rev. B **68**, 115406 (2003).

[2] Y. Xue and M. A. Ratner, *Microscopic study of electrical transport through individual molecules with metallic contacts. II. Effect of the interface structure*, Phys. Rev. B **68**, 115407 (2003).

[3] K. Stokbro, J. Taylor, M. Brandbyge, J. L. Mozos, and P. Ordejón, *Theoretical study of the nonlinear conductance of di-thiol benzene coupled to Au(111) surfaces via thiol and thiolate bonds*, Comp. Mat. Sci. **27**, 151 (2003).

[4] K. Stokbro, J. Taylor, M. Brandbyge, and P. Ordejón, *TranSIESTA – A Spice for Molecular Electronics*, Ann. N.Y. Acad. Sci. **1006**, 212 (2003).

[5] J. Nara, W. T. Geng, H. Kino, N. Kobayashi, and T. Ohno, *Theoretical investigation on electron transport through an organic molecule: Effect of the contact structure*, J. Chem. Phys. **121**, 6485 (2004).

[6] R. B. Pontes, F. D. Novaes, A. Fazzio, and A. J. R. da Silva, *Adsorption of Benzene-1,4-dithiol on the Au(111) Surface and Its Possible Role in Molecular Conductance*, J. Am. Chem. Soc. **128**, 8996 (2006).

[7] J. C. Love, L. A. Estroff, J. K. Kriebel, R. G. Nuzzo, and G. M. Whitesides, *Self-Assembled Monolayers of Thiolates on Metals as a Form of Nanotechnology*, Chem. Rev. **105**, 1103 (2005).

[8] R. Hoft, M. Ford, and M. Cortie, *Prediction of increased tunneling current by bond length stretch in molecular break junctions*, Chem. Phys. Lett. **429**, 503 (2006).

[9] L. Romaner, G. Heimel, M. Gruber, J.-L. Brédas, and E. Zojer, *Stretching and Breaking of a Molecular Junction*, Small **2**, 1468 (2006).

[10] R. Hoffmann, *Interaction of orbitals through space and through bonds*, Acc. Chem. Res. **4**, 1 (1971).

[11] G. C. Solomon, C. Herrmann, T. Hansen, V. Mujica, and M. A. Ratner, *Exploring local currents in molecular junctions*, Nat Chem **2**, 223 (2010).

[12] R. Liu, S.-H. Ke, H. U. Baranger, and W. Yang, *Intermolecular effect in molecular electronics*, J. Chem. Phys. **122**, 044703 (2005).

[13] H. Kondo, H. Kino, J. Nara, T. Ozaki, and T. Ohno, *Contact-structure dependence of transport properties of a single organic molecule between Au electrodes*, Phys. Rev. B **73**, 235323 (2006).

[14] J. Ulrich, D. Esrail, W. Pontius, L. Venkataraman, D. Millar, and L. H. Doerrer, *Variability of Conductance in Molecular Junctions*, J. Phys. Chem. B **110**, 2462 (2006).

[15] M. Hybertsen, L. Venkataraman, J. Klare, A. Whalley, M. Steigerwald, and C. Nuckolls, *Amine-Linked Single Molecule Circuits: Systematic Trends Across Molecular Families*, J. Phys.: Condens. Matter **20**, 374115 (2008).

[16] G. C. Liang, A. W. Ghosh, M. Paulsson, and S. Datta, *Electrostatic potential profiles of molecular conductors*, Phys. Rev. B **69**, 115302 (2004).

[17] Y. Xue, S. Datta, and M. A. Ratner, *First-principles based matrix Green's function approach to molecular electronic devices: general formalism*, Chem. Phys. **281**, 151 (2002).

[18] J. Reichert, R. Ochs, D. Beckmann, H. B. Weber, M. Mayor, and H. v. Löhneysen, *Driving Current through Single Organic Molecules*, Phys. Rev. Lett. **88**, 176804 (2002).

[19] M. Mayor, H. B. Weber, J. Reichert, M. Elbing, C. von Hänisch, D. Beckmann, and M. Fischer, *Electric Current through a Molecular Rod - Relevance of the Position of the Anchor Groups*, Angew. Chem. Int. Ed. **42**, 5834 (2003).

[20] X. Xiao, L. A. Nagahara, A. M. Rawlett, and N. Tao, *Electrochemical Gate-Controlled Conductance of Single Oligo(phenylene ethynylene)s*, J. Am. Chem. Soc. **127**, 9235 (2005).

[21] R. Huber, M. T. González, S. Wu, M. Langer, S. Grunder, V. Horhoiu, M. Mayor, M. R. Bryce, C. Wang, R. Jitchati, et al., *Electrical Conductance of Conjugated Oligomers at the Single Molecule Level*, J. Am. Chem. Soc. **130**, 1080 (2008).

[22] S.-H. Ke, H. U. Baranger, and W. Yang, *Role of the exchange-correlation potential in ab initio electron transport calculations*, J. Chem. Phys. **126**, 201102 (2007).

[23] R. Stadler, V. Geskin, and J. Cornil, *Towards a theoretical description of molecular junctions in the Coulomb blockade regime based on density functional theory*, Phys. Rev. B **78**, 113402 (2008).

[24] K. Kaasbjerg and K. Flensberg, *Strong Polarization-Induced Reduction of Addition Energies in Single-Molecule Nanojunctions*, Nano Lett. **8**, 3809 (2008).

[25] F. Mirjani and J. M. Thijssen, *Density functional theory based many-body analysis of electron transport through molecules*, Phys. Rev. B **83**, 035415 (2011).

6

TRANSPORT THROUGH PORPHYRIN SYSTEMS

We extend our transport method with a complementary approach which accounts for image-charge effects at a metal-molecule interface. A simple model allows us to calculate the adjustment of the molecular transport levels due to the polarization of the electrodes as the device is (dis)charged. We apply our approach to a detailed study of image-charge effects in the porphyrin-derivative devices recently studied experimentally by Perrin et al.[1]

Parts of this chapter have been submitted to Nat. Nano; other parts are in preparation for submission.

Understanding the physics determining charge transport at interfaces between metal electrodes and molecules is critical to progress in the field of molecular electronics. In a molecular device, the alignment of frontier molecular orbital levels relative to the metals' Fermi energies determines the contribution of the different channels available for transport. Due to their proximity to the electrodes, the levels themselves are shifted relative to those of the molecule in gas phase, and may hybridize with electrode levels as well. Together, level alignment and hybridization determine electron transport in the molecular junction.

In this chapter we describe an approach to investigating these effects based on density-functional theory (DFT)[2] and the non-equilibrium Green's functions (NEGF) formalism.[3–11] DFT is frequently used in calculations of charge transport because of its efficiency, and because computationally it scales well to realistic nanoscale junction sizes. It does suffers from a few drawbacks, however, the most important of which are poor predictions of one- and two-particle excitations.[2,12] A standard tool for one-particle excitations, the ΔSCF method,[2] gives quite good predictions for addition energies and ionization potentials. The reason for the failure of DFT to predict excitation energies from a single neutral-state calculation is mainly due to the inclusion of spurious self-interactions,[13,14] and the omission of dynamic polarization effects.[15,16] Both effects are captured in GW calculations,[16–18] usually within the COHSEX approach,[15] and time-dependent density-functional theory (TDDFT).[19–21] However, these are rather computationally expensive and not (yet) feasible for large systems, in contrast to DFT-based approaches.

Approximate methods have been proposed and used with some success to address the shortcomings of DFT in predicting the excitations. These include the use of a scissors-operator[22,23] and simple image-charge models based on atomic charges,[16,23–25] used to address the location of resonant levels in the transport region of the molecular device.

Here, we focus on the latter and argue that image charges used in an electrostatic-energy calculation should be taken from the molecule in the presence of contacts rather than from the gas phase. These are calculated from different charge states of the molecule as charge is added and removed, which we address by using a gate field to shift the molecular levels in the presence of the contacts. In section 6.1 we provide a brief introduction to static and dynamical interface effects, which alter the alignment between molecular levels and the Fermi energy of a metal surface. We then outline our method for the calculation of static and dynamical image-charge effects. In section 6.2, we apply our method to the Zn-porphyrin devices studied in recent experiments by Perrin *et al.*,[1] which illustrates the importance of static and dynamical image-charge effects. There, we also compare our results with various other simplified approaches which have been proposed and applied in the study of image-charge effects in molecular devices.[22,23,25]

Our approach is broadly applicable to understanding the level alignment essential to transport at organic-metallic interfaces, and allows us to obtain a detailed quantum-chemical understanding of the device at considerably lower computational expense than more sophisticated approaches.

6.1 INTERFACE EFFECTS AND POLARIZATION

We illustrate the most important physical effects as a molecule approaches a clean metal surface in Fig. 6.1, following Ishii *et al.*.[26] There is a net positive charge just inside the surface and a net negative charge just outside it due to "spill-out" of the wavefunctions of the electrons in the metal. The resulting dipole raises the potential at the surface to V_s which lies above the vacuum level V_∞ far from the metal. This causes the Fermi energy and the surface work function ϕ_m to differ.

When a metal-molecule junction is formed, two different kinds of effects occur. The first are effects due to interface dipoles created in the process of physi– or chemisorption, and the static image-charge effect we will introduce in the next section. These have in common that, similar to applying an electrostatic gate to the molecule, they all induce a similar "rigid" shift of the molecular levels. The second class of effects are those which shift occupied and unoccupied molecular levels differently, causing the gap between them to close ("renormalize") as the molecule approaches the surface. When combined with the static effects this yields the combined adjustment of levels illustrated in Fig. 6.1a. We discuss these two classes of effects further in the next sections.

6.1.1 STATIC INTERFACE EFFECTS

Level alignment at an interface is mainly driven by surface- and interface dipoles.[26–30] First, if the molecule is physisorbed onto the surface the electron cloud of the molecule will "push-back" the spill-out (known as the "pillow effect").[31,32] Second, in molecules which chemisorb rather than physisorb at the interface, formation of the bond causes charge transfer, which alters the surface dipole substantially. Third, there is also a "zero-bias" or "static" image-charge effect (SICE), which is generated by the charge distribution of the (possibly neutral) molecule which is felt by any charge added to/removed from the molecule during transport.

These effects together are combined in a rigid correction Δ to V_s (in principle is distance-dependent), and contribute to a static background potential which raises/lowers the molecular potential-well relative to the gas-phase (as in Fig. 6.1b). They are similar to electrostatically gating the molecule. In principle DFT captures at least part of this shift, but evaluating the dependence on the molecule-metal separation requires many separate DFT calculations. Oszwaldowski, Vazquez *et al.* have introduced a related many-body method based on DFT[33] for capturing some of this dependence, deriving from dipole and pillow effects. Our focus, however, will be on the contribution of the static image-charge effect to Δ, and the following considerations guide us:

- The length scale over which the changes to the energy landscape due to a surface dipole layer take place is related to the extent of the surface dipole

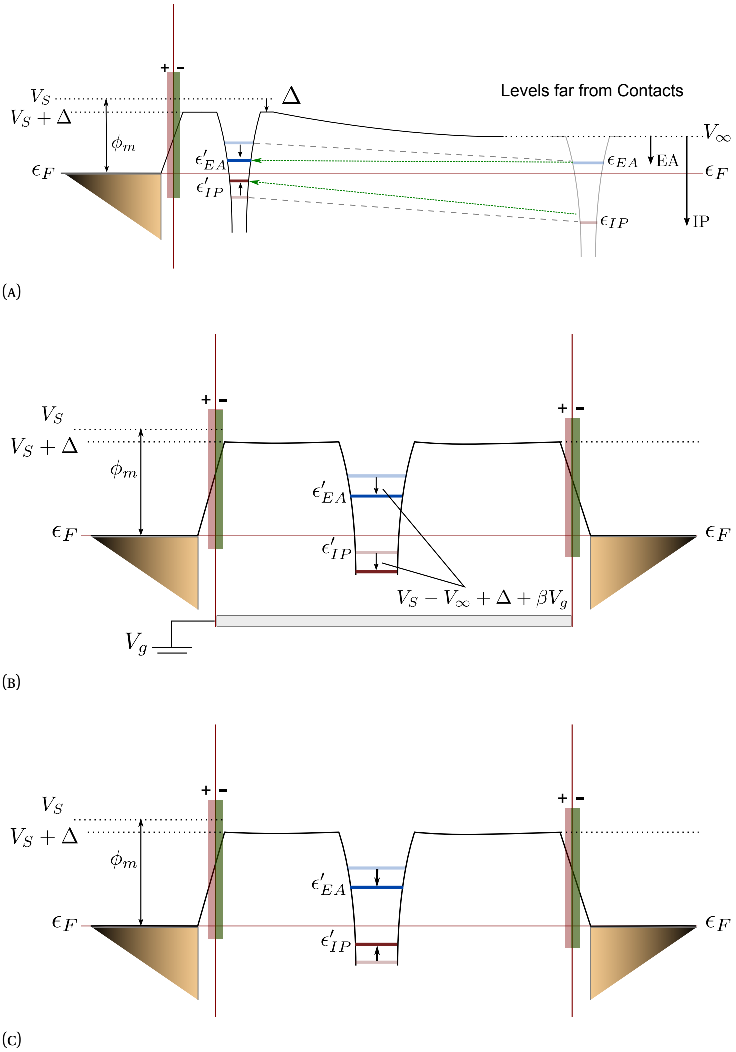

FIGURE 6.1: **Energy landscape during the formation of a metal-molecule interface.** (a) Combined static and dynamical image-charge effects on molecular levels at a single interface, relative to the molecule in isolation far away. These are a superposition of (b) and (c), where in (b) the surface dipole (shaded red/green) raises the background potential by $V_s - V_\infty$. The static image-charge effect, intrinsic molecular and interface dipoles shift the molecular levels back by Δ, while electrostatic gating shifts by βV_g. (c) Levels are also subject to renormalization of the gap between the electron affinity ϵ_{EA} and the ionization potential ϵ_{IP} levels, where the prime indicates the position after the shift.

layer formed at the metal surface. This is typically the scale of the electrode in a mechanically controlled break-junction (MCBJ) experiment, on the order of 5 nm.[a] This scale is also relevant for the other static interface effects, as they are all typcially induced by proximity of the molecular charge distribution to the metal surface.

- In a chemisorbed system, the shift is driven by charge transfer, which replaces the intrinsic surface dipole.

- The static image-charge effect can be a significant component of Δ, as remarked above.

- The magnitude of Δ is suggested by the measurements summarized by Ishii: roughly $0.5 - 1$ eV, typically a negative correction on an Au substrate for H_2TPP and ZnTPP films (without thiols).[26,28]

Measurements by Koch *et al.*[34–36] on thin-films with different molecules support these considerations: they find a constant-shift region very near the interface, followed by a linear shift of ~ 1 eV over a range of roughly 8 Å beyond which a regime with constant Δ sets in.

6.1.2 DYNAMICAL INTERFACE EFFECTS

Note that the effects in the preceding section shift all molecular levels in the same direction, which is in contrast with the closing ("renormalization") of the energy separation ("gap") between occupied and unoccupied levels we discuss in this section. We are concerned with the chemical potentials associated with charge addition and removal, derived from the frontier molecular orbitals, and will refer to these as the highest occupied and lowest unoccupied levels in analogy with the gas-phase HOMO and LUMO. The gap between these levels in the junction is the "transport gap," in analogy with the HOMO-LUMO gap (which omits charging effects). It maps directly to the electron affinity (EA) and ionization potential (IP) of the molecule in gas-phase, which are altered by the proximity to the metal electrodes. As a result of the polarization of the electrodes as charge is added to or removed from the molecule, the transport gap becomes smaller with decreasing metal-molecule separation, as illustrated in Fig. 6.1c, which we refer to as the "transport-induced" or "dynamical" image-charge effect (DICE).

It has been extensively discussed in the literature that transport-gap renormalization is indeed described by the dynamical image-charge effect,[15,16,18,22,37] and the polarization response to charge added near a metal surface, for smaller molecular systems, was shown by Neaton *et al.*[16] to be generally well-fit by an image-potential of the form $-\frac{1}{4x}$ beyond the image plane of the metal contact. To see how the image-charge effect leads to a reduction of the HOMO-LUMO gap, consider a single

---

[a] Estimated from the fits of the junction area in Perrin *et al.*'s experiments[1], which fit this as 28 nm^2 and considered the range of $10 - 50$ nm^2 as representative.

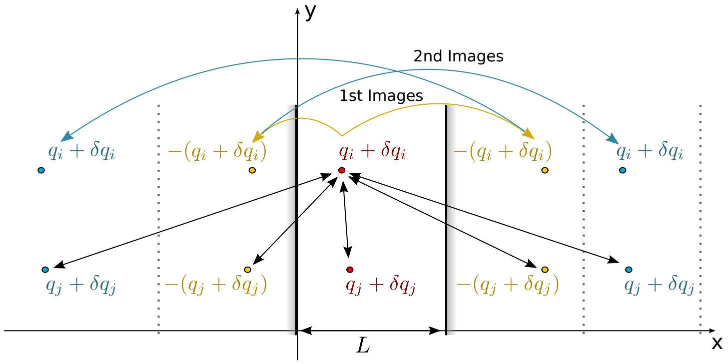

FIGURE 6.2: Point charges between parallel plates, leading to an infinite series of image charges (first set of images in yellow, second set (images of images) in blue, *etc*). Note the δq_i added to the charges q_i of the N^{th} charge state, in going to the $(N+1)^{\text{st}}$ charge state: these also induce a series of repeated images.

point-charge $\delta q = \pm e$ added to a neutral N electron system, near an infinite conducting plate. The charge addition induces an additional energy term $-\frac{\delta q^2}{4x}$, with x the distance from the plate, which decreases the ionization potential:

$$IP \equiv E^{N-1} - E^N \mapsto (E^{N-1} - \frac{\delta q^2}{4x}) - E^N \,, \tag{6.1}$$

and *raises* the HOMO-like occupied level $\epsilon_{IP} = -IP$ relative to the vacuum level V_∞. Similarly, it increases the electron affinity:

$$EA \equiv E^N - E^{N+1} \mapsto E^N - (E^{N+1} - \frac{\delta q^2}{4x}) \,, \tag{6.2}$$

and *lowers* the LUMO-like unoccupied level $\epsilon_{EA} = -EA$ relative to the vacuum level V_∞. Together, these effects renormalize the transport gap: $IP - EA = E^{N+1} + E^{N-1} - 2E^N - 2\frac{\delta q^2}{4x}$.

The effects are important in *most* nanoscale molecular systems, as has been argued on both experimental[24,38,39] and theoretical grounds recently.[16,18,22,23,25,37] Accounting for it is thus crucial for understanding and designing future molecular devices.

6.1.3 FULL IMAGE-CHARGE EFFECT MODEL

Following Kaasbjerg & Flensberg[25] and Mowbray & Thygesen[23], we simplify the image-charge effects for the full spatial charge density by considering atomic point charges. These are calculated from the charge states with $N-1$, N (neutral) and $N+1$ electrons on the molecule. The atomic charges are denoted q_j, and are located at $\boldsymbol{r}_j$. Their images are denoted as $q_j^I = -q_j$, located at $\boldsymbol{r}_j^I$. When the total charge on the molecule changes, the atomic charges change by δq_j, which induce additional image charges δq^I_j. The correction to a molecular level for a change in the charge state is then:

$$\begin{aligned}\Delta_{\text{ICE}} = {} & \sum_{i\neq j} \frac{\delta q_i q_j}{|\boldsymbol{r}_i - \boldsymbol{r}_j|} + \sum_{i\neq j} \frac{\delta q_i q^I_j}{|\boldsymbol{r}_i - \boldsymbol{r}^I_j|} + \sum_{i<j} \frac{\delta q_i \delta q^I_j}{|\boldsymbol{r}_i - \boldsymbol{r}^I_j|} \\ & - \sum_i \underbrace{\frac{\delta q_i q_i}{|\boldsymbol{r}_i - \boldsymbol{r}^I_i|}}_{2x_i} - \sum_i \underbrace{\frac{\delta q_i^2}{2|\boldsymbol{r}_i - \boldsymbol{r}^I_i|}}_{4x_i} + \sum_i U_{\text{self}}(\delta q_i)\end{aligned} \qquad (6.3)$$

which is derived by considering the work involved in assembling the point-charge configuration.

The superscript I implies a summation over the images: a single image for the single-plane case, and an infinite series for planes which face and mirror each other, as in Fig. 6.2. This series is discussed for two facing planes in Appendix 6.2.5.

The first term is the direct Coulomb interaction of δq_i with the resident charge distribution $\{q_j\}$. Terms two and four, involving q^I_j, account for the contribution of the static reference configuration, which we refer to as the static image-charge effect. Terms three and five, by contrast, are the dynamical effect due to a charge being added or removed only, and hence called the dynamical image-charge effect.[b] Eq. (6.3) not only accounts for the gap renormalization but also for the contribution of the static polarization to the rigid shift Δ introduced earlier. Note that terms two and four can be combined into a single expression, and likewise terms three and five. Term six corrects for the energy effects of adding charge an atom of the molecule, modeled by atomic charges, when there is already resident charge.[c] Like the first term, this does not dependent on the distance to the image plane, and so will be ignored.

When there is only one plane, and we neglect the self-interaction, the image-charge effect reduces to:

$$\Delta_{\text{ICE}} = -\frac{2q\,\delta q + \delta q^2}{4x}\ ,$$

where we recognize the extra term representing the static image-charge effect, when compared with Eq. (6.1). As an example, suppose the resident charges add up to roughly $q \approx \frac{1}{3}\delta q$, $\delta q = \pm e$ in magnitude, rather than charge neutral. Using this simple one-plane model, we find a significantly stronger effect than when the resident charges are ignored: $\Delta_{\text{ICE}}(x) = -\frac{\left(1+\frac{2}{3}\right)}{4x}e^2$.

---

[b] Note that terms 4 and 5 split out the diagonal elements of terms 2 and 3 for the geometry in Fig. 6.2.

[c] To describe this properly in quantum mechanics requires taking the orbital structure into account and correcting for self-interaction errors made by DFT, which are being ignored in an atomic point-charge model.

6.1.4 MOLECULAR CHARGE DISTRIBUTIONS

To evaluate the model in the previous section, we need the atomic charges for different molecular charge states. For this, several charge decomposition techniques are available.[40] We prefer Hirshfeld or Voronoi decompositions due to their nature as spatial decompositions, as opposed to the basis-set decomposition involved in Mulliken decompositions. Two approaches will be compared in section 6.2 of this chapter:

1. Using the charge distributions of the N and $N \pm 1$ electron charge states in *gas-phase*, where one electron is added to or removed from the molecule without taking the interactions with the electrodes into account. This is the approach taken by *e.g.* Mowbray *et al.*,[23] with the additional assumption motivated by Hybertsen *et al.*[15] and Neaton *et al.*[22] that taking only the atomic charges involved in addressing the IP already captures the image effects for both occupied and unoccupied levels.

2. Starting from the reference charge state of the molecule in a *junction*, *i.e.* the state in the absence of bias or gate fields. The molecule is then gated by a constant field, such that the charge is changed by $\pm e$. As in the previous approach, this yields three sets of atomic charges, but now in a description with the interaction with the electrodes taken into account. To the best of our knowledge, this approach has not previously been reported in the literature.

In section 6.2.4 we compare the methods for the specific case of Perrin *et al.*'s Zn-porphyrin single-molecule experiments, and argue that the extra physics captured in the second approach is essential for understanding low-bias transport.

6.1.5 IMAGE-CHARGE CALCULATION SUMMARY

Before applying our method to a concrete example, we summarize the steps:

1. A set of DFT+NEGF transport calculations is performed with a geometry that models the junctions in the experiments. Rather than performing a single transport calculation, we perform three. In these calculations a gate field is applied to the molecule in the junction, tuned such that it has a charge corresponding to $\pm 1e$ relative to the (partially charged) reference state, characterized by zero bias and gate voltage.

2. The charge-distributions from these calculations are then used in our image-charge model (6.3), yielding a distance-dependent trend for the static and dynamical image-charge effects.

3. The effects are calculated for infinite-plane electrodes. We have also estimated the reduction of the effects for more realistic electrode geometries. This is performed only once, to obtain a single correction factor which reduces the magnitude of the calculated level shifts.

For comparison, DFT calculations of the molecule in gas-phase are also performed, in order to understand the nature of the molecular levels and the baseline atomic charge distribution which is altered by proximity to the electrodes. The link between the two situations is made by inspection of which gas-phase levels contribute to the peaks in the transmission. This yields additional insight into the transport process in general, and the image-charge effect in particular.

6.2 Au-ZnTPPdt Molecular Devices

We now proceed to a non-trivial application of the method, which allows for a comparison with recent experiments that reveal image-charge effects on both occupied and unoccupied molecular levels.

6.2.1 Experimental Results

We first discuss the recent experimental findings of Perrin *et al.*[1] who studied thiol-terminated zinc-porphyrin molecules [Zn(5,15-di(p-thiolphenyl)-10,20-di(p-tolyl)-porphyrin)], abbreviated as ZnTPPdT. The molecules were chosen because they offer great architectural flexibility and rich optical properties, as is well-established in the literature. These aspects also motivated previous studies by Perrin *et al.*[41,42]

The experiments were carried out in a mechanically-controlled break-junction (MCBJ) setup, as in Fig. 6.3.[43,44] Fig. 6.3a illustrates the setup schematically. Pressure is slowly applied along the green arrows, which when balanced against the counter support causes the electrodes to move closer together or apart in a controlled way. This allows one to make and break contact on a nanometer scale, sufficiently small to create gaps in which to trap single molecules, which then bridge the separated electrodes and close the electrical circuit. The experiments take place under cryogenic conditions in vacuum, which dramatically reduce the presence of impurities, and allow study of quantum mechanical effects which would otherwise be “washed out” by thermal noise.

Current-voltage characteristics (IV’s) can be taken as a function of electrode spacing in two- and three-terminal MCBJ’s, while in the case of three-terminal devices the dependence on the gate voltage can also be measured, yielding stability diagrams. Physical realizations of the two device types are shown in Fig. 6.3b as colorized scanning electron microscope (SEM) pictures.

The derivative of an IV, the differential conductance ($\frac{\partial I}{\partial V}$), is the main instrument used to study such molecular devices. Peaks in the differential conductance typically correspond to resonant transport through a molecular level, which may have been brought into resonance with the chemical potentials of the leads by either gating or biasing the device. In a typical $\frac{\partial I}{\partial V}$, resonances indicating transport through a single level will correspond to two peaks: one at positive and one at negative bias. When considered as a function of the spacing of the electrodes, these resonances show a marked “mechanical gating” effect, where a level shift is induced by a change in the metal-molecule distance The efficiency of the effect can be expressed by a mechanical gate coupling (MGC): the change in bias voltage needed to address the resonance with varying electrode separation (in units of V/nm).

We show experimental data for the observed mechanically-induced shifts in Fig. 6.5, where the measurements show a distance-dependent resonance, again expressed as the bias required to address the level in transport. A linear fit of the resonance positions was used to find the MGC.

Histograms and basic statistics of the observed MGC's are plotted in Figs. 6.6b–6.6c, which show that there is a (sometimes) large spread in the observed MGC, but that each sample has its own characteristic distribution. Various jumps in the resonance position are also visible in Fig. 6.6a, which are presumably caused by changes in the geometrical configuration. As ZnTPPdT is not a rod-like molecule, it can form molecular junctions with various geometries, as has been reported previously for similar molecules.[42] In the experiments a wide range of shifts is found, but generally they are in the range of 0.2 – 1 V/nm (where $V = V_b$, the bias voltage).[d] Combined with a typical range of 0.5 nm over which the junctions formed are stable, this means that levels shift observably over roughly 50 – 250 meV in energy, if we assume the bias voltage to drop symmetrically.

By itself these observations would not, however, determine whether the resonance is associated with a HOMO-like (initially occupied) or a LUMO-like (initially unoccupied) level. To establish those associations, the gate electrode was used to determine the electrostatic gate coupling (EGC), defined as the shift in voltage of the conductance peak per unit gate voltage applied (units of V V^{-1}).

This is illustrated in Fig. 6.4, which shows a positive EGC corresponding to HOMO-like occupied levels (gating moves them away from the Fermi level, thus a larger bias is needed to address them), and a negative EGC corresponding to LUMO-like unoccupied levels (gating moves them towards the Fermi level, reducing the bias necessary to address them).

On average the couplings appear to be on the around 0.51 ± 0.33 V/nm (corresponding to 0.25 ± 0.16 eV/nm, assuming a symmetric bias drop over the molecule), but the histograms in Fig. 6.6 indicate that there can be a significant spread in the observed MGC over different opening and closing traces. This probably reflects the occurrence of some conformational changes in the junction during measurements separated in time.

Moreover, when identification of the level using the gate is added, we find that individual samples can exhibit significantly large occupied/unoccupied level shift asymmetries, as we illustrate in Fig. 6.5 (0.40 V/nm *vs.* 0.18 V/nm). However, the number of samples is too small to draw general conclusions, despite the stability of the effects in individual samples. This stability is nonetheless remarkable, and is illustrated for a number of consecutive making/breaking cycles in Fig. 6.6a.

---

[d] The distance between the molecule and the electrodes is roughly half this on either side, implying that the one-sided shift magnitude is doubled.

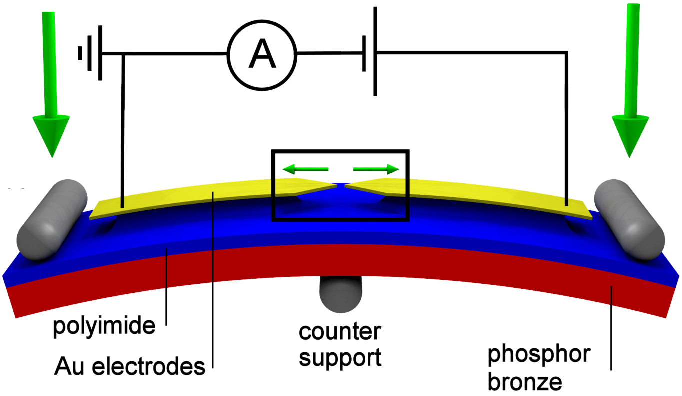

(a)

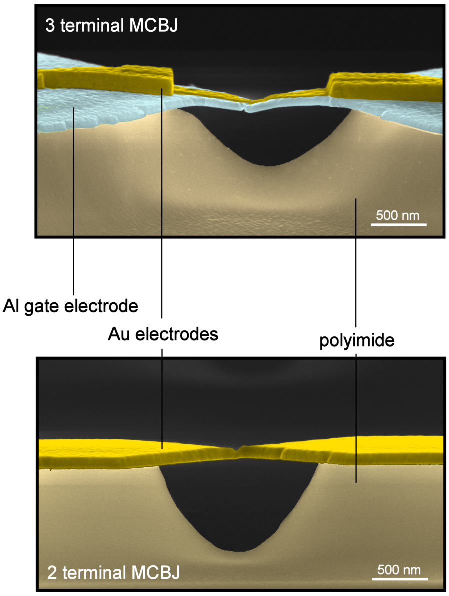

(b)

Figure 6.3: (a) Illustration of the measurement setup in a MCBJ experiment. (b) Colorized SEM picture of one of the device fabricated for the measurements reported by Perrin *et al.*,[1] with and without an Al gate electrode underlying the Au break-junction (a three- and two-terminal device, respectively)

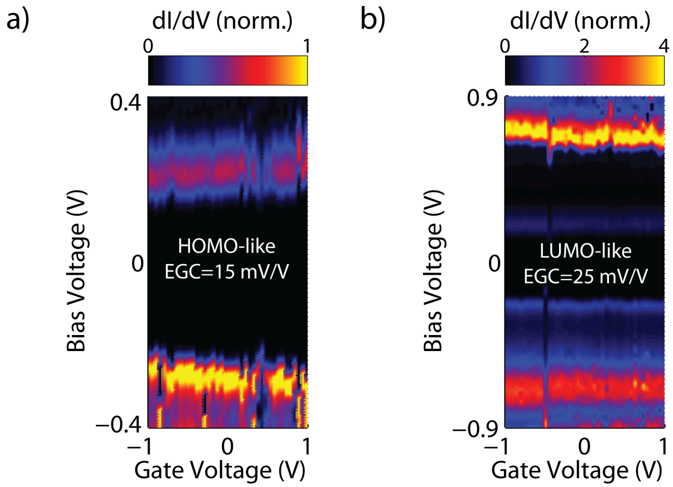

FIGURE 6.4: Representative measurement on AU-ZNTPPDT,[1] showing electrostatic gate coupling of (a) occupied or HOMO-like levels (moving outwards) and (b) unoccupied or LUMO-like levels (moving inwards) respectively.

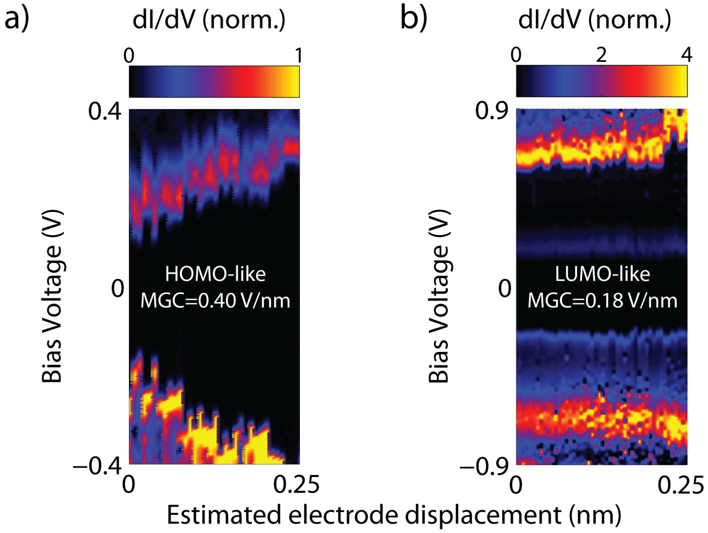

FIGURE 6.5: (a) Representative measurement on AU-ZNTPPDT,[1] showing (a) HOMO-like mechanical gate-coupling (MGC) of occupied levels, and (b) LUMO-like MGC of an unoccupied level, respectively. Note the dilation of the y-axis in the case of LUMO-like resonances. Both move inwards towards the Fermi level with decreasing distance.

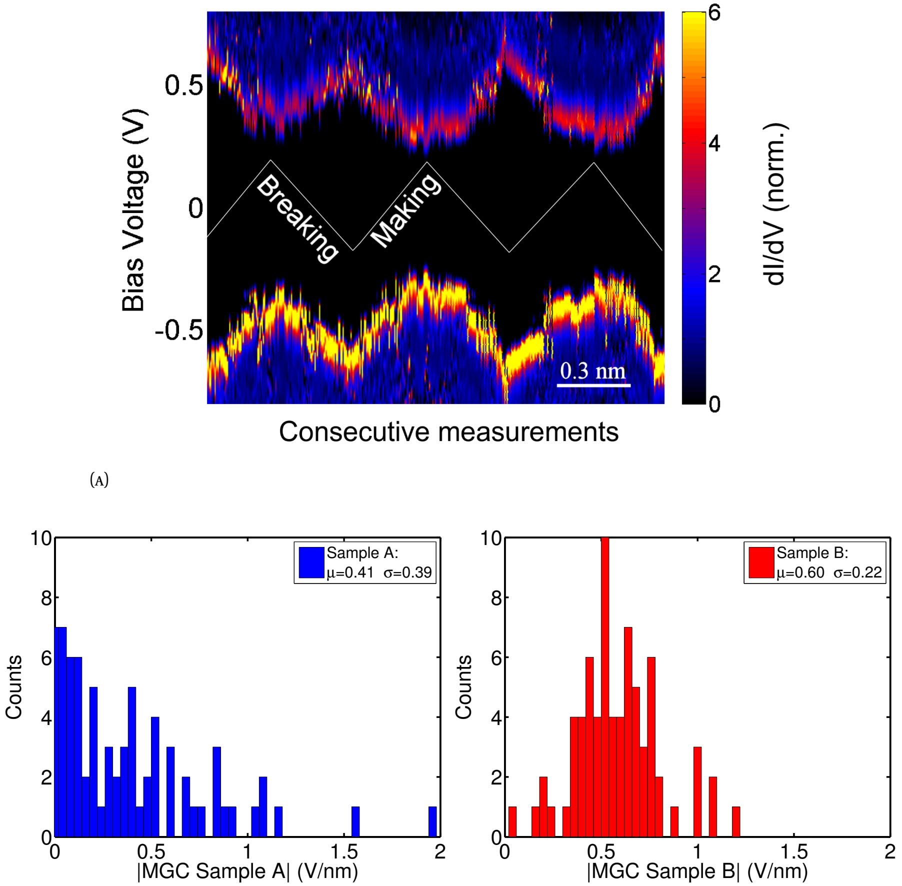

(a)

(b)

(c)

Figure 6.6: (a) Representative measurement,[1] showing reproducibility of observed MGC's over repeated making and breaking of the junction. (b)–(c) Histograms, means and standard deviations of the (absolute value of the) observed MGC for repeated measurements on two experimental samples.

We will now show that our approach yields trends matching the experiment, and predicts an asymmetry in the shifts found between occupied and unoccupied levels. While it produces results for an idealized geometry, these can be corrected to yield better quantitative estimates for more realistic geometries, as we will show.

6.2.2 ZNTPPDT ELECTRONIC STRUCTURE

To apply our method to this molecular system, we first consider the electronic structure of the molecules in gas phase. Geometry optimizations were performed, using ADF,[45,46] for the ZnTPPdT molecule in gas-phase, as well as Au-ZnTPPdT-Au fragments. These fragments are the simplest approach to a thiolated Au-ZnTPPdT system: two Au ad-atoms stabilize the molecule, in the place of the H's detached from the terminating thiol groups. We discuss the details in section 6.3. The geometries are illustrated in Fig. 6.7 and the resulting electronic structure is shown schematically in Fig. 6.8 for the three relevant gas-phase charge states.

The relevant molecular levels for transport in Fig. 6.8 are those which are near the Fermi level of the Au electrodes. We show the levels HOMO-2 through LUMO+1 for the fragment and gas-phase systems in Figs. 6.9 and 6.19 respectively. Most levels are characterized by an orbital wave-function which extends at least somewhat onto the arms which connect the molecule to the electrodes, and the coupling from the arms to the electrodes almost fully determines the relevance of the orbital for transport. The HOMO-like levels extend more onto the arms than the LUMO, and as is suggested by the fragments in Fig. 6.9, also hybridize more strongly with the gold, in Fig. 6.11.

Most of the fragment orbitals can be related to gas-phase orbitals by considering their symmetry on the molecule. For a number of levels, the correspondence is less trivial, such as for those formed in the gap between the gas-phase HOMO and LUMO due to hybridization with the gold (*cf.* Fig. 6.10). Their charge density is located mostly on the arms, and they appear to be stabilized by the interface. In the following, we will refer to these levels without gas-phase counterparts as “interface levels”; the remaining levels will be denoted by the character of the corresponding gas-phase orbitals: HOMO, LUMO, *etc.*

Finally, with regard to the gas-phase HOMO-LUMO gap, by means of ΔSCF calculations (taking energy differences between two calculations for charge states $N, N+1$) we find it to be 1.8 eV in our LDA and GGA calculations and 2.7 eV using the B3LYP functional, consistent with the reports of Park *et al.*[47], and in general agreement with their redox measurements of roughly 2.2 eV. In the experiments, assuming a symmetric bias drop over the junction, this would require a bias on the order of 4 V to be applied, which is beyond the experimentally accessible range of the MCBJ-based devices in Perrin *et al.*'s experiments.

6.2.3 TRANSPORT THROUGH ZNTPPDT JUNCTIONS

Our Au-ZnTPPdT binding geometry is based on a phenyl ring bonded to a gold surface via a thiolate bond,[48–51] as shown in Fig. 6.7c. In the calculations, ZnTPPdT's

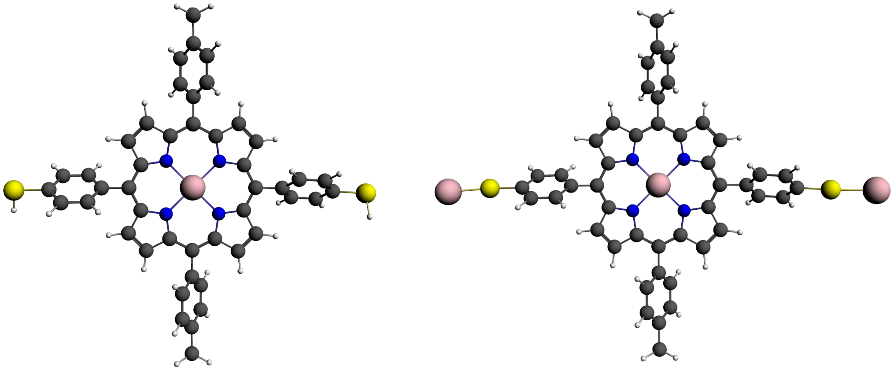

(a) ZnTPPdT Geometry

(b) Au-ZnTPPdT Fragment Geometry

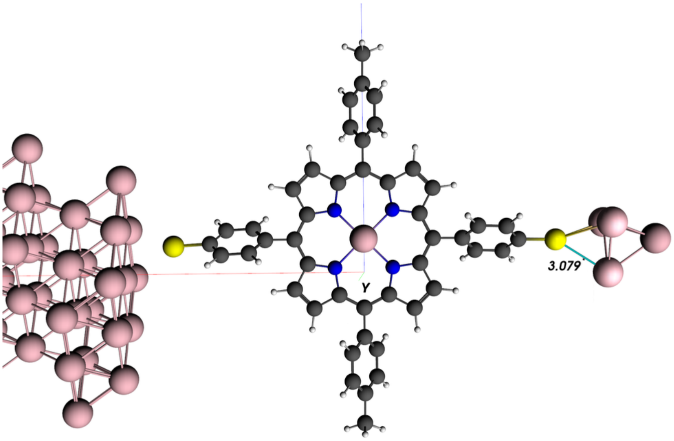

(c) Au-ZnTPPdT Junction Geometry

Figure 6.7: Geometries of ZnTPPdT in (a) gas-phase and (b) as a fragment. Metal ions are pink-grey. (c) Typical binding geometry. Left Au atoms show placement relative to a (111) surface layer, right atoms show the positions of nearest neighbors participating in the hollow-site Au-S binding. In the transport calculations bulk-like contacts are present on both sides.

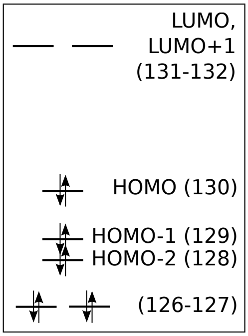

FIGURE 6.8: Highest occupied and lowest unoccupied level structure of the ZnTPPdT molecule in gas phase, from a DFT calculation with 260 valence electrons (lower-lying levels treated in the frozen-core approximation). The corresponding orbitals are illustrated in Figs. 6.9 and 6.19.

binding is characterized by chemisorption, with significant charge transfer to the thiols, which act as acceptors. This is in agreement with the literature on such bindings.[52–56] The calculations are performed with a perpendicular hollow-site binding to a FCC (111) surface, though we discuss tilt and other departures from the perpendicular geometry further in section 6.2.6. We nonetheless emphasize that this choice is in no way essential: it is merely representative of what is thought to be a typical single-molecule device geometry.

We performed a series of calculations for varying gate fields, and show the cases where roughly $\pm e$ is added to/removed from the reference state in the junction in Fig. 6.12. We extract the (Hirshfeld) projected charges on different parts of the system, which indicate that at zero gate-field, the reference state has a net charge of $-0.05e$, with roughly $-0.34e$ on the thiols and $+0.29e$ on the rest of the molecule. The latter is dominated by the core Zn ion.

All calculations were performed using a TZP-basis of numerical atomic orbitals on the molecule, using the LDA functional in our implementation of NEGF-based transport in the ADF/Band quantum chemistry package,[11,57,58] with thiols located at a 2.59 Å from the electrodes. For further details about the calculations, see the appendix at the end of this chapter.

We study the composition of the transmission peaks found in our transport calculations using the decomposition technique of Appendix B, in which we project the transporting levels from the DFT+NEGF calculation onto orbitals of the Au-ZnTPPdT fragment, illustrated in Fig. 6.9. Fig. 6.10 shows the transmission of a typical transport calculation for the MCBJ geometry of Fig. 6.7c, using a representative nearest neighbor Au-S distance of 3.08 Å, corresponding to a 2.59 Å offset from the electrodes in a 24.26Å gap. We observe a cluster of HOMO-like peaks near ϵ_f (defined as 0 eV), some features in the gap near 0.4 eV, and the nearly-degenerate LUMO and LUMO+1 around 1.7 eV.

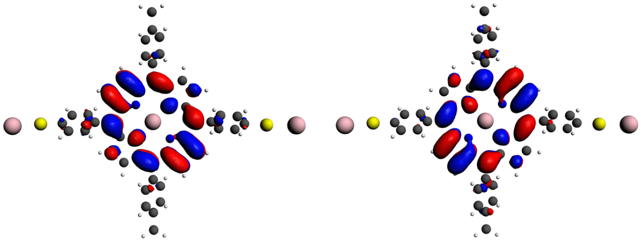

(a) LUMO+1 (b) LUMO

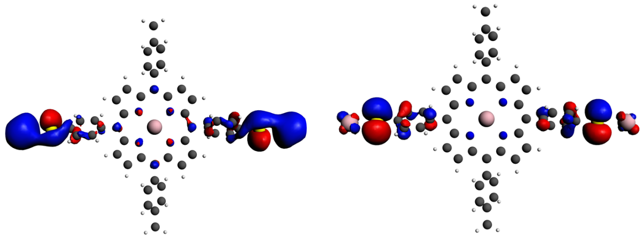

(c) Typical "Interface Level" A (d) Typical "Interface Level" B

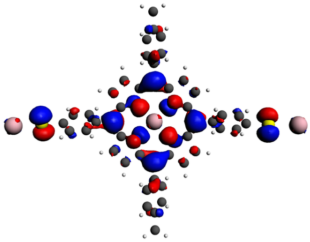

(e) HOMO

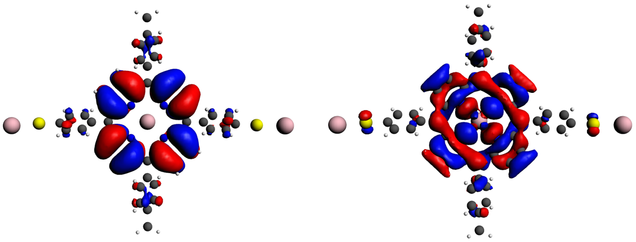

(f) HOMO-1 (g) HOMO-2

Figure 6.9: Orbitals of gas-phase Au-ZnTPPdT-Au Fragment. (c)–(d) Typical interface levels which form on hybridizing with Au: 6 total between the analogue of the gas-phase HOMO and LUMO (*cf.* Fig. 6.19), forming three sets of bonding/anti-bonding pairs, of which two sets with HOMO character and one set with LUMO character.

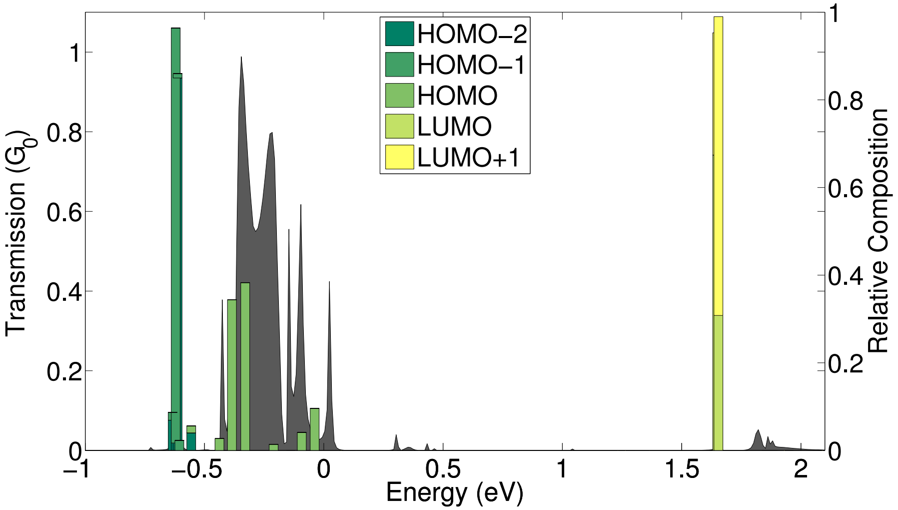

(a) Peaks decomposition with molecular orbital levels

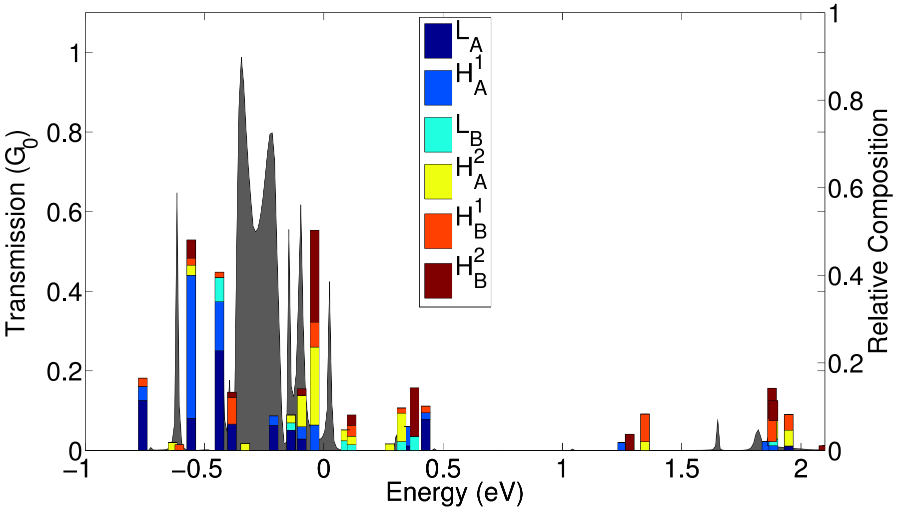

(b) Peaks decomposition with interface levels

Figure 6.10: (a) Composition of peaks in transport, constructed by projection onto fragment molecular orbitals. A state with value 1 is a decoupled state (completely un-hybridized, *e.g.* HOMO−4 through −7), while HOMO, HOMO-1 and −2 are strongly hybridized with each other *and* the Au electrodes (30-50% representation in the junction levels, with the rest originating from Au). The LUMO and LUMO+1 peaks are likewise strongly mixed with each other, but couple much less to Au, reflected in the much narrower transport peaks near 1.7 eV. (b) As in (a) for the interface levels rather than the levels directly identifiable with gas-phase molecular levels.

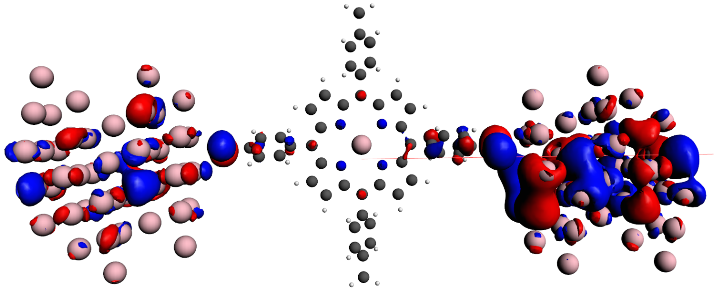

(A) Hybridized HOMO for $(N+1)e$ in Junction

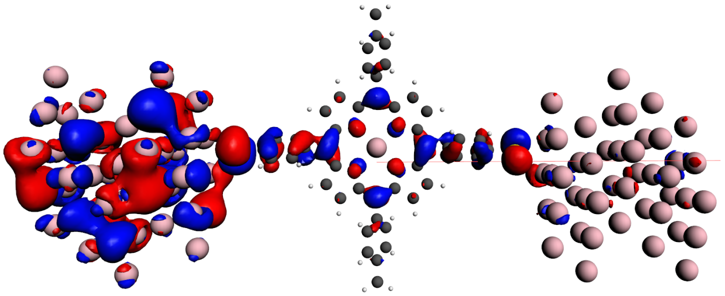

(B) Hybridized HOMO in MCBJ geometry

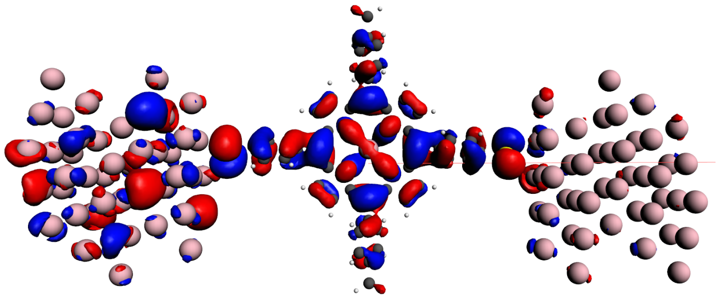

(C) Hybridized HOMO for $(N-1)e$ in Junction

FIGURE 6.11: Hybridization in the Au-ZnTPPdT junction: effective HOMO levels relative to the Fermi energy, gated such that (a) is the HOMO when there are roughly $N+1$ electrons on the molecule in the junction (interface state-like), (b) roughly N electrons (HOMO-like, reference state has $V_g = 0$ eV, net charge is $-0.05e$ but $+0.29e$ on the molecule excluding the negative thiols, *cf.* Fig. 6.12) and (c) roughly $N-1$ electrons (also HOMO-like, as HOMO is double occupied in neutral ground-state).

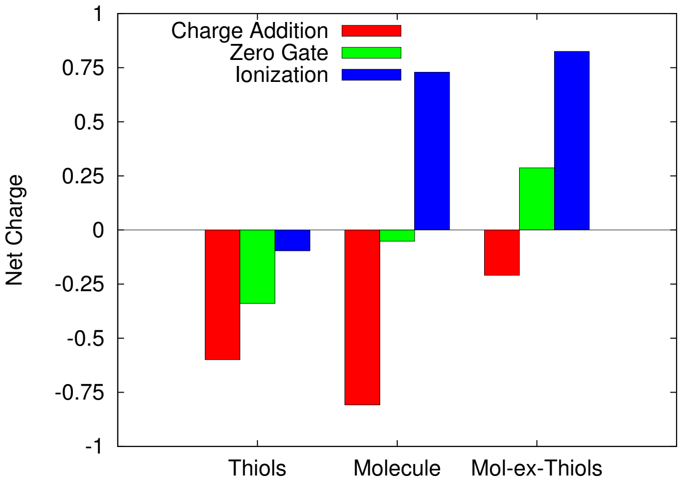

FIGURE 6.12: Partial charges for the three gated transport levels (the reference state and gated such that the net charge is ≈ ±e), showing the difference in charging the molecule, thiols and molecule-without-thiols as the gating is varied (roughly ±50 meV). At zero-field, the molecule is roughly neutral, with negative thiols and a positive core.

The HOMO and two nearest occupied levels dominate transport near ϵ_f, with the HOMO appearing as a broad peak while HOMO-1 and HOMO-2 mostly contribute to a lower lying, less-coupled state. HOMO-3 and below do not contribute much to transport (appearing as levels which do not hybridize). The peaks right below the Fermi level derive mostly from the HOMO,[e] with significant amounts of interface levels (*cf.* section 6.2.2) mixed in. Fig. 6.10b shows the role of the 6 interface levels labeled $L_{A,B}$, $H^1_{A,B}$ and $H^2_{A,B}$, derived from hybridization of HOMO and LUMO with the gold. The levels in the fragment appear to be of a bonding/anti-bonding character, with splittings on the order of 0.1 eV. The charge density deviates most strongly from neutral near the interface due to the chemisorption-induced charge transfer. The hybridization associated with the chemisorption is responsible for the smearing of the sharp resonances of molecular levels into broader peaks in transport near ϵ_f. Our conclusions from these calculations may be summarized as follows:

- It is unlikely that the LUMO level is available within the experimental bias-window of roughly ±0.75 eV, given that zero-bias transport is HOMO-dominated, with the LUMO resonance at 1.7 eV above the Fermi energy in Fig. 6.10. More accurate calculations of the EA with GGA and B3LYP functionals in the ΔSCF approach, yields values for the addition energy $IP-EA$ in the range of $1.8-2.7$ eV.

- The dominant spectral feature just above ϵ_f is a resonance with a distinct

---

[e] Identified by analyzing the orbital symmetries of the wavefunctions of these levels.

HOMO-derived interface level's orbital character remarked earlier. Its presence in the transport gap suggests it as the likely mechanism for accessible LUMO-like behavior.

6.2.4 IMAGE-CHARGE CALCULATIONS

The most relevant molecular levels (*cf.* Fig. 6.19) are likely to be the HOMO-derived levels near the Fermi level of the Au electrodes, and not the orbitals derived from the gas-phase LUMO. Consequently, as argued by Perrin *et al.*,[1] we conclude that when both electron and hole transport are observed, the reference state (at zero bias and gate) is one in which the molecule has already lost some charge (though not necessarily a full electron, due to partial charge-transfer at the interface). This suggests that the atomic charges in a junction geometry (obtained from a NEGF+DFT calculation) will lead to more representative results than when gas-phase charges are used.

Charge distributions for the higher and lower charge states are obtained by gating the levels nearest ϵ_f across roughly $\approx$ 100 meV relative to the reference state, changing the net charge by $\approx \pm e$. Fig. 6.13 shows the resulting charge distributions, comparing the results from gas-phase with those for a gated single-molecule junction.

We apply the image model, Eq. (6.3), summing the electrostatic interactions with all image charges for the device geometry between two parallel plates (*cf.* section 6.2.5). The resulting shifts as a function of distance are plotted in Fig. 6.14b with uncertainty bands accounting for a ±0.25 Å uncertainty in the position of the image plane, taken at 1 Å outside the outermost plane of metal atom centers (Fig. 6.14a), consistent with the literature.[22,59–61] Our calculations predict MGC's in the range of 0.5 – 1.4 eV/nm for an occupied level and 0.2 – 1.1 eV/nm for an unoccupied level (in opposite directions), depending on electrode separation (*cf.* Fig. 6.14b).

Fig. 6.15 compares the image-charge effects above with those calculated from atomic charges taken in gas-phase. As the gap closes, the image effects derived from the charges in the junction become significantly stronger, due to the relatively strongly-charged thiols being brought closer to the contacts. For large electrode separations, on the other hand, the trend of the unoccupied level, in particular, is quite similar for charges from gas-phase and in the junction.

The shifts shown in Fig. 6.14b can be split into static and dynamical image-charge terms (*cf.* Fig. 6.14c). In section 6.1 we introduced Δ, the correction to the background potential, and argued that it should have a common "static" effect on both occupied and unoccupied levels, in the range of -0.5 to -1 eV for H_2TPP and ZnTPP films.[26,28] For samples in which the reference state is (partially) charged, we expected the static image-charge effect (SICE) to contribute substantially to this Δ-shift. In Fig. 6.14c, we indeed find that the SICE is relatively constant as a function of distance, and has a magnitude of roughly 0.35 to 0.45 eV, though there is some distance dependence that contribute to the overall trend of the image-charge effects.

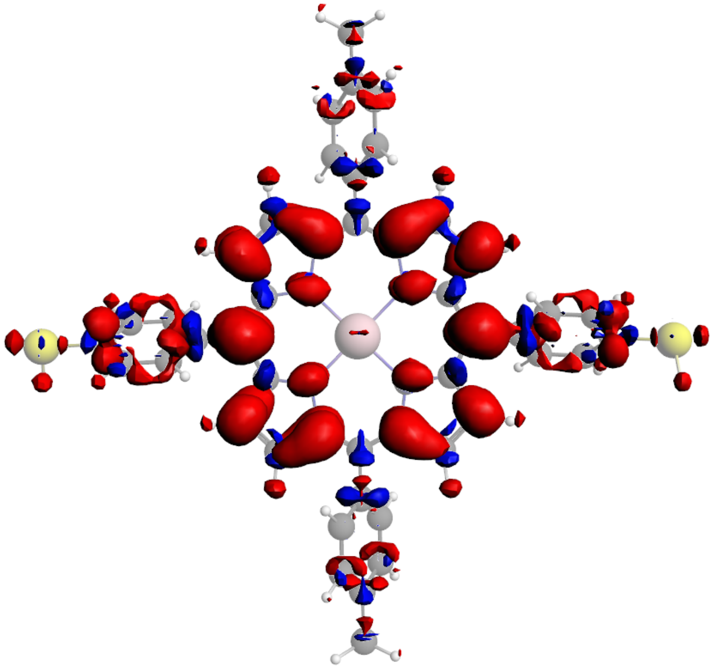

(a)

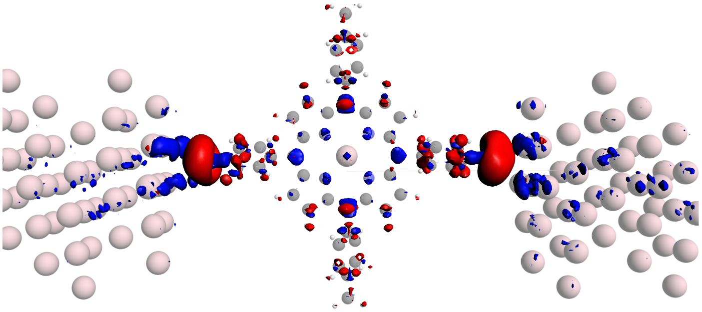

(b)

Figure 6.13: Difference in charge distribution in the $N + 1$ relative to the N electron charge states. Red indicates the increase of negative charge when adding an electron; blue the decrease. Differences for (a) gas-phase DFT calculations (LUMO like difference) and (b) for gated DFT+NEGF transport calculations (recalling the interface levels of Fig. 6.9).

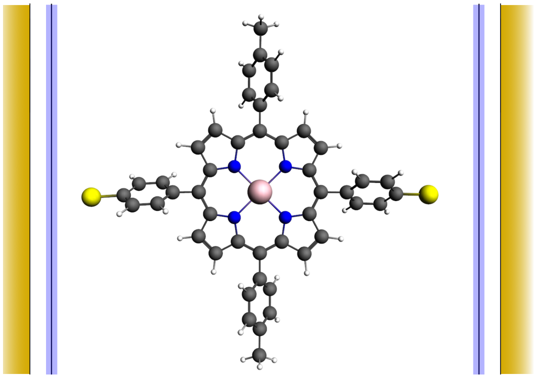

(a) Geometry for Image-Charge Shifts

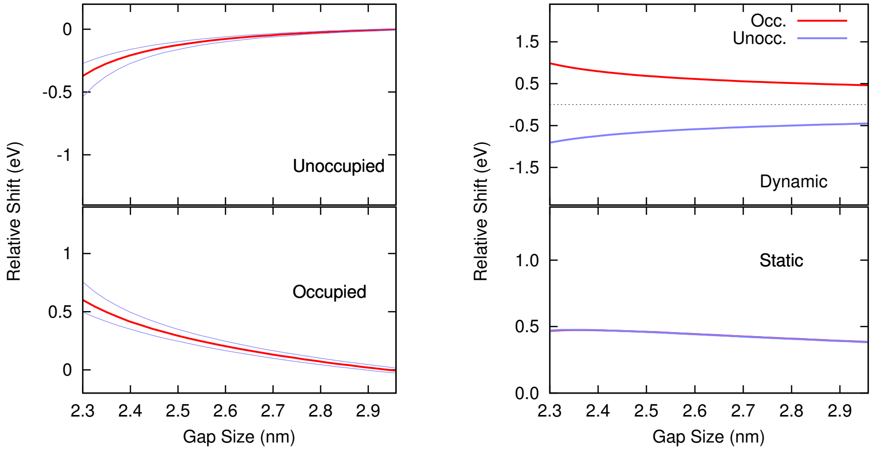

(b) Transport Gap Renormalization

(c) Static *vs.* Dynamical Image-Charge Effect

Figure 6.14: (a) Geometry used in the image-charge model, and (b) shifts predicted by the model (with uncertainties) showing the occupied- and unoccupied-levels both shifting towards ϵ_f with MGC's (the derivative with distance) in the range of 0.2 – 1.4 eV/nm, expressed in the symmetrically applied bias. (c) Splitting of shift of Eq. (6.3) into static and dynamical terms. Derivatives are of the same order, but the dynamical terms dominate. Static terms give same trend for both levels, while dynamical terms show opposite behavior, with net asymmetry causing the occupied level to shift more strongly, as in the experiment.

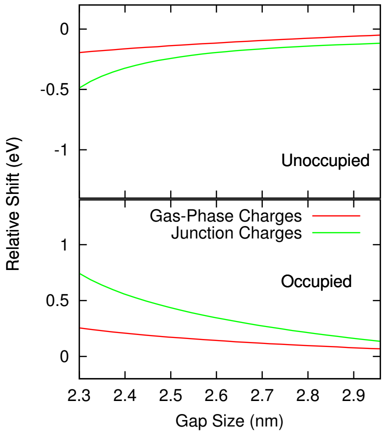

FIGURE 6.15: Comparison of results for total image-charge corrections using charges from gas-phase calculations of ZnTPPdT, and from calculations on the ZnTPPdT molecular junction.

The sign, however, may be negative or positive, depending on the details of the charge distribution on the molecule, which can be understood as follows. If we consider *just* the (negative) charging of the thiols, we would expect positive image charges to dominate, lowering the potential for charge addition to the molecule in the junction. This is already clear in the image model for a single site near a metal surface. We can simplify the analysis of our more complicated molecule by introducing a 3-site toy-model as in Fig. 6.16. We take equal negative charges near the interface, representing the thiols at the extremes of the molecule, and a positive "core" in between. We find $\Delta_{\mathrm{SICE}} < 0$ for charges similar to our Hirshfeld decomposition. However, for electrode separations and bindings where the charges on the thiols are not as dominant, we can find an opposite sign for the SICE. This then agrees with what we find for the full atomic charge distribution in Fig. 6.14c.

This observation is particularly relevant in the context of the experiments, since Fig. 6.5 suggests an asymmetry such that the occupied level shifts more strongly than the unoccupied one. If the dynamical image-charge effect is dominated by the charging of the thiols near the interfaces, it may be roughly symmetric (recalling the image-charge effect for a single charge), as Fig. 6.14c suggests. The model's prediction of asymmetry in the trends in the experiments is, in this case, due to the static image-charge effect. In order to explain the measurements in Fig. 6.3, $\Delta_{\mathrm{SICE}} > 0$ is then essential, and both such a 3-site model and our full transport calculations suggest that it can occur in some (though not all) metal-molecule configurations and charge states.[f]

---

[f] Depending on, among other things, the junction geometry and electrode separation, as they are reflected in the exact location of the HOMO-like transmission peaks relative to ϵ_f.

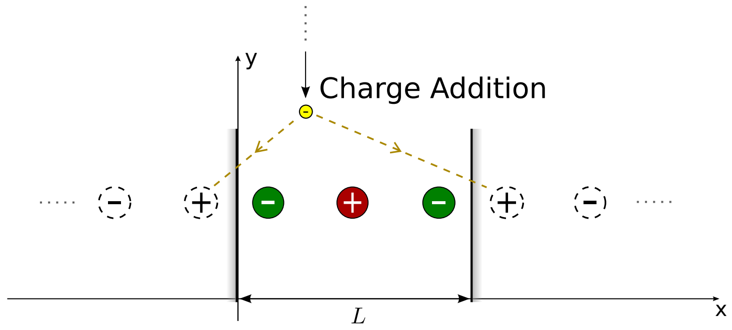

Figure 6.16: 3-site charging model, where the images of the charges nearest the interface dominate the static image-charge effect as charge is added, indicated by yellow dashed lines.

We conclude that image-charge effects explain the distance-dependent renormalization of the position of the molecular orbital levels with respect to the Fermi level of the electrodes. Our calculations reveal that the static image-charge effect contributes to the MGC to an extent comparable with the dynamical effect (roughly half as strong), as expected for a charged reference state. We emphasize that agreement between theory and experiment is found assuming a *partially charged* reference state for the molecule in the junction. Taking the reference state to be the gas-phase neutral state suppresses the asymmetry between the shifts for occupied and unoccupied levels, as is clear in Fig. 6.15. This supports our conclusion that for the measurements of Fig. 6.3 an interface-stabilized level of the fragment has lost some charge, as is suggested by the peak above the Fermi level in our transport calculations, and that this level is being addressed in electron transport through the unoccupied state.

6.2.5 Kaasbjerg & Mowbray Models

For comparison with our results, we have implemented the previously noted model by Kaasbjerg[25] as follows:

$$\begin{aligned}\Delta E_{\mathrm{K}} = \sum_{\sigma,\tau}\sum_{i,j} q_i q_j \cdot \sigma \frac{\epsilon_r+\tau}{\epsilon_r+1}\tau \Bigg(&\overbrace{\frac{1}{\sqrt{(x_i-\sigma x_j)^2+(y_i-\tau y_j)^2+(z_i-z_j)^2}}}^{\text{direct Coulomb when } \sigma=\tau=1} \\ &+ \sum_{n=1}^{\infty}\Bigg(\frac{1}{\sqrt{(x_i-\sigma x_j-2nL)^2+(y_i-\tau y_j)^2+(z_i-z_j)^2}} \\ &+ \frac{1}{\sqrt{(x_i-\sigma x_j+2nL)^2+(y_i-\tau y_j)^2+(z_i-z_j)^2}}\Bigg)\Bigg),\end{aligned} \tag{6.4}$$

where the image terms that we are concerned with correspond to $\tau = 1, \sigma = 1, \frac{\epsilon_r+\tau}{\epsilon_r+1} = 1$. In Kaasbjerg's formulation in terms of classical Green's functions, the

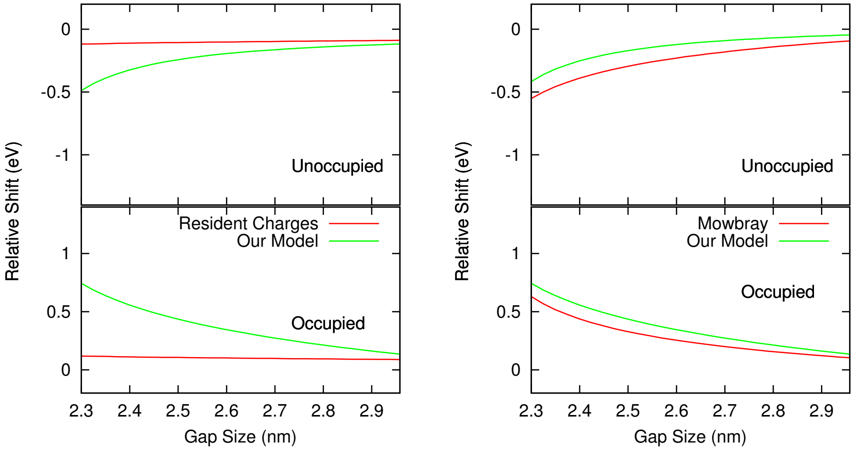

(A) (B)

FIGURE 6.17: Comparison of our model with Mowbray's (equivalently, Kaasbjerg's) approach, using (a) neutral-state resident charges $\{q_i\}$ in the junction, and (b) the charged-state's added charges $\{\delta q_i\}$ in the junction.

direct term is dropped and one proceeds with only the Green's function $\tilde{G}(x_i, x_j)$ corresponding to the induced potential: all the terms minus the direct one. Then $\phi_i^{\text{induced}} = \sum_j q_j \tilde{G}(x_i, x_j)$ and $\Delta E = \frac{1}{2}\sum_i q_i \phi_i^{\text{induced}}$ where we recover the usual factor $\frac{1}{2}$ associated with double counting when assembling the charges in the induced potential field. Mowbray includes this factor $\frac{1}{2}$ explicitly, while Kaasbjerg recovers it when going from the potential to the associated energy for the charges in the field. In Mowbray's[23] very similar approach:

$$\begin{aligned}\Delta E_{\mathrm{M}} = -\frac{1}{2}\sum_{i,j} q_i q_j \sum_{n=1}^{\infty}\Bigg(& \frac{1}{\sqrt{(x_i + x_j - 2nL)^2 + (y_i - y_j)^2 + (z_i - z_j)^2}} \\ & + \frac{1}{\sqrt{(x_i + x_j + 2(n-1)L)^2 + (y_i - y_j)^2 + (z_i - z_j)^2}} \\ & - \frac{1}{\sqrt{(x_i - x_j - 2nL)^2 + (y_i - y_j)^2 + (z_i - z_j)^2}} \\ & - \frac{1}{\sqrt{(x_i - x_j + 2nL)^2 + (y_i - y_j)^2 + (z_i - z_j)^2}}\Bigg). \end{aligned} \tag{6.5}$$

We see that the two models map onto one another, with the extra offset in the second of Mowbray's summed terms corresponding to the $n = 1$ term. Numerically, correcting for this gives perfect agreement, without it we get the correct behavior for the $2(n-1)L = 0$ term and the large-n asymptotics, and the numbers are generally close in between. In evaluating our Eq. (6.3), we convolve the charge terms in the numerator with the same kernel as the two models just discussed (specifically, Eq. (6.5)).

If we consider only the difference between charge states, we are assuming $q_i = 0$ in the above expressions. Making this substitution we recover precisely:

$$\sum_{j \neq k} \frac{\delta q_j \cdot \delta q_k^I}{|\boldsymbol{r}_j - \boldsymbol{r}_k^I|} - \sum_j \frac{\delta q_j^2}{4x_j} \tag{6.6}$$

which are the terms corresponding to the buildup of image charges in the absence of a resident charge distribution. This yields exactly the terms outlined by Kaasbjerg & Flensberg when summed over all repeated images between two infinite planes. We thus find that Eq. (6.3) is an extension of their approach, where the charge distribution in the reference charge-state is explicitly taken into account in the static-image-charge effect. As with their work, we account for the gap renormalization at the interface, but in addition also add the contribution of the static polarization to the rigid shift Δ, allowing for an asymmetry in the shifts of the occupied and unoccupied levels respectively.

Finally, in Fig. 6.17 we make the comparison between these models and ours, using the neutral-state resident charges (in the junction), finding that the behavior is significantly different. On the other hand, we compare the use of our model with charges corresponding to a partially charged the molecule in the junction. We then find much better agreement, with a roughly constant shift corresponding to the omission of the static image-charge effect in the latter approach, which reports symmetric shifts of occupied and unoccupied levels.

6.2.6 Orientation and Finite-Size Corrections

So far, we have assumed that the molecule is oriented with its ‘arm’ perpendicular to an infinite, flat surface. In this section we investigate the effect of deviations from this idealized situation.

Though it is possible in general, we do not expect that the molecule lies flat (angle ∼ 0°) on the surface, as no highly asymmetric bias-coupling was observed in these experiments. We have investigated the dependence on the orientation by repeating the procedure for different angles between the lateral axis of the molecule and the surface, finding only a weak dependence of the MGC with angle.

At low angles (where the molecule lies nearly flat) there may be different charging patterns due to different charge-injection pathways made possible by the proximity of the rest of the molecule to the contact surface, modifying this conclusion.

A second issue is that in the MCBJ experiments, we do not expect to have large “parallel plate” electrodes, but more needle-like few-atom contacts. This implies that the capacity for screening by the electrons available locally is reduced, and so the image-charge effects will be smaller than in the infinite plane case.

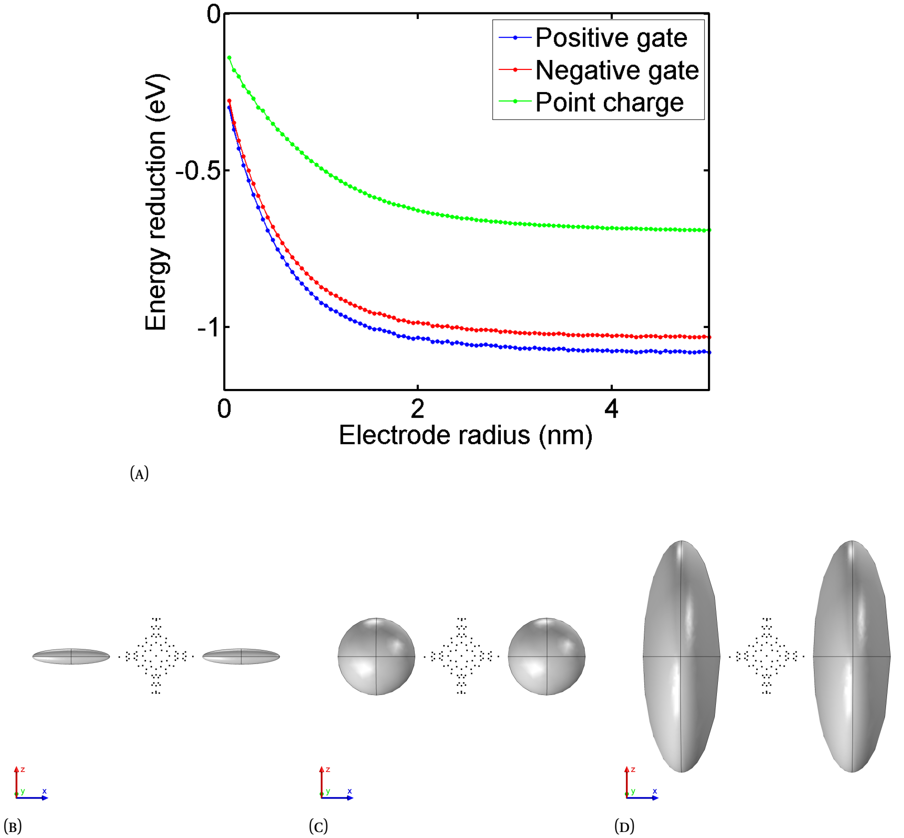

(a)

(b)

(c)

(d)

Figure 6.18: (a) Image charge correction (reduction in magnitude) as a function of electrode radius for the charge distributions obtained when applying a positive and a negative gate with a point charge e in the center of the junction. (b–d) Geometry used in COMSOL to calculate the image charge correction for an electrode radius of 0.2 nm, 1 nm, and 3 nm respectively.

To investigate this difference, we have used the finite element electrostatic solver in COMSOL Multiphysics 4.2 and calculated the reduction of the electrostatic energy of the point charges as a function of electrode size, using elliptical electrodes of a few Å across (the expected size of a few-atom contact in a MCBJ experiment).

The electrodes were modeled as ellipsoids with the semi-axis in the transport direction fixed at 1 nm. The semi-axes perpendicular to transport were varied from 0.2 nm to 5 nm, as illustrated in Fig. 6.18(b)–(c). Using this electrode geometry, we first calculate the reduction of the image effect for a point charge e in the center of the junction as a function of electrode size, which goes to a "large electrode limit," comparable with the planar contact results. For needle-like few-atom contacts, a 0.5 nm radius would be reasonable, and we find a reduction of the image-charge effect by roughly a factor of 1.5 on comparing the energy reduction at this radius with the large electrode limit in Fig. 6.18a.

For comparison, we have also calculated the reduction for the full atomic charges for the ZnTPPdT molecule. Again, we find reductions on the same order. These calculations imply that for needle-like electrodes in a break-junction experiment, the range of MGC predicted by the image-charge model would be reduced from 0.2 – 1.4 eV/nm to the range 0.1 – 0.9 eV/nm, in better quantitative agreement with the experiments.

6.3 Conclusions

In summary, we have presented a method for calculating the image-charge effects which change the alignment of the occupied and unoccupied levels in molecular devices with the Fermi levels of the electrodes. Our approach is based on modeling the charge distribution of the molecule in the junction, in different charge states, using atomic point-charges. It is essential to use these rather than their gas-phase equivalents for two reasons. First, the relevant charge states have a different character in gas-phase molecules and molecules in a junction, due to the formation of "interface levels" in the latter. These are stabilized by the metal-molecule interface, and have no counterpart in the gas phase. Second, unlike in the gas phase, the reference state in the junction (at zero bias and gate) can carry a net charge, which implies a significant contribution to the reduction of the metal work function upon chemisorption of a molecule.

In Perrin *et al.*'s[1] experiments on Au-ZnTPPdT in gated mechanically-controlled break junctions, a distance-dependent shift of the levels nearest the metal Fermi level is observed. This can be described by our approach, which corrects these levels by static and dynamical image-charge effects that strongly depend on distance. The agreement of our model with the experimentally determined shifts is within a factor of two. More importantly, we find that the qualitative trend matches the experimental observations, predicting an asymmetry whereby the occupied levels shift more strongly than the unoccupied levels, in agreement with the experiments.

Standard DFT+NEGF calculations do not take dynamical image-charge effects into account, but do account for at least the part of the rigid shift of the surface work-function that includes the static image-charge effect. There is distance dependence of the static-image charge contribution, however, which is accounted for by our model calculations. It is particularly strong when the reference state of the system is charged, and the sign of this charge then determines the trend of the overall correction.

Together with the dynamical image-charge effects, which have often been suspected of playing a critical role in transport experiments, we arrive at an intuitive overall picture by the combined use of electronic structure theory, transport theory and a detailed model of image-charge induced spectral adjustment. The different computational tools allow us to illuminate the structure underlying the behavior in transport near the Fermi level, and provide an efficient way to evaluate these effects in novel chemical systems.

COMPUTATIONAL DETAILS

All quantum-chemical calculations in this chapter were performed using the ADF/Band package, while the NEGF formalism for modeling transport has been implemented by us in the ADF/Band quantum chemistry package, and was used to obtain the conductance as a function of energy for representative junctions discussed below.

In analyzing Au-ZnTPPdT junctions, we use a TZP basis on the molecule, and SZ on the Au atoms in DFT. Results were converged to energy changes of less than 10^{-3} hartree per step, together with energy gradients of less than 10^{-3} hartree/Å maximum and $< 6.7 \cdot 10^{-4}$ hartree/Å RMS. Transport calculations were likewise performed using a TZP-basis of numerical atomic orbitals on ZnTPPdT and a SZ-basis on Au, using the LDA functional in our transport implementation. Note also that while we show LDA results, GGA-level calculations with the PBE functionals do not qualitatively alter the results shown.

The relevant geometries are illustrated in Fig. 6.7. The resulting orbitals of the gas-phase molecule are shown in Fig. 6.19, while the results for the fragment used in the transport calculations was previously shown in Fig. 6.9.

We next modeled the image-charge effects central to this chapter using small models implemented in Python, which take the results of the preceding quantum chemical calculations as inputs. These were then further supplemented by a study of electrode size effects using the COMSOL finite-element electrostatics package.

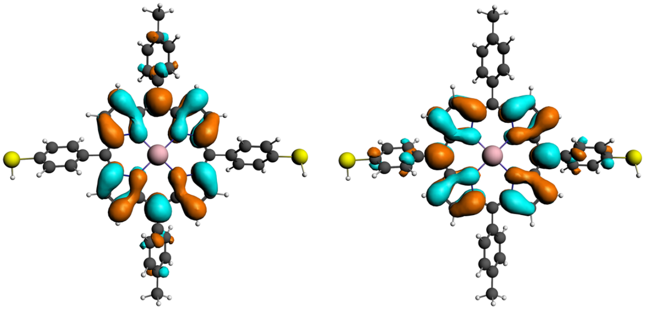

(a) LUMO+1

(b) LUMO

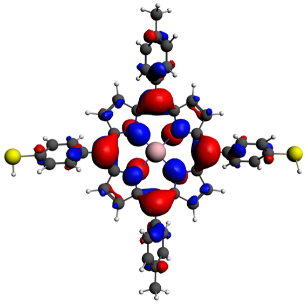

(c) HOMO

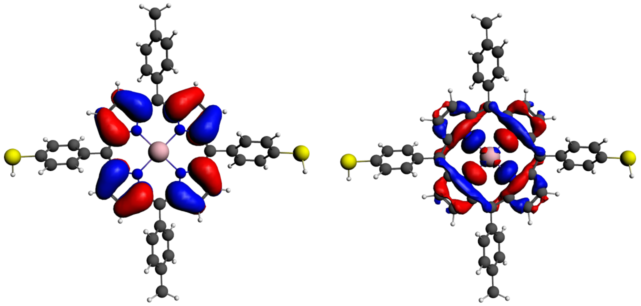

(d) HOMO-1

(e) HOMO-2

Figure 6.19: Orbitals of gas-phase ZnTPPdT

REFERENCES

[1] M. L. Perrin, C. J. O. Verzijl, C. A. Martin, A. J. Shaikh, R. Eelkema, J. H. van Esch, J. M. van Ruitenbeek, J. M. Thijssen, H. S. J. van der Zant, and D. Dulić, *Large tunable image-charge effects in single-molecule junctions* (2012), submitted to Nat. Nano.

[2] R. O. Jones and O. Gunnarsson, *The density functional formalism, its applications and prospects*, Rev. Mod. Phys. **61**, 689 (1989).

[3] Y. Meir and N. S. Wingreen, *Landauer formula for the current through an interacting electron region*, Phys. Rev. Lett. **68**, 2512 (1992).

[4] S. Datta, *Nanoscale device modeling: the Green's function method*, Superlatt. Microstruct. **28**, 253 (2000).

[5] M. Brandbyge, J.-L. Mozos, P. Ordejón, J. Taylor, and K. Stokbro, *Density-functional method for nonequilibrium electron transport*, Phys. Rev. B **65**, 165401 (2002).

[6] K. Stokbro, J. Taylor, M. Brandbyge, and P. Ordejón, *TranSIESTA – A Spice for Molecular Electronics*, Ann. N.Y. Acad. Sci. **1006**, 212 (2003).

[7] F. Evers, F. Weigend, and M. Koentopp, *Coherent transport through a molecular wire: DFT calculation*, Physica E: Low-dimensional Systems and Nanostructures **18**, 255 (2003), 23rd International Conference on Low Temperature Physics (LT23).

[8] A. R. Rocha, V. M. García-Suárez, S. Bailey, C. Lambert, J. Ferrer, and S. Sanvito, *Spin and molecular electronics in atomically generated orbital landscapes*, Phys. Rev. B **73**, 085414 (2006).

[9] F. Evers and A. Arnold, *CFN Lectures on Functional Nanostructures*, vol. 2 of *Springer Lecture Notes in Physics* (Springer, 2006), 1st ed.

[10] A. Arnold, F. Weigend, and F. Evers, *Quantum chemistry calculations for molecules coupled to reservoirs: Formalism, implementation, and application to benzenedithiol*, J. Chem. Phys. **126**, 174101 (2007).

[11] C. J. O. Verzijl and J. M. Thijssen, *A DFT-based Molecular Transport Implementation in ADF/BAND*, J. Phys. Chem. C (2012), accepted.

[12] K. Burke, *Perspective on density functional theory*, J. Chem. Phys. **136**, 150901 (pages 9) (2012).

[13] J. P. Perdew and A. Zunger, *Self-interaction correction to density-functional approximations for many-electron systems*, Phys. Rev. B **23**, 5048 (1981).

[14] C. Toher, A. Filippetti, S. Sanvito, and K. Burke, *Self-Interaction Errors in Density-Functional Calculations of Electronic Transport*, Phys. Rev. Lett. **95**, 146402 (2005).

[15] M. S. Hybertsen and S. G. Louie, *Electron correlation in semiconductors and insulators: Band gaps and quasiparticle energies*, Phys. Rev. B **34**, 5390 (1986).

[16] J. B. Neaton, M. S. Hybertsen, and S. G. Louie, *Renormalization of Molecular Electronic Levels at Metal-Molecule Interfaces*, Phys. Rev. Lett. **97**, 216405 (2006).

[17] F. Aryasetiawan and O. Gunnarsson, *The GW method*, Rep. Prog. Phys. **61**, 237 (1998).

[18] K. S. Thygesen and A. Rubio, *Renormalization of Molecular Quasiparticle Levels at Metal-Molecule Interfaces: Trends across Binding Regimes*, Phys. Rev. Lett. **102**, 046802 (2009).

[19] G. Stefanucci and C.-O. Almbladh, *Time-dependent partition-free approach in resonant tunneling systems*, Phys. Rev. B **69**, 195318 (2004).

[20] S. Kurth, G. Stefanucci, C.-O. Almbladh, A. Rubio, and E. K. U. Gross, *Time-dependent quantum transport: A practical scheme using density functional theory*, Phys. Rev. B **72**, 035308 (2005).

[21] E. Perfetto, G. Stefanucci, and M. Cini, *Correlation-Induced Memory Effects in Transport Properties of Low-Dimensional Systems*, Phys. Rev. Lett. **105**, 156802 (2010).

[22] S. Quek, L. Venkataraman, H. Choi, S. Louie, M. Hybertsen, and J. Neaton, *Amine–Gold Linked Single-Molecule Circuits: Experiment and Theory*, Nano Lett. **11**, 3477 (2007).

[23] D. J. Mowbray, G. Jones, and K. S. Thygesen, *Influence of functional groups on charge transport in molecular junctions*, J. Chem. Phys. **128**, 111103 (pages 5) (2008).

[24] P. Hedegård and T. Bjørnholm, *Charge transport through image charged stabilized states in a single molecule single electron transistor device*, Chem. Phys. **319**, 350 (2005).

[25] K. Kaasbjerg and K. Flensberg, *Strong Polarization-Induced Reduction of Addition Energies in Single-Molecule Nanojunctions*, Nano Lett. **8**, 3809 (2008).

[26] H. Ishii, H. Oji, E. Ito, N. Hayashi, D. Yoshimura, and K. Seki, *Energy level alignment and band bending at model interfaces of organic electroluminescent devices*, J. Lumin. **87-89**, 61 (2000).

[27] K. Seki, E. Ito, and H. Ishii, *Energy level alignment at organic-metal interfaces studied by UV photoemission*, Synth. Met. **91**, 137 (1997), International Conference on Electroluminescence of Molecular Materials and Related Phenomena.

[28] H. Ishii, K. Sugiyama, E. Ito, and K. Seki, *Energy Level Alignment and Interfacial Electronic Structures at Organic-Metal and Organic-Organic Interfaces*, Adv. Mat. **11**, 605 (1999).

[29] H. Vázquez, F. Flores, R. Oszwaldowski, J. Ortega, R. Pérez, and A. Kahn, *Barrier formation at metal-organic interfaces: dipole formation and the charge neutrality level*, Appl. Surf. Sci. **234**, 107 (2004), the Ninth International Conference on the Formation of Semiconductor Interfaces.

[30] H. Vázquez, R. Oszwaldowski, P. Pou, J. Ortega, R. Pérez, F. Flores, and A. Kahn, *Dipole formation at metal/PTCDA interfaces: Role of the Charge Neutrality Level*, Europhys. Lett. **65**, 802 (2004).

[31] H. Vázquez, Y. J. Dappe, J. Ortega, and F. Flores, *Energy level alignment at metal/organic semiconductor interfaces: "Pillow" effect, induced density of interface states, and charge neutrality level*, **126**, 144703 (2007).

[32] F. Flores, J. Ortega, and H. Vazquez, *Modelling energy level alignment at organic interfaces and density functional theory*, Phys. Chem. Chem. Phys. **11**, 8658 (2009).

[33] R. Oszwaldowski, H. Vázquez, P. Pou, J. Ortega, R. Pérez, and F. Flores, *Exchange-correlation energy in the orbital occupancy method: electronic structure of organic molecules*, J. Phys.: Condens. Matter **15**, S2665 (2003).

[34] S. Duhm, G. Heimel, I. Salzmann, H. Glowatzki, R. L. Johnson, A. Vollmer, J. P. Rabe, and N. Koch, *Orientation-dependent ionization energies and interface dipoles in ordered molecular assemblies*, Nat. Mater. **7**, 326 (2008).

[35] B. Bröker, O. T. Hofmann, G. M. Rangger, P. Frank, R.-P. Blum, R. Rieger, L. Venema, A. Vollmer, K. Müllen, J. P. Rabe, et al., *Density-Dependent Reorientation and Rehybridization of Chemisorbed Conjugated Molecules for Controlling Interface Electronic Structure*, Phys. Rev. Lett. **104**, 246805 (2010).

[36] J. Niederhausen, P. Amsalem, J. Frisch, A. Wilke, A. Vollmer, R. Rieger, K. Müllen, J. P. Rabe, and N. Koch, *Tuning hole-injection barriers at organic/metal interfaces exploiting the orientation of a molecular acceptor interlayer*, Phys. Rev. B **84**, 165302 (2011).

[37] M. Hybertsen, L. Venkataraman, J. Klare, A. Whalley, M. Steigerwald, and C. Nuckolls, *Amine-Linked Single Molecule Circuits: Systematic Trends Across Molecular Families*, J. Phys.: Condens. Matter **20**, 374115 (2008).

[38] S. Kubatkin, A. Danilov, M. Hjort, J. Cornil, J.-L. Bredas, N. Stuhr-Hansen, P. Hedegård, and T. Bjornholm, *Single-electron transistor of a single organic molecule with access to several redox states*, Nature **425**, 698 (2003).

[39] C. Bruot, J. Hihath, and N. Tao, *Mechanically controlled molecular orbital alignment in single molecule junctions*, Nat. Nano **7**, 35 (2012).

[40] C. Fonseca Guerra, J.-W. Handgraaf, E. J. Baerends, and F. M. Bickelhaupt, *Voronoi deformation density (VDD) charges: Assessment of the Mulliken, Bader, Hirshfeld, Weinhold, and VDD methods for charge analysis*, J. Comput. Chem. **25**, 189 (2004).

[41] M. L. Perrin, C. A. Martin, F. Prins, A. J. Shaikh, R. Eelkema, J. H. van Esch, J. M. van Ruitenbeek, H. S. J. van der Zant, and D. Dulić, *Charge transport in a zinc-porphyrin single-molecule junction*, Beilstein J. Nanotechnol. **2**, 714 (2011).

[42] M. L. Perrin, F. Prins, C. A. Martin, A. J. Shaikh, R. Eelkema, J. H. van Esch, T. Briza, R. Kaplanek, V. Kral, J. M. van Ruitenbeek, et al., *Influence of the Chemical Structure on the Stability and Conductance of Porphyrin Single-Molecule Junctions*, Angew. Chem. **123**, 11419 (2011).

[43] C. A. Martin, D. Ding, H. S. J. van der Zant, and J. M. van Ruitenbeek, *Lithographic mechanical break junctions for single-molecule measurements in vacuum: possibilities and limitations*, New J. Phys. **10**, 065008 (2008).

[44] C. A. Martin, J. M. van Ruitenbeek, and H. S. J. van der Zant, *Sandwich-type gated mechanical break junctions*, Nanotechnology **21**, 265201 (2010).

[45] C. Fonseca Guerra, J. G. Snijders, G. te Velde, and E. J. Baerends, *Towards an order-N DFT method*, Theor. Chem. Acc. **99**, 391 (1998).

[46] G. te Velde, F. Bickelhaupt, S. van Gisbergen, C. Fonseca Guerra, E. Baerends, J. Snijders, and T. Ziegler, *Chemistry with ADF*, J. Comput. Chem. **22**, 931 (2001).

[47] J. K. Park, H. R. Lee, J. Chen, H. Shinokubo, A. Osuka, and D. Kim, *Photoelectrochemical Properties of Doubly β-Functionalized Porphyrin Sensitizers for Dye-Sensitized Nanocrystalline-TiO2 Solar Cells*, J. Phys. Chem. C **112**, 16691 (2008).

[48] J. Nara, W. T. Geng, H. Kino, N. Kobayashi, and T. Ohno, *Theoretical investigation on electron transport through an organic molecule: Effect of the contact structure*, J. Chem. Phys. **121**, 6485 (2004).

[49] D. Q. Andrews, R. Cohen, R. P. V. Duyne, and M. A. Ratner, *Single molecule electron transport junctions: Charging and geometric effects on conductance*, J. Chem. Phys. **125**, 174718 (2006).

[50] H. Kondo, H. Kino, J. Nara, T. Ozaki, and T. Ohno, *Contact-structure dependence of transport properties of a single organic molecule between Au electrodes*, Phys. Rev. B **73**, 235323 (2006).

[51] R. B. Pontes, A. R. Rocha, S. Sanvito, A. Fazzio, and A. J. R. da Silva, *Ab Initio Calculations of Structural Evolution and Conductance of Benzene-1,4-dithiol on Gold Leads*, ACS Nano **5**, 795 (2011).

[52] Y. Xue and M. A. Ratner, *Microscopic study of electrical transport through individual molecules with metallic contacts. I. Band lineup, voltage drop, and high-field transport*, Phys. Rev. B **68**, 115406 (2003).

[53] Y. Xue and M. A. Ratner, *Microscopic study of electrical transport through individual molecules with metallic contacts. II. Effect of the interface structure*, Phys. Rev. B **68**, 115407 (2003).

[54] J. C. Love, L. A. Estroff, J. K. Kriebel, R. G. Nuzzo, and G. M. Whitesides, *Self-Assembled Monolayers of Thiolates on Metals as a Form of Nanotechnology*, Chem. Rev. **105**, 1103 (2005).

[55] R. Hoft, M. Ford, and M. Cortie, *Prediction of increased tunneling current by bond length stretch in molecular break junctions*, Chem. Phys. Lett. **429**, 503 (2006).

[56] L. Romaner, G. Heimel, M. Gruber, J.-L. Brédas, and E. Zojer, *Stretching and Breaking of a Molecular Junction*, Small **2**, 1468 (2006).

[57] G. te Velde and E. J. Baerends, *Precise density-functional method for periodic structures*, Phys. Rev. B **44**, 7888 (1991).

[58] G. Wiesenekker and E. J. Baerends, *Quadratic integration over the three-dimensional Brillouin zone*, J. Phys.: Condens. Matter **3**, 6721 (1991).

[59] N. V. Smith, C. T. Chen, and M. Weinert, *Distance of the image plane from metal surfaces*, Phys. Rev. B **40**, 7565 (1989).

[60] B. Cordero, V. Gomez, A. E. Platero-Prats, M. Reves, J. Echeverria, E. Cremades, F. Barragan, and S. Alvarez, *Covalent radii revisited*, Dalton Trans. pp. 2832–2838 (2008).

[61] J. D. Barr, C. A. Stafford, and J. P. Bergfield, *Effective field theory of interacting π electrons*, Phys. Rev. B **86**, 115403 (2012).

7

EVALUATING TRANSPORT APPROXIMATIONS

The transport properties of nanoscale systems are notoriously expensive to calculate, which makes it tempting to use rather drastic approximations. However, few studies have compared the accuracy and performance of the different schemes in use. In this chapter we put the commonly-used wide-band limit approximation, and more sophisticated post–self-consistent transport calculations under the microscope, to see how they fare when compared to fully self-consistent transport calculations.

Parts of this chapter have been submitted to J. Chem. Phys.

In recent years, approaches to molecular transport based on density-functional theory (DFT) in combination with the non-equilibrium Green's function formalism (NEGF) have received considerable attention in the literature, driven by the rapid progress in experimental work on realizing molecular nano-devices.[1–4] A number of codes[5–11] have been developed, including our own implementation within the ADF/BAND quantum chemistry package.[12–16]

As the methods have matured, scalability and the computational effort involved in studying progressively larger molecular systems have become important issues. In recent years, the focus of the field has shifted towards systems where the molecule predominantly determines the transport properties, rather than the metal-molecule interface. Examples include systems where quantum interference plays a role.[17–20] This necessitates accurate quantum chemical modeling of the molecule, while the details of the electrodes may be of lesser importance to transport. Several approximations exist that trade sophistication for efficiency in the description of the electrodes,[21–25] but to the best of our knowledge, there have been no systematic studies of the quality of the results obtained with such approximations.

In this chapter we consider methods that treat the molecule at the *ab initio* level of quantum chemical DFT, but vary in the treatment of the electrodes. The most common approach is to use a wide-band limit (WBL) description, which amounts to taking the density of states (DOS) in the electrodes to be constant (see below). In order to account for the effects of the metal-molecule interface, parts of the electrodes can be included in the DFT calculation, resulting in a so-called "extended molecule."

In the more sophisticated approaches the effect of semi-infinite electrodes is included via self-energies in the self-consistent DFT calculation of the extended molecule. However, this requires the use of a DFT package capable of transport calculations. A common simplifying approach is therefore to perform the DFT calculations on the extended molecule without the self-energies, and only add them afterwards in the calculation of the transport properties. This has the advantage that it can be implemented as a post-processing step which does not require modification of the underlying DFT code (*e.g.* the ARTAIOS package[26]). Since the open-system character of an extended molecule with self-energies can lead to convergence problems, the closed-system character of this approximation may be advantageous.

Here, we explore the limits of these approximations, both with and without a bias voltage applied over the molecular junction. We first briefly review the transport formalism which is based on non-equilibrium Green's functions (NEGF). We then introduce the hierarchy of approximations we consider, and compare their computational expense. We evaluate their quality by applying the methods to several junctions containing on phenyl-derivatives, both fully-conjugated and with broken conjugation.

Although the WBL approximation works well for systems with bulk metal electrodes, it is known to break down for one-dimensional systems. We will show this explicitly in the case of a monatomic chain, but this can be an issue in other (quasi-) one-dimensional systems such as carbon nanotubes. Our results provide an understanding of the applicability and performance of the various approximations for different types of metal-molecule junctions.

7.1 THE WIDE-BAND LIMIT

As we have outlined previously, in transport theory the device is typically partitioned into electrodes (or leads) and a transport region between them, *cf.* Figs. 3.1–3.2. In the Landauer-Büttiker formalism, the current through a junction is given by

$$I = \frac{2e}{h} \int \mathrm{d}\epsilon \; [f_L(\epsilon, \mu_L) - f_R(\epsilon, \mu_R)]\, T(\epsilon)\,, \tag{7.1}$$

where $f_L(\epsilon)$ and $f_R(\epsilon)$ are the Fermi distributions in the left and right electrodes respectively. These are kept at chemical potentials differing by the bias voltage $V_b = (\mu_L - \mu_R)/e$. $T(\epsilon)$ is the transmission, which is given by:

$$T(\epsilon) = \mathrm{Tr}\left[\boldsymbol{\Gamma}_L(\epsilon)\, \boldsymbol{G}(\epsilon)\, \boldsymbol{\Gamma}_R(\epsilon)\, \boldsymbol{G}^\dagger(\epsilon)\right], \tag{7.2}$$

where $\boldsymbol{\Gamma}_L(\epsilon)$ and $\boldsymbol{\Gamma}_R(\epsilon)$ are the couplings to the electrodes and $\boldsymbol{G}(\epsilon)$ and $\boldsymbol{G}^\dagger(\epsilon)$ are the retarded and advanced Green's functions of the transport region, respectively. The retarded Green's function is

$$\boldsymbol{G}(\epsilon) = \left[\epsilon \boldsymbol{S} - \boldsymbol{H} - \boldsymbol{\Sigma}_L(\epsilon) - \boldsymbol{\Sigma}_R(\epsilon)\right]^{-1}, \tag{7.3}$$

where $\boldsymbol{S}$ is the overlap matrix of the molecule, $\boldsymbol{H}$ the Hamiltonian, and $\boldsymbol{\Sigma}_L(\epsilon)$ and $\boldsymbol{\Sigma}_R(\epsilon)$ are the self-energies due to the contacts. They can be written as:[27,28]

$$\boldsymbol{\Sigma}_{L,R}(\epsilon) = \boldsymbol{\Lambda}_{L,R}(\epsilon) - \frac{\mathrm{i}}{2}\boldsymbol{\Gamma}_{L,R}(\epsilon)\,, \tag{7.4}$$

where both $\boldsymbol{\Lambda}_{L,R}$ and $\boldsymbol{\Gamma}_{L,R}$ are real (Hermitian). The real part of the self-energy, $\boldsymbol{\Lambda}(\epsilon)$, induces a shift of the orbital resonances (*i.e.* the poles of the Green's function), while $\boldsymbol{\Gamma}(\epsilon)$ leads to a broadening. In the case of a monatomic chain, the self-energies can be calculated analytically (*cf.* Appendix C.3).

It seems natural to identify the transport region with the molecule, in which case the self-energy is defined on the molecule, specifically near its interface with the metal. However, the self-energy then strongly depends on the contact geometry of the junction and the metal is not allowed to deform its electron density self-consistently near the interface in the presence of the molecule.

Therefore, it is common to include part of the electrodes in the transport region, which becomes a so-called "extended molecule" as introduced in Chapter 3. This defining the self-energy near a metal-metal interface deeper inside the contacts. This makes it possible to use a bulk calculation for the leads to obtain the self-energies, which has the added benefit that they only have to be calculated once for a given electrode, and do not depend on the molecule.

The imaginary part of the self-energy has the following form:[27,28]

$$\Gamma_{nm}^{L,R}(\epsilon) = 2\pi \sum_k V_{k,n}^{L,R}\, V_{k,m}^{L,R*}\, \delta\left(\epsilon - \epsilon_k\right) , \tag{7.5}$$

where $V_{k,n}^{L,R}$ couples an electron with momentum state k in the electrodes to an orbital n on the molecule. Near the Fermi energy, $V_{k,n}^{L,R}$ are generally slowly-varying functions of the momentum k.[29] We can therefore write:

$$\Gamma_{nm}^{L,R}(\epsilon) \approx 2\pi V_n^{L,R}\, V_m^{L,R*} \sum_k \delta\left(\epsilon - \epsilon_k\right) = 2\pi V_n^{L,R}\, V_m^{L,R*} \rho(\epsilon) , \tag{7.6}$$

where $\rho(\epsilon)$ is the DOS in the electrode. For metals such as gold, the DOS is approximately constant near the Fermi energy. To a first approximation, we can therefore take $\mathbf{\Gamma}$ to be independent of ϵ. In combination with neglecting the level-shift $\mathbf{\Lambda}(\epsilon)$, we obtain the "wide-band limit approximation" (WBL). For a non-orthogonal basis, this yields a self-energy of the form:

$$\mathbf{\Sigma}_{L,R} = -\frac{\mathrm{i}}{2}\Gamma_{L,R}\,\boldsymbol{S} , \tag{7.7}$$

where we have effectively replaced the complexity of the full self-energy by a single parameter $\Gamma_{L,R}$. Although $\Gamma_L \neq \Gamma_R$ in general, in this paper we take them to be the same.

Computationally, the main advantage of the WBL is that the eigenspace of the Green's function (Eq. (7.3)) becomes independent of the energy ϵ.[a] We can therefore diagonalize the Green's function before evaluating the transport properties, dramatically reducing the computational cost.

7.2 TRANSPORT METHODS

We evaluate four different approximations by comparing their results for a typical metal-molecule-metal junction, within the NEGF+DFT approach. In decreasing order of sophistication and computational expense, these are:

1. **Full-SCF**: A fully self-consistent transport calculation, where the full self-energies of the metal electrodes are taken into account during the calculation. This corresponds to the steady state of an open system. This approach allows us to include a bias voltage by varying the chemical potential of the electrodes.
2. **Post-SCF**: A calculation of a closed system, consisting only of the extended molecule, which includes a finite part of the electrodes. The self-energy of the semi-infinite electrodes is then added *after* reaching convergence, in order to enable the calculation of transport properties.

---

[a] Technically, this only holds for an orthonormal basis, but it is always possible to transform to such a basis using Löwdin orthogonalization.[30]

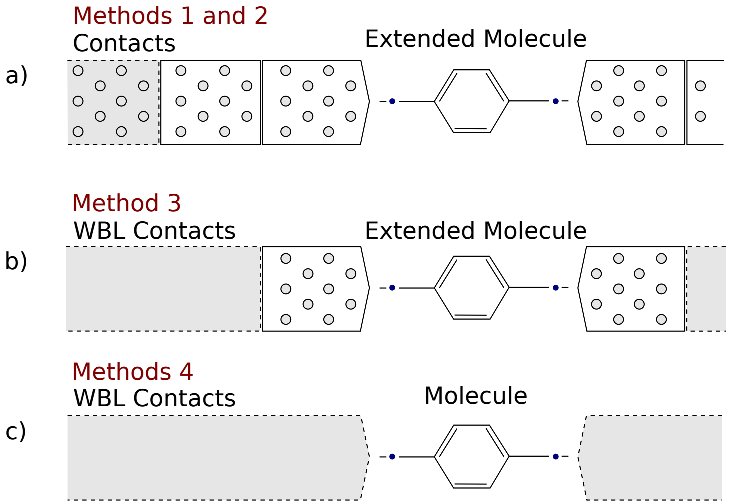

Figure 7.1: Illustration of geometries corresponding to the four approximations discussed in section 7.2. a) Full- and Post-SCF methods, with bulk contacts attached to extended molecule region, and full $\mathbf{\Sigma}$'s corresponding to semi-infinite contacts behind these. b) WBL-Metal approach, with WBL $\mathbf{\Sigma}$'s attached to the extended molecule at a metal-metal interface. c) WBL-Molecule approach with WBL $\mathbf{\Sigma}$'s attached directly to the molecule.

3. **WBL-Metal**: Similar to Post-SCF, but instead of using the full self-energies in the calculation of the transport properties, the wide-band limit is employed at a metal-metal interface in the electrode.

4. **WBL-Molecule**: Similar to WBL-Metal, but here the wide-band self-energies are coupled directly to the molecule, and no metal atoms are actually present in the calculation.

The corresponding implications for the geometry of the models are illustrated in Fig. 7.1.

In the Full-SCF method the bias voltage is applied by varying the chemical potential in the electrodes and simultaneously introducing an electric field inside the junction. Because the calculation is done self-consistently, this yields the correct potential profile in the junction. This cannot be achieved by the other methods, but the effect of the bias voltage can be approximated by introducing an electric field over the molecule. In practice this only works for the isolated molecule, since applying it over an extended molecule tends to lead to convergence difficulties. Finite-bias calculations are therefore only feasible with the Full-SCF and WBL-Molecule methods.

In molecular junctions the magnitude of the field is typically of the order of 1 V/nm. Since this is much smaller than the internal field of the molecule, the perturbation of the Hamiltonian is effectively linear in the field. In practice, the

Method	Electrodes	(Extended) Molecule	Transport Properties
Full-SCF	36 min	2.5 hrs	33 min
Post-SCF	23 min	4 min	16 min
WBL-Metal	–	4 min	13 s*
WBL-Molecule	–	7 s	1 s*

TABLE 7.1: Comparison of computational expense of the four approaches applied to a typical molecular junction. All calculations have been performed on an 8 core 3 GHz Intel Xeon workstation. *The calculations of the transport properties with the WBL methods have been performed on a single core.

Hamiltonian therefore only has to be calculated twice: at zero and at maximum bias. For other voltages the Hamiltonian can then be obtained by linear interpolation. Since the cost of the transport calculation is negligible in the case of WBL-Molecule (*cf.* Table 7.1), this makes efficient evaluation of the full current-voltage (I-V) characteristics feasible.

Table 7.1 summarizes the computational expense of the four methods for a typical molecular junction (illustrated in Fig. 7.2a and discussed in the next section). Timings for the electrode calculations include both DFT and the evaluation of the self-energies. These are not required for the WBL methods, and for the Full-SCF and Post-SCF calculations only need to be performed once, and are therefore never a bottleneck. The difference in run time between Full-SCF and Post-SCF is due to the underlying DFT code (*cf.* Appendix 7.5 for details).

There are large differences between the timings of the (extended) molecule calculations. The difference between Full-SCF and Post-SCF is caused by the fact that calculating the electron density of an open system requires integrating the Green's function at every cycle in the DFT calculation.[16] The remainder of the difference is again due to the underlying DFT code. The Post-SCF and WBL-Metal methods use the same calculation of the extended molecule and therefore have the same timings, while the difference with the WBL-Molecule method is due to the absence of the electrodes.

The calculation of the transport properties is similar for Full-SCF and Post-SCF, resulting in comparable timings. In the WBL methods, on the other hand, the Green's function can be diagonalized independent of energy (*cf.* section 7.1), leading to a speedup of more than two orders of magnitude.

We will now compare the quality of the different methods by applying them to typical molecular junctions with gold (Au) electrodes, and investigate the effect of the bias voltage on the transmission. For molecular junctions with bulk electrodes both WBL methods give good agreement with the more sophisticated methods. However, in the case of one-dimensional systems it breaks down, as we will demonstrate explicitly for a monatomic aluminum (Al) chain.

7.3 METAL-MOLECULE-METAL JUNCTIONS

Fig. 7.2 shows the transmission of a single benzenedithiol (BDT) molecule sandwiched between two Au FCC (111) surfaces. 27 Au atoms are included on either side in the extended molecule (Fig. 7.2a). In order to approximate the geometric configuration of single-molecule break-junction experiments, we do not employ periodic boundary conditions (PBCs), but rather use needle-like ("non-PBC") electrodes,[16] as illustrated in Fig. 7.2a, and previously discussed in Chapter 3. We do however, briefly consider the difference in the DOS between these cases in Fig. 7.2b.

The Full-SCF calculation (black lines in the panels of Fig. 7.2a) shows a broad peak structure slightly below the Fermi energy (set to 0 eV), corresponding to the HOMO and lower orbitals, and a narrower peak for the LUMO. The HOMO-LUMO gap in the transmission is approximately 2.5 eV. This transmission is typical for BDT calculations in the literature.[6,7,16,31,32] The red line shows the Post-SCF result, where the HOMO-LUMO gap is the same, but the peaks are slightly broadened with respect to the Full-SCF calculation.

The blue line in Fig. 7.2a shows the transmission calculated with the WBL-Metal approach. The peak structure of the HOMOs and the LUMO corresponds well to the Full-SCF and Post-SCF results, but there is a slight over-estimation of the HOMO-LUMO gap.

The reason that the WBL works well in this particular case is that the density of states of bulk Au is essentially constant near the Fermi energy. This is shown in Fig. 7.2b (red line). Although for non-PBC contacts the DOS (green line) does show some peak structure near the Fermi energy reminiscent of the van Hove singularities occurring in one-dimensional systems (*cf.* Appendix C.3), the self-energy of the contacts is nearly constant (Fig. 7.2b). At higher energies (above 2 eV), the DOS and self-energies are no longer approximately constant, and the transmissions of the different approaches begin to diverge.

In the WBL, the magnitude of the imaginary part, which causes a broadening of the peaks, determines the quality of the approximation. This is shown in Fig. 7.3, where we have plotted the transmission for several values of Γ. We find that a value of 2 eV yields the best results. Note that this fit parameter corresponds to the coupling of a metal-metal interface, and is therefore independent of the molecule in the junction.

Finally, the bottom left panel of Fig. 7.2a (green line) shows the WBL-Molecule result. Although the transmission reproduces the double-peak structure of the HOMOs and the sharper peak of the LUMO, but the gaps between the orbitals are overestimated (relative to a Full-SCF calculation) by roughly a factor of 2. This is a result of the fact that the calculation is performed on a molecule in gas-phase. This misses hybridization of the molecular levels with the electrodes, which is found to significantly reduce the gap in the other approaches. Note also that, by omitting the electrodes, in WBL-Molecule calculations there is no clear definition of the Fermi energy; hence the transmission has been shifted to align the HOMO-peak with that of the Full-SCF calculation.

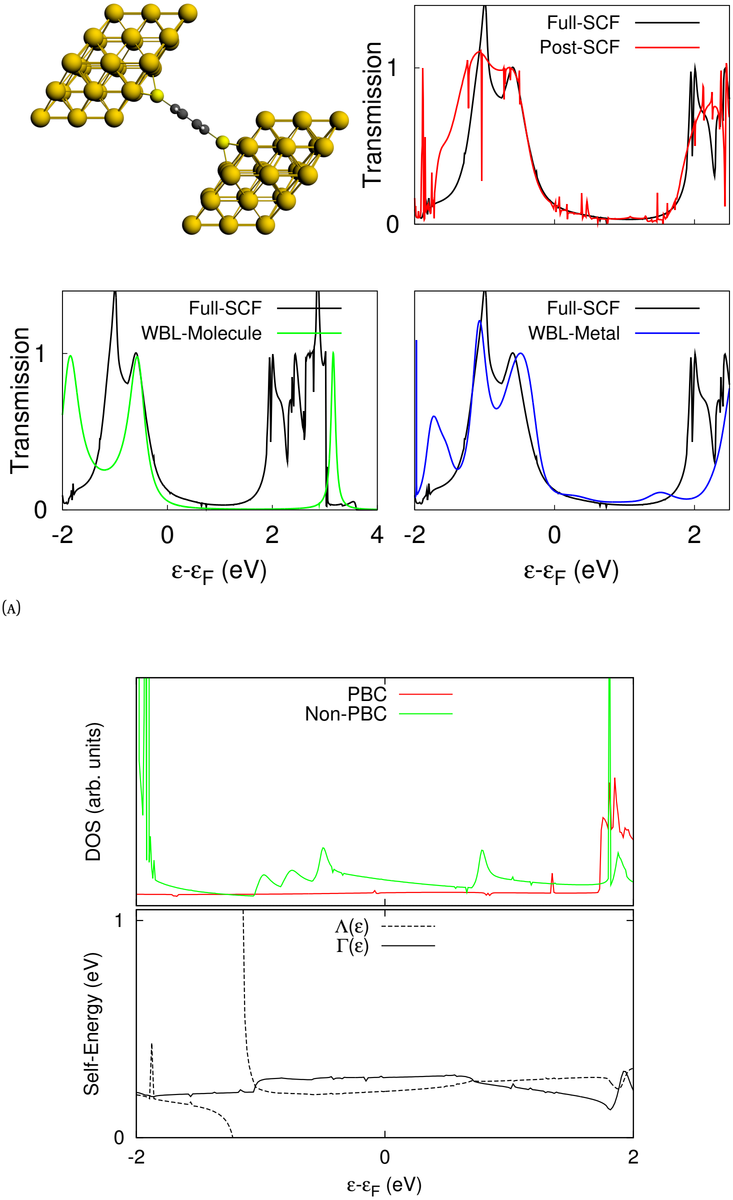

(A)

(B)

Figure 7.2: (a) Transmission of an Au-BDT-Au junction (top left) calculated with four different approximations (see text). The Fermi energy is set to 0 eV, and the WBL-Molecule transmission is shifted by −0.5 eV to align the HOMO peak with that of the Full-SCF calculation. Γ = 2 eV the WBL-Metal and Γ = 0.5 eV in the WBL-Molecule calculations. (b) **Top:** DOS of bulk Au calculated with and without periodic boundary conditions. **Bottom:** Magnitude of the real and imaginary parts of the self-energy of bulk Au without PBCs. The magnitude is defined as the average of the diagonal elements of $\mathbf{\Sigma}(\epsilon)$.

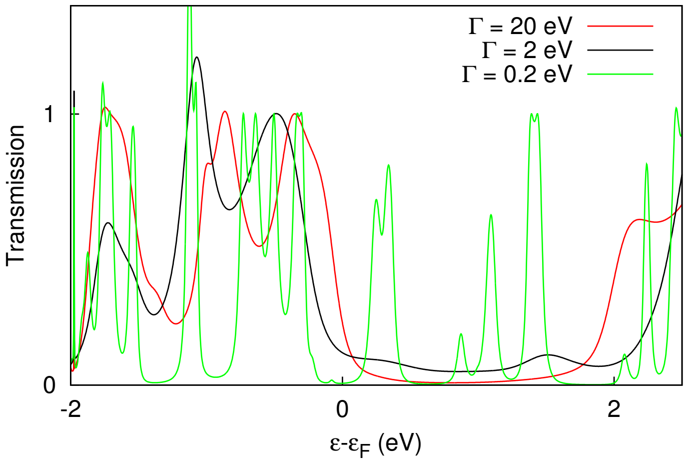

Figure 7.3: Transmission of BDT calculated with the WBL-Metal approximation for different values of the (scalar) coupling strength Γ (compare Fig. 7.2a).

For small molecules, the transmission is dominated by the metal-molecule interface, and WBL-Molecule is a poor approximation. For larger molecules, especially ones where the conductance is small (for example, due to broken conjugation), the transmission is instead dominated by properties of the molecule, and the use of WBL-Molecule becomes appropriate. This is especially clear in the case of finite-bias calculations.

Fig. 7.4 shows the transmission of two oligophenylene-ethynylene (OPE-2) derivatives as a function of bias voltage, calculated with the Full-SCF and WBL-Molecule methods. On the left, the transmission of the fully conjugated OPE-2 molecule is shown. In the Full-SCF calculation two HOMO peaks are visible near the Fermi energy. Upon application of a bias voltage, the peaks move apart and their magnitude decreases. This effect is not reproduced in the WBL-Molecule calculation, where only the HOMO peak shifts and drops in magnitude. As with BDT, the WBL-Molecule approximation overestimates the splitting between the two peaks.

When we break the conjugation (right-hand side of Fig. 7.4c), only one peak is visible close to the Fermi energy at zero bias, which splits into two peaks for higher bias voltages. Moreover, even at zero bias, the transmission is significantly less than one. This effect is reproduced in the WBL-Molecule calculation, although the height of the peak is overestimated.

These differences between the two cases can be understood by considering how the bias voltage is distributed over the junction. For a conjugated molecule where the π-electron cloud is easily deformed, resulting in a high polarizability, the voltage drop

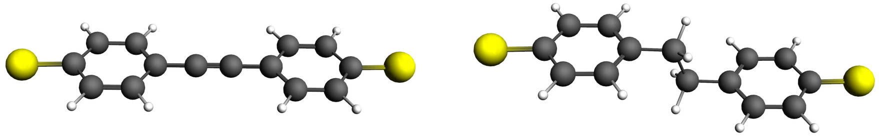

(a) OPE-2 (Conjugated)

(b) OPE-2 (Broken-Conjugation)

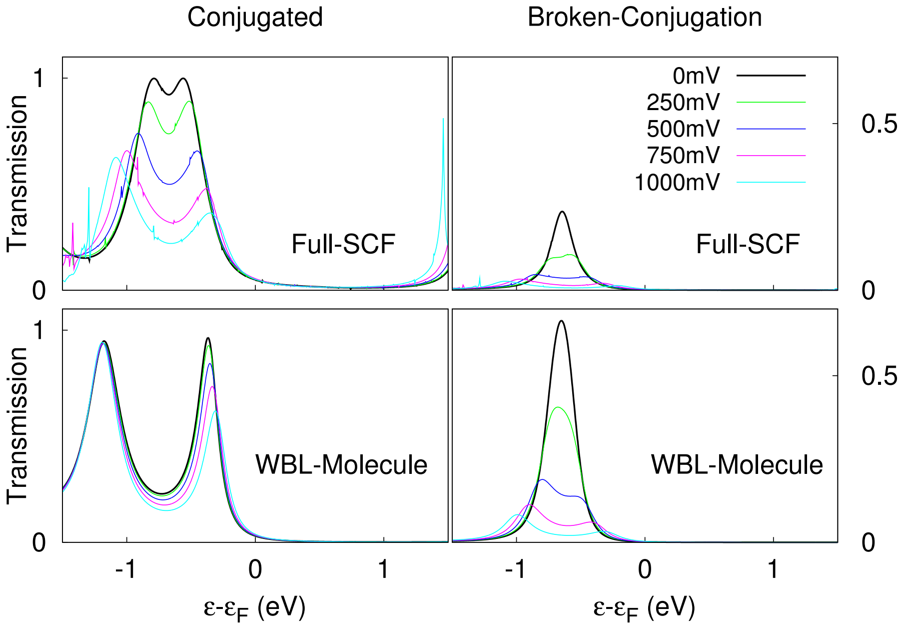

(c)

Figure 7.4: Transmissions under bias through (a) conjugated and (b) non-conjugated variants of the OPE-2 molecule. (c) Left panels show transmissions for conjugated molecule using the Full-SCF (top) and WBL-Molecule (bottom) approaches. Right panels show the same for broken conjugation, where only a single resonance is visible and the WBL-Molecule approach performs better.

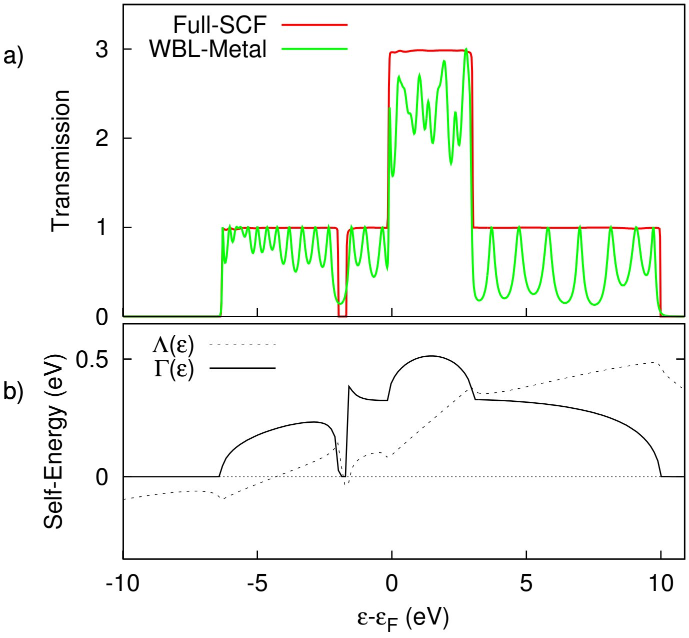

Figure 7.5: (a) Transmission of a monatomic Al chain, calculated with both the Full-SCF and WBL-Metal approaches. The latter uses a coupling of $\Gamma = 0.5$ eV. (b) Real and imaginary parts of the trace of the self-energy, showing a nearly-perfect superposition of the behavior discussed in Appendix C.3.

7

occurs at the metal-molecule interface. Since this interface is not taken into account in the WBL-Molecule calculation, its results do not agree with the Full-SCF approach. When we break the conjugation, we introduce a barrier, and the voltage drop will occur primarily inside the molecule.[33] Since the molecule is accurately modeled in the WBL-Molecule approach, the Full-SCF result is qualitatively reproduced.

Analysis of the levels involved in transport reveals that the HOMO and HOMO-1 are composed of bonding and anti-bonding combinations of orbitals located on of the phenyl rings. In the case of the conjugated OPE-2, the coupling is strong (388 meV for WBL-Molecule), and the peaks are split at zero bias. In the case of broken conjugation, the coupling is much weaker (70 meV), resulting in the appearance of a single peak at low bias. Additionally the low coupling causes a reduction in the magnitude of the transmission.

7.4 Monatomic Chains

In the case of bulk contacts the WBL-Metal approximation shows good quantitative agreement with the Full-SCF approach. However, this approximation breaks down in the limit of one-dimensional electrodes. In this case the DOS is no longer approximately constant, but shows Van Hove singularities.[34] We show this explicitly for a monatomic chain, which can be calculated analytically in the tight-binding approximation (*cf.* Appendix C.3).

Fig. 7.5a shows the transmission of a monatomic aluminum (Al) chain, calculated with the Full-SCF (red line) and WBL-Metal (green line) approaches. The Full-SCF transmission shows two plateaus, one at a transmission of 1, with a small dip at -2 eV, and one at a transmission of 3. Although the WBL-Metal approach reproduces the maxima of the transmission and the dip at -2 eV, it does not reproduce the plateaus, but it oscillates instead.

This behavior can be understood by considering the self-energy shown in Fig. 7.5b. For each plateau, $\Lambda(\epsilon)$ has a linear, and $\Gamma(\epsilon)$ a semi-elliptical energy-dependence (*cf.* Appendix C.3). $\Lambda(\epsilon)$ induces an energy-dependent shift of the peaks which merges them into a plateau. Although $\Gamma(\epsilon)$ is approximately constant at its maximum, the fact that it drops to zero at the band edge of the chain is responsible for the step-function behavior of the transmission. Neither of these effects is captured by the wide-band limit approach, and so the transmission remains a series of broadened peaks.

7.5 CONCLUSIONS

In conclusion, we have compared four different approaches commonly used in transport calculations, which vary in sophistication and computational expense. The cheapest of these is the wide-band limit approximation for an isolated molecule (WBL-Molecule), for which the total calculation takes only a few seconds on a modern workstation. Including part of the electrodes in the extended molecule (WBL-Metal) increases the computational cost of the DFT calculation to a few minutes. When the self-energies of the electrodes are included in the transport calculation in a non self-consistent way (Post-SCF), the latter becomes the bottleneck. Due to the open nature of the system, including the self-energies in the DFT calculation as well (Full-SCF) can increase the computation time to several hours.

The Full-SCF approach has the benefit that it takes the metal-molecule interface into account in a self-consistent way, and allows for the application of a finite bias voltage. The Post-SCF approach quantitatively reproduces the zero-bias transmission, but does not allow for finite bias-voltage calculations. The WBL-Metal approach also gives rather good results for a molecule coupled to three-dimensional electrodes, but it breaks down for one-dimensional electrodes. Finally, the WBL-Molecule approach qualitatively reproduces the main features of the transmission, and in cases where the transmission is dominated by the properties of the molecule, can even reproduce the bias-voltage dependence. However, the estimated energy-gaps can be off by a significant amount due to the omission of interface effects such as chemisorption.

In practice we recommend starting with the WBL-Molecule approach as it is computationally very cheap on any modern workstation. Additionally, lack of hybridization of the orbitals with the electrodes greatly simplifies the analysis of the features in the transmission. This is especially important for molecules which are expected to exhibit interference effects.

For quantitative predictions, the WBL-Metal, Post-SCF and Full-SCF approaches give similar results at zero bias. If a dedicated transport code is available, we recommend the Full-SCF approach (which also accounts for the application of a bias voltage); if not, the other approaches can be implemented as post-processing steps after a conventional DFT calculation. However, with WBL-Metal care must be taken when modeling junctions using 1D or 2D electrodes (such as carbon nanotubes[35,36] or graphene[37]), and more generally electrodes with a more complicated electronic structure near the Fermi energy.

COMPUTATIONAL DETAILS

All DFT calculations in this chapter have been performed with the Amsterdam Density Functional (ADF) quantum-chemistry package,[12–16] using the LDA exchange-correlation potential.[b] A single-ζ (SZ) basis-set was used for the electrodes, and a triple-ζ polarized (TZP) basis-set was used for the molecule, although we find similar results with a DZP basis.

For the electrodes, we use non-periodic contacts with a FCC (111) surface consisting of 3×3 Au atoms (*cf.* Fig. 7.2a). The thiolated molecules are situated perpendicular to this surface above a hollow site with a Au–S distance of 2.40 Å.

We have implemented the Full-SCF method in the periodic band-structure code BAND, which is a part of ADF. The Post-SCF and WBL-Metal methods have both been implemented in the GREEN module in ADF, while the WBL-Molecule method is a simple Python program. Complementary Post-SCF and WBL-Metal method implementations are also present in the transport component in the BAND code.

In the Full- and Post-SCF methods, the self-energies are obtained from a calculation of bulk electrodes. These are modeled as a stack of principal layers, each of which consists of three 3×3 atomic layers. In the Post-SCF and WBL-Metal calculations, the extended molecule includes a principal layer on either side of the molecule, for a total of 54 Au atoms. For technical reasons, a Full-SCF calculation contains 90 Au atoms.[16] Finally, in the WBL-Molecule approach, the WBL self-energies are coupled directly to the p_z orbital on the thiols, which our studies indicate to be the dominant charge-injection pathway into the molecular system.

---

[b] Using the PBE GGA potential shifts the transmission slightly, but otherwise leaves the spectrum unchanged.

REFERENCES

[1] N. Agraït, A. L. Yeyati, and J. M. van Ruitenbeek, *Quantum properties of atomic-sized conductors*, Phys. Rep. **377**, 81 (2003).

[2] L. Venkataraman, J. E. Klare, C. Nuckolls, M. S. Hybertsen, and M. L. Steigerwald, *Dependence of single-molecule junction conductance on molecular conformation*, Nature **442**, 904 (2006).

[3] E. A. Osorio, K. O'Neill, M. Wegewijs, N. Stuhr-Hansen, J. Paaske, T. Bjørnholm, and H. S. J. van der Zant, *Electronic excitations of a single molecule contacted in a three-terminal configuration*, Nano Lett. **7**, 3336 (2007).

[4] S. Quek, L. Venkataraman, H. Choi, S. Louie, M. Hybertsen, and J. Neaton, *Amine–Gold Linked Single-Molecule Circuits: Experiment and Theory*, Nano Lett. **11**, 3477 (2007).

[5] J. Taylor, H. Guo, and J. Wang, *Ab initio modeling of quantum transport properties of molecular electronic devices*, Phys. Rev. B **63**, 245407 (2001).

[6] Y. Xue, S. Datta, and M. A. Ratner, *First-principles based matrix Green's function approach to molecular electronic devices: general formalism*, Chem. Phys. **281**, 151 (2002).

[7] F. Evers, F. Weigend, and M. Koentopp, *Coherent transport through a molecular wire: DFT calculation*, Physica E: Low-dimensional Systems and Nanostructures **18**, 255 (2003), 23rd International Conference on Low Temperature Physics (LT23).

[8] Z. Qian, R. Li, S. Hou, Z. Xue, and S. Sanvito, *An efficient nonequilibrium Green's function formalism combined with density functional theory approach for calculating electron transport properties of molecular devices with quasi-one-dimensional electrodes*, J. Chem. Phys. **127**, 194710 (2007).

[9] M. Brandbyge, J.-L. Mozos, P. Ordejón, J. Taylor, and K. Stokbro, *Density-functional method for nonequilibrium electron transport*, Phys. Rev. B **65**, 165401 (2002).

[10] K. Stokbro, J. Taylor, M. Brandbyge, and P. Ordejón, *TranSIESTA – A Spice for Molecular Electronics*, Ann. N.Y. Acad. Sci. **1006**, 212 (2003).

[11] A. R. Rocha, V. M. García-Suárez, S. Bailey, C. Lambert, J. Ferrer, and S. Sanvito, *Spin and molecular electronics in atomically generated orbital landscapes*, Phys. Rev. B **73**, 085414 (2006).

[12] C. Fonseca Guerra, J. G. Snijders, G. te Velde, and E. J. Baerends, *Towards an order-N DFT method*, Theor. Chem. Acc. **99**, 391 (1998).

[13] G. te Velde, F. Bickelhaupt, S. van Gisbergen, C. Fonseca Guerra, E. Baerends, J. Snijders, and T. Ziegler, *Chemistry with ADF*, J. Comput. Chem. **22**, 931 (2001).

[14] G. te Velde and E. J. Baerends, *Precise density-functional method for periodic structures*, Phys. Rev. B **44**, 7888 (1991).

[15] G. Wiesenekker and E. J. Baerends, *Quadratic integration over the three-dimensional Brillouin zone*, J. Phys.: Condens. Matter **3**, 6721 (1991).

[16] C. J. O. Verzijl and J. M. Thijssen, *A DFT-based Molecular Transport Implementation in ADF/BAND*, J. Phys. Chem. C (2012), accepted.

[17] M. Ernzerhof, M. Zhuang, and P. Rocheleau, *Side-chain effects in molecular electronic devices*, J. Chem. Phys. **123**, 134704 (2005).

[18] G. C. Solomon, D. Q. Andrews, T. Hansen, R. H. Goldsmith, M. R. Wasielewski, R. P. Van Duyne, and M. A. Ratner, *Understanding quantum interference in coherent molecular conduction*, J. Chem. Phys. **129**, 054701 (2008).

[19] J. Rincón, K. Hallberg, A. A. Aligia, and S. Ramasesha, *Quantum Interference in Coherent Molecular Conductance*, Phys. Rev. Lett. **103**, 266807 (2009).

[20] T. Markussen, J. Schiötz, and K. S. Thygesen, *Electrochemical control of quantum interference in anthraquinone-based molecular switches*, J. Chem. Phys. **132**, 224104 (2010).

[21] M. Di Ventra, S. T. Pantelides, and N. D. Lang, *First-Principles Calculation of Transport Properties of a Molecular Device*, Phys. Rev. Lett. **84**, 979 (2000).

[22] M. Di Ventra and N. D. Lang, *Transport in nanoscale conductors from first principles*, Phys. Rev. B **65**, 045402 (2001).

[23] S.-H. Ke, H. U. Baranger, and W. Yang, *Electron transport through molecules: Self-consistent and non-self-consistent approaches*, Phys. Rev. B **70**, 085410 (2004).

[24] F. Evers and A. Arnold, *CFN Lectures on Functional Nanostructures*, vol. 2 of *Springer Lecture Notes in Physics* (Springer, 2006), 1st ed.

[25] A. Arnold, F. Weigend, and F. Evers, *Quantum chemistry calculations for molecules coupled to reservoirs: Formalism, implementation, and application to benzenedithiol*, J. Chem. Phys. **126**, 174101 (2007).

[26] C. Herrmann and G. C. Solomon, Tech. Rep., Northwestern University (2010).

[27] A.-P. Jauho, N. S. Wingreen, and Y. Meir, *Time-dependent transport in interacting and noninteracting resonant-tunneling systems*, Phys. Rev. B **50**, 5528 (1994).

[28] H. Haug and A.-P. Jauho, *Quantum Kinetics in Transport and Optics of Semi-conductors* (Springer-Verlag, 1997), 1st ed.

[29] Y. Meir and N. S. Wingreen, *Landauer formula for the current through an interacting electron region*, Phys. Rev. Lett. **68**, 2512 (1992).

[30] P.-O. Löwdin, *On the Non-Orthogonality Problem Connected with the Use of Atomic Wave Functions in the Theory of Molecules and Crystals*, J. Chem. Phys. **18**, 365 (1950).

[31] K. Stokbro, J. Taylor, M. Brandbyge, J. L. Mozos, and P. Ordejón, *Theoretical study of the nonlinear conductance of di-thiol benzene coupled to Au(111) surfaces via thiol and thiolate bonds*, Comp. Mat. Sci. **27**, 151 (2003).

[32] H. Kondo, H. Kino, J. Nara, T. Ozaki, and T. Ohno, *Contact-structure dependence of transport properties of a single organic molecule between Au electrodes*, Phys. Rev. B **73**, 235323 (2006).

[33] Y. Xue and M. A. Ratner, *Microscopic study of electrical transport through individual molecules with metallic contacts. I. Band lineup, voltage drop, and high-field transport*, Phys. Rev. B **68**, 115406 (2003).

[34] N. Ashcroft and N. Mermin, *Solid State Physics* (Brooks/Cole, 1976).

[35] X. Guo, J. P. Small, J. E. Klare, Y. Wang, M. S. Purewal, I. W. Tam, B. H. Hong, R. Caldwell, L. Huang, S. O'Brien, et al., *Covalently Bridging Gaps in Single-Walled Carbon Nanotubes with Conducting Molecules*, Science **311**, 356 (2006).

[36] A. K. Feldman, M. L. Steigerwald, X. Guo, and C. Nuckolls, *Molecular Electronic Devices Based on Single-Walled Carbon Nanotube Electrodes*, Acc. Chem. Res. **41**, 1731 (2008).

[37] F. Prins, A. Barreiro, J. W. Ruitenberg, J. S. Seldenthuis, N. Aliaga-Alcalde, L. M. K. Vandersypen, and H. S. J. van der Zant, *Room-Temperature Gating of Molecular Junctions Using Few-Layer Graphene Nanogap Electrodes*, Nano Lett. **11**, 4607 (2011).

A

SURFACE GREEN'S FUNCTIONS

We give a more concrete picture of the recursion algorithm for obtaining the Green's function of the contacts' surface, which we use in order to derive the (mean-field) self-energies $\mathbf{\Sigma}_{1,2}(\epsilon)$ *of the semi-infinite contacts.*

The method described in this appendix has been implemented in the module `SGF` in the Amsterdam Density Functional (ADF) quantum chemistry package.[1,2]

Recall the key idea behind the method, previously discussed in §3.4: we describe a semi-infinite electrode in k–space using tight-binding representation of H^{KS}, with an infinite surface. We consider the metal as being composed of an infinite number of layers in space, and then find the relation between elements of the Green's function for 2^k and 2^{k+1} principal layers by recursively eliminating the layers in between. The following is then a restatement of the algorithm developed by Sancho *et al.*[3] and formulated by Henk & Schattke roughly as we now do.[4]

A.1 THE SURFACE GREEN'S FUNCTION ALGORITHM

This approach allows us to treat the structure of $\mathbf{\Sigma}$, which we obtain from the surface Green's functions, without approximations such as the wide-band limit or absorbing boundary conditions, and that it converges quickly, for realistic structures.

- The use of localized basis functions allows a restructured matrix corresponding to principal and adjacent (interacting) layers, as in Figs. 3.3–3.4:

$$\boldsymbol{H} = \begin{pmatrix} h & \tau & 0 & \cdots & \\ \tau^\dagger & h & \tau & 0 & \cdots \\ 0 & \tau^\dagger & h & \tau & 0 \\ \vdots & 0 & \ddots & \ddots & \ddots \end{pmatrix}$$

  We suppress (sub)matrix notation for simplicity, but each element in this matrix will in general be a submatrix of $\boldsymbol{H}$, rather than a scalar.

- Multiplying this by the (undetermined) matrix Green's function gives us a series of equations:

$$\begin{aligned} (\epsilon - h) g_{00} &= I + \tau\, g_{10} \\ (\epsilon - h) g_{10} &= \tau^\dagger g_{00} + \tau\, g_{20} \\ &\cdots \\ (\epsilon - h) g_{n0} &= \tau^\dagger g_{n-1,0} + \tau\, g_{n+1,0} \end{aligned}$$

- This inspires a 2^k layer recursion, starting with:

$$\left(\epsilon - h - \tau(\epsilon - h)^{-1}\tau^\dagger\right) g_{00} = I + \tau(\epsilon - h)^{-1}\tau\, g_{20}$$

  which allows us to link a surface Green's function to one two layers apart, which generalizes as follows. Note first that g_{20}, for example, is the correlation between layers 2 and 0 (the edge of the semi-infinite contact).

Applying that idea iteratively (starting from the correlation between layers 0 and n), we find:

$$\begin{aligned}
(\epsilon - h_i^*) g_{00} &= I + \alpha_i \, g_{2^i \cdot n, 0} && \longrightarrow \quad I \,, \\
(\epsilon - h_i) g_{2^i \cdot n, 0} &= \beta_i \, g_{2^i \cdot (n-1), 0} + \alpha_i \, g_{2^i \cdot (n+1), 0} && \longrightarrow \quad 0 \,, \\
(\epsilon - h_i) g_{2^i \cdot n, 2^i \cdot n} &= I + \beta_i \, g_{2^i \cdot (n-1), 2^i \cdot n} + \alpha_i \, g_{2^i \cdot (n+1), 2^i \cdot n} && \longrightarrow \quad I \,,
\end{aligned}$$

where the large i limits indicated by the arrows follow as the correlation between exponentially separated layers $g_{2^i \cdot n, 0}$ drops to zero. In this relation, the coefficients are recursively related as follows:

$$\begin{aligned}
h_0 &= h \,, \\
h_i^* &= h_{i-1}^* + \alpha_{i-1} (\epsilon - h_i^*)^{-1} \beta_{i-1} \,, \\
h_i &= h_{i-1} + \alpha_{i-1} (\epsilon - h_i)^{-1} \beta_{i-1} + \beta_{i-1} (\epsilon - h_i)^{-1} \alpha_{i-1} \,, \\
\alpha_0 &= \tau \,, \\
\alpha_i &= \alpha_{i-1} (\epsilon - h_i)^{-1} \alpha_{i-1} \,, \\
\beta_0 &= \tau^\dagger \,, \\
\beta_i &= \beta_{i-1} (\epsilon - h_i)^{-1} \beta_{i-1} \,.
\end{aligned}$$

On convergence, this yields $\boldsymbol{G}_c = \lim_{n\to\infty} g_{00}$ from which we construct self-energy matrices as in section 3.4: $\boldsymbol{\Sigma}_c \equiv (\epsilon \boldsymbol{S}_\tau^\dagger - \boldsymbol{\tau}^\dagger) \, \boldsymbol{G}_c \, (\epsilon \boldsymbol{S}_\tau - \boldsymbol{\tau})$.

REFERENCES

[1] C. Fonseca Guerra, J. G. Snijders, G. te Velde, and E. J. Baerends, *Towards an order-N DFT method*, Theor. Chem. Acc. **99**, 391 (1998).

[2] G. te Velde, F. Bickelhaupt, S. van Gisbergen, C. Fonseca Guerra, E. Baerends, J. Snijders, and T. Ziegler, *Chemistry with ADF*, J. Comput. Chem. **22**, 931 (2001).

[3] M. P. López-Sancho, J. M. López-Sancho, and J. Rubio, *Highly convergent schemes for the calculation of bulk and surface Green functions*, J. Phys. F: Met. Phys. **15**, 851 (1985).

[4] J. Henk and W. Schattke, *A subroutine package for computing Green's functions of relaxed surfaces by the renormalization method*, Comput. Phys. Commun. **77**, 69 (1993).

B

TRANSMISSION PEAK DECOMPOSITIONS

We determine the compositions of peaks in the transmission by using a fragment-decomposition technique, in which we project the eigenstates of the transport calculation onto the orbitals of a molecular fragment DFT calculation.

In order to understand the composition of the peaks present in the transmission through a junction, we represent the contribution of the fragments orbitals to the transmission peaks as follows.

From a DFT calculation of the fragment in BAND we store the eigensystem $\{\epsilon_j,\ |\phi_j\rangle\}$ of the fragment. We then perform the transport calculation in band, obtaining the transmission from

$$T(\epsilon) = \mathrm{Tr}\left[\ \mathbf{\Gamma}_1(\epsilon)\boldsymbol{G}(\epsilon)\mathbf{\Gamma}_2(\epsilon)\boldsymbol{G}^\dagger(\epsilon)\ \right]$$

which contains the Green's function

$$\boldsymbol{G}(\epsilon) = \Big(\epsilon\boldsymbol{S} - \boldsymbol{H} - (\mathbf{\Sigma}_1(\epsilon) + \mathbf{\Sigma}_2(\epsilon))\Big)^{-1} .$$

At the end of the SCF calculation, in addition to calculating transport properties, BAND also diagonalizes the (aligned) Fock matrix $\boldsymbol{H}$ to obtain a discrete set of transporting levels $\{\varepsilon_i,\ |\psi_i\rangle\}$.

We use the fragment-calculation functionality of the ADF package to project the subset of molecular levels of interest (HOMO, LUMO, *etc.*) onto the full set of transporting levels, and obtain a table of the projections $|\langle\psi_i|\phi_j\rangle|$, which are the "peak decompositions"[a] we referred to in the main text in Chapters 5 and 6. Each component $0 \leq |\langle\psi_i|\phi_j|\rangle \leq 1$ tells us to what extent the transporting level is composed of the $|\phi_j\rangle$, which we then visualize (*e.g.* in Fig. 5.4) as a stacked bar chart. The bar chart is overlaid onto the transmission, with each bar centered at the corresponding ε_i.

The correspondence between this discrete set of decompositions and the transmission $T(\epsilon)$ is not exactly one-to-one, given that the spectrum ε_i is that of the Fock matrix $\boldsymbol{H}$, while the running variable ϵ in the transmission corresponds to the spectrum of $\boldsymbol{G}(\epsilon)$, which includes the effect of $\mathbf{\Sigma}_1(\epsilon)$ and $\mathbf{\Sigma}_2(\epsilon)$. It is nonetheless a rather good correspondence, as verified by considering the levels $|\psi_i\rangle$ nearest the ϵ of a given peak in the transmission.

---

[a] Strictly speaking, because we do not project onto the density matrix obtained from the Green's function, it is a fragment projection, rather than a true peak decomposition, since the peaks are obtained from the full $\boldsymbol{G}(\epsilon)$.

C

ONE DIMENSIONAL CHAINS

Generalizing from the simplest two-dot or two-level system, we derive the Hamiltonian, the spectrum and the self-energies of a monatomic chain.

C.1 A TWO-LEVEL SYSTEM

One dot is characterized by an energy level ϵ. The simplest model for two equivalent dots would be having a degenerate state on each at ϵ, where degeneracy is then broken by the coupling τ between them, leading to energies $\epsilon_{1,2} = \epsilon \pm \tau$, and such that the total energy of the system remains $\epsilon_1 + \epsilon_2 = 2\epsilon$. This result is found simply by writing:

$$\begin{aligned} \hat{H} &= \epsilon(d_1^\dagger d_1 + d_2^\dagger d_2) + \tau d_1^\dagger d_2 + \tau^* d_2^\dagger d_1 && \text{(C.1)} \\ &= \begin{pmatrix} \epsilon & \tau \\ \tau^* & \epsilon \end{pmatrix} && \text{(C.2)} \end{aligned}$$

in the basis of creation and annihilation operators. Diagonalizing the matrix yields the eigenvalues above for real $\boldsymbol{\tau}$. For three dots, we may take the same model, but it is more interesting to consider the infinite chain for our purposes, because we want to see what the progressive splittings by interaction do as the number of sites grows large. Note that we should recover the bands of an infinite periodic system, as in introductory solid-state physics, in this limit.

C.2 SPECTRUM OF A MONATOMIC CHAIN

Consider a chain spaced by a lattice-spacing a. Assuming levels initially at ϵ_0 and hopping transport via only nearest-neighbor couplings τ, Eq. (C.1) generalizes to the Hamiltonian:

$$\hat{H} = \sum_{m=-\infty}^{\infty} \epsilon_0 d_m^\dagger d_m + \tau d_{m-1}^\dagger d_m + \tau^* d_m^\dagger d_{m-1} \tag{C.3}$$

As an ansatz, we take a traveling wave solution, which in real space is $\psi(x) = e^{ikx} \equiv e^{ik\cdot ma}$ for a lattice. We will solve the eigenvalue problem $\hat{H}|\psi\rangle = \epsilon|\psi\rangle$, for which we need a second quantization version of our ansatz $\psi(x)$. It is constructed from the set of functions:

$$\begin{aligned} &\{e^{ik\cdot ma}|m\rangle\}_m \qquad \text{such that:} \\ |\psi\rangle &= \sum_{m=-\infty}^{\infty} e^{ik\cdot ma}|m\rangle && \text{(C.4)} \end{aligned}$$

Note that this preserves the property:

$$\langle\psi|\psi\rangle = \sum_{m=-\infty}^{\infty} \langle m|m\rangle = \langle\psi(x)|\psi(x)\rangle$$

Substituting we find

$$\hat{H}|\psi\rangle = \sum_m \epsilon_0 e^{ikma}|m\rangle + \tau e^{ikma}|m-1\rangle + \tau^* e^{ik(m-1)a}|m\rangle \tag{C.5a}$$

$$= \sum_m \epsilon_0 e^{ikma}|m\rangle + \tau e^{ik(m-1)a} e^{ika}|m-1\rangle + \tau^* e^{ikma} e^{-ika}|m\rangle \tag{C.5b}$$

$$= \sum_m \left(\epsilon_0 + \tau e^{ika} + \tau^* e^{-ika}\right) e^{ikma}|m\rangle \tag{C.5c}$$

Thus for the simple case of real τ we find energies for the infinite chain of

$$\epsilon(k) = \epsilon_0 + 2\tau\cos(ka)\ . \tag{C.6}$$

C.3 SELF-ENERGY OF A MONATOMIC CHAIN

In the case of a monatomic chain in the tight-binding approximation, it is possible to go further and obtain the self-energy, DOS and transmission analytically.[1,2] For two atoms, the Green's function is given by:

$$\boldsymbol{G} = \begin{pmatrix} \epsilon-\epsilon_0 & \tau \\ \tau & \epsilon-\epsilon_0 \end{pmatrix}^{-1} = \frac{1}{(\epsilon-\epsilon_0)^2-\tau^2}\begin{pmatrix} \epsilon-\epsilon_0 & -\tau \\ -\tau & \epsilon-\epsilon_0 \end{pmatrix}\ , \tag{C.7}$$

where ϵ_0 is the energy of the sites, and τ the coupling between them. The diagonal elements, *i.e.* the Green's functions of the single atoms, are given by:

$$g = \left(\epsilon - \epsilon_0 - \frac{\tau^2}{\epsilon-\epsilon_0}\right)^{-1} = \left(g_0^{-1} - \Sigma\right)^{-1}\ ,$$

where $g_0 = (\epsilon-\epsilon_0)^{-1}$ is the Green's function of an isolated atom and $\Sigma = \tau g_0 \tau$. For an infinite chain, we obtain the Green's function of the atoms by letting $g_0 \mapsto g$ in Σ. Solving for g yields:

$$g(\epsilon) = \frac{1}{\tau^2}\left(\frac{\epsilon-\epsilon_0}{2} \pm \sqrt{\left(\frac{\epsilon-\epsilon_0}{2}\right)^2 - \tau^2}\right)\ , \tag{C.8}$$

from which we obtain the self-energy:

$$\Sigma = \tau\, g\, \tau = \frac{\epsilon-\epsilon_0}{2} \pm \sqrt{\left(\frac{\epsilon-\epsilon_0}{2}\right)^2 - \tau^2} \tag{C.9}$$
$$\equiv \Lambda - \frac{\mathrm{i}}{2}\Gamma\ ,$$

and the full Green's function $G(\epsilon)$ (from which transport properties like $D(\epsilon)$ and $T(\epsilon)$ in Fig. C.1) from:

$$G(\epsilon) = \left(g(\epsilon)^{-1} - \Sigma(\epsilon)\right)^{-1}.$$

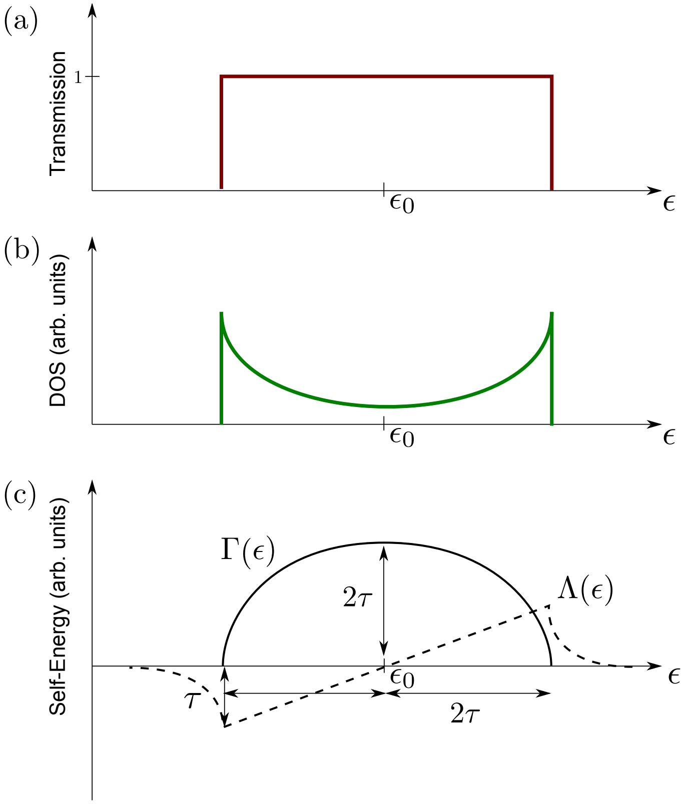

FIGURE C.1: (a) Transmission through a single-site monatomic chain, (b) corresponding DOS and (c) analytical form of the real and imaginary parts of the self-energy.

When $|\epsilon - \epsilon_0| < 2\tau$, this can be split into real and imaginary parts (see Eq. 7.4):

$$\Lambda(\epsilon) = \frac{\epsilon - \epsilon_0}{2} \,, \tag{C.10}$$

$$\Gamma(\epsilon) = \sqrt{(2\tau)^2 - (\epsilon - \epsilon_0)^2} \,. \tag{C.11}$$

These correspond to a linear shift of the orbital energies and a semi-elliptical dependence of the broadening on ϵ. The combination of these terms results in a unit transmission in a band of width 4τ around ϵ_0 (see Fig. C.1c). Beyond the band edges, the transmission drops to zero since $\Gamma(\epsilon) = 0$ and $\Lambda(\epsilon)$ decays quadratically. Note that although the DOS is approximately constant around ϵ_0, it exhibits singularities at the band edge (so-called van Hove singularities).

REFERENCES

[1] D. M. Newns, *Self-Consistent Model of Hydrogen Chemisorption*, Phys. Rev. **178**, 1123 (1969).

[2] P. W. Anderson, *Localized Magnetic States in Metals*, Phys. Rev. **124**, 41 (1961).

D

ACCELERATION OF CONVERGENCE

We discuss our extension of the DIIS algorithm in the presence of charge constraints, as used in the alignment stage of our calculations.

The method described in this appendix has been implemented as the `Transport CDIIS` keys in the BAND code modified for transport calculations, part of the Amsterdam Density Functional (ADF) quantum chemistry package.[1–5]

D.1 CONSTRAINED DIRECT INVERSION OF ITERATIVE SUBSPACES

We outline our expansion on the technique introduced by Pulay[6] for the acceleration of self–consistent field algorithms by direct inversion of iterative subspaces (DIIS). We have extended this to the specific case of handling a charge constraint in the quantum chemical system, the charge on the extended molecule during the self–consistent alignment calculation.

While beyond the scope of this thesis to explore, we also remark the strong similarity of this approach to the method of Wu and Van Voorhis for reformulating constrained DFT (CDFT).[7,8]

D.2 ADF/BAND'S SCF IMPLEMENTATION

Take some vector "input" V, typically a potential or a density; operated on by *e.g.* the Fock matrix, but in any case by a linear operator $F(V) = V'$ giving us the "output" value. After n iterations we can construct the set $\{(V^{(i)}, V^{(i)\,\prime})\}_{i=0}^{n-1}$.

Now consider iteration n. We want as "input" $V^{(n)} = \sum_{i=0}^{n-1} c_i V^{(i)}$, subject to the constraint $\sum_i c_i = 1$ on the weights, which will give as "output" $V^{(n)\,\prime} \equiv F(V^{(n)}) = \sum_{i=0}^{n-1} c_i V^{(i)\,\prime}$. Note that any modifications we make later should preserve this linearity.

To evaluate the quality of this result a metric is required, which is obtained by first defining an error relative to the converged situation $F(V) = V$.

$$V^{(n)} - V^{(n)\,\prime} = \sum_i c_i (V^{(i)\,\prime} - V^{(i)}) \,. \tag{D.1}$$

This induces a norm:

$$\begin{aligned} \|V^{(n)\,\prime} - V^{(n)}\| &= \sum_i \sum_j c_i c_j \langle V^{(i)\,\prime} - V^{(i)} | V^{(j)\,\prime} - V^{(j)} \rangle \\ &= \boldsymbol{c}^\top B \boldsymbol{c} \;; \end{aligned} \tag{D.2}$$

where $\boldsymbol{c} = (c_0, c_1, \ldots, c_{n-1})$ and $B = \left[b_{ij} \equiv \langle V^{(i)\,\prime} - V^{(i)} | V^{(j)\,\prime} - V^{(j)} \rangle \right]$. This norm is then minimized in the cost function

$$J = \boldsymbol{c}^\top B \boldsymbol{c} - \lambda \boldsymbol{c}^\top \mathbb{1}$$

such that $\nabla_{\boldsymbol{c}} J = 0$ implies that $B\boldsymbol{c} = \lambda \mathbb{1}$, which is a simple linear algebra problem. Solving it determines the optimal coefficients $\boldsymbol{c}$ for forming $V^{(n)}$, and the Lagrange multiplier λ is found by first solving for $\tilde{\boldsymbol{c}} = B^{-1}\mathbb{1}$ such that $\boldsymbol{c} = \lambda \tilde{\boldsymbol{c}}$. The constraint $\sum_i c_i = 1 = \sum_i \lambda \tilde{c}_i$ then sets the value of the multiplier:

$$\lambda = \frac{1}{\sum_i c_i} \tag{D.3}$$

So far this is just Pulay's scheme:[6] nothing more, nothing less. In the BAND implementation this is extended by forming the new trial vector not from the original vectors $V^{(i)}$ only, but instead from the mixed vectors

$$\begin{aligned} V_\gamma^{(i)} &= V^{(i)} + \gamma\left(F(V^{(i)}) - V^{(i)}\right) \\ &= (1-\gamma)V^{(i)} + \gamma F(V^{(i)}) \end{aligned}$$

such that $V^{(n)} = \sum_{i=0}^{n-1} c_i V_\gamma^{(i)}$ instead.

This allows DIIS to be used at every step by growing the vector space, in contrast to Pulay's scheme where $V^{(n)} \in \text{span}\{V^{(i)}\}_{i=0}^{n-1}$ by definition, such that you *need* to do normal (i.e. non-DIIS) iterations in between to avoid linear dependence.

D.3 EXTENDING DIIS

In normal Pulay DIIS the SCF process is cast as a linear(-izable) mapping $F(V)$ of some vector V, which in DFT are typically the Fock operator and the density of the system (in discretized real space) respectively. Normally one would simply have:

$$V^{(n+1)} = F\left(V^{(n)}\right) \tag{D.4}$$

for the $n+1^{\text{st}}$ iteration, and iterate until convergence. Pulay's insight was to seek the optimal combination of a history of previous iterations (an iterative subspace):

$$V^{(n)} = \sum_{i=0}^{n-1} c_i V^{(i)} \tag{D.5}$$

subject to $\sum_i c_i = 1$ for normalization of the result. Let the iterates $V^{(n)}$ denote the input to the Fock operator, and denote the output by $V_*^{(n)} = F\left(V^{(n)}\right)$. Then we have also constructed a history

$$V_*^{(n)} = \sum_{i=0}^{n-1} c_i V_*^{(i)} ,$$

trivially. To quantify the quality of this linear combination, a norm is again introduced on the error:

$$V_*^{(n)} - V^{(n)} = \sum_i^{n-1} c_i \left(V_*^{(i)} - V^{(i)} \right) \quad \text{such that} \tag{D.6}$$

$$\begin{aligned} \|V_*^{(n)} - V^{(n)}\| &= \sum_i^{n-1} \sum_j^{n-1} c_i c_j \langle V_*^{(i)} - V^{(i)} | V_*^{(j)} - V^{(j)} \rangle \\ &= \boldsymbol{c}^\top B \boldsymbol{c} \end{aligned} \tag{D.7}$$

where $\boldsymbol{c} = (c_0, \ldots, c_{n-1})^\top$ and B has elements $b_{ij} = \langle V_*^{(i)} - V^{(i)} | V_*^{(j)} - V^{(j)} \rangle$ formed by an inner product. This can be recast as a cost function including the constraint:

$$J = \boldsymbol{c}^\top B \boldsymbol{c} - \lambda \boldsymbol{c}^\top \mathbb{1} \ , \tag{D.8}$$

minimized by:

$$\nabla J = 0 \ni B\boldsymbol{c} = \lambda \mathbb{1} \ . \tag{D.9}$$

with Lagrange multiplier $\lambda = \left(\sum_i c_i\right)^{-1}$.

During and alignment run we extend this approach as follows. Our goal is to allow the SCF cycle, using the DIIS algorithm, to become aware of the constraint that at convergence,

$$\mathrm{Tr}\left[\, \rho S \,\right]_{\mathrm{EM}} \to Q_{\mathrm{EM}}^0$$

should hold, with Q_{EM}^0 the correct bulk (valence) charge on the EM composed of bulk material. Observing that this is already in the same units of charge as the relevant vector V, the DIIS approach can be extended, defining the excess charge on the extended molecule $Q_x \equiv \mathrm{Tr}\left[\, \rho S \,\right]_{\mathrm{EM}} - Q_{\mathrm{EM}}^0$, as follows:

$$V \to (V,\ Q_x\,) \tag{D.10}$$

i.e. extending the vector by a single scalar, and

$$b_{ij} \to b_{ij} + \left(Q_{x*}^{(i)} - Q_x^{(i)} \right) \left(Q_{x*}^{(j)} - Q_x^{(j)} \right) \ , \tag{D.11}$$

where B preserves its meaning as the matrix of error norms or correlations. Note that DIIS convergence implies that the vector (*i.e.* the density) becomes stationary, and likewise for the excess charge. We can also choose to use $b_{ij} + Q_x^{(i)} Q_x^{(j)}$ instead, which is the formally more desirable condition that the excess charge go to 0 directly, but then we depart somewhat from the spirit of the Pulay approach.

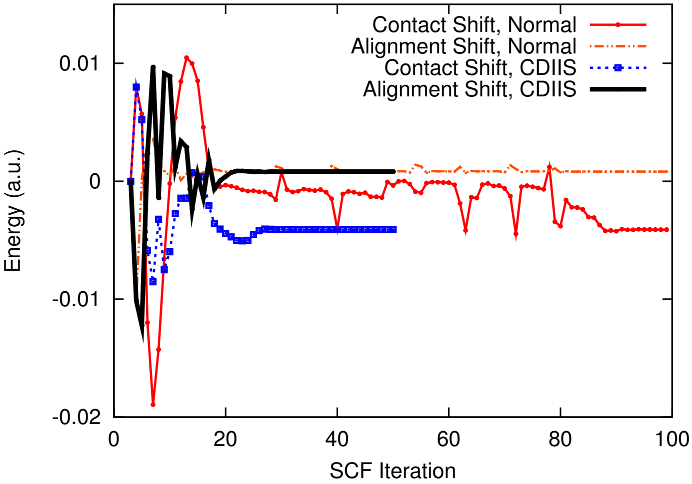

FIGURE D.1: Convergence of alignment shifts for the Al chain: $\Delta\phi_{0,1}$ with and without CDIIS. Note the significantly better performance of the CDIIS procedure.

D.4 CONVERGENCE OF THE CDIIS SHIFTS

The last issue to address in discussing DIIS itself is the idea of freezing. There is a noticeable iteration lag between arriving at stable alignment offsets $\Delta\phi_{0,1}$ for the Hamiltonians, and the overall convergence of the density which terminates the SCF cycle. The straightforward approach is to test whether the shifts have converged, and once they have, to freeze them and release DIIS.

The algorithm is straightforward, but the criterion for convergence is a subtle issue. We have used a criterion on the charge relative to a 5-point moving average, within a tolerance of *e.g.* 10^{-4} a.u. ($\sim$ 25 meV).

$$\vec{\Delta}_0 \equiv \frac{1}{5}\sum_{i=i_0-4}^{i_0} \begin{pmatrix} \Delta\phi_0^{(i)} \\ \Delta\phi_1^{(i)} \end{pmatrix}, \qquad \text{where } i_0 \text{ is the current iteration} \tag{D.12}$$

$$\Delta\phi_{\text{tol}} \geq \begin{pmatrix} \Delta\phi_0^{(i)} \\ \Delta\phi_1^{(i)} \end{pmatrix} - \vec{\Delta}_0, \qquad \forall i \in \{i_0 - 4, i_0\} \text{ is the condition being tested.} \tag{D.13}$$

We remark that in principle $\Delta\phi_0$ is always floating, and so shouldn't matter. Nonetheless in practice we find it to be a strong indicator of convergence, motivating its use in this way. In Fig. D.1 we illustrate the effect of CDIIS on the convergence speed of the alignment calculation for an Al chain, cutting the number of required iterations roughly in half.

REFERENCES

[1] C. Fonseca Guerra, J. G. Snijders, G. te Velde, and E. J. Baerends, *Towards an order-N DFT method*, Theor. Chem. Acc. **99**, 391 (1998).

[2] G. te Velde, F. Bickelhaupt, S. van Gisbergen, C. Fonseca Guerra, E. Baerends, J. Snijders, and T. Ziegler, *Chemistry with ADF*, J. Comput. Chem. **22**, 931 (2001).

[3] G. te Velde and E. J. Baerends, *Precise density-functional method for periodic structures*, Phys. Rev. B **44**, 7888 (1991).

[4] G. Wiesenekker and E. J. Baerends, *Quadratic integration over the three-dimensional Brillouin zone*, J. Phys.: Condens. Matter **3**, 6721 (1991).

[5] C. J. O. Verzijl and J. M. Thijssen, *A DFT-based Molecular Transport Implementation in ADF/BAND*, J. Phys. Chem. C (2012), accepted.

[6] P. Pulay, *Convergence acceleration of iterative sequences. The case of SCF iteration*, Chem. Phys. Lett. **73**, 393 (1980).

[7] Q. Wu and T. Van Voorhis, *Direct optimization method to study constrained systems within density-functional theory*, Phys. Rev. A **72**, 024502 (2005).

[8] Q. Wu and T. Van Voorhis, *Direct Calculation of Electron Transfer Parameters through Constrained Density Functional Theory*, J. Phys. Chem. A **110**, 9212 (2006).

E

CODE HIERARCHY

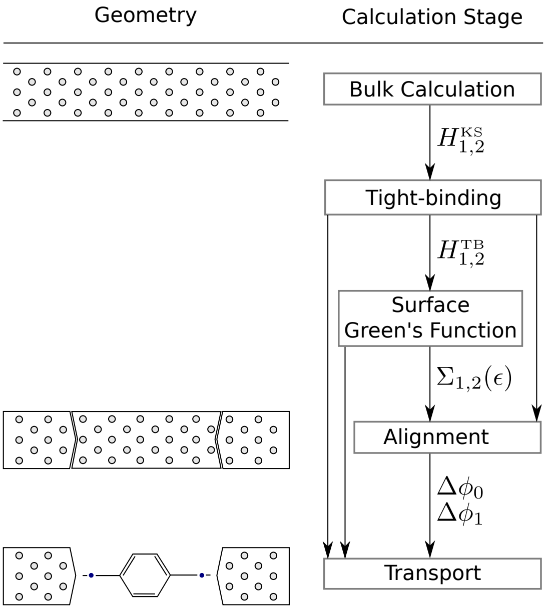

FIGURE E.1: Calculation flow with corresponding schematic geometries. Arrows indicate flow of calculation outputs between different stages.

E.1 CALCULATION STAGES

The normal "path" of the multi-stage transport calculation is as follows, as discussed in Chapter 3.

1. Calculation of infinite bulk contacts' Hamiltonian $\boldsymbol{H}^{\text{KS}}$,
2. Determination of a tight-binding representation of the converged $\boldsymbol{H}^{\text{KS}}$,
3. Calculation of the self-energies $\boldsymbol{\Sigma}_{1,2}(\epsilon)$ of semi-infinite bulk contacts,
4. Alignment of the leads with the central extended-molecule region composed of bulk material,
5. Transport calculation proper, with extended-molecule region now comprising the molecule coupled to part of the electrodes.

In Fig. E.1 we outline this flow as before, but with the accompanying geometry "types" to indicate the differences at each stage.

E.2 CODE ORGANIZATION

The code for the tight-binding and surface Green's function calculations are combined in the `SGF` module in the ADF package, which is implemented as an independent utility, broken down by code file in Table E.1. It takes the outputs of a bulk calculation as inputs, and generates the TB Hamiltonian and overlap matrices $\boldsymbol{H}^{\text{TB}}$, $\boldsymbol{S}^{\text{TB}}$ self-energy matrices $\boldsymbol{\Sigma}_{1,2}(\epsilon)$, and diagnostic plots such as the real and imaginary traces of the self-energies and densities of states as outputs. The matrices generated are then used as inputs to an alignment or transport calculation. The structure of the NEGF transport implementation in the BAND code is as outlined in Table E.2.

Location	File	Comment
init/		Initialization code
	bytes.f90	
	inputt.f90	
	sgfinit.f90	Setup environment
	sgfkey.f90	Define keys
io/		
	rqsurface.f90	Read surface Green's function keys
	rqtb.f90	Read tight-binding keys
lbfgs/		L-BFGS Solver[1]
	lb1.d	
	lb2.d	
	lbfgs.d	
	mcsrch.d	
	mcstep.d	
misc/		Utility code
	fldl.f90	
	numtag.f90	Convert tags
	readmat.f90	Load matrices
	sgfinv.f90	Invert matrix for Green's function
nolib/		Control routines
	ctllst.f90	
	isParallelProgram.f90	
	kfexit.f90	
	nolib.f90	
	sgfexit.f90	
	stopit.f90	
surface/		SGF Code
	calcgf.f90	Green's functions
	mmulcc.f90	Complex matrix multiplies
	ppdatacollect.f90	Parallel data routines
	surface.f90	SGF driver
	surfacemodule.f90	Module data
tb/		Tight-binding Main Code
	randmodule.f90	Random numbers
	readbanddata.f90	Read BAND output
	tb.f90	Tight-binding driver
	tbmodule.f90	Module data
sgf.f90		Driver Code
sgfmodule.f90		Module Code

TABLE E.1: Organization of the SGF module code, locations relative to root of the ADF package tree.

Location	File	Comment
options:		NEGF Options Definition & Loading
	options/DefNEGF.d90	Define keys
	options/DefineOptions.d90	Definitions loader
	util/ctllst.d90	
	io/getinp.d90	Read keys
diis/		(C-)DIIS code
	pulay.dmodl	Main Pulay-based DIIS routine
	plymat.dmodl	Pulay matrix constructor
kpnt/		*k*-points Code
	gemtry.d90	
	NEGFKPoints.dmodl	Alternate path for NEGF
negftransport/		NEGF Main Code
	NEGFDebug.f90	Diagnostic code
	NEGFPMat.f90	Density matrix code
	NEGFPotential.f90	Potential code
	NEGFSelfEnergies.f90	Self-energies code
	NEGFTransport.f90	Transport variables
	NEGFUtilities.f90	Utility routines
	PPNEGFData.f90	Data-parallelization routines
scf/		SCF Iteration Driver
	scf.f90	SCF Driver Code
	eigsys.f90	Eigensystem driver
	eigsolve.f90	Eigensystem diagonalization
	FockMatrixEvaluator.f90	Fock matrix, hooks to potential code

Table E.2: Organization of the NEGF code for the implementation in BAND.

E.3 Keys

TRANSPORT	Perform transport calculation
TRANSPORT%TRANSDIR	Transport direction
TRANSPORT%PLOT	Control plot frequency (DOS and Transmission)
TRANSPORT%NEMATOMS	Number of atoms considered as extended molecule for alignment
TRANSPORT%CONTACTSHIFT	Sets baseline offset $\Delta\phi_0$
TRANSPORT%OFFSETSHIFT	Sets permanent offset $\Delta\phi_1$
TRANSPORT%NOSHIFTFLOAT	Turns off $\Delta\phi_0$ floating in transport, makes it permanent
TRANSPORT%FREEZESTOP	Controls how/when $\Delta\phi_0$ float starts in transport (-1 = Never: Post-SCF Calculation)
TRANSPORT%TESTMATCH	Do extensive testing of HMAT matches
TRANSPORT%WBLFLAT	Activate Wide Band Limit, using $\boldsymbol{\Sigma} = i\Gamma \boldsymbol{S}$, and set Γ
TRANSPORT%WBL	Activate Wide Band Limit, using $\boldsymbol{\Sigma}(\epsilon_f)$
TRANSPORT%WBLIMONLY	Do “WBL” $\boldsymbol{\Sigma}(\epsilon_f)$ with only imaginary part
TRANSPORT%WBLPLOTONLY	Turn WBL of any kind off in SCF cycle, but do use in plots
TRANSPORT%DEFERSIGMA	Load $\boldsymbol{\Sigma}$’s on the fly
TRANSPORT%HMATMIXSTEPS	controls over how many steps to mix in bulk HMats after FreezeStop

ALIGN	Alignment of the potential of the system
ALIGN%MIX	Alignment mixing parameter
ALIGN%STARTALIGN	Start cycle of alignment procedure
ALIGN%PMATSHIFT	Use shifting of $\boldsymbol{\rho}$-matrix as convergence aid
ALIGN%CDIIS	Use constrained DIIS
ALIGN%CDIISDAMP	Damping for constrained DIIS
ALIGN%CDIISPRINT	Print CDIIS details during run
ALIGN%EMCHARGE	True EM valence charge for alignment

BIAS	Bias
BIAS%phi1	Potential at contact 1
BIAS%phi2	Potential at contact 2
BIAS%X1	x_1 Measurement coordinates in contact 1
BIAS%Y1	y_1
BIAS%Z1	z_1
BIAS%X2	x_2 Measurement coordinates in contact 2
BIAS%Y2	y_2
BIAS%Z2	z_2
BIAS%DELTAX	δx Measurement box size
BIAS%DELTAY	δy
BIAS%DELTAZ	δz
BIAS%TC1	Transport coordinate 1
BIAS%TC2	Transport coordinate 2
BIAS%PLOT	Control plot frequency (DOS and Transmission)
BIAS%ITERATIVE	Apply bias ramp iteratively instead of fixed
BIAS%BLOCK	Apply bias as block in contacts, rather than a ramp

GATE	Gate
GATE%PHI	Potential of gate field
GATE%PLOT	Control plot frequency (DOS and Transmission)
GATE%BASFNC	Last basis function on metal atoms

`CDFT`	Constrained DFT Implementation in Transport
`CDFT%BASFNC`	Last basis function on metal atoms (remaining = molecule)
`CDFT%QExcess`	Excess charge
`CDFT%CDFTMix`	Mixing strength
`CDFT%Field`	Field strength
`CDFT%BasisLim`	Sets basis-function to start constraining from
`CDFT%StartCDFT`	Sets starting iteration

`GMIX`	Mixing ρ-matrix depending on charge
`GMIX%STOPMIX`	Number of iterations to apply mixing procedure
`GMIX%EXTRAMIX`	Extra mixing factor
`GMIX%MINMIX`	Minimum mixing factor

REFERENCES

[1] W. Press, S. Teukolsky, W. Vetterling, and B. Flannery, *Numerical Recipes* (Cambridge University Press, 2007), 3rd ed., the Art of Scientific Computing.

F

SAMPLE INPUT FILES

Input files with discussion of most important keys. The reference for the remaining keys is the official BAND documentation, as maintained online by SCM, (currently) available at http://www.scm.com/Doc/Doc2012/ .

We first note some generally important keys.

- Generally useful debugging keys are: `PRINT TIMING, PRINT KOPS, PRINT OCCUP, PRINT ORBITALS`; these print information which may be of considerable use in understanding a difficult or badly-performing calculation.

- Generally useful functionality keys are: `SCF, DIIS, CDIIS`. These control the self-consistency cycle, the DIIS convergence acceleration algorithm in general, and the constrained-DIIS procedure in an alignment calculation (*cf.* Appendix D) respectively.

- Typically necessary keys in transport are: `SYMMETRY 1, ALLOW CHARGEERROR`. The first forces the system to be one dimensional, which is the starting point for all calculations which are not intended to model a system with two- or three-dimensional periodic boundary conditions. The second stops the code from enforcing charge-neutrality, which is neither necessary nor guaranteed in our approach to transport, as discussed in Chapter 3.

- Taking a sufficiently large unit cell makes a 1D calculation effectively zero-dimensional. This can in fact be forced by controlling the screening cut-off via the key `SCREENING` in relation to the definition of `LATTICE`, and verified by the keyword `CELLS` in the resulting output.

F.1 Bulk Calculation

We show the input for a bulk calculation for a one-dimensional Al chain, which we have discussed in Chapters 4 and 7. Note particularly the instruction `StoreHamiltonian`. Also, we use an orbital cutoff to ensure the validity of the principal layers approach in the next step, but the value should be tuned to ensure that we're still modeling a physical system.

```
Title AluminiumWire BULK

UNITS
  length Angstrom
  angle Degree
END

DEFINE
  d=2.83
END

XC
  LDA VWN
END

BASIS
  NONORTHOGONALSCFBASIS
END

ACCURACY 4.5
KSpace 7

PRINT KOPS
PRINT OCCUP

STOREHAMILTONIAN

SCF
  PMatrix
END

DOS
  FILE dos1.plt
  ENERGIES 500
  MIN -0.4
  MAX 0.4
END

LATTICE
  d
END

ATOMS Al
  0.0
END

AtomType Al
DIRAC Al
VALENCE
  5 3
  1S
  2S
  2P
  3S
  3P 1
SUBEND
BASISFUNCTIONS
  3S 1.05
  3P 1.35
SUBEND
FITFUNCTIONS
  1S  23.00
  2S  21.89
  2S  12.96
  3S  11.37
  3S   7.30
  4S   6.24
  4S   4.23
  4S   2.86
  5S   2.43
  5S   1.71
  5S   1.20
  2P  16.15
  3P  11.98
  4P   8.86
  4P   5.24
  5P   3.90
  5P   2.43
  5P   1.51
  3D  12.41
  4D   8.67
  4D   4.85
  5D   3.43
  5D   2.03
  5D   1.20
  4F   5.00
  4F   3.00
  5G   4.00
SUBEND
CONFINEMENT
  Radius 4.6
  Delta  0.3
SUBEND
END

END INPUT
```

The second contact is run by changing the input key `LATTICE` to:

```
LATTICE
  -d
END
```

F.2 Tight-binding Representation

Next is the tight-binding representation of the Fock matrix, which takes `greendata1.dat` (from the stored output of the bulk calculation of the first electrode, generated by the `StoreHamiltonian` key) as input and provides `OutputTB1.dat` as output. Note that the settings commented out have been implemented as default values now, and so are only needed when intending to change the defaults. Further, we require the option `IODIM` specifying whether the calculation is one- or three-dimensional, so that certain matrices can be allocated correctly internally.

```
cp greendata1.dat greendata.dat
$ADFBIN/sgf   << eor

TIGHTBINDING

   XTOL 1E-6
   MaxRange 6E0
   MaxMerit 1E-10
   IODIM 1

END
```

F.3 SELF-ENERGY CALCULATION

The following stage is the surface Green's function calculation, which generates and stores large, binary, $\mathbf{\Sigma}$ matrix key-files. `NLayers` sets the number of atomic layers (which correspond to the bulk calculation above) in a principal layer, and will correspond to the contact geometry in the next section.

`KGrid` sets the grid in k-space, which becomes denser for higher values, corresponding to a larger wide cell in the plane transverse to transport.[a] The rest are technical parameters controlling the complex contour integration, and the energy points to store Σ for, and control the bias[b] as needed later for transport.

```
cp OutputTB1.dat OutputTB.dat
$ADFBIN/sgf   << eor

SURFACEGF

  Nlayers 4
  TransDir 1
  KGrid 1
  NFPoles 2
  NArcPts 50
  NEqLinePts 100
  NNonEqLPts 200

  KT 0.001
  Delta 0.002
  Eta 0.00001
  CPMargin 10.0

  NDOSPts 1000
  MinDOS -0.4
  MaxDOS  0.4

  MinValence -1.0
  MuUpper  0.0
  MuLower -0.1
  Phi1   0.00
  Phi2   0.00
  BANDMU -0.0401

  Contact 1
  NE 3

END
```

---

[a] A larger electrode surface, *i.e.* more atoms in the simulation: 3×3 *vs.* 2×2, *etc.*

[b] The bias, moreover, needs to be set the same in the input for *both* contacts (only one is shown), as we will calculate two contours per contact which must match!

F.4 ALIGNMENT CALCULATION

The next input is an alignment run, where the bias is kept at 0 V and the “molecule" is just bulk material. Adjusting these to the correct molecular device geometry would make it a transport run. Note the correspondence of the orbital cutoff to that used in the bulk calculation. Also, we take `KSpace = 1`, *i.e.* the Γ-point approximation; our calculation can yield higher ***k*** results, depending on the settings in the surface calculation, but this is implemented separately from BAND's `KSpace` key, and the setting here is the one currently relevant to transport.

```
$ADFBIN/band << eor
Title AluminiumWire ALIGN

Units
  length Angstrom
  angle Degree
END

XC
  LDA VWN
END

Define
  d=2.83
END

LATTICE
  25*d
END

Accuracy 4.5
KSpace 1

PRINT TIMING
SYMMETRY 1
ALLOW CHARGEERROR

TRANSPORT
  TRANSDIR 1
  PLOT 1000
  NEMAtoms 6
END

ALIGN
  MIX 0.001
  STARTALIGN 5
  CDIIS
END

BIAS
  phi1 0.0
  phi2 0.0
  deltax 0.1*d
  deltay 1*d
  deltaz 1*d
  X1 -5.0*d
  X2  5.0*d
  PLOT 10
END

SCF
  PMATRIX
END

DIIS
  NCycleDamp 5
  DIMIX 0.15
END

ATOMS Al
! LEFT Contact = 1
! Ordering surface inwards
 -3.5*d
 -4.5*d
 -5.5*d
 -6.5*d+.0001

! RIGHT Contact = 2
! Ordering surface inwards
  3.5*d
  4.5*d
  5.5*d
  6.5*d+.0001

! Molecule
 -2.5*d
 -1.5*d
 -0.5*d
  0.5*d
  1.5*d
  2.5*d
END

AtomType Al
DIRAC Al
VALENCE
  5 3
  1S
  2S
  2P
  3S
  3P 1
SUBEND
BASISFUNCTIONS
  3S 1.05
  3P 1.35
SUBEND
FITFUNCTIONS
  1S  23.00
  2S  21.89
  2S  12.96
  3S  11.37
  3S   7.30
  4S   6.24
  4S   4.23
  4S   2.86
  5S   2.43
  5S   1.71
  5S   1.20
  2P  16.15
  3P  11.98
  4P   8.86
  4P   5.24
  5P   3.90
  5P   2.43
  5P   1.51
  3D  12.41
  4D   8.67
  4D   4.85
  5D   3.43
  5D   2.03
  5D   1.20
  4F   5.00
  4F   3.00
  5G   4.00
SUBEND
CONFINEMENT
  Radius 4.6
  Delta  0.3
SUBEND
END

END Input
```

F.5 TRANSPORT CALCULATIONS

The simplest transport calculation is as the alignment calculation in the previous section, but with the key `ALIGNMENT` omitted, and the geometry extended with the molecule's atoms. Additionally, a specification of the converged alignment shifts $\Delta\phi_0$, $\Delta\phi_1$ is added to the `TRANSPORT` key:

```
TRANSPORT
  TRANSDIR 1
  PLOT 1000
  NEMAtoms 30
  CONTACTSHIFT   -4.0962761E-03
  OFFSETSHIFT     8.1191692E-04
END
```

If corresponding self-energies have been calculated, an adjusted bias may be specified as well:

```
BIAS
   phi1  50.0/27211.0
   phi2 -50.0/27211.0
   deltax 0.1*d
   deltay 1*d
   deltaz 1*d
   X1 -5.0*d
   X2  5.0*d
   PLOT 1000
END
```

where in this example a 100 meV bias has been applied symmetrically. If run without change to the geometry, the code can also be used to test the validity of the aligned result.

F.6 GATED CALCULATIONS

In order to gate the molecule, as discussed in section 3.8, the following key is added in a transport run:

```
Gate
  PHI 5e-2
  BASFNC 90*6
  PLOT 1000
End
```

The `BASFNC` key specifies the number of basis functions corresponding to the metal electrode atoms,[c] such that the basis functions from `BasFnc+1 : N` correspond to the molecule. This is required both to apply the gate as a constant shift $\beta V_g \boldsymbol{S}$ in the Fock matrix, and to trace out a PDOS on the molecule proper rather than just on the extended molecule.

It should also be exploited in an un-gated system to calculate the latter, simply by setting the gate field to zero.

---

[c] At time of writing, this is nontrivial to obtain directly from BAND's internal variable sets, and so has been implemented as specified-by-user.

F.7 Post-SCF Calculations

Post-SCF calculations are implemented via a very simple extension of the `Transport` key, which has a subkey `FreezeStop` to control a temporary freezing of the potential shifts at the start of a run in order to aid convergence. Doing all transport Post-SCF is implemented by setting `FreezeStop` to -1 (“infinity”, rather than the default value 0), such that a BAND calculation is run through convergence:

```
TRANSPORT
  TRANSDIR 1
  PLOT 1000
  NEMAtoms 30
  CONTACTSHIFT   -4.0962761E-03
  OFFSETSHIFT     8.1191692E-04
  FreezeStop -1
END
```

F.8 Wide-Band Limit Calculations

A WBL calculation is similarly implemented as a modification to the `Transport` key, for which there are also a number of debug options:

```
TRANSPORT
  Plot 1000
  NEMAtoms 20
  Transdir 1
  ContactShift -6.2317643E-03
  OffsetShift   2.0129368E-03
  Freezestop 0
  WBLFlat 0.05
  WBLPlotOnly
END
```

Here, the setting `WBL` turns the wide-band limit approximation on while a special trick, `WBLPlotOnly`, instructs the code to only apply it in the calculation of transport properties after convergence, but not *during* a converging run. Provided as an example only, `WBLPlotOnly` is not a necessary part of a WBL run.

G

VALORIZATION

We close with a brief comment on the context of the development work underlying this thesis, performed in collaboration with industrial partner Scientific Computing & Modelling N.V.

It is perhaps unusual for a theorist to say something concrete about the valorization of his or her research, given that the perception of isolated, monastic work appreciated only by the initiated is often only slightly exaggerated. This, fortunately, has not been the experience of my Ph.D.

Instead, the work performed has been, beginning to end, integrated into the existing source code of the BAND density functional theory code, part of the larger Amsterdam Density Functional (ADF) software package. This is a high-performance commercial quantum chemistry code, covering both the gas-phase and solid-state ends of the spectrum in terms of physics/chemistry. On the basis of an agreement between J.M. Thijssen on behalf of the TU Delft, with Scientific Computing and Modelling (SCM) N.V., we obtained access to the entire ADF codebase in exchange for contributing all development work on our molecular transport implementation.

The transport code outlined in this thesis has since been integrated with the ADF package and is in principle available to developers already. It is expected to be released to the wider audience of all academic and industrial users as part of the ADF2013 release in the coming year.

This undertaking is of course valorization in a broader sense than a spin-off from the research group in which the work was performed. It is perhaps better understood as a public-private partnership, with the caveat that the resulting software is not publicly available under an open-source licensing arrangement. Nonetheless, the advantages for the user community, both academic and non-academic (primarily chemical, pharmaceutical and materials-science based research & development) are that:

- The code is, on release, immediately available as an extension of a well-known, widely-used software package;
- The code will be maintained in the future, regardless of the developments within the particular research group in which it originated, and
- The code can be developed further by essentially any other interested party on the same terms, through future such public-private partnerships with SCM, which are in fact a part of their standard business model.

In light of these points, it is hoped that this valorization arrangement will give the work described here a longer useful lifespan than might normally be the case for an academic code, and expose it to a significantly larger potential user community.

SUMMARY

In this thesis we discuss *ab initio* studies of quantum transport through molecular devices, using a combination of techniques from quantum chemistry and many-body physics. The promise of such molecular devices lies partly in the promise for alternative solutions to problems of heat dissipation and reliable fabrication of devices at the nano-scale. However, as a technological pathway, it also opens up possibilities of combining many other degrees of freedom into functional device design, such as spin, electrical and mechanical switching, vibrational and optical excitations and their coupling to electronic transport, just to name a few. These all ultimately originate in the versatility of design by synthetic chemistry. While they introduce beautiful opportunities for theoretical study, they also demand a versatile, scalable tool set.

The molecular transport calculations discussed here are based on the "DFT+NEGF" approach to molecular transport, precisely to this end. We first outline the density functional theory (DFT) and non-equilibrium Green's functions (NEGF) formalisms. We discuss the assumptions behind their combined use, as well as consequent limitations to the computational results we have obtained. We then present a novel implementation of the first-principles approach to molecular charge transport, combining DFT with the NEGF formalism. This has been implemented as a custom, scalable extension of the ADF/BAND quantum chemistry package originally developed in the theoretical chemistry group at the VU University Amsterdam, and currently developed and commercialized by Scientific Computing and Modelling N.V.

We first discuss solely the implementation, adding details of complementary techniques such as the implementation of density-constrained convergence acceleration, constant gating of the molecular region, wide-band limit (WBL) approximations and post self-consistent transport calculations. Our implementation allows us to compare contacts with– and without periodic boundary conditions, the latter being particularly useful for modeling the needle-like electrodes used in mechanically-controlled break-junction experiments.

We next discuss the first major test of our methods, on simple one- and three-dimensional metal contacts. We consider lithium, aluminum and gold as contact materials. For the monatomic chains we find excellent agreement with intuitive results from elementary solid-state physics. Our results on the gold nano-contacts indicate that the geometry of finite contacts has significant consequences for the transmission through them, which remains true as they couple to a molecular device.

We then proceed to the second major test of our methods, on phenyl-ring systems. We consider the prototype which has been perhaps most thoroughly studied in the literature: a benzenedithiol (BDT) single-molecule device. We focus particularly

on where our results diverge from previous studies in the literature due to subtle modeling choices. The primary drivers are on the one hand the distinction between periodic and non-periodic boundary conditions, and on the other hand (within the latter class), the geometry of the narrow tube-like contacts used. We find good agreement with previous studies provided we use the same, periodic, boundary conditions – appropriate for large bulk-like electrodes. Without periodic boundary conditions our results diverge, to a degree depending on the shape of the contacts used.

Increasing chemical complexity from these single-ring systems, we next study conjugated multi-ring systems. We focus on the next few systems from the oligo-phenylene-ethynylene family, with two (OPE-2) and three rings (OPE-3) in particular, where we find that the same qualitative results hold, for both types of contacts.

We then turn to more complex systems such as the porphyrin-derivative devices recently studied experimentally by Perrin *et al.* To address the polarization effects suspected to be behind the mechanical gating effects observed in the experiments, we extend our transport method with a complementary approach which accounts for image-charge effects at a metal-molecule interface. The resulting simple model allows us to calculate the adjustment of the transport levels due to the polarization of the device electrodes, as charge is added to and removed from the molecule. For this we use the charge distributions of the molecule between two metal electrodes in several charge states, rather than in gas-phase. These are obtained from our transport code by simulating the effects of charging using a gate field in the potential. We find good agreement with the renormalization of the HOMO-LUMO gap observed in the experiments, which cannot be explained by competing effects such as charge-transfer or the formation of static– and interface dipoles.

Finally, we address the fact that the transport properties of nano-scale systems are notoriously expensive to calculate in their full chemical detail. This makes it tempting to use rather drastic approximations, but few studies have compared the accuracy and performance of the different schemes in use. In our final chapter we put the commonly-used WBL approximation and more sophisticated post–self-consistent transport calculations under the microscope to see how they compare with fully self-consistent transport calculations.

We find reasonably good agreement between all schemes for systems in which the molecule (and not the metal-molecule interface) dominates the transport properties. We find that for systems where the interface dominates transport, (part of) the electrodes need to be included in the calculation. The WBL yields good results if the electrodes have a constant density of states near the Fermi energy. Typically its use is limited when the device is biased, but provided the voltage drop occurs primarily inside the molecule, the approximate method still provides results in reasonable agreement with fully self-consistent calculations.

SAMENVATTING

In dit proefschrift bespreken wij *ab initio* studies van kwantumtransport door moleculaire schakelingen, gebruikmakende van technieken uit de kwantumchemie en veeldeeltjes fysica. De belofte van dergelijke moleculaire schakelingen ligt deels aan de mogelijkheid tot alternatieve oplossingen voor de uitdagingen op gebied van warmteafvoer en fabricage in apparaten op nanometer-schaal. Echter, als technologisch vooruitzicht schept het ook de mogelijkheid om vele andere vrijheidsgraden in een functioneel ontwerp te combineren, zoals spin, elektrisch en mechanisch schakelen, trillings- en optische excitaties en hun koppeling aan elektronisch transport, om slechts een paar te noemen. Deze vinden uiteindelijk allemaal hun oorsprong in de veelzijdigheid van de synthetische chemie. Hoewel ze leiden tot prachtige mogelijkheden voor theoretisch onderzoek, eisen ze ook een veelzijdige, schaalbare gereedschapskist.

De berekeningen van moleculair transport die hier besproken worden zijn juist daarom gebaseerd op de “DFT+NEGF” benadering. We geven eerst een overzicht van de dichtheidsfunctionaaltheorie (DFT) en non-equilibrium Green’s functies (NEGF) formalismen. We bespreken de veronderstellingen achter het combineren ervan, alsmede de daaruit voortvloeiende beperkingen van de rekenkundige resultaten die we hebben behaald. Vervolgens geven we een nieuwe implementatie van een dergelijke model voor moleculair ladingstransport, door DFT met het NEGF formalisme te combineren. Dit model is geïmplementeerd als een schaalbare uitbreiding van het ADF/BAND kwantumchemiepakket, ooit ontwikkeld in de theoretische chemie groep aan de Vrije Universiteit, en momenteel verder ontwikkeld en gecommercialiseerd door Scientific Computing and Modelling N.V.

We behandelen eerst de implementatie, onder bespreking van nuttige details van complementaire technieken zoals dichtheids-beperkte versnelling van de convergentie, constante gating van het moleculair gebied, breedbandlimiet (WBL) benaderingen en post zelf-consistente transportberekeningen. Onze implementatie stelt ons in staat contacten te vergelijken met en zonder periodieke randvoorwaarden, waarbij de laatste vooral nuttig zijn bij het modelleren van de naaldvormige elektrodes die gevormd worden in experimenten met mechanische breekjuncties.

We bespreken vervolgens als eerste grote test van onze methode eenvoudige een– en drie-dimensionale metalen elektroden van lithium, aluminium en goud. Bij de monatomische ketens vinden we zeer goede overeenstemming met intuïtieve resultaten uit de vastestoffysica. Onze resultaten voor gouden nanocontacten tonen aan dat de geometrie van eindige contacten belangrijke consequenties heeft voor de transmissie, die van belang blijven bij integratie in een moleculaire schakeling.

Hierna bestuderen we als tweede grote test moleculen met fenylgroepen. We beschouwen eerst het meest uitvoerig bestudeerde referentiesysteem: een benzeendithiol enkel-molecuul schakeling. Wij zijn met name geïnteresseerd in waar onze resultaten afwijken van eerdere studies in de literatuur, als gevolg van subtiele modelleringskeuzes. De belangrijkste factoren zijn enerzijds het verschil tussen de periodieke en niet-periodieke randvoorwaarden en anderzijds bij laatstgenoemde, de geometrie van de naaldvormige contacten. We vinden goede overeenstemming met eerdere studies wanneer we dezelfde periodieke randvoorwaarden gebruiken – geschikt voor grote bulkachtige elektroden. Zonder periodieke randvoorwaarden verschillen onze resultaten in een mate afhankelijk van de vorm van de gebruikte contacten. Wanneer we de chemische complexiteit laten toenemen, vervolgen we onze studie met geconjugeerde moleculen met meerdere fenylgroepen. Wij richten ons op systemen uit de oligo-fenyleen-ethynyleen (OPE-*n*) familie, met twee resp. drie fenylgroepen, waar we kwalitatief dezelfde resultaten vinden voor beide soorten contacten.

We richten ons vervolgens op complexere systemen zoals de porfyrine-derivaten die recent door Perrin *et al.* experimenteel bestudeerd zijn. Daarbij zijn mechanische-gating effecten waargenomen, waarvan vermoed wordt dat deze door polarisatieverschijnselen te verklaren zijn. Wij breiden onze transportmethode uit met een complementaire benadering die rekening houdt met beeldladingsverschijnselen nabij een metaal-molecuul grensvlak. Dit eenvoudige model stelt ons in staat de aanpassing van de transportniveaus als gevolg van de polarisatie van de elektroden te berekenen, bij op/ontlading van het molecuul. Hierbij worden de ladingsverdelingen van het molecuul tussen twee metalen elektroden in meerdere ladingstoestanden gebruikt, in plaats van die in de gasfase. We berekenen deze met onze transport code door het effect van op/ontladen te simuleren met een gate veld in de potentiaal. Dit stemt goed overeen met de renormalisatie van de HOMO-LUMO gap die in de experimenten wordt geconstateerd, welke niet verklaard kan worden door concurrerende effecten zoals ladingsoverdracht of de vorming van statische– en interface dipolen.

Tenslotte richten we ons op het feit dat de transporteigenschappen van zulke systemen berucht duur zijn om in hun volledige chemische detail door te rekenen. Dit maakt het verleidelijk om soms drastische benaderingen te doen, maar er zijn maar weinig studies die de nauwkeurigheid en prestaties van zulke benaderingen vergelijken. In het laatste hoofdstuk nemen we de veelgebruikte WBL benadering en geavanceerdere post zelf-consistente berekeningen onder de loep om te beoordelen hoe deze zich vergelijken met een volledig zelf-consistente transport berekening.

We vinden redelijk goede overeenstemming tussen alle benaderingen wanneer het molecuul (en niet het metaal-molecuul grensvlak) de transporteigenschappen domineert. Echter, voor systemen waarbij het grensvlak domineert, dient (een deel van) het contactgebied te worden opgenomen in de berekening. De WBL levert goede resultaten wanneer de elektroden karakteriseerbaar zijn door een constante toestandsdichtheid nabij de Fermi energie. Het nuttige gebruik ervan is beperkter wanneer het apparaat onder spanning staat, maar op voorwaarde dat de spanningsval voornamelijk plaatsvindt in het molecuul, kan de benadering alsnog resultaten leveren die in redelijke overeenstemming zijn met volledig zelf-consistente berekeningen.

ACKNOWLEDGMENTS

PROFESSIONAL

This research was carried out with financial support from the Dutch Foundation for Fundamental Research on Matter (FOM) within the Project-86 grant agreement, and from the European Union Seventh Framework Programme (FP7/2007-2013) under the "SINGLE" and "ELFOS" grant agreements.

The computational aspects of this work were also sponsored in part by the National Computing Facilities Foundation under the grants SH-180-10 and SH-180-11 for the use of supercomputer facilities, made possible by financial support from the Netherlands Organization for Scientific Research (NWO).

I would first like to thank J. S. Seldenthuis, M. L. Perrin, D. Dulić, C. A. Martin, A. J. Shaikh, R. Eelkema, J. H. van Esch, J. M. van Ruitenbeek, H. S. J. van der Zant and particularly J. M. Thijssen for the interesting discussions and fruitful collaborations which led to each of the papers which have come out of this work, of which we are co-authors.

With regard to the rather large amount of implementation and software-engineering which is featured in my doctoral work, I would first like to thank M. Leijnse for the initial development work on transport in BAND. I am particularly indebted to P. Philipse, lead developer for BAND and A. Yakovlev, lead developer for ADF at Scientific Computing & Modelling N.V. for their assistance and guidance in the development process. Without their expertise the implementation work, particularly in terms of scalability and high-performance optimization of the physics code, would certainly not have been possible within the framework or time-frame of the Ph.D. I would also like to thank SCM for inviting me to attend the APS 2011 March Meeting as their guest, and for the hospitality extended by M. Kundrat on their behalf in Dallas.

To M. Ratner and P. Duxbury, my thanks for the great hospitality you showed me in the US, year after year, and together with F. Evers, A. Bagrets, K. Park, V. García-Suarez, P. Hedegård, J. Paaske, G. C. Solomon and C. Hermann, I am deeply indebted to you all for the deep dives discussing what's really going on in molecular transport.

Finally, I would like to express my sincerest appreciation to J. S. Seldenthuis, G. Labadze, X. Wang, C. A. Molanus, C. A. Martin and C. Padurariu for the fun, instructive and challenging chats we've had over the past few years.

PERSONAL

And then we came to the end. Skipped here, didn't you? That's okay.

I have no story to tell but mine, so let me, in fact, tell a story. I came to Delft in 2000, determined to be an aerospace engineer, and now I finish a doctorate in physics, ever surprised by life. But only two things matter to me: what I have learned and who I have met. To everyone I might here forget, my apologies.

I joined the theory group in the winter of 2007, but that's not the start of the story. The start is getting bored on the only down-time in aerospace engineering, spring 2003, and taking a quantum mechanics class with Leo Kouwenhoven. Fascinating, intelligible, and just hints of something deep. Time for a change, so I signed up for the whole undergrad program right after the summer. Fast-forward to 2005, and I'm in Herre's lab, just split from QT, burning the midnight oil on single-molecule experiments with Edgar, and mocked as a failed gamer by Benoît. Good times, but MED comes later.

Put physics on hold, and hit fast-forward again to find myself back from 21st Street, graduating in math and engineering, and talking to Jos T. about putting those computational skills to use on the theory side of single-molecule transport. This sounded like a good idea, and while you took a chance on me, the converse is also true. Yet of all the decisions I've taken, this I don't regret: choosing to learn from you. A master teacher: *doctor*, in the truest sense of the word. In fact, my memory won't be Delft, but rather breakfast at the Unicorn in Evanston, over coffee and bagels, talking physics old and new.

So in 2007, one day after defending my thesis, I joined the theory group, and found something *entirely* different from the lab, from math, and let alone from engineering. But some fun guys helped me settle in quickly. Omar (ghost-of-the-asylum), Xuhui, Fabian, Jeroen, Marnix, Stefan, Henri, Hongduo and Jiang, thanks for the welcome to the theory group. Moosa, R.I.P.

The constants of the group have of course been the staff. Miriam with boundless enthusiasm, Yaroslav with kind and well-considered words, Gerrit with the laughter of a man enjoying his life and career thoroughly, and Yuli. Yuli, who sees much more in the lives of the group than most realize, and who taught me the limits of engaging my need to explain myself. More can and should be said, but I will leave that to his own students.

Nevertheless the group changed over time, and new people joined. Let us speak of the ladies, who I begin by mentioning in one breath. Fatemeh M., Alina, Mireia, Fateme J. and Kim, you have no idea how much of a breath of fresh air you were to the group when you joined. Later came many other fascinating people, but I'm telling a story, not giving a history lesson.

Fatemeh, we shared a boss, but sadly, so little collaboration. On the other hand, I see the wisdom in you keeping a nice, safe distance from the work I was doing. Conferences were always fun together, and in the end it turns out we had so much in common. I wish you and Ali all good things in the careers to come ..

Alina, in long walks and shared coffees are deep things rooted; such time is never wasted, only spent. Mireia, the committed, the activist, but also the Catalan with whom I spoke my best Portuguese, such as it was. Se quiser podemos ter essa conversa sobre religião, que parecia estar tão preocupado em ofender-me; deixe-me saber.

Having spoken of one, there is also another Fateme. The Fateme I never understood, until you told me a story of two psychologists. And then everything made sense. It's been real, and fun, and even, as the Americans would say, real fun. I wish you patience and perseverance through the end of this journey, because you already know deep down: impossible is nothing.

As for Kim, a kindred spirit. I have no other way to describe you. From Michigan to Den Haag, and a year hence, probably back. And for free, in meeting you, I met Erin, with whom I have learned, taught, laughed, and eaten spectacularly well (usually thanks to Kim, and Tungky besides). Kim, Fateme, Erin and Tungky: perhaps our paths lead to Toronto, as all paths possibly do ..

But mentioning Tungky brings us to island people.

First there are the ones from Down Under, dear Gemma (my "other" favorite chemist) and the great Doctor Phil. But being counseled by Dr. Phil (on the best surfing spots) leads to us teaching the ICCP course, and from there we meet Tungky, who sadly never got to join us in the snows of Michigan.

Now there's something about people from the islands, and we all recognize each other. Tungky, my friend, it's been a pleasure talking life, over a hot stove filled with food so good it came with disclaimers of liability for everyone's health.

And if we're going to talk about islands and food anyways, too bad Patricia, that we never bet a burger on my finishing a Ph.D., but Mike made up for it in spades in introducing us to Cantine Mousel in Luxembourg. Quant à toi mon demi-frère, et ta chère mère, j'espère bien que nous nous verrons desormais plus souvent, de préférence aux Antilles.

In the same vein there was our postdoc Toni, also ever in for good food and good drink, and good physics besides, but an island man if ever I met one. Every time some poor naive colleague would say something that could be taken an island way, he knew exactly what I was thinking, and so I discovered that this isn't limited to the Caribbean at all ..

Now Marnix and Stefan set the tone of the early group, although they probably didn't realize it. Guys, your openness and friendship always made your office a great place to kick back and trade nerdy jokes. Stefan, in particular, I will also thank for the honor of bretzels with weißwurst in the morning snow in Munich. Fabian, you tried to balance the group but failed whenever your inner nerd peeked out, and if this piques you, do remember that a language nerd, a travel nerd and a food nerd, are all still nerds.

And speaking of nerds, we arrive at the man in pink himself, Xuhui. Man, I owe to you my deeper interest in finance, but you may not realize the encouragement you gave in science as I made a sharp transition to physicist. Thank you. You have been a friend I did not expect, and I meant what I said when Noura arrived. Together with Vera, you three are always welcome at my door, wherever it may be.

Now under this heading I should continue, but a case apart is Ciprian, who dances on the thin grey line that divides the world. I hope that you will pick sides one day, when you find something worth fighting for. In the meanwhile, I leave you some easter eggs to enjoy.

Rakesh joined the group around the same time as Toni, and was more staff than postdoc in truth. Moreover, it was great having you around both in Delft and Den Haag, and to see you and Nicole do the impossible. You took this long list of physicists, threw them in a room with a bunch of artists, and let chemistry happen. Amazing parties resulted. I still owe you for the cooking lessons, to say nothing of introducing me to Graham, Louella and Eleonore: my life has been enriched by our exchanges, of which there have surely been too few ..

François was an unusual character, and to him I owe some deep insight into physics, and my introduction to the Canard Enchaîné. Merci de m'avoir régalé de ton ironie français, mais je te remercie aussi pour notre conversation de ce matin dans le train de Paris, qui a éclairé beaucoup pour moi.

Some of the newer guys I have only just started getting to know, but so far there's still hope for the group .. The elders who stay awhile, such Antonio, Mihajlo, Peng, Hujun and Berlinson. But also the younger generation. Subtle Frans, finally relieving me of the burden of being the group's "Dutchman," Dima, (Chairman) Yan-Ting, the ever-energetic life of the party Akash, and Rodrigo who takes a sound mind in a sound body to a whole new level: please bear witness that you're both the present and the future of the group!

Having spoken about the people who sojourned long with us, I will also mention some who passed through more briefly. Rutger, met more often at festivals than colloquia, Kevin, perhaps the most laid-back office-mate of all, and Schaafsma: de lange gesprekken over geloof en politiek waren altijd de moeite waard. Then Bas & Sasja, who announced spring to the group, and Rianne, who I shoulda never let go to St. Maarten. Joost de G. who we "introduced" to spices, Omer who rocked on down I-94 with me, and Guen, the entrepreneur I expect to see in Silicon Valley some day: it's been fun.

So ending the theoretical tale I come to my office mates. Drostie: physicist, hacker, dreamer, and voted most likely to found his own religion two years running; it's been a pleasure. And Marcin, someone I nearly missed out on getting to know better, which I'd surely regret. I fear that you may yet contribute extensively to my knowledge of all things alcoholic and behavioral. Cheers to you and Cecile.

Then finally Gio, my brother. You give me pause. I have spoken much but also listened, and learned, so much from both you and Keti. Zoetermeer was a good place for us by fours and sixes more than once, but the walks have done me just as well.

May the road always rise up to meet you ..

Sitting between the groups at opposite ends of the corridor, I will also thank, and thank sincerely, the secretaries who kept everything running. You made my life much easier than it had to be (truly a rare occurrence). Yvonne en Marjolein bij theorie enerzijds, Monique, Irma en Maria bij MED anderzijds, echt bedankt voor alle hulp, suggesties en ondersteuning. De TU heeft niet door wat jullie waard zijn.

So having talked about one surrogate family, I can do no less in addressing another. MED, home of the "glorious leader" (all Edgar's terminology, of course). Such a shame that he shot down Bo's full-faculty salute. Herre, you will give that intreerede one day, and all of us will be waiting ..

Unofficially though, I am possibly the current oldest ghost haunting MED, since I outrank even Seldenthuis. Good times in the lab with Edgar and Benoît led to a more distant relationship from the halls of theory, but the advent of "my friend!!" Diana quickly cured that. Moreover, I always felt like Seldenthuis' office was my second home anyways, so it's not like I wasn't around. But I had to hide at times, hunted by the Franco-Serbian alliance .. though in seriousness, the collaboration with you, Diana, and Mickael, our rock climbing physics-ninja, was a highlight of the Ph.D. Let it also be said that the "little rounds" were always fun, though I thought that after August I would have to miss them. Turns out "de Bank" believes in them too ..

Now Manohar, Samir and Alexander .. what happens in Dallas, stays in Dallas, but you guys taught me a new motto that deserves to be shared: "the random is good; embrace the random." Sasha, much luck to you and your family in the wonderful world of technology in Eindhoven. Samir, keep me in the loop on where you end up in science, and may the random be with you always.

And then I come to Ferry, my favorite chemist. As if I'm the only one who's ever said that to you. But truly man, you were the octopus, with so many projects running simultaneously, you made the rest of us feel bad. Much luck and success in Boston, where I know you're already no doubt at the start of something big.

Then there was Christian, a subtle man, and perhaps the kindest I know. Together with Dapeng, you guys made a great team in physics and comedy ("yes"), but Christian, I swear I've never heard you utter a harsh word about anyone. I hope to make up failing to see Nature London as soon as possible, lest it be about me.

Ben, Ronald, Hidde, Harold, Warner, Carlos, Andres, Michele, and the rest, I'm impressed with how you've managed to keep some of the original spirit of the group, while giving it some flavor of your own, and it's good to see Gary and Sander settled in as well. I hope that you will all succeed in passing what you take from the super-postdocs and ghosts on to new generations to come.

Yet at the end of this story, I find Jos, our unusually tall, blonde and dutch-accented American. We began at nearly the same time, and seems like we've always been working on something or other together. There was Evanston and Chicago, more than once, and Mons, and Copenhagen, and Switzerland, to say nothing of all the talks we gave on the other guy's research. For both of us the future is uncharted, but I sincerely hope we'll work together again, and finally sit down one Sunday as well.

Two friends remain, who should not pass without mention. Chris, we've been scheming since we were 15, from redirecting traffic and filtering lakes to building hovercrafts and Tesla coils, and I still feel like we could simply trade places at my defense without a care in the world. Thanks for being there. Joost, who cannot be here, thanks for how hard you tried, and irmão, muito obrigado por tudo nestes últimos anos, ainda que nos tivéssemos visto muito pouco.

So now I will say something for myself, which is an acknowledgment of another kind. Life isn't easy, but in the name of everyone who's been through the past 6 years with our (extended) family, let me recall "what we say to death, when we meet him in the street. Not today."

There is bitter and sweet, but all that I might want to say on the subject is summed up better than I ever could by the preacher: "[there is] a time to weep, and a time to laugh; a time to mourn, and a time to dance." In my time in the Netherlands, there have been ample amounts of each, and in each of the four I have found new friendship, and fallen in love again with life. In the time to weep, thank you Kim and Erin. In the time to laugh, thank you to all the friends who have walked by my side (trippin' all the way) and in particular, Marlo & Bas, Chris, Joost, Big Mike, Chicco, van Delden, Pieter & Paul, Li & Nuno. In the time of mourning, Vela, Percey and Johnny Z, and alas recently Eric, Jessika and Little Mary too. Finally, in the dancing first Perle, Joost, Meltem and Dorien, and later Vanessa, Chris and Mel, then Alina, and once again Perle.

Tenslotte aan Vanessa, en de familie .. waar, en wie zou ik zijn zonder jullie warmte, diepte, knuffels, luisterend oor, en alles waarin jullie mij hebben gevormd, orkaan na storm, van wijs-neus tot weledelgestrenge tong. Wie had ooit gedacht dat we zo lang in Nederland zouden blijven, ondanks de blijvende drang om zo snel mogelijk weg te wezen? En sterker nog, dat er een heus jaar is geweest waarin we zelfs allemaal "gezellig" in Nederland hebben gewoond. Daar zijn we ook met elkaar doorheen gekomen, en dat mag best gezegd worden!

Daarom, naast alles anders: diep bedankt voor jullie steun, ik hou van jullie.

POSTSCRIPT

And having said enough, there remain two things.

First, to express my deep joy to the people who've been a part of my life for the past 5 years; the second, to those who have understood me best, and also least.

How we danced through the night,
with the hackers and painters
Physicists, sculptors, minds and bodies as one
Speaking, then laughing and pushing our limits
Pinay and Caribe,
Indian, Catalan.
We danced and we drank and we dreamed of the future
When all now inside us
might well memory be
So we opened our hearts and we spun one another
and we danced through the night,
just us, subtle makers.

December 2011

Not all who seek, desire the same ends,
Not all who speak, say the same by common tongue,
And not all who wander, are lost.

July 2012

Curriculum Vitæ

2007–2012	**TU Delft, Kavli Institute of Nanoscience** **PhD Researcher** in Theoretical Physics, with thesis: *On Conductance and Interface Effects in Molecular Devices* Promotor: Prof. dr. ir. H. S. J. van der Zant Supervisor: Dr. J. M. Thijssen
2003–2007	**TU Delft, Faculty of Applied Sciences** **BS in Applied Physics,** *cum laude*, with thesis: *Transport through Single OPV-5 Molecules*
2005–2007	**TU Delft, Department of Applied Mathematics** **MS in Applied Mathematics,** *cum laude*, with thesis: *On the Determination of Approximations of First Integrals for Few–Body Gravitational Problems*
Fall 2005	**University of Texas at Austin, Center for Space Research** **Internship** with Dr. C. Ocampo
2004–2007	**TU Delft, Faculty of Aerospace Engineering** **MS in Aerospace Engineering,** *cum laude*, with thesis: *On the Integral–Conservative Numerical Solution of Few–Body Gravitational Problems*
2000–2004	**BS in Aerospace Engineering,** with collaborative thesis: *SIREN Mission: Feasibility Study for a Low Cost Space Telescope*
1994–2000	**H. Milton Peters College, St. Maarten** **VWO diploma**

Christopher was born in Willemstad, Curaçao in 1982, and grew up on the friendly island of St. Maarten. He has been, at times, a water rat, a lab rat, a consulting engineer and a researcher, and still has no idea what he wants to be when he grows up.

LIST OF PUBLICATIONS

4. C. J. O. Verzijl, M. L. Perrin, D. Dulić, H. S. J. van der Zant and J. M. Thijssen,
   Accounting for Image Effects in Transport Calculations,
   · · · (in preparation for submission)

3. C. J. O. Verzijl, J. .S. Seldenthuis and J. M. Thijssen,
   Comparing Transport Approximations in the DFT+NEGF Approach,
   · · · (submitted to J. Chem. Phys.)

2. M. L. Perrin, C. J. O. Verzijl, C. A. Martin, A. J. Shaikh, R. Eelkema, J. H. van Esch, J. M. van Ruitenbeek, J. M. Thijssen, H. S. J. van der Zant and D. Dulić,
   Large Tunable Image-Charge Effects in Single-Molecule Junctions,
   · · · (submitted to Nat. Nano.)

1. C. J. O. Verzijl and J. M. Thijssen,
   A DFT-based Molecular Transport Implementation in ADF/BAND,
   · · · (accepted for publication in J. Phys. Chem. C, 2012; doi:10.1021/jp3044225)

Kindness in words creates confidence.
Kindness in thinking creates profoundness.
Kindness in giving creates love.

Lao Tzu